Two-Dimensional Magneto-Optical Trap as a Cold Atomic Beam Source for High-Precision Spectroscopy on Lithium-6

Dissertation zur Erlangung des akademischen Grades „Doktor der Naturwissenschaften“

am Fachbereich Physik, Mathematik und Informatik
der Johannes Gutenberg-Universität in Mainz

vorgelegt von

Gregor Schwendler

geboren in Wiesbaden

Mainz, den 26. Februar 2026

Betreuer: Prof. Dr. Randolf Pohl
Gutachter: Prof. Dr. Patrick Windpassinger

To Paula

Abstract

High-precision laser spectroscopy of light atoms provides experimental tests of bound-state quantum electrodynamics, enables the determination of fundamental constants, and probes nuclear structure. As the lightest alkali metal, lithium is of particular interest: its three-electron structure allows high-accuracy tests of few-electron atomic theory, while isotope shift measurements combined with predictions from theory enable the extraction of nuclear charge radius differences. Recent determinations of the ^{6,7}Li isotope shift have revealed inconsistencies in the measurements of the D lines [1].

This thesis presents the realization of a two-dimensional magneto-optical trap (2D MOT) [2] as a source of a cold atomic ^{6}Li beam. Compared to conventional hot beam experiments, the atomic velocities are reduced by at least one order of magnitude. This setup drastically suppresses the first-order Doppler shift in the single-photon D line transitions and still enables spectroscopy outside the inhomogeneous magnetic fields of a MOT responsible for Zeeman shifts.

We demonstrate a 2D MOT with an optimized atomic areal density of $\sim 3 \times 10^7\,\mathrm{cm}^{-2}$ in the center of the atomic cloud and a trapped atom number of typically 2×10^5 to 4×10^5 with a loading time of $\sim 2\,\mathrm{ms}$. Atoms are extracted from the trap using a pulsed continuous-wave, blue detuned push beam. Time-of-flight and Doppler shift measurements demonstrate tunable mean axial velocities between 60 m/s and 120 m/s, with velocity spreads ranging from 10 m/s to 35 m/s (FWHM). Due to geometric collimation, the transverse velocity is constrained to below approximately 1 m/s. The system can provide an estimated total cold atomic flux on the order of 10^8 atoms/s.

Preliminary fluorescence spectroscopy on the ^{6}Li D_2 transition yields results consistent with previous measurements and allows for a quantitative assessment of the dominant systematic effects. We achieved count rates on the order of $\sim 1 \times 10^4$/s, comparable to those of previous hot beam experiments, reaching a statistical uncertainty on the order of 10 kHz for the line center within a few minutes.

These results establish the 2D MOT as a platform for high-precision lithium spectroscopy and outline a path toward sub-10 kHz precision on the D lines through the planned implementation of magnetic field compensation and an active fiber-based retroreflector [3]. Ultimately, this work aims to improve determinations of the ^{6,7}Li isotope shift and stringent tests of atomic theory through comparison with more precise nuclear charge-radius measurements from muonic lithium.

Zusammenfassung

Die hochpräzise Laserspektroskopie leichter Atome ermöglicht die experimentelle Überprüfung der Quantenelektrodynamik gebundener Zustände, die Bestimmung fundamentaler Konstanten und die Untersuchung der Kernstruktur. Lithium, als leichtestes Alkalimetall, ist dabei von besonderem Interesse: Die relativ einfache elektronische Struktur ermöglicht hochpräzise Tests der Atomtheorie mit drei Elektronen, während die Messung der Isotopieverschiebung in Kombination mit theoretischen Vorhersagen die Bestimmung von Differenzen der Kernladungsradien ermöglicht. Bisherige Bestimmungen der ^{6,7}Li-Isotopieverschiebung weisen jedoch Unstimmigkeiten in den Messungen der D-Linen auf [1].

Hier zeigen wir den Aufbau und die Optimierung einer zweidimensionalen magneto-optischen Falle (2D-MOT) [2] als Quelle für einen kalten atomaren ^{6}Li-Strahl. Im Vergleich zu herkömmlichen Experimenten mit heißem Atomstrahl wird die mittlere Atomgeschwindigkeit um mindestens eine Größenordnung reduziert. Dadurch wird die Doppler-Verschiebung erster Ordnung in den Einzelphotonen-Übergängen der D-Linie drastisch reduziert. Außerdem ermöglicht der Aufbau Spektroskopie außerhalb des inhomogenen Magnetfelds einer MOT, welches zu Zeeman-Verschiebungen führen würde.

Wir präsentieren eine 2D-MOT mit einer atomaren Flächendichte von $\sim 3 \times 10^7\,\mathrm{cm}^{-2}$ in der Mitte der Wolke und typischerweise 2×10^5 bis 4×10^5 gefangenen Atomen innerhalb von $\sim 2\,\mathrm{ms}$. Die Atome werden mit einem gepulsten, kontinuierlichen, blau verstimmten Laserstrahl aus der Falle beschleunigt. Messungen der Flugzeit und der Dopplerverschiebung zeigen einstellbare mittlere Axialgeschwindigkeiten zwischen $60\,\mathrm{m/s}$ und $120\,\mathrm{m/s}$ mit einer Geschwindigkeitsbreite im Bereich von 10 bis $35\,\mathrm{m/s}$ (FWHM). Aufgrund geometrischer Kollimation kann die Transversalgeschwindigkeit auf weniger als etwa $1\,\mathrm{m/s}$ begrenzt werden. Vorläufige Fluoreszenzspektroskopie am ^{6}Li D_2-Übergang liefert Ergebnisse, die mit bisherigen Messungen übereinstimmen und ermöglicht eine quantitative Bewertung der dominanten systematischen Effekte. Wir erreichen Zählraten in der Größenordnung von bis zu $\sim 1 \times 10^4/\mathrm{s}$, vergleichbar mit denen früherer Experimente am heißen Strahl, und erreichen innerhalb weniger Minuten eine statistische Unsicherheit in der Größenordnung von $10\,\mathrm{kHz}$ auf die Übergangsfrequenz.

Unsere Ergebnisse zeigen, dass eine 2D-MOT als Plattform für hochpräzise Lithiumspektroskopie geeignet ist, und skizzieren den Weg zu einer Genauigkeit unterhalb von $10\,\mathrm{kHz}$ durch die geplante Implementierung einer Magnetfeldkompensation und eines aktiven faserbasierten Retroreflektors [3]. Das Ziel des Experiments ist eine verbesserte Bestimmung der ^{6,7}Li-Isotopieverschiebung und Überprüfung der Atomtheorie durch den Vergleich mit verbesserten Messungen der absoluten Kernladungsradien mittels myonischem Lithium.

Contents

1 Introduction

High-precision laser spectroscopy of light atomic systems has long been a cornerstone for testing bound-state quantum electrodynamics (QED), determining fundamental constants, and probing nuclear structure [4–7].

For several decades, atomic hydrogen has served as a benchmark system for precision tests of QED in bound states [8–10]. Growth in the field has been accelerated with laser spectroscopy of muonic hydrogen [11], which led to the so-called *proton radius puzzle*. In muonic atoms, the muon's approximately 200-times larger mass compared to the electron results in a much smaller Bohr radius, greatly enhancing sensitivity to the nuclear charge distribution and amplifying finite-size effects.

Precision measurements were also extended to deuterium [12] and later to muonic deuterium [13], allowing for stringent consistency checks of nuclear structure effects across isotopes.

In parallel, there has been substantial progress in calculations of higher order QED terms for two-electron systems [14–16]. This can be combined with precision spectroscopy of helium [17] and helium-like ions such as Li^+ [18] and C^{4+} [19]. These systems provide stringent tests of the fine-structure constant and higher-order QED contributions, while for example helium-like lithium ions offer the additional advantage of probing the nuclear structure of lithium in a two-electron system.

Complementary measurements of the nuclear charge radii of muonic helium-3 [20] and helium-4 [21] have further enriched this picture. The comparison of results from elastic electron scattering, electronic spectroscopy, and muonic atom spectroscopy have repeatedly revealed discrepancies that challenge our understanding of nuclear structure and bound-state QED.

Motivated by these developments, current research is now extending beyond two-electron systems toward more complex atoms such as lithium. It offers a unique testing ground for many-body QED effects, nuclear structure contributions, and isotope-dependent phenomena.

1.1 High-Precision Spectroscopy on Lithium

As the lightest alkali atom, lithium is of particular interest for high-precision spectroscopy. Accurate isotope shift measurements, in combination with state-of-the-art theory, enable the determination of nuclear charge radius differences and provide stringent tests of few-electron atomic theory. It is unique among the alkali metals in appearing as both a stable fermionic isotope, ^{6}Li with nuclear spin $I = 1$, and a stable bosonic isotope, ^{7}Li with nuclear spin $I = 3/2$.

Like all alkali metals, lithium exhibits an optically accessible electric-dipole transition directly from the ground state. The corresponding D line transitions (from $2s\,^2S_{1/2}$ to $2p\,^2P_J$) can be exited near a wavelength of 671 nm and have a natural

linewidth of approximately 5.9 MHz [22]. A comprehensive overview of the atomic properties of ^{6}Li can be found, for example, in the Appendix of Ref. [23].

Figure 1.1 shows the energy levels and allowed hyperfine transitions for the D lines of the stable lithium isotopes together with the isotope shift (IS). Relative line intensities on a frequency scale are shown at the bottom.

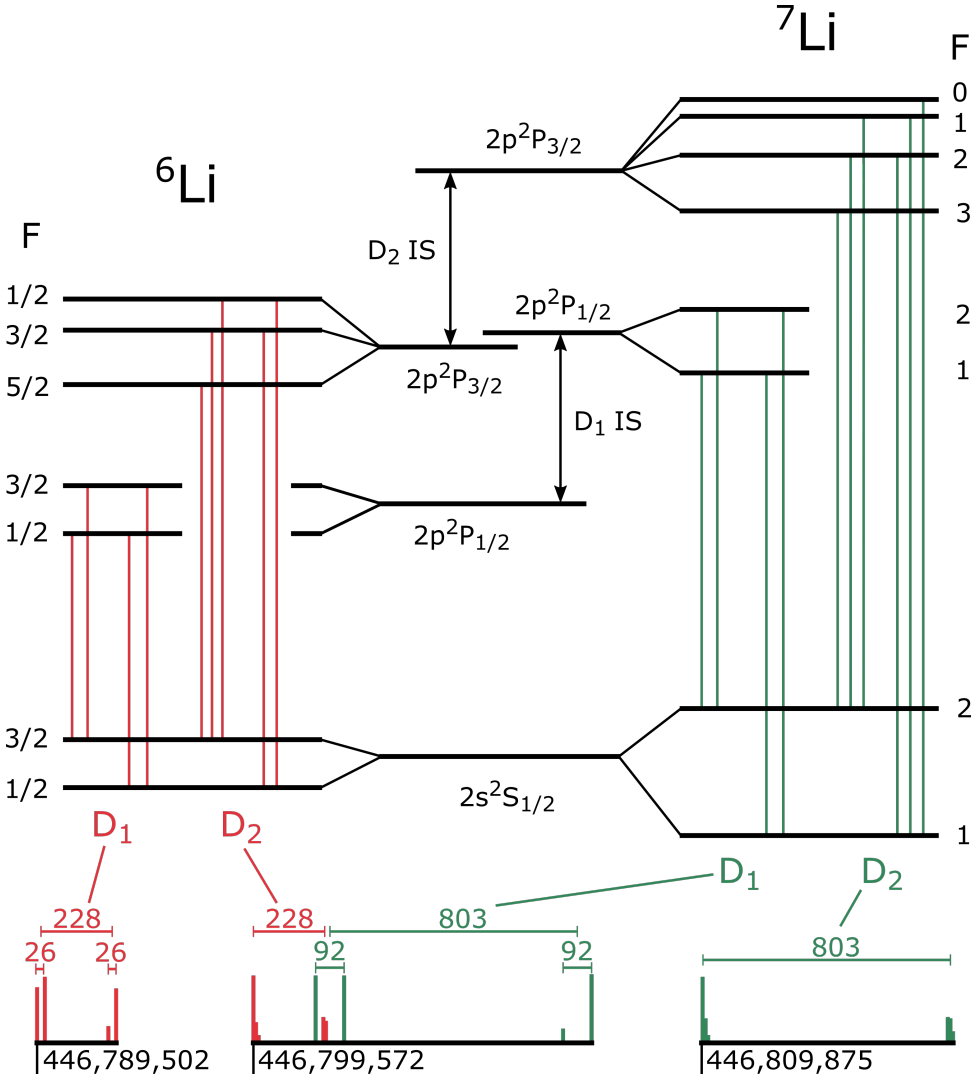

Figure 1.1: Energy levels and allowed hyperfine transitions for the D lines of the stable lithium isotopes, including the isotope shift (IS). Relative transition strengths are indicated at the bottom on a frequency scale. Resolved hyperfine splittings and absolute transition frequencies are given in MHz. Figure adapted from Ref. [24].

These properties make lithium an ideal system for extending precision tests of bound-state QED beyond one- and two-electron atoms. At the same time, its nontrivial nuclear structure allows for the investigation of nuclear-size and nuclear-polarization effects [25]. Nuclear-structure effects in lithium have recently been addressed using *ab initio* nuclear methods [26]. For example, Yang *et al.* performed precise calculations of Zemach radii and nuclear-structure contributions to the hyperfine splitting of lithium isotopes [27].

Complementary to electronic spectroscopy, within the QUARTET collaboration, x-ray spectroscopy of muonic lithium isotopes is currently being pursued, aiming to improve the error on the nuclear charge radii by one order of magnitude [28]. On the theory side, dedicated studies of muonic lithium have been initiated to support and interpret these measurements [29].

Lithium also offers a platform to test physics beyond the Standard Model by comparing results from electronic laser spectroscopy with complementary measurements in muonic atoms or electron scattering. Discrepancies between these methods would point to effects beyond current atomic and nuclear theory as pointed out for the proton [30–32].

Recent theoretical advances have further underscored the relevance of lithium spectroscopy. High-precision QED calculations of transition frequencies, isotope shifts, and fine structure splittings have been performed by Puchalski, Pachucki, and collaborators [33–35].

1.1.1 Theoretical Framework: Perturbative Nonrelativistic QED

Achieving accurate theoretical predictions for the energy levels of light atomic systems requires the inclusion of relativistic, recoil, and quantum electrodynamic (QED) effects beyond the nonrelativistic Schrödinger description. The most fundamental approach for few-electron systems is based on the nonrelativistic QED (NRQED) framework [36], in which all corrections are obtained perturbatively as an expansion in powers of the fine-structure constant α and the reduced electron mass to nuclear mass ratio $\eta = -m_e/(m_e + m_N)$, where m_e and m_N denote the electron and nuclear mass, respectively. Within this framework, the energy of each level is given by [33]:

$$\begin{aligned} E = {} & m\alpha^2 \left[\mathcal{E}^{(2,0)} + \eta\mathcal{E}^{(2,1)} + \eta^2\mathcal{E}^{(2,2)}\right] \\ & + m\alpha^4 \left[\mathcal{E}^{(4,0)} + \mathcal{F}^{(4,0)} + \eta\left(\mathcal{E}^{(4,1)} + \mathcal{F}^{(4,1)}\right)\right] \\ & + m\alpha^5 \left[\mathcal{E}^{(5,0)} + \eta\mathcal{E}^{(5,1)}\right] \\ & + m\alpha^6\mathcal{E}^{(6,0)} + m\alpha^7\mathcal{E}^{(7,0)} + \ldots, \end{aligned} \tag{1.1}$$

where $\mathcal{E}^{(m,n)}$ and $\mathcal{F}^{(m,n)}$ are dimensionless spin-independent and spin-dependent coefficients, respectively. The superscripts (m, n) denote the order in α^m and η^n.

The leading contribution $\mathcal{E}^{(2,0)} \equiv \mathcal{E}_0$ is obtained from the solution of the nonrelativistic Schrödinger equation,

$$\mathcal{H}_0\Psi = \mathcal{E}_0\Psi, \tag{1.2}$$

$$\mathcal{H}_0 = \sum_a \left(\frac{p_a^2}{2} - \frac{Z}{r_a}\right) + \sum_{a<b} \frac{1}{r_{ab}}. \tag{1.3}$$

Here, Ψ denotes the nonrelativistic electronic wave function, $p_a = -\mathrm{i}\nabla_a$ is the momentum operator of electron a, r_a is the electron–nucleus distance, r_{ab} is the interelectronic distance, and $Z = 3$ is the nuclear charge number.

Successive orders in the expansion account for increasingly subtle effects. The $m\alpha^4$ terms include fine-structure splitting and the leading finite nuclear size correction. The $m\alpha^5$ terms represent the dominant QED contribution, including the computa-

tionally demanding Bethe logarithm $\ln k_0$, which determines the dominant part of the electron self-energy [37]. The relativistic $m\alpha^6$ corrections are particularly challenging to calculate; closed-form expressions exist only for two-electron systems, while approximate formulas based on hydrogenic values must be used for lithium. Complete formulas for the $m\alpha^6$ contributions in the QED corrections to the $2P_{1/2} - 2P_{3/2}$ fine structure splitting are provided in Ref. [35]. Higher-order contributions such as $m\alpha^7$ are estimated using formulas derived for hydrogenic systems [5].

Table 1.1 summarizes the spin-independent contributions to the 2P − 2S transition frequencies in ^{6}Li and ^{7}Li, as well as their contributions to the isotope shift.[1] While the dominant contribution to the absolute transition frequency arises from the nonrelativistic term $m\alpha^2$, the isotope shift of approximately 10.5 GHz is primarily determined by the recoil correction of order $m\alpha^2\eta$, commonly referred to as the *normal mass shift*. In contrast, the leading nuclear size contribution $\mathcal{E}_{\text{fs}}^{(4,0)}$ and the field-shift coefficient C_{AB} contribute only at the level of a few megahertz, corresponding to the so-called *field shift* (see Section 1.1.2). Detailed discussions of these contributions can be found in Refs. [33, 35, 38, 39].

Table 1.1: Spin-independent contributions to the transition energy $\nu(2P - 2S)$ for ^{6}Li and ^{7}Li, and to the isotope shift $\Delta\nu_{67}$, adapted from Ref. [33]. The nuclear charge radius for ^{6}Li is taken as $r_c = 2.56\,\text{fm}$ [40].

Energy	$\mathcal{E}^{(m,n)}$	ν_6 (MHz)	ν_7 (MHz)	$\Delta\nu_{67}$ (MHz)
$m\alpha^2$	0.067 903 791 259 0(16)	446 785 483.5(1)	446 785 483.5(1)	
$m\alpha^4$	0.267 612 1(4)	93 765.1(2)	93 765.1(2)	
$m\alpha^5$	−3.469(3)	−8 870(8)	−8 870(8)	
$m\alpha^6$	−14.4(1.4)	−269(26)	−269(26)	
$m\alpha^7$	217(54)	30(7)	30(7)	
$m\alpha^2\eta$	0.123 007 926 0(3)	−73 826.6	−63 293.1	−10 533.510 5
$m\alpha^4\eta$	−0.267 591(2)	8.6	7.3	1.220 2
$m\alpha^5\eta$	1.134(3)	−0.3	−0.2	−0.037 7(1)
$m\alpha^6\eta$	−46(12)			0.011(3)
$m\alpha^2\eta^2$	−0.004 870(4)			−0.070 7
$\mathcal{E}_{\text{fs}}^{(4,0)}$	$-1.045608\,r_c^2$	−16.0	−14.0	
C_{67}				$-2.465\,8$ /fm^2
Total		446 796 306(28)	446 806 840(28)	−10 532.388(3)

The uncertainty of the absolute transition frequencies is dominated by the incompletely known $m\alpha^6$ QED contributions. However, these mass-independent terms presented here are identical for both isotopes and therefore cancel in the isotope shift, resulting in a significantly higher theoretical precision for $\Delta\nu_{67}$.

Table 1.2 presents the theoretical contributions to the spin-dependent fine-structure splitting $\nu(2P_{3/2} - 2P_{1/2})$ in ^{6}Li and ^{7}Li, along with the corresponding fine-structure isotope shift. The dominant contribution arises from the $m\alpha^4$ term, which is identi-

[1] Note that the $m\alpha^5$ contribution for ^{6}Li has been corrected to account for a typographical error in the original reference (confirmed by K. Pachucki, private communication).

cal for both isotopes. The mass-dependent $m\alpha^4\eta$ term contributes differently to each isotope, giving rise to a small isotope shift of approximately $-0.4\,\mathrm{MHz}$. Higher-order QED corrections at orders $m\alpha^6$ and $m\alpha^7\ln(\alpha)$ have been calculated by Puchalski and Pachucki [35]. Additionally, mixing between the $2\mathrm{P}_{3/2}$ and $2\mathrm{P}_{1/2}$ levels due to hyperfine interaction contributes differently to the two isotopes [39].

Table 1.2: Theoretical contributions to the fine-structure splitting in ^{6}Li and ^{7}Li, and the fine-structure splitting isotope shift (SIS) in MHz, taken from Ref. [33, 35]. The uncertainty of the total value comes mainly from numerical inaccuracies of terms in the order of $m\alpha^6$ and from the neglected terms in the order of $m\alpha^7$, which are negligible only for the isotope shift.

Energy (MHz)	$\nu_6(2\mathrm{P}_{3/2}-2\mathrm{P}_{1/2})$	$\nu_7(2\mathrm{P}_{3/2}-2\mathrm{P}_{1/2})$	$\Delta\nu_{67}(2\mathrm{P}_{3/2}-2\mathrm{P}_{1/2})$
$m\alpha^4$ [39]	10 053.7072(83)	10 053.7072(83)	
$m\alpha^4\eta$ [39]	−2.7868(6)	−2.3891(5)	−0.3977(8)
$m\alpha^6$ [35]	1.63(5)	1.63(5)	
$m\alpha^7\ln(\alpha)$ [35]	0.15	0.15	
Mixing [39]	0.012 17	0.159 16	−0.146 99
Total	10 052.72(6)	10 053.25(6)	−0.5447(1)
Experiment [1]	10 052.779(17)	10 053.310(17)	−0.531(24)

The uncertainty of absolute fine-structure splitting comes mainly from the numerical inaccuracies of terms in the order of $m\alpha^6$ and from the neglected terms in the order of $m\alpha^7$, resulting an uncertainty of approximately 60 kHz. This is currently larger than the experimental uncertainty of 17 kHz achieved by Brown *et al.* [1].

In contrast, the splitting isotope shift (SIS) $\Delta\nu_{67}(2\mathrm{P}_{3/2}-2\mathrm{P}_{1/2})$ provides a stringent test of theory. In this difference quantity, the dominant QED and nuclear size contributions largely cancel, leaving primarily mass-dependent and hyperfine-mixing contributions. As shown in Table 1.2, the theoretical prediction of −0.5447(1) MHz is nearly two orders of magnitude more precise than the experimental value of −0.531(24) MHz [1], highlighting the potential for future experimental improvements.

1.1.2 Nuclear Size Effect and Isotope Shift

In addition to relativistic and QED effects, atomic energy levels are modified by the finite spatial extent of the nucleus. For an extended nucleus, the leading-order finite-size contribution to the energy is given by

$$\mathcal{E}_{\mathrm{fs}}^{(4,0)} = \frac{2\pi Z}{3}\,\frac{r_c^2}{\lambda\!\!\!^{-2}}\sum_a \left\langle \delta^3(\mathbf{r}_a)\right\rangle, \tag{1.4}$$

where r_c^2 denotes the mean-square nuclear charge radius and $\lambda\!\!\!^{-} = \hbar/(m_e c)$ is the reduced Compton wavelength of the electron. The operator $\delta^3(\mathbf{r}_a)$ is the three-dimensional Dirac delta function, which probes the electronic wave function at the position of the nucleus.

Given the theoretical prediction for the isotope shift excluding finite nuclear size effects, $\Delta\tilde{\nu}_{\text{theo}}$, and the field-shift coefficient C_{AB}, the mean-square nuclear charge radius of an isotope A can be determined from a precise measurement of the experimental isotope shift $\Delta\nu_{\text{exp}}$ relative to a reference isotope B. The relation is given by

$$r_{cA}^2 = r_{cB}^2 + \frac{\Delta\tilde{\nu}_{\text{theo}} - \Delta\nu_{\text{exp}}}{C_{AB}}, \tag{1.5}$$

where r_{cB}^2 denotes the known mean-square charge radius of the reference isotope.

So, if the absolute charge radius of one isotope (the *anchor*) is known independently, absolute nuclear charge radii for the entire isotope chain can be deduced. Nörtershäuser *et al.* [41] demonstrated that, once the absolute radius of a reference isotope (here ^{6}Li) is known, absolute charge radii of other isotopes, including short-lived species such as ^{8}Li, ^{9}Li, and ^{11}Li, can be deduced.

Figure 1.2 shows the nuclear charge radii r_p of the lithium isotopes as extracted from isotope-shift measurements (black) together with predictions by different nuclear models. The shaded gray band illustrates the dominant systematic uncertainty associated with the reference charge radius.

This highlights the need for improved anchor measurements, which could, for example, be provided by spectroscopy of muonic lithium. If the nuclear charge radius were improved by an order of magnitude, as proposed, the extraction of charge radii from isotope shifts would no longer be limited by the uncertainty of the absolute reference radius. This would enable tests of the combined predictions of atomic theory and isotope shift measurements against absolute charge radius determinations.

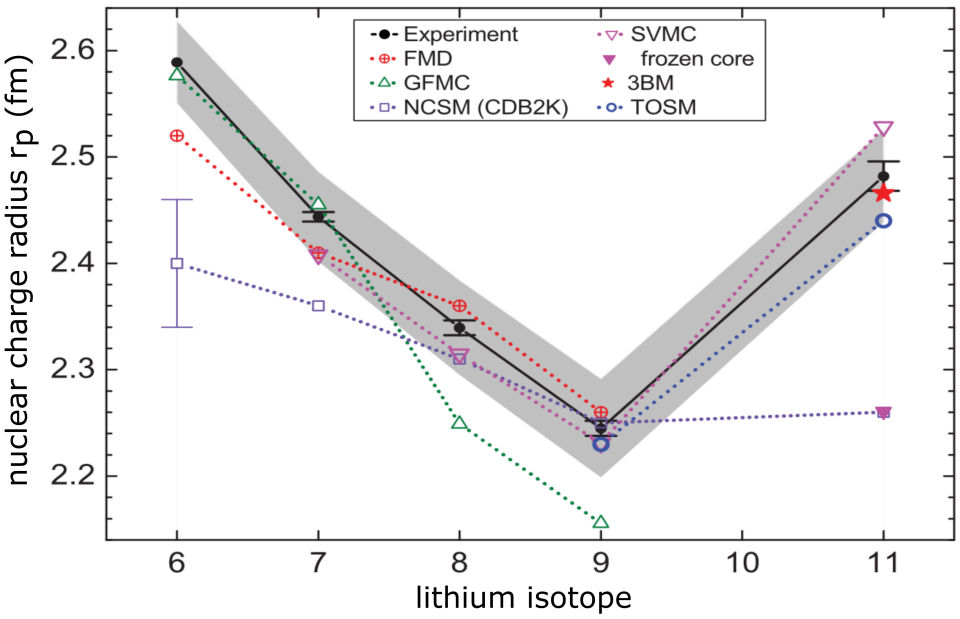

Figure 1.2: Nuclear charge radii r_p of the lithium isotopes as extracted from isotope-shift measurements (black). The error bars represent the uncertainties from the isotope shift determination only. The additional systematic uncertainty associated with the reference charge radius (here ^{6}Li) is indicated by the shaded gray band. This can be compared to predictions by different nuclear models. Figure adapted from Ref. [42].

1.1.3 Previous Measurements on Lithium

The first determinations of the isotope shift were obtained from elastic electron-nucleus scattering experiments [40, 43–45].

Figure 1.3 summarizes the experimental determinations of the difference in mean-square charge radii between ^{7}Li and ^{6}Li. The results are shown in chronological order and grouped according to the measurement technique. The spectroscopic results are based on precision measurements of the 2s–3s [46–49] and 2s–2p (D line) [50–55] atomic transitions. It can be seen that the determinations of the difference in mean-square charge radii from the D_1 and D_2 transitions exhibit a noticeable scatter.

The most recent value in this figure was obtained by Sansonetti *et al.* [1], who measured the D lines of ^{6}Li and ^{7}Li with a relative accuracy of 5×10^{-11} and an absolute uncertainty of about 20 kHz. As shown in Table 1.2, their measurements of the absolute fine structure splittings are more accurate than current theoretical predictions, while their splitting isotope shift measurement is nearly two orders of magnitude less precise than theory.

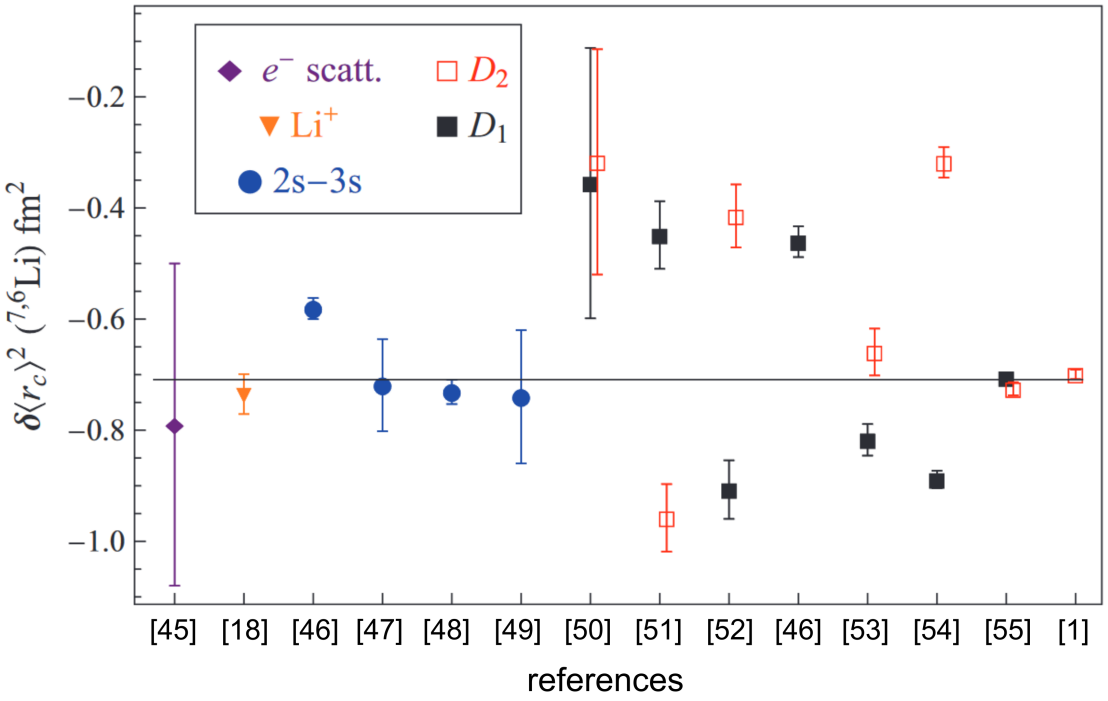

Figure 1.3: Measurements of the difference in mean-square charge radius between ^{7}Li and ^{6}Li. The data points are grouped by measurement type and ordered chronologically within each group. The solid black line represents the weighted average of the results from Refs. [18, 45, 48, 55]. Figure adapted from Ref. [1].

In their experiment, Sansonetti *et al.* employed a hot lithium atomic beam generated from an oven operated at 450 °C. The mean atomic velocity was approximately $v \approx 1300$ m/s. The beam was collimated using a 135 cm-long tube with a 2 mm diameter aperture, which resulted in an atomic flux on the order of 10^9 atoms/s and a residual Doppler broadening of about 4 MHz.

A simplified schematic of their setup is shown in Figure 1.4. A weak probe laser beam with a power of approximately 3 µW intersected the collimated atomic beam at a right angle and was retroreflected using a corner cube. The retroreflected beam could be modulated with a chopper wheel, and the resulting atomic fluorescence was collected with a photomultiplier tube (PMT), yielding count rates on the order of 1×10^3/s to 1×10^4/s. The linear polarization of the spectroscopy beam was controlled by a rotatable half-wave plate.

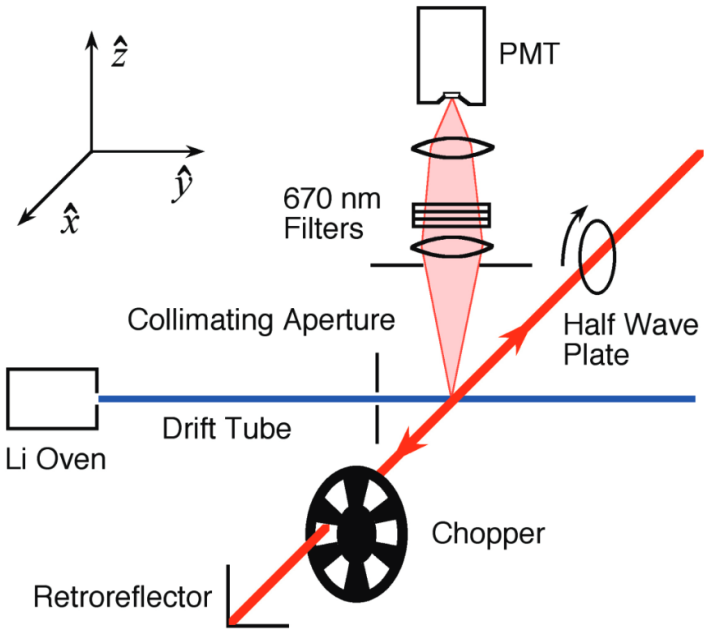

Figure 1.4: Simplified schematic of the experimental setup used by Sansonetti *et al.* [55] for high-precision laser spectroscopy of lithium. A collimated hot atomic beam (blue) intersects a retroreflected probe laser (red). The fluorescence is collected with a photomultiplier tube (PMT). Figure taken from Ref. [1].

In the course of these measurements, the effect of quantum interference (QI), described by Horbatsch and Hessels [56], was clearly observed and investigated. When two neighboring atomic resonances are present, the observed spectral line shape deviates from a simple Lorentzian profile [57]. If the line shape is fitted with a simple Lorentzian profile as expected without QI this would lead to a systematic shift of the line center.

This effect is particularly enhanced for the lithium D lines, since their natural linewidth is in the same order of magnitude as the hyperfine splitting. The effective shift for the ^{7}Li D_2 transition is shown in Figure 1.5, here the apparent line center obtained from a Lorentzian fit depends on the polarization angle θ_L between the laser polarization vector and the detection axis. In a complete description of the line shape, the extracted transition frequency is independent of polarization. At the so-called *magic angle*, $\theta_L \approx 54.7°$, the QI-induced shift is zero [57]. The presence of QI in lithium spectroscopy may also help to explain part of the scatter observed in the determination of the difference in mean-square charge radius shown in Figure 1.3, since a QI-induced shift of 1 MHz would correspond to a nuclear size shift of approximately 0.4 fm^2.

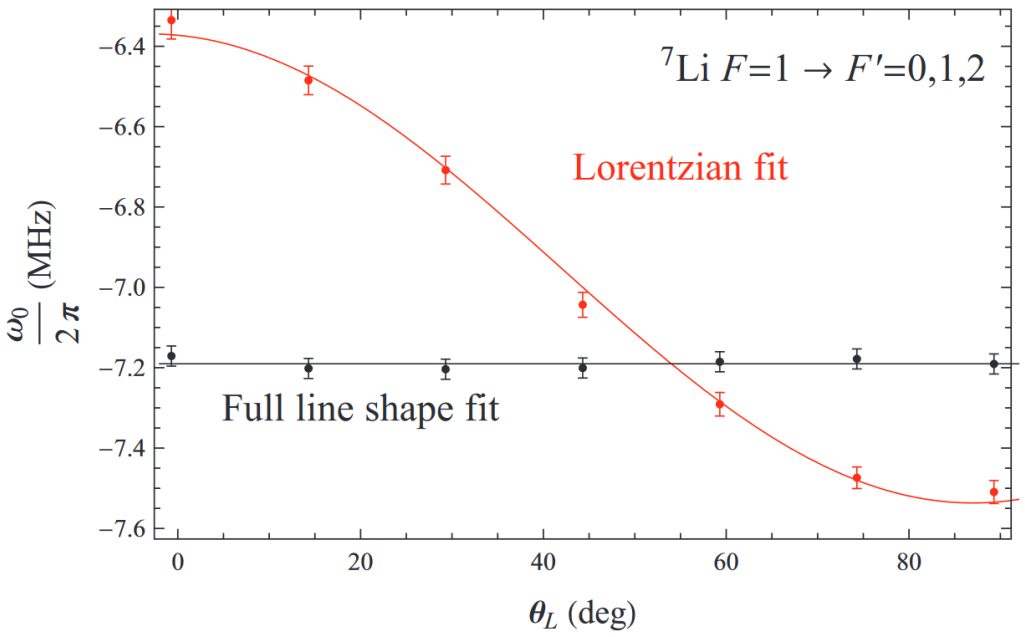

Figure 1.5: Quantum interference in the D_2 transition of ^{7}Li. The line center ω_0 extracted from Lorentzian fits shifts with the polarization angle θ_L. Only a complete line shape model yields polarization-independent results. Figure taken from Ref. [1].

1.2 Spectroscopy on a Cold Atomic Beam

After taking quantum interference effects into account, the Doppler shift remains one of the dominant sources of uncertainty in high-precision spectroscopy of lithium. This provides strong motivation to perform spectroscopy on cold lithium atoms.

This approach has also been pursued by other groups. For example, Ref. [58] reports spectroscopy performed on atoms cooled in a 3D MOT, followed by gray-molasses cooling, achieving a precision at the level of 20 kHz.

In our group at the University of Mainz, an initial attempt focused on slowing a thermal lithium beam using a Zeeman slower and subsequently loading the atoms into a 3D MOT [59]. However, this approach encountered several challenges, including a substantial hot atomic background from uncooled atoms traversing the Zeeman slower and the difficulty of rapidly switching off the magnetic fields, which is an essential requirement for high-precision spectroscopy.

These considerations motivated a transition to a two-dimensional magneto-optical trap-based setup.

1.2.1 The Two-Dimensional Magneto-Optical Trap

Two-dimensional magneto-optical traps (2D MOTs) have been widely used sources of cold atomic beams for a variety of heavier atomic species, including rubidium [60], cesium [61], sodium [62], ytterbium [63], and dysprosium [64]. The concept was first demonstrated for ^{6}Li by Tiecke *et al.* [2], and since then several groups have implemented 2D MOTs for lithium-based experiments [65, 66].

Figure 1.6 illustrates the basic mechanism of a magneto-optical trap for a simple two-level atom with a $J = 0 \rightarrow J = 1$ transition. The working principle of a MOT relies on combining a velocity-dependent damping force arising from Doppler cooling by counter-propagating, red-detuned laser beams (optical molasses), and a position-dependent restoring force generated by a spatially varying Zeeman shift in a magnetic field gradient. Together these mechanisms confine the atoms near the magnetic field minimum, where they can be cooled to temperatures on the order of the Doppler limit. More information on laser cooling can be found in Ref. [67].

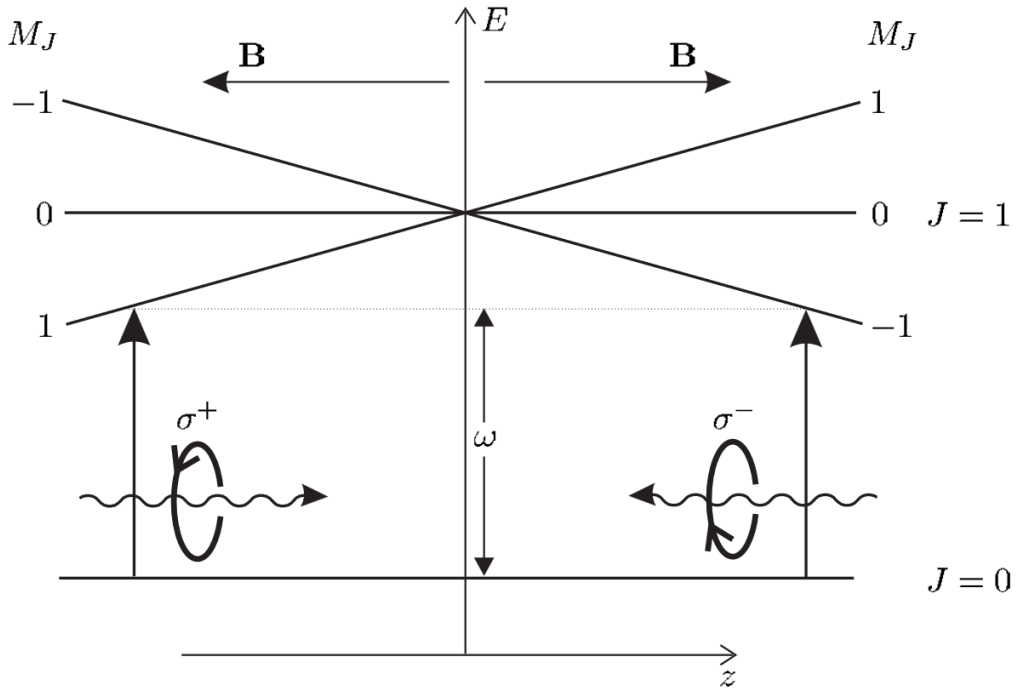

Figure 1.6: Basic principle of a magneto-optical trap for an atom with a two-level $J = 0 \rightarrow J = 1$ transition. In a magnetic field gradient, the Zeeman splitting of the excited-state sublevels depends on the atom's position. Two counter-propagating circularly polarized laser beams interact with the atom. Due to the selection rules they experience a restoring scattering force. Figure taken from Ref. [67].

In the recent years we have built a 2D MOT inspired by the design of Tiecke *et al.* [2] in our group [68–71]. The general setup will be explained in Chapter 2. The characterization and optimization will be presented in Chapter 3. Furthermore, a Monte Carlo simulation of the MOT is employed to validate the experimental results and generate predictions [72].

1.2.2 Cold Atomic Beam

To perform high-precision spectroscopy outside the inhomogeneous magnetic field of the 2D MOT, the atoms must be extracted from the trapping region. For this purpose, an additional laser, referred to as the *push beam* is used to accelerate the atoms out of the 2D MOT and form a cold, directed atomic beam.

Figure 1.7 summarizes key results obtained by Tiecke *et al.* [2], showing both the recapturable flux into a downstream 3D MOT and the most-probable axial velocity of the atomic beam in dependence of push beam intensity.

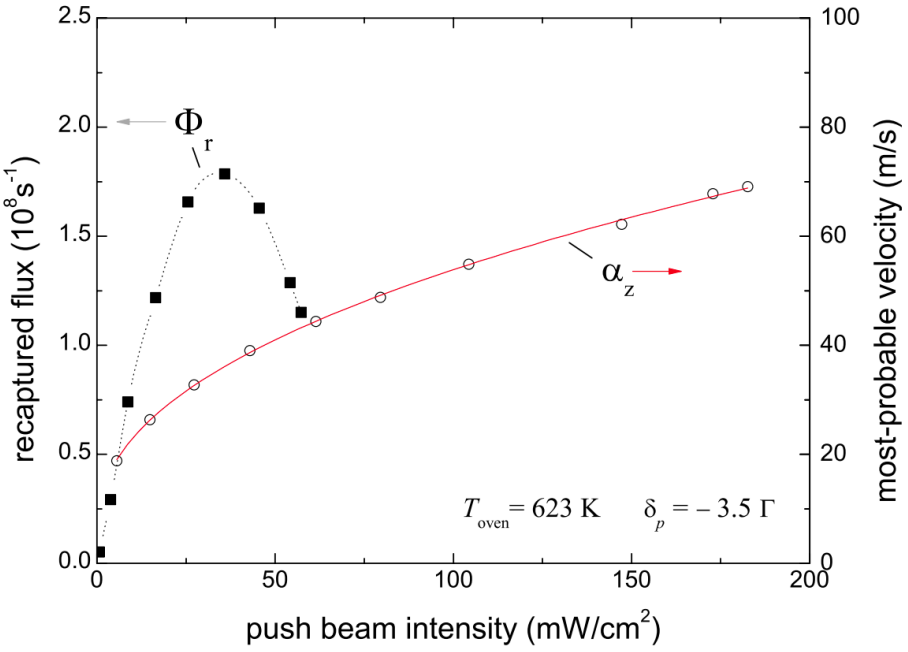

Figure 1.7: Recapturable flux into a 3D MOT (black) and most-probable axial velocity (red) as a function of push beam intensity. Figure taken from Ref. [2].

Tiecke *et al.* demonstrated that a 2D MOT can efficiently load a 3D MOT, achieving a recapture rate on the order of 1×10^8/s. They further showed that the most probable velocity of the extracted atomic beam can be tuned between 18 m/s and 70 m/s by adjusting the push beam intensity, enabling precise control of the axial beam velocity. The resulting atomic beam is relatively monoenergetic, exhibiting a full width at half maximum (FWHM) of approximately 11 m/s at an axial velocity of 36 m/s. In Chapter 4 we will demonstrate how the mean axial velocity and the velocity distribution of our cold atomic beam can be controlled by adapting the push beam parameters.

1.2.3 Toward High-Precision Spectroscopy

Once a cold atomic beam with sufficient flux is established, various techniques from high-precision spectroscopy can be applied in order to perform transverse (perpendicular) laser spectroscopy. A crucial element in this context is the *active fiber-based retroreflector* (AFR), first introduced by the hydrogen group at MPQ Garching [3]. It uses a high-reflective mirror and a fiber as an aperture for the retroreflected beam. The principal idea of first-order Doppler cancellation is illustrated in Figure 1.8. Even if the spectroscopy laser is not perpendicular to the atomic beam ($\alpha \neq 90°$), or if transverse atomic velocities introduce an effective angular spread $\Delta\alpha$, the center-of-gravity of the spectral line remains free of first-order Doppler shifts when an ideal retroreflector is used.

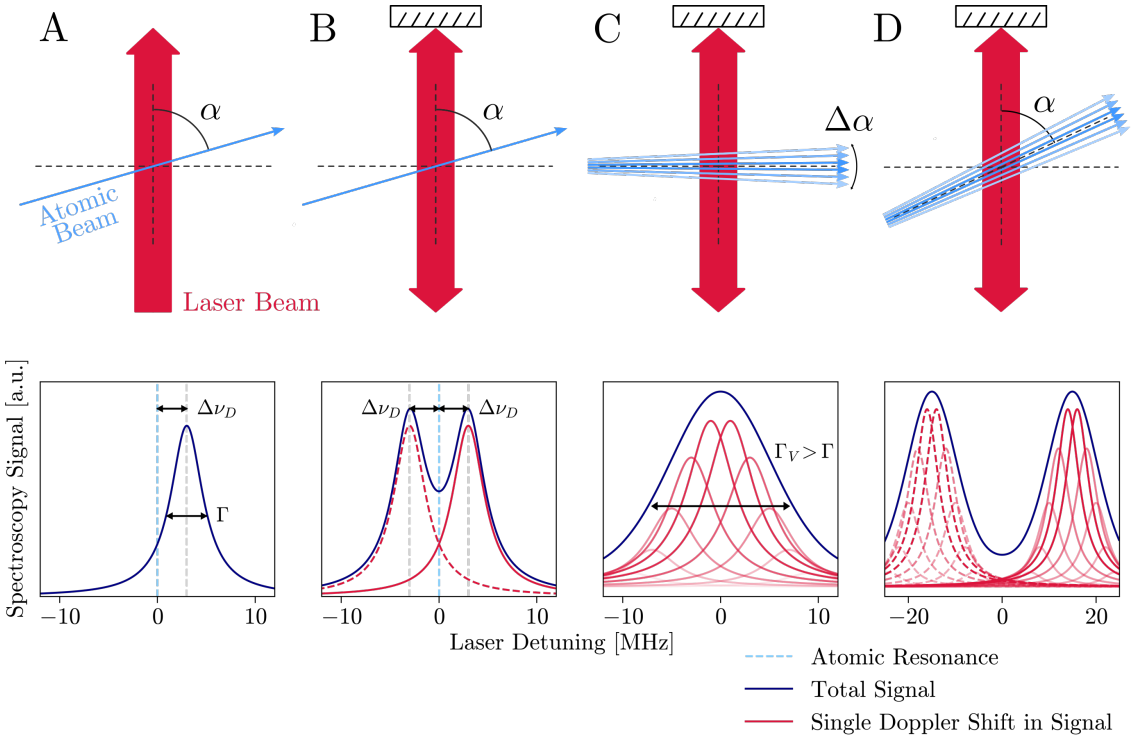

Figure 1.8: Principle of first-order Doppler cancellation for an ideal retroreflector with the corresponding spectroscopy signals shown below. (A) Without a retroreflector: The spectroscopy beam intersects the atomic beam under an angle $\alpha \neq 90°$ leading to an uncorrected detuning $\Delta\nu_{\mathrm{D}}$. With a retroreflector: (B) the reflected spectroscopy beam introduces a second Lorentzian component. (C) A finite divergence of the atomic beam $\Delta\alpha$ results in a broadened profile. (D) A residual offset angle α_0 between the spectroscopy beam and the symmetry axis of the atomic beam leads to two broadened profiles. For an ideal retroreflector, the center-of-gravity of the total signal remains unshifted. Figure adapted from Ref. [73].

A first prototype of our AFR (see Section F.3) has already been constructed and tested [73]. For the method to operate at the required level of precision, the forward and retroreflected wavefronts must overlap perfectly, which necessitates a high-quality beam-collimation system. Due to delays in component delivery, final performance measurements and full characterization are still pending.

In Chapter 5 we present first spectroscopy results and outline the next steps toward achieving Doppler-free, high-precision spectroscopy on the cold atomic beam.

Several key technical requirements for high-precision spectroscopy have been developed during this thesis. These include the ability to lock the spectroscopy laser to an ultra-stable reference cavity, frequency calibration via a frequency comb also possible over a 100 m optical fiber link [74], as well as the development of power-stabilization systems [75, 76] and testing of a narrow-linewidth external-cavity diode laser [77].

2 Experimental Setup

This chapter describes the experimental setup for precision measurements on ^{6}Li. Figure 2.1 shows a schematic overview of the complete setup. The vacuum setup is divided into two sections: the *2D MOT section*, which serves as the source for our cold lithium beam, and the *spectroscopy section*, where the cold lithium can be studied. Each section can be evacuated separately with a turbomolecular pump[1] (A) and is equipped with a Pirani sensor[2] (B) and a hot ion gauge[3]. The pressure during operation is always kept well below 1×10^{-6} mbar in the whole vacuum chamber. Both sections are separated by a CF-40 gate valve. This allows the spectroscopy setup to be changed without exposing the lithium to air or requiring a purge gas.

The solid lithium[4] is stored in a CF-16 tube welded to a CF-40 six-way cross. This lithium oven can be heated up to 450 °C, by using a heating wire[5]. The hot atoms from the lithium oven are optically cooled in a two-dimensional magneto-optical trap (2D MOT). The *MOT beams* (red) are prepared outside the vacuum chamber (see Section 2.1.2), exiting an optical fiber[6], passing a quarter-wave plate and a collimating lens. The two upper MOT beams are prepared in a cage system clamped onto the CF-40 six-way cross. The lower MOT beams are prepared on the optical table and redirected upwards (see Figure C.2). All laser beams enter the vacuum chamber through anti-reflection (AR)-coated wedged windows[7]. The magnet holder is clamped onto the MOT six-way cross. The setup of our 2D MOT is described in more detail in the following Section 2.1.

Atoms trapped in the 2D MOT are extracted perpendicular to the cooling plane by a blue detuned *push beam* (blue). This beam accelerates the atoms toward the spectroscopy section, forming a cold atomic beam. After exiting the MOT region, the atomic beam passes through two iris diaphragms that reduce the flux of hot background atoms and limit the transverse velocity of the cold atomic beam. The beam then enters a CF-40 six-way cross for beam characterization. A perpendicular *spectroscopy beam* (turquoise) excites the atoms, and the resulting fluorescence (violet) is collected by a lens and detected with a photomultiplier tube[8]. The measurements and the detailed setup are further described in Chapter 4. Downstream of the characterization region, the atomic beam enters a CF-160 six-way cross where we plan to place the active fiber-based retroreflector (AFR) (see Section F.3) to perform high-precision spectroscopy. Supplementary pictures of the setup can be found in Appendix C.

[1] Leybold, Turbovac 90i and 90iX.
[2] Agilent, ConvecTorr P-Type Gauge.
[3] Agilent, UHV-24 - Bayard-Alpert Ion Gauge Tube.
[4] Aldrich, 340421 - enriched lithium, with 95% ^{6}Li.
[5] Horst, 020101- heating wire, 0.6 m, 75 W.
[6] Thorlabs, polarization-maintaining Patch Cable, PANDA, 630 nm, FC/APC, 5 m.
[7] Thorlabs, VPWW42-B - Ø 1.5" UVFS window, 30 min wedge, BBAR 650-1050 nm.
[8] Thorlabs PMT1001/M multialkali amplified PMT.

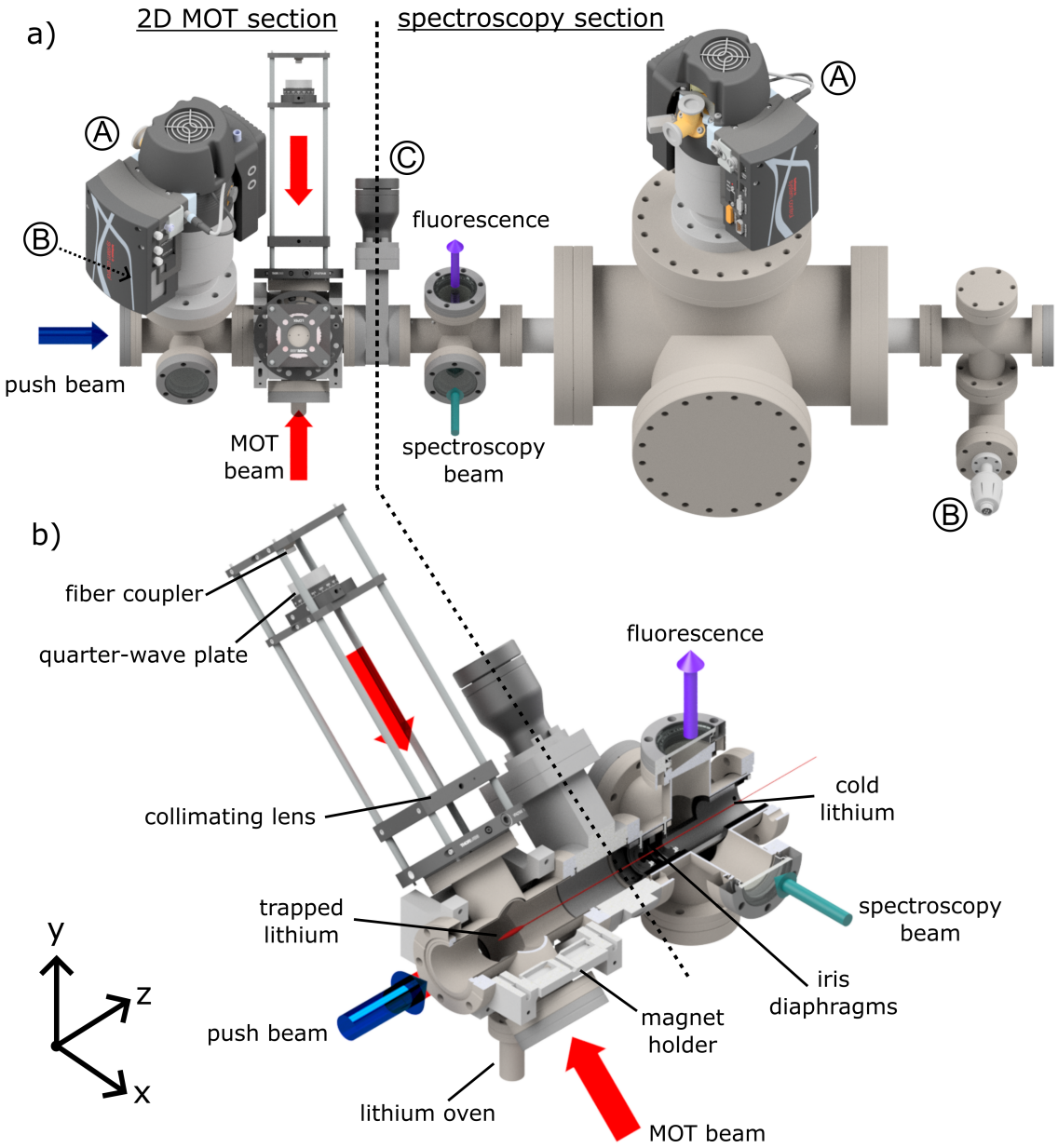

Figure 2.1: Overview of the cold lithium beam apparatus. a) Full vacuum system schematic showing the 2D MOT section (left) and spectroscopy section (right) separated by a gate valve (C). Each section is independently evacuated by a turbomolecular pump (A) and monitored with vacuum gauges (B). Laser beam paths are indicated: MOT beams (red), push beam (blue), probe beam (turquoise), and fluorescence (violet). b) Zoom into the inner parts of the setup. Trapped lithium atoms are extracted from the MOT by the push beam, pass through collimating iris diaphragms, and form a cold atomic beam that is probed in the adjacent vacuum cross. All optical viewports use wedged, anti-reflection-coated windows to suppress interference and light scattering effects.

2.1 Two-Dimensional Magneto-Optical Trap

The setup for our two-dimensional magneto-optical trap (2D MOT) is based on the design of Tiecke *et al.* [2]. A schematic drawing of the 2D MOT setup is shown in Figure 2.2. Solid lithium is heated in a reservoir at the bottom of a CF-16 tube which is flanged to an adapter that is welded to the bottom of a CF-40 six-way cross. To prevent conductive heating of the whole cross, a water cooling copper bracket is installed between the reservoir and the MOT six-way cross. A fan (not shown) is also installed to prevent convective heating of the magnets. The hot atoms travel upwards along the y-axis and are further characterized in Section 3.1. The magnetic quadrupole field is produced by four stacks of three permanent magnets: Two with the field pointing upwards and two with the field pointing downwards. The magnetic field is further described in Section 3.2. The four MOT beams enter the six-way cross each through a vacuum window. The MOT beams are circularly polarized with the handedness indicated in the schematic. For the MOT profile measurements (Section 3.4) and all measurements of the extracted cold atomic beam (Chapter 4), the handedness of the two lower MOT beams is interchanged. For more information see Appendix A.

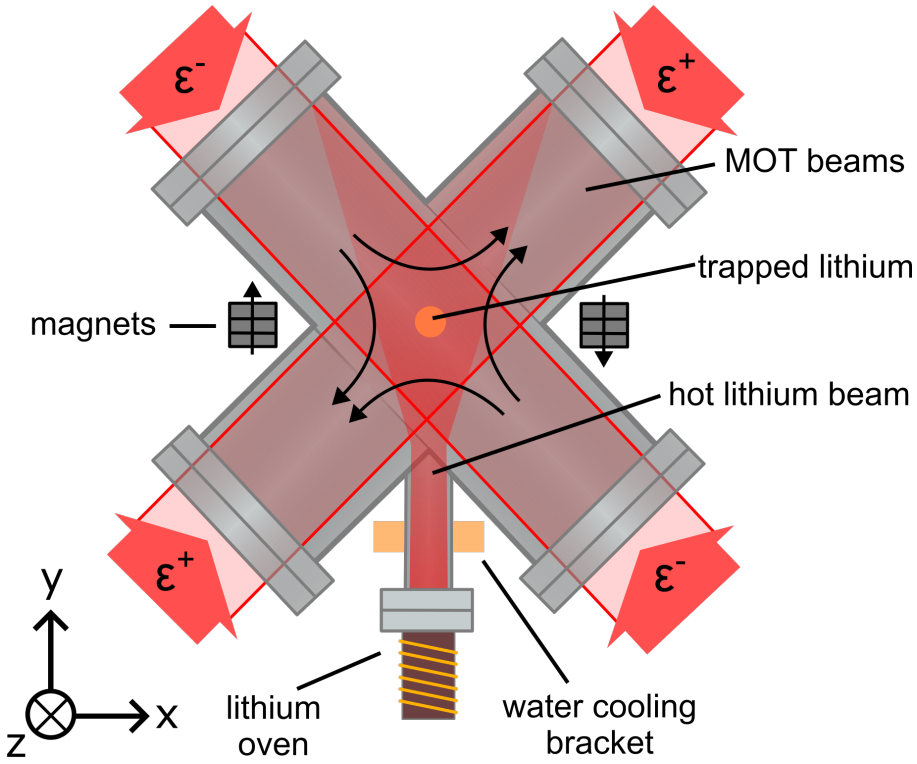

Figure 2.2: Schematic drawing of the 2D MOT setup. Solid lithium is heated in a reservoir at the bottom. A water cooling bracket is installed above. The hot atoms travel upwards along the y-axis. The magnetic quadrupole field in the xy-plane is created by four stacks of three magnets. The MOT beams are circular polarized with the handedness indicated in the schematic. The atoms are then trapped in the center of the six-way cross, where their fluorescence can be observed. A picture of the setup can be seen in Figure C.2.

The atoms are then trapped in the center of the six-way cross, where a fluorescence can be observed (see Figure C.4). As a difference from the setup of Tiecke *et al.*, we switched from two retro-reflected beams to four independent beams. This way we can change power ratios between the upper and lower beams (see Section 3.4.7).

2.1.1 Laser Frequencies

Trapping and cooling will be performed on the D_2 transition: While the $^2S_{1/2}$ ground state hyperfine splitting is approximately 228 MHz [78], the excited $^2P_{3/2}$ state hyperfine splitting is smaller than the natural linewidth of 5.9 MHz [22] and hence unresolved.

This explains the necessity of using two lasers, called *trap laser* and *repump laser*. The latter helps avoiding atoms getting trapped in the $S_{1/2}(F = \frac{1}{2})$ *dark state*. In the following the *trap laser* will drive the $S_{1/2}(F = \frac{3}{2}) \rightarrow P_{3/2}(F' = \frac{1}{2}, \frac{3}{2}, \frac{5}{2})$-transition and the *repump laser* will drive the $S_{1/2}(F = \frac{1}{2}) \rightarrow P_{3/2}(F' = \frac{1}{2}, \frac{3}{2})$-transition. Each laser has a detuning δ_{trap} and δ_{repump} specified relative to the $P_{3/2}$ hyperfine centroid. The MOT and push beam transitions are depicted in Figure 2.3.

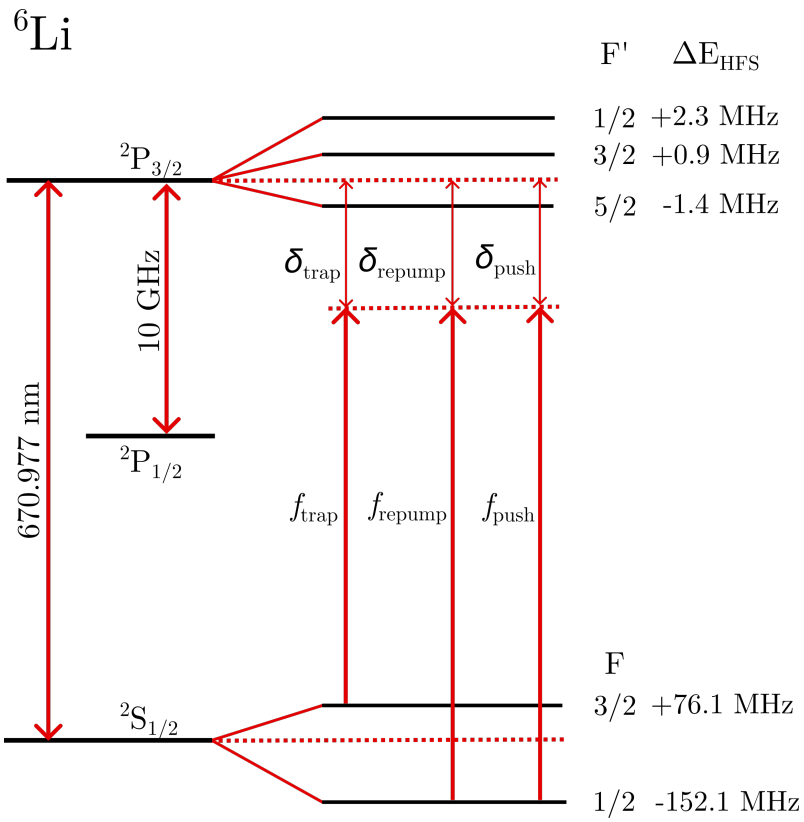

Figure 2.3: Overview of the MOT and push beam transitions. The trap beam with frequency f_{trap} and detuning δ_{trap} addresses the upper ground state and the repump beam with frequency f_{repump} and detuning δ_{repump} addresses the lower ground state. The push beam has a frequency f_{push} with a detuning δ_{push}.

2.1.2 MOT Beam Preparation

For the *MOT beams*, we use a ring-cavity titanium-sapphire laser (Ti:Sa)[1], providing a continuous-wave beam with a power of approximately 2 W at a wavelength of 671 nm. The beam radius is approximately 2 mm at the output of the Ti:Sa (see Figure C.5). The Ti:Sa can be locked onto an external tunable cavity[2] while its frequency $f_{\text{Ti:Sa}}$ can be tuned by scanning a piezo-actuated mirror of this external cavity. To change the frequency of the repump beam, we use an acousto-optic modulator (AOM) in a double pass configuration. This allows us to change the repump frequency, without significantly affecting the power coupled into the optical fibers.

The optical setup for the 2D MOT beam preparation is shown in Figure 2.4. The output from the Ti:Sa passes a 1:1 telescope, where a chopper blade can be positioned in the focus to perform measurements on the loading of our MOT (see Section 3.3). The total optical power is actively stabilized by monitoring the output power with a photodetector (PD) placed behind a backside-polished mirror. The measured photodetector signal is used in a feedback loop to control a motorized half-wave plate ($\lambda/2$) in combination with a polarizing beamsplitter (PBS). Further details on the active power stabilization system can be found in Ref. [75].

The beam is then split in two parts: the repump beam is directed toward the AOM double pass, and the trap beam continues unperturbed. The repump beam is then passing through a 3:1 Galilean telescope, to reduce the beam waist radius[3] to $(235 \pm 15)\,\mu\text{m}$ to fit the aperture of the AOM[4]. The first order of the diffraction passes a lens and gets retroreflected by a mirror. The center of the AOM and the surface of the mirror are both placed in the focus of the lens, to ensure a good retracing of the beam. This way we can reach an efficiency of $(74 \pm 1)\,\%$ for an AOM driving frequency f_{AOM} in a range from 105 MHz to 115 MHz (more information on the setup can be found in Ref. [71]).

The frequency-shifted repump beam passes through an additional Galilean telescope to match its divergence to that of the trap beam, compensating for mismatches caused by misalignment in the AOM double pass and differences in optical path length. This ensures that both beams can be coupled into optical fibers[5] with equal efficiency.

Both beams are then overlapped in a 50:50 non-polarizing beamsplitter and afterwards split into four different beams using half-wave plates and polarizing beamsplitters. We use additional polarizing beamsplitters and beam dumps (BD) to set the power of each MOT beam independently. Each *MOT beam* is then coupled into a polarization-maintaining fiber and transported to the vacuum chamber (Figure 2.1). This way we create four beams with a trap frequency $f_{\text{trap}} = f_{\text{Ti:Sa}}$ and a repump frequency $f_{\text{repump}} = f_{\text{Ti:Sa}} + 2 \cdot f_{\text{AOM}}$ to accomplish the trap an repump scheme shown in Figure 2.3, with a nearly Gaussian transverse mode. Depending on the optical alignment each of the four beams can have a power of up to 120 mW.

[1] Sirah Lasertechnik, Matisse 2 TX-Light.
[2] Sirah Lasertechnik, confocal resonator with a free spectral range of 600 MHz and a finesse of typical 15 to 20.
[3] Measured with a beam profiler: DataRay, WinCamD-LCM.
[4] Gooch & Housego, AOMO 3110-120.
[5] Thorlabs, polarization-maintaining Patch Cable, PANDA, 630 nm, FC/APC, 10 m.

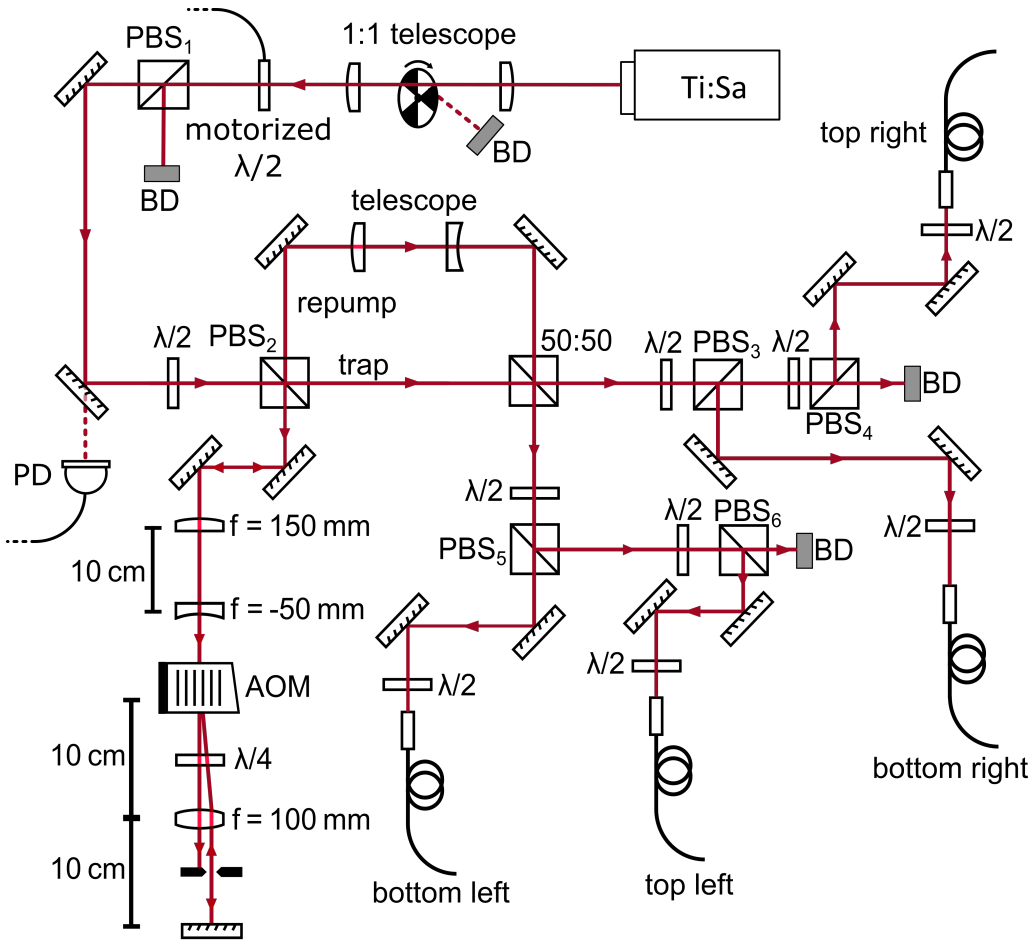

Figure 2.4: Schematic of MOT beam preparation. Output from the titanium-sapphire laser (Ti:Sa) is split in two beams. The repump beam frequency is shifted with an acousto-optic modulator (AOM) in a double pass configuration. Both beams are then overlapped in a 50:50 non-polarizing beamsplitter (50:50) and afterwards split into four different MOT beams using half-wave plates ($\lambda/2$) and polarizing beamsplitters (PBS). These are then coupled into polarization-maintaining fibers and transported to the vacuum chamber (Figure 2.1). The total power is monitored with a photodiode (PD), and unused light is directed into beam dumps (BD). Pictures of the setup are presented in Figure C.7 and Figure C.8.

2.2 Push Beam

The push beam serves two purposes: first, it accelerates the cold atoms out of the 2D MOT and into the spectroscopy section; second, it is used for absorption measurements to characterize the cloud of cold atoms (see Chapter 3). A schematic of the push beam setup is shown in Figure 2.5. For the pushing we use a custom-built external cavity diode laser (ECDL) with a tapered amplifier[1] in combination with

[1]more information on the custom-built ECDL system can be found in [59].

the preparation setup shown in Section 2.2.1. For the absorption measurements we use a commercial ECDL[1], since it can be scanned over a larger frequency range.

The push beam enters the setup via a polarization-maintaining fiber and passes through a film polarizer[2]. To control the beam waist size and position, we use a lens system consisting of two $f = 100\,\text{mm}$ plano-convex lenses spaced approximately 200 mm apart, in combination with a $f = 500\,\text{mm}$ bi-convex lens.

The beam is then split into two paths of equal power: the push beam, which passes through the vacuum setup via two wedged AR-coated windows[3], and a reference beam that passes vacuum setup unperturbed. Both beams are then focused onto a balanced photodetector[4]. This enables us to measure small changes in the push beam power, e.g. from the absorption by lithium atoms. The position of the push beam can be controlled with a custom-build motorized periscope (see Figure C.10). This allows us to probe the MOT at different positions and measure absorption profiles (see Section 3.4). The motorized periscope is further described in [71].

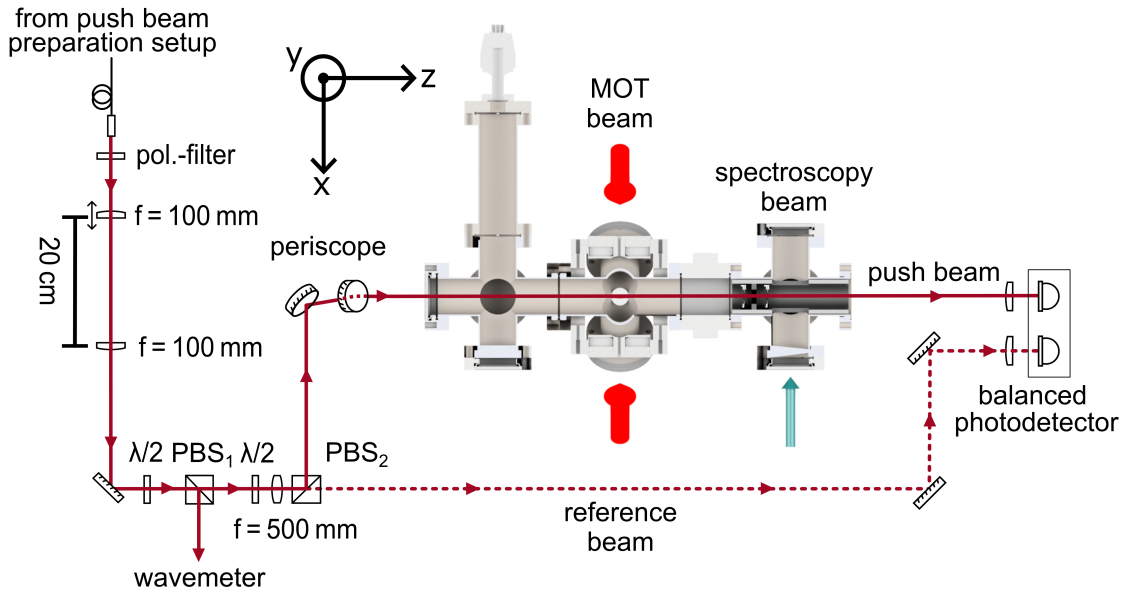

Figure 2.5: Push beam setup (top view). The output of the push beam preparation setup (see Figure 2.6) is coupled into the setup via a polarization-maintaining fiber and passes through a film polarizer. For the MOT characterization (see Chapter 3) a part of the beam is coupled out by the PBS_2 to serve as a reference laser (dashed), suppressing systematic uncertainties from laser intensity fluctuations. The remaining part is the push beam passing the MOT and the vacuum chamber. Both beams are then focused onto a balanced photodiode for relative detection. The position of the push beam can be controlled with a motorized periscope to obtain profile measurements.

[1]Toptica, TA pro 670-3V0.
[2]Thorlabs, LPVISE2X2- 2" x 2" Dichroic Film Polarizer Sheet, 400 - 700 nm, for a more stable power distribution between push and reference beam.
[3]Thorlabs, VPWW42-B - Ø 1.5" UVFS window, 30 min wedge, BBAR 650-1050 nm.
[4]Thorlabs, PDB220A2/M - Free-Space Balanced Photodetector, UV-Enhanced Si, 4.1 mm active diameter, for 190-1100 nm.

2.2.1 Push Beam Preparation

We use the following preparation setup for the push beam in the cold atomic beam measurements. To perform spectroscopy on the cold lithium beam, it is necessary to temporally modulate the push beam, as it operates at the same wavelength as the spectroscopy transition and would otherwise interfere with the fluorescence measurements. Additionally, fast switching of the push beam is required for time-of-flight measurements (see Section 4.2.1). For more effective acceleration of the cold atoms, the push beam should also have an option to contain a repump frequency.

Figure 2.6 shows a schematic of the push beam preparation. The output from a custom-build external cavity diode laser (ECDL) coming from a polarization-maintaining fiber is passing two acousto-optic modulators (AOM) in a double pass configuration. The first one can be used for quickly switching of the push beam. In the second double pass the iris diaphragm is opened such that the zeroth and first order can pass through it. When the AOM is driven at 114 MHz a repump beam can be added to the push beam. After passing a polarizing beamsplitter (PBS) and a half-wave plate ($\lambda/2$), the beam is coupled into polarization-maintaining fiber[1] going to the push beam setup shown above (Figure 2.5).

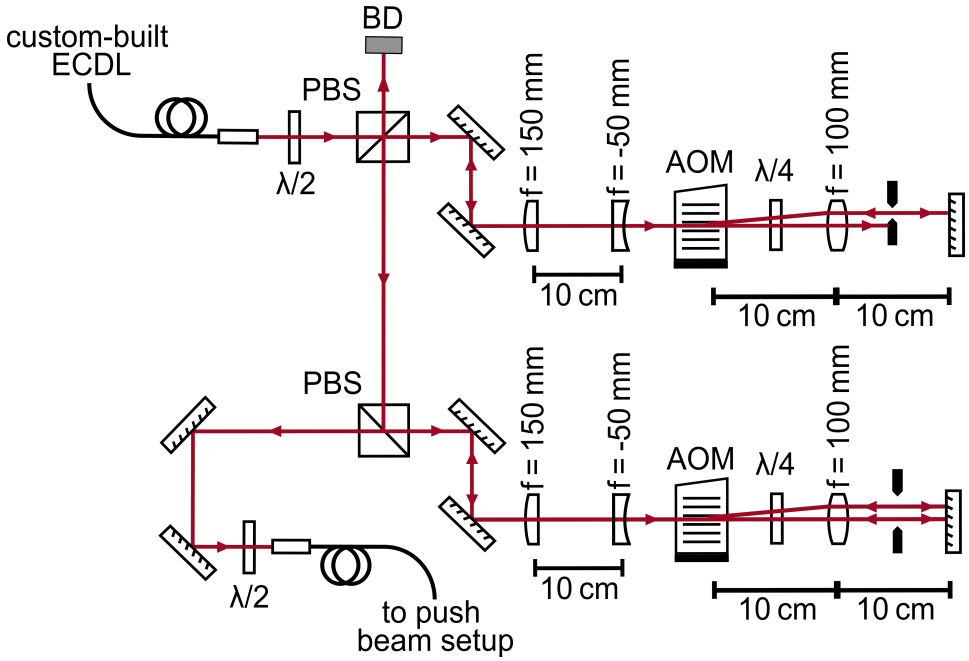

Figure 2.6: Schematic of the push beam preparation. The output from a custom-build external cavity diode laser (ECDL) is passing two acousto-optic modulators (AOM) in a double pass configuration. The first one can be used for quickly switching push beam and the second one to add a repump frequency to the beam. After passing a polarizing beamsplitter (PBS) and a half-wave plate ($\lambda/2$), the beam is coupled into polarization-maintaining fiber going to the push beam setup (see Figure 2.5). A picture of the setup is shown in Figure C.8.

[1] Thorlabs, polarization-maintaining Patch Cable, PANDA, 630 nm, FC/APC, 10 m.

2.3 Spectroscopy Beam

The spectroscopy measurements require a laser source with good frequency and power stability. For this purpose, we employ a commercial external cavity diode laser (ECDL)[1] that is frequency-stabilized to an ultra-stable reference cavity[2] using a Pound–Drever–Hall (PDH) locking scheme as illustrated in Figure 2.7.

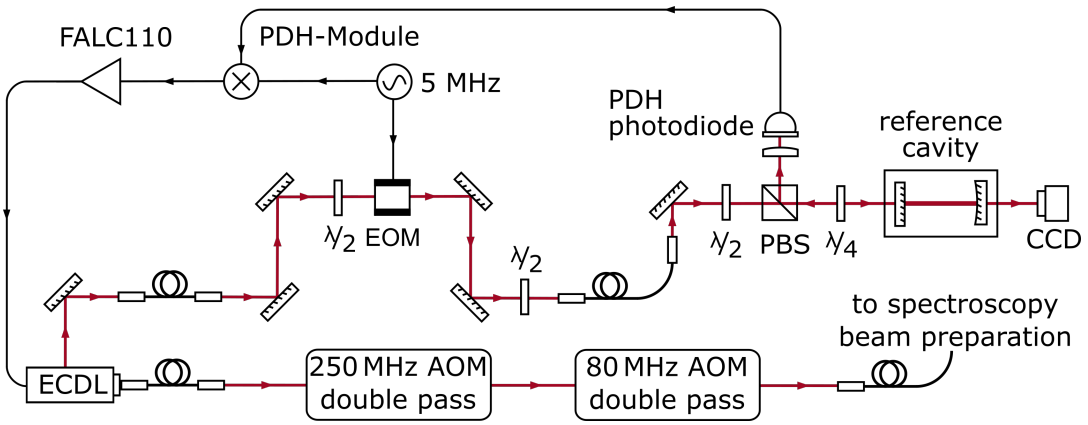

Figure 2.7: Schematic of the spectroscopy beam lock and scan setup. The seed output of the external cavity diode laser (ECDL) is modulated at 5 MHz by an electro-optic modulator (EOM) and coupled into a reference cavity. The reflected signal is used for Pound–Drever–Hall (PDH) locking, while the transmitted transverse cavity mode can be monitored on a CCD camera. The amplified output of the ECDL is frequency-shifted using two AOMs in double pass configuration, analogous to the setup shown in Figure 2.6. This configuration enables laser frequency scans of up to 150 MHz while maintaining frequency lock and power.

The ECDL frequency is phase-modulated at 5 MHz using an electro-optic modulator (EOM)[3], which is driven by the PDH module output of the ECDL controller at an amplitude of 11.3 dBm. The error signal derived from the cavity reflection is processed by a fast locking module[4], which stabilizes the laser frequency via current modulation of the seed diode. More information on the frequency stabilization can be found in Section F.2.

To enable frequency scans for spectroscopic measurements while maintaining the lock, we employ two acousto-optic modulators (AOMs) in double pass configuration, each driven by an independent RF signal generator[5]. A key challenge during frequency sweeps is the intrinsic frequency-dependent diffraction efficiency of the AOMs, which would otherwise introduce unwanted variations in the output power. We compensate for this effect by adjusting the RF drive amplitude as a function of frequency. In addition, the overall laser power is actively stabilized by adjusting the injection current of the tapered amplifier (TA). This combination enables continu-

[1]Toptica, TA pro 670-3V0.
[2]Stable Laser Systems, VH106020-4.
[3]QUBIG, PM7-NIR_5.
[4]Toptica, FALC 110.
[5]Rohde & Schwarz - SMG and SMGU.

ous scans over approximately 150 MHz while maintaining a constant spectroscopy beam power across the full scan range.

Further details of the spectroscopy setup, including beam alignment and the downstream detection scheme, are presented in Section 4.1, where the characterization of the cold atomic beam is discussed.

2.3.1 Spectroscopy Beam Preparation

For the characterization of the cold atomic beam (see Chapter 4), it proved useful to be able to add a repump frequency component into the spectroscopy beam to enhance the florescence signal. Figure 2.8 shows a schematic diagram of the spectroscopy beam preparation.

The output from the external cavity diode laser (ECDL) is split into two paths. One of the beams passes through an acousto-optic modulator (AOM) in a double pass configuration to add a frequency-shifted repump component. To ensure proper polarization matching between the frequency-shifted and unshifted beam, it is advantageous to employ a combination of a half-wave plate ($\lambda/2$) and a quarter-wave plate ($\lambda/4$) in one of the beams. The two beams are then overlapped in a 50:50 beamsplitter (50:50) and coupled into two polarization-maintaining optical fibers: one directed toward the spectroscopy setup, and the other to a wavemeter[1] for frequency monitoring. More information on the frequency measurements and uncertainties can be found in Section B.1.3.

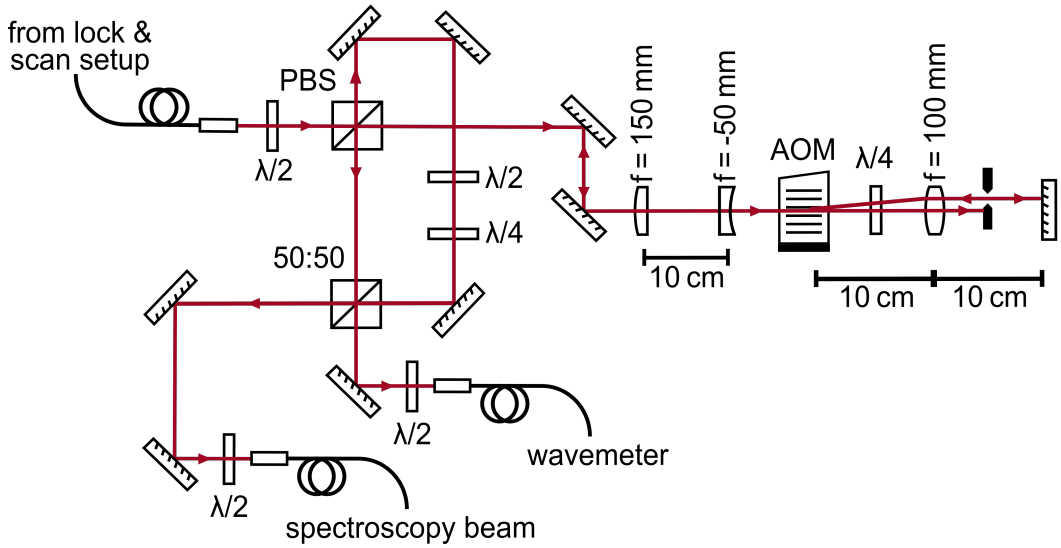

Figure 2.8: Schematic of the spectroscopy beam preparation. The output from the external cavity diode laser (ECDL) setup (see Figure 2.7) is split in two beams. One is passing an acousto-optic modulator (AOM) in a double pass configuration to add a repump frequency to the beam. Both beams are then overlapped in a 50:50 beamsplitter (50:50). After passing a half-wave plate ($\lambda/2$), the beam is coupled into two polarization-maintaining fibers, one going to the spectroscopy beam setup and one to the wavemeter. A picture of the setup is shown in Figure C.12.

[1] High Finesse, WS7-30.

3 Characterization of the Two-Dimensional Magneto-Optical Trap

Achieving a high-flux and low-temperature atomic lithium beam for spectroscopy requires careful characterization and optimization of the two-dimensional magneto-optical trap (2D MOT) which here serves as the cold atom source. In particular, we investigate the number and spatial distribution of trapped atoms, as well as how these quantities depend on experimental parameters such as the powers and detunings of the MOT beams and the temperature of the lithium oven.

As a first step, we analyze the distribution of atoms emitted from the lithium oven to estimate the capturable flux (Section 3.1). This is followed by a detailed study of the magnetic field configuration in the MOT region, including a proposal for its optimization (Section 3.2). Subsequently, we determine the MOT loading dynamics and provide an estimate of the maximum cold atom flux that can be extracted from the trap (Section 3.3). Finally, we measure the absorption profile of the cold atomic cloud, which allows us to estimate the total number of trapped atoms (Section 3.4).

3.1 Hot Atomic Beam Source

To characterize the atomic beam emerging from the heated lithium reservoir (Section 3.1.1), we use absorption spectroscopy with a weak, collimated push beam to probe its spectral and spatial characteristics (Section 3.1.2). The measured absorption spectra provide insights into the velocity distribution, areal density, and effective atomic temperature of the hot lithium flux. We use a semi-empirical kinetic model to estimate the total atomic flux (Section 3.1.3). By comparing the experimental results with Monte Carlo simulations that model atomic trajectories and their interaction with the push beam (Section 3.1.4), we estimate the true atomic temperature and calibrate the set oven temperature (Section 3.1.5). Further we make an estimate on the capturable flux and its velocity distribution orthogonal to the trapping plane.

3.1.1 Measurement Setup and Oven Geometry

As described in the experimental setup (Section 2.1), the 2D MOT is loaded from below by a heated lithium reservoir. To characterize the hot atomic beam emitted from the oven, we perform absorption spectroscopy using the push beam as a probe. Figure 3.1 shows a schematic of the oven geometry and the corresponding measurement configuration.

The lithium reservoir has a diameter of $d_{\mathrm{Li}} = (16.3 \pm 0.5)\,\mathrm{mm}$ and is filled with lithium to a height h_{Li}. During filling of the reservoir with lithium, exposure to air was minimized by performing the procedure under an argon atmosphere. This

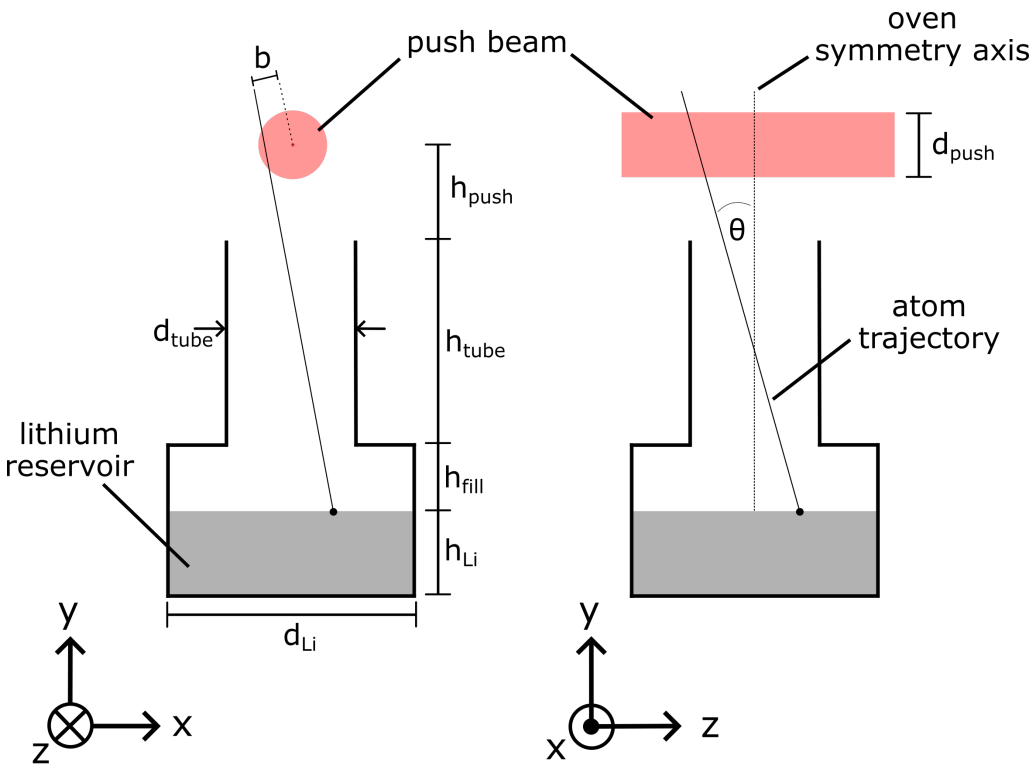

Figure 3.1: Schematic oven geometry for hot atomic beam absorption measurement setup and simulation. The oven is modeled as two vertically stacked cylindrical tubes. The lithium reservoir has a diameter of d_{Li} and is filled with lithium to a height h_{Li}. An example of an atom trajectory is shown: The emission angle θ is defined relative to the y-axis. The atom traverses the filling height h_{fill} and subsequently enters a tube with diameter d_{tube} and height h_{tube}. The atoms trajectory then intersects the push beam with an offset b. The push beam, with diameter d_{push}, is positioned in the center of the trap region at a height h_{push} above the oven exit. Figure adapted from Ref. [71].

precaution prevents the formation of lithium nitride and lithium oxide, which would otherwise reduce the flux of hot lithium atoms emitted from the oven.

When heated above approximately 300 °C, lithium atoms are thermally emitted from the surface of the reservoir. A representative atomic trajectory is shown in Figure 3.1. An atom leaves the reservoir at a height h_{Li}, traverses the filling height $h_{\mathrm{fill}} = (14 \pm 5)\,\mathrm{mm}$, and propagates upward at an angle θ with respect to the y-axis. Subsequently, it enters a tube of diameter $d_{\mathrm{tube}} = (12.7 \pm 0.5)\,\mathrm{mm}$ and height $h_{\mathrm{tube}} = (83 \pm 2)\,\mathrm{mm}$.

After exiting the tube, the atom travels into the 2D MOT region, where it may intersect with the push beam in the center of the trapping plane, located at a height of $h_{\mathrm{push}} = (19.1 \pm 0.5)\,\mathrm{mm}$. The push beam has a diameter of $d_{\mathrm{push}} = (750 \pm 50)\,\mu\mathrm{m}$ and a power of $(1.35 \pm 0.05)\,\mu\mathrm{W}$, corresponding to approximately 10 % of the saturation intensity of the lithium D_2 transition. Each atomic trajectory intersects the push beam with an offset b from the beam center.

3.1.2 Absorption Measurements

The absorption of the push beam is detected using a balanced photodetector (see Figure 2.5). During this measurement, the permanent magnets are removed from the 2D MOT to reduce Zeeman splitting effects in the absorption spectrum. Figure 3.2 shows a representative absorption spectrum of the hot atomic beam emitted from the lithium oven at a set temperature of $(400 \pm 2)\,^{\circ}\mathrm{C}$.

The measured absorption spectrum exhibits Doppler broadening and displays two distinct peaks corresponding to the hyperfine ground states of ^{6}Li. These peaks originate from the transitions $\mathrm{S}_{1/2}(F = \frac{3}{2}) \rightarrow \mathrm{P}_{3/2}(F' = \frac{1}{2}, \frac{3}{2}, \frac{5}{2})$ at approximately 446.799 57 THz and $\mathrm{S}_{1/2}(F = \frac{1}{2}) \rightarrow \mathrm{P}_{3/2}(F' = \frac{1}{2}, \frac{3}{2})$ at approximately 446.799 80 THz. For simplicity, we neglect the hyperfine splitting of the excited $\mathrm{P}_{3/2}$ state and the minor contributions from residual ^{7}Li in the atomic beam.

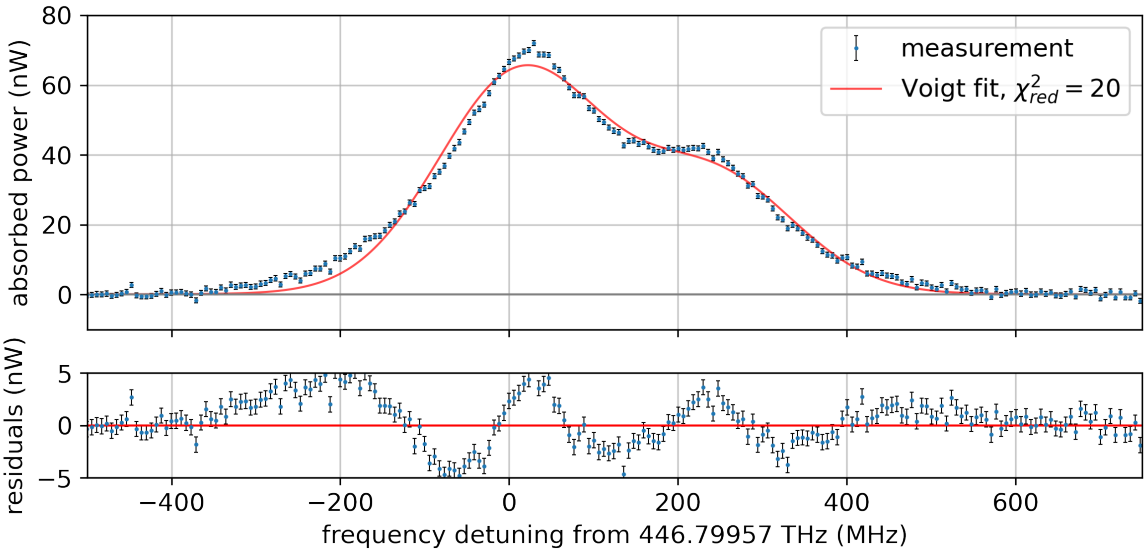

Figure 3.2: Absorption measurement of the hot atomic beam emitted from the lithium oven set to $(400 \pm 2)\,^{\circ}\mathrm{C}$. The push beam has a diameter of $(750 \pm 50)\,\mu\mathrm{m}$, a power of $(1.35 \pm 0.05)\,\mu\mathrm{W}$ and intersects the atomic beam $(116 \pm 5)\,\mathrm{mm}$ above the lithium reservoir. A fit consisting of two Voigt profiles, each with a Lorentzian width fixed to the natural linewidth, is shown as a red line. The fit parameters are summarized in Table 3.1. The residuals shown below reveal systematic deviations, indicating that the fit does not fully capture the measured line shapes. The observed narrower features can be attributed to geometric velocity selection, as demonstrated by Monte Carlo simulations (see Figure 3.4).

We fit the measured spectrum using a sum of two Voigt profiles (detailed in Section B.3) with identical broadening parameters and Lorentzian widths fixed to the natural linewidth of the D_2 transition (5.9 MHz). The resulting fit is shown as a red line in Fig. 3.2, with the residuals displayed below.

The peak associated with the upper ground state ($F = \frac{3}{2}$) exhibits approximately twice the amplitude of the lower ground state peak ($F = \frac{1}{2}$), consistent

with their difference in degeneracy: the $F = \frac{3}{2}$ state has four magnetic sublevels ($m_F = -\frac{3}{2}, -\frac{1}{2}, +\frac{1}{2}, +\frac{3}{2}$), while the $F = \frac{1}{2}$ state has only two ($m_F = -\frac{1}{2}, +\frac{1}{2}$).

However, the fit model does not fully reproduce the experimental data; the fitted peaks appear broader than the measured features. This discrepancy suggests that the actual velocity distribution along the z-axis is narrower than a Gaussian distribution assumed in the fit, which will be discussed later in the context of our Monte Carlo simulation (Section 3.1.4).

The extracted fit parameters are summarized in Table 3.1. The measured peak positions agree with literature values to within the absolute accuracy of the wavemeter (30 MHz), which was used for frequency calibration. The measured ground state hyperfine splitting matches the expected value of 228.2 MHz [78] within the statistical uncertainty of the fit, as systematic frequency offsets cancel when calculating the splitting between the two peaks.

Table 3.1: Fit parameters and areal density at $T_{\text{set}} = (400 \pm 2)\,^{\circ}\text{C}$.

Fit parameter	**Value**
amplitude A_1	(63.19 ± 0.09) nW
amplitude A_2	(33.66 ± 0.10) nW
amplitude ratio A_1/A_2	(1.88 ± 0.01)
peak detuning δ_1	$(13.1 \pm 0.2 \pm 30.0)$ MHz
peak detuning δ_2	$(241.1 \pm 0.4 \pm 30.0)$ MHz
peak separation $\delta_2 - \delta_1$	(228.0 ± 0.4) MHz
broadening σ	(96.0 ± 0.2) MHz
axial velocity distribution Δv_z	~ 64 m/s
reduced chi squared χ^2_{red}	20
areal density	$(1.5 \pm 0.1)\,10^8/\text{cm}^2$

From the Gaussian width parameter σ of the Voigt profile, we extract an estimate for the width of the velocity distribution along the z-axis via the first-order Doppler shift: $\Delta v_z = c \cdot \sigma / f_{\text{Li6,D2}} \approx 64$ m/s, where $f_{\text{Li6,D2}} = 446.8$ THz is the transition frequency and c is the speed of light. This experimentally determined velocity distribution width provides a benchmark for comparison with the Monte Carlo simulation predictions discussed in Section 3.1.4.

Given the limitations of the Voigt profile fit discussed above, we employ a line shape independent method to extract the areal density from the absorption measurements. This approach, based on numerical integration of the measured absorption signal, is described in detail in Section 3.4.3.

Corresponding spectra recorded at oven set temperatures of 420 °C and 440 °C are shown in Figure D.1 and Figure D.2, respectively. As expected the areal density increases with the oven temperature, rising from $(1.5 \pm 0.1) \times 10^8/\text{cm}^2$ at 400 °C to $(4.9 \pm 0.3) \times 10^8/\text{cm}^2$ at 440 °C (see Figure 3.8). Additionally, the velocity distribution FWHM along the z-axis shows a modest increase with temperature, consistent with the higher thermal velocities at elevated temperatures.

3.1.3 Calculation of the Total Atomic Flux

Motivated by the semi-empirical kinetic model presented in Ref. [2] we estimate the total atomic flux emitted by the lithium oven using the expression:

$$\Phi_{\text{tot}} = \frac{1}{4} n_s \bar{v} A_{\text{Li}}, \tag{3.1}$$

where $A_{\text{Li}} = \pi \left(d_{\text{Li}}/2\right)^2$ is the surface area of the lithium reservoir, $\bar{v}$ is the mean thermal velocity of the atoms, and n_s is the atomic number density at the reservoir surface. The prefactor $1/4$ arises from integrating the angular emission distribution proportional to $\cos(\theta)$ and normalizing over the full solid angle of a sphere (see Ref. [79], Chapter 7). The mean thermal velocity $\bar{v}$ is given by the Maxwell-Boltzmann distribution:

$$\bar{v} = \sqrt{\frac{8 k_B T}{\pi m_{\text{Li6}}}}, \tag{3.2}$$

where m_{Li6} is the atomic mass of ^{6}Li. The atomic number density n_s is calculated via the ideal gas law: $n_s = p_s/(k_B T)$. Around $T = 623\,\text{K}$ ($\approx 350\,^\circ\text{C}$) the saturated vapor pressure is given by:

$$p_s = p_a \cdot \exp\left(\frac{-L_0}{k_B T}\right), \tag{3.3}$$

where $p_a = 1.15 \times 10^{10}\,\text{Pa}$ and $L_0/k_B = 18\,474\,\text{K}$ [80] with the latent heat of vaporization L_0. Figure 3.3 shows the theoretical prediction of the total hot atomic flux emitted by the reservoir in dependence of the lithium temperature. For a temperature of $400\,^\circ\text{C}$ the total hot atomic flux would be over 10^{16} atoms per second.

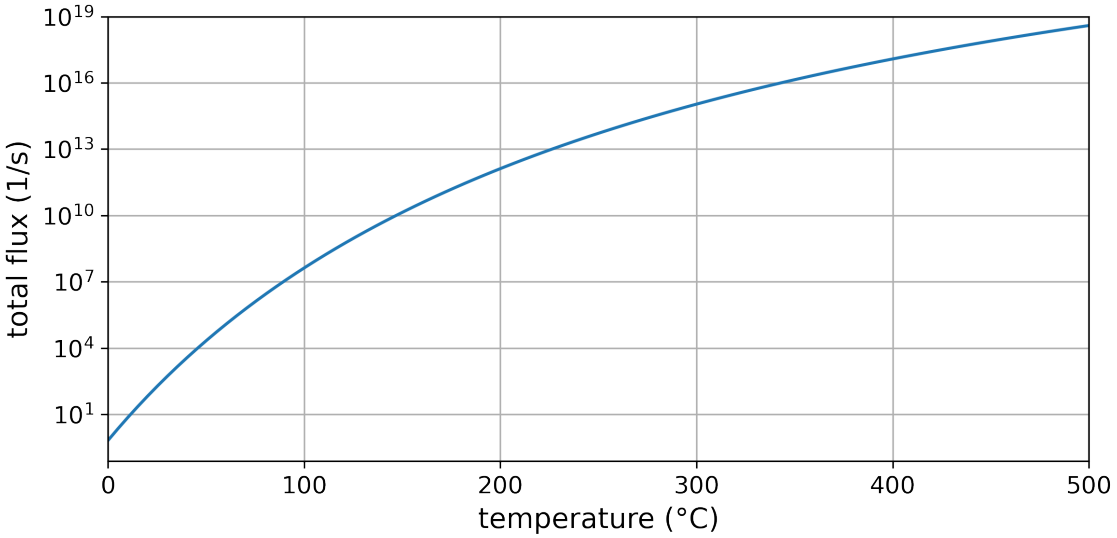

Figure 3.3: Theoretical prediction of the total hot atomic flux emitted by the reservoir in dependence of the temperature according to Equation 3.1.

3.1.4 Monte Carlo Simulation

To estimate the atomic flux reaching the trap region and the areal density in the push beam volume, we employ a Monte Carlo simulation. This simulation framework was originally developed as part of two master's theses [69, 71].

Atoms are initialized by randomly selecting starting positions on the surface of the lithium reservoir. The emission direction follows a cosine angular distribution $\cos(\theta)$, while the velocity magnitude is sampled from a Maxwell-Boltzmann distribution at simulation temperature T_{sim}.

Figure 3.4 shows the initial z-position and velocity distribution of all simulated atoms ($N = 1{\times}10^8$) at $T_{\text{sim}} = 400\,^{\circ}\text{C}$ (shown in gray). Atoms are propagated through the oven geometry, and only those that escape the reservoir and tube without wall collisions (see Section 3.1.6) and reach either the push beam or trap volume are retained for analysis.

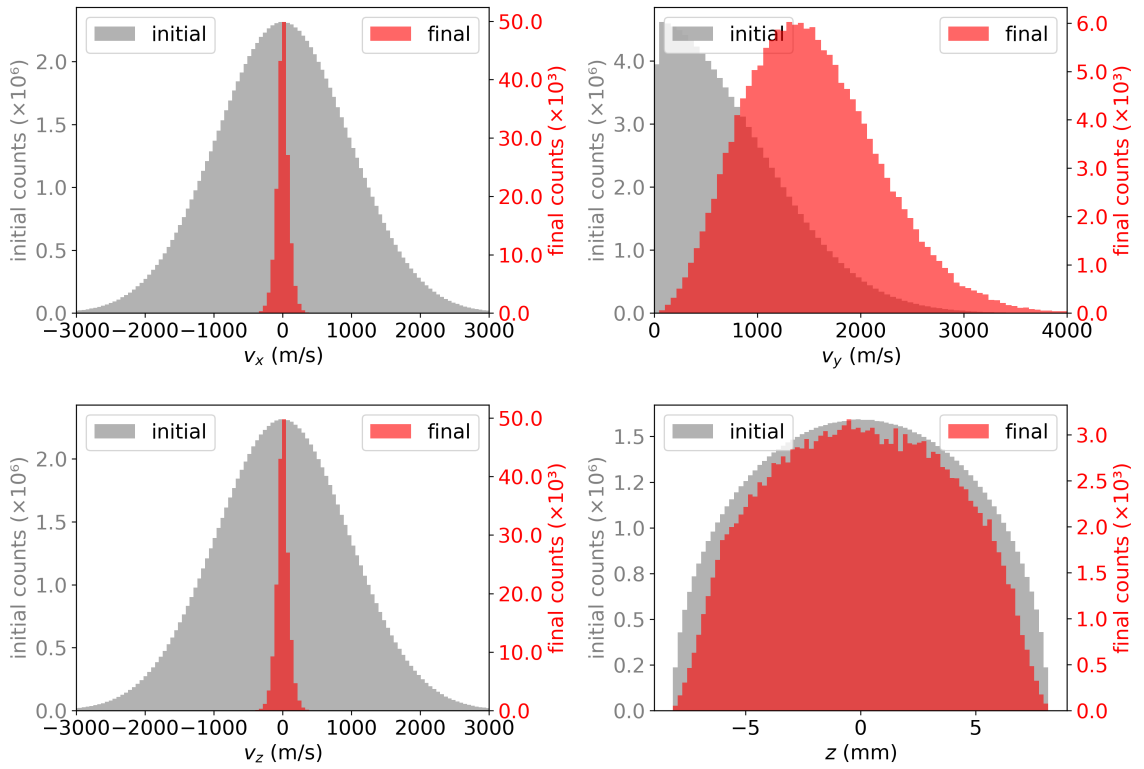

Figure 3.4: Simulated hot atomic flux emitted by the lithium oven at 400 °C reaching the trap volume for initially 1×10^8 atoms. The initial distribution of the atoms is shown in gray (order of 1×10^6). The final distribution of atoms reaching the trap volume is shown in red (order of 1×10^3).

We approximate the push beam volume as an infinite rectangle with $|x| < d_{\text{push}}/2$, and estimate the trap volume using an elliptical condition:

$$\left(\frac{x}{r_{\text{MOT}}}\right)^2 + \left(\frac{z}{\sqrt{2} \cdot r_{\text{MOT}}}\right)^2 < 1, \tag{3.4}$$

where r_{MOT} is the $1/e^2$ of the MOT beams in the center. The final positions and velocities of atoms reaching the trap volume are highlighted in red.

Figure 3.5 shows analogous distributions for atoms intersecting the push beam under identical simulation conditions.

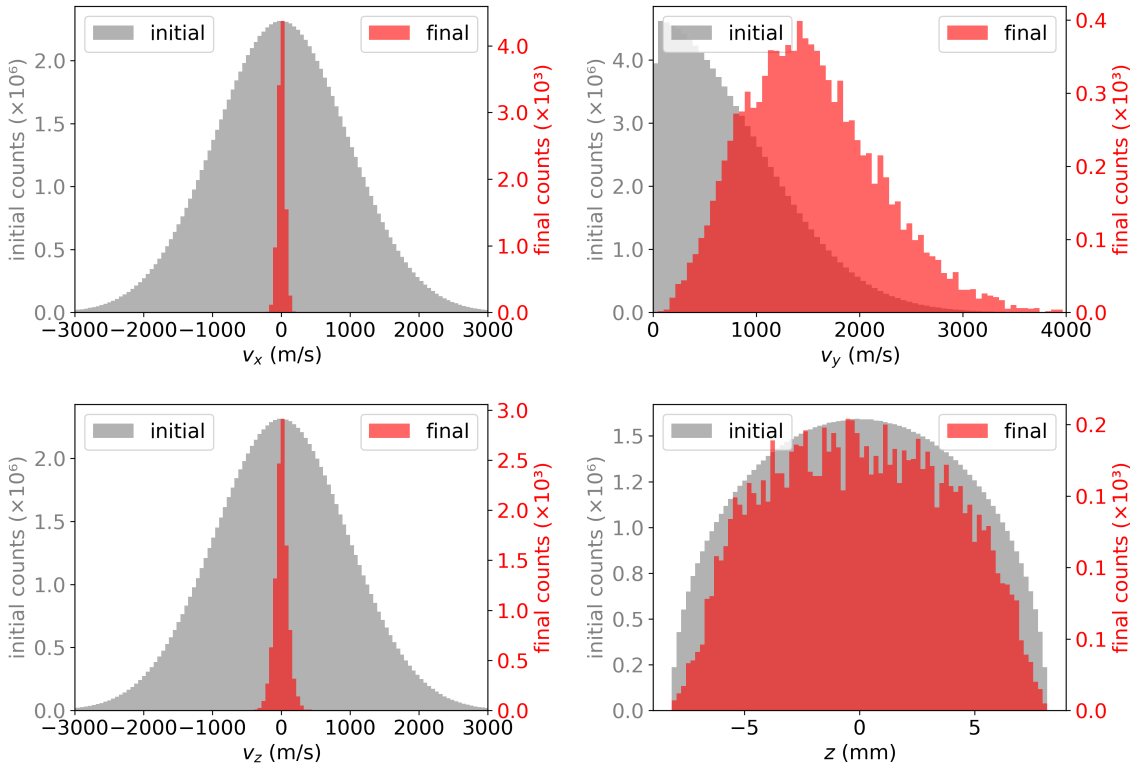

Figure 3.5: Simulated hot atomic flux emitted by the lithium oven at 400 °C reaching the push beam for initially 1×10^8 atoms. The initial distribution of the atoms is shown in gray (order of 1×10^6). The final distribution of the atoms is shown in red (order of 1×10^3).

Only a fraction of approximately 2×10^{-3} of the initially emitted atoms reach the trap volume, with merely 1×10^{-4} reaching the push beam volume. With a total emitted flux of $\sim 1 \times 10^{17}\,\mathrm{s}^{-1}$ at for example $T_{\mathrm{sim}} = 400\,^{\circ}\mathrm{C}$, this yields an atomic flux of $\sim 2 \times 10^{14}\,\mathrm{s}^{-1}$ in the trap volume.

As expected from symmetry, the mean velocity components along the x- and z-directions show only a small spread around zero. The geometric collimation imposed by the oven tube significantly narrows the final velocity distributions compared to the initial thermal distribution, explaining the narrower spectral features observed experimentally (Section 3.1.2).

Figure 3.6 presents the velocity distribution along the z-axis in the trap region for a lithium oven at 400 °C. The trap volume exhibits a z-velocity standard deviation of $\sigma_z \approx 90\,\mathrm{m/s}$, while the push beam volume shows $\sigma_z \approx 100\,\mathrm{m/s}$ (see Figure D.3). This is approximately 50% larger than the velocity distribution evaluated from the absorption measurement.

To save computational time we restrict our analysis of the hot atomic beam to the sub-ensemble of atoms with total velocity below a certain velocity of $v_c = 85\,\mathrm{m/s}$. This value was experimentally determined by Tiecke *et al.* [2] and is consistent with our 2D MOT simulations showing no capture above this threshold for any MOT

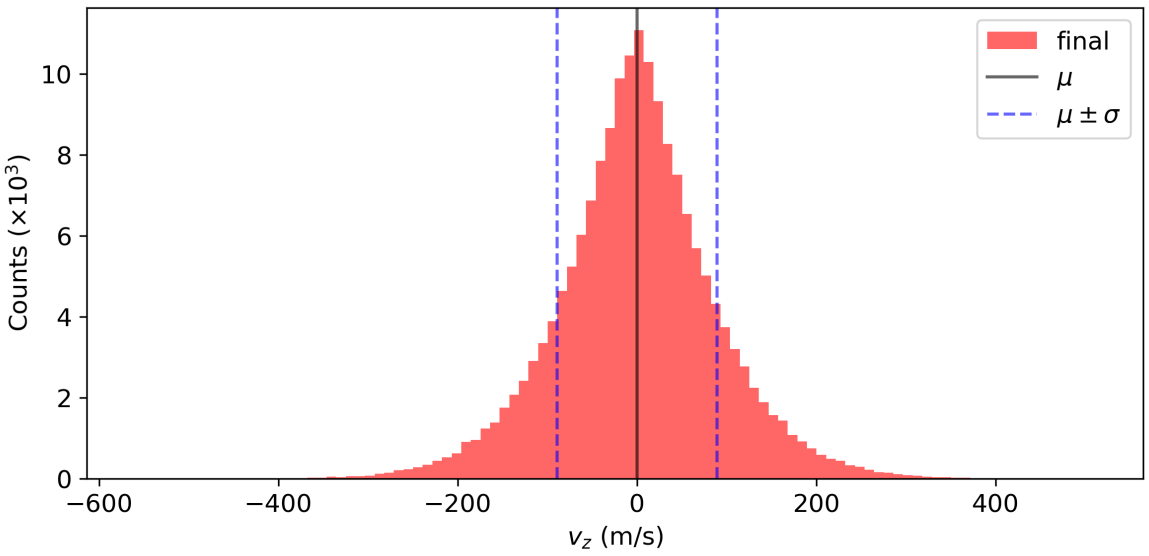

Figure 3.6: Simulated velocity distribution in the trap region along z-axis for a lithium oven at 400 °C and for initially 1×10^8 atoms. The mean μ of the distribution is around zero and the standard deviation σ is approximately 90 m/s.

parameters [72]. Therefore, we only simulate a fraction of approximately 2×10^{-4} compared to the total flux given by the Maxwell-Boltzmann distribution.

Approximately 0.2 % of initially emitted atoms reach the trap volume. Multiplying this fraction by the total atomic flux at 400 °C and scaling by the fraction of the Maxwell-Boltzmann distribution below v_c, we estimate a capturable flux of approximately $4 \times 10^{10}\,\mathrm{s}^{-1}$.

Figure 3.7 shows the z-velocity distribution for capturable atoms with a total velocity below 85 m/s in the trap region from a 400 °C lithium oven, simulated with $N = 1 \times 10^6$ atoms. The distribution is centered at $\mu \approx 0$ with standard deviation $\sigma = 3.6$ m/s. We will later compare this to the absorption measurements on the cold atoms in the MOT (see Section 3.4.1).

Furthermore, we observe that the width of the axial velocity distribution increases with increasing capture velocity. For a capture velocity of $v_c = 100$ m/s, the standard deviation increases by approximately 20 % to $\sigma \approx 4.3$ m/s (see Figure D.4). Such an increase in capture velocity could, in principle, be achieved by using larger MOT beam diameters (see Section 3.4.8).

However, since this Monte Carlo simulation considers only geometric constraints, we observe no significant change in either the capture fraction or the velocity distribution once the MOT beam diameters exceed the diameter of the oven tube, which then becomes the limiting aperture (see Figure D.5).

To obtain a more complete understanding of the capture process, we therefore performed Monte Carlo simulations of the full MOT cooling dynamics, including the complete atomic transition matrix (see Ref. [72]). Nevertheless, the velocity distributions obtained from the hot beam simulations provide realistic initial conditions for the subsequent 2D MOT simulations.

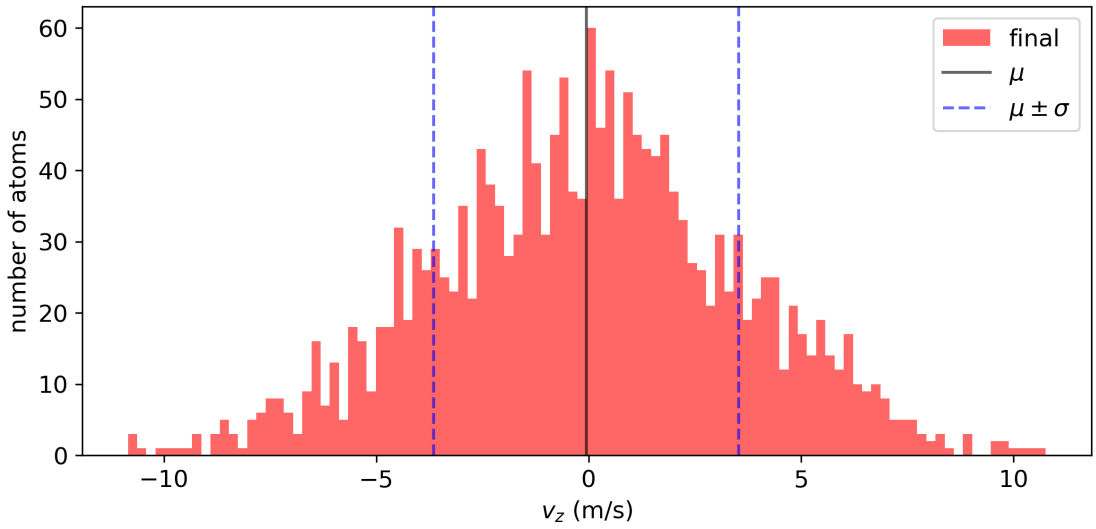

Figure 3.7: Simulated velocity distribution of capturable atoms in the trap region along z-axis for a lithium oven at 400 °C and for initially 1×10^6 atoms with a total velocity below 85 m/s and a MOT beam radius of 11.5 mm. The mean μ of the distribution is approximately zero and the standard deviation is $\sigma = 3.6$ m/s.

3.1.5 Temperature Calibration

To validate the simulation and calibrate the actual lithium temperature against the oven set temperature, we compare the simulated areal density in the push beam region with the experimental measurements.

The areal density of lithium atoms in the push beam area can be calculated from the simulation by determining the mean interaction time $\bar{t}_{\text{int}}$ of atoms traversing the beam volume:

$$n = \frac{\bar{t}_{\text{int}} \Phi_{\text{tot}}}{A_{\text{push}}}, \tag{3.5}$$

where A_{push} is the cross-sectional area of the push beam. To account for the isotopic composition, we scale this result by the ^{6}Li natural abundance of 95 % in the enriched reservoir.

The mean interaction time is computed by calculating the path length of each simulated atom through the push beam volume, dividing by its velocity to obtain the individual interaction time, and then averaging over all atoms that intersect the beam. As expected from kinetic theory, the mean interaction time decreases with increasing temperature due to higher atomic velocities (see Figure D.6). The simulation results are well described by a linear function, which we use for subsequent analysis.

By combining the fitted mean interaction time with the total atomic flux from Equation 3.1, we obtain a predicted areal density as a function of atomic temperature. Figure 3.8 shows the experimentally measured areal densities projected onto

this simulated prediction curve. This projection allows us to infer the actual atomic temperature corresponding to each oven set temperature.

We observe that the actual atomic temperature is systematically 40 °C to 60 °C lower than the set temperature in the region of interest, indicating incomplete heat transfer from the heating wire to the lithium reservoir. The temperature offset increases with higher set temperatures (see Figure D.7), likely due to enhanced radiative and conductive heat losses.

For subsequent 2D MOT measurements, we primarily operate at a set temperature of 400 °C, which corresponds to an actual atomic temperature of approximately 355 °C. This is comparable to the operating temperature of 350 °C reported by Tiecke *et al.* [2].

While this temperature offset has minimal impact on the capture velocity distribution or capture fraction, it significantly affects the absolute atomic flux. The 45 K difference would reduce the total emitted flux by approximately a factor of 5 compared to the nominal set temperature (see Figure 3.3). This would result in a total emitted flux of 2×10^{16} 1/s, correspondingly reducing the capturable flux incident on the 2D MOT area to approximately 8×10^{9}/s.

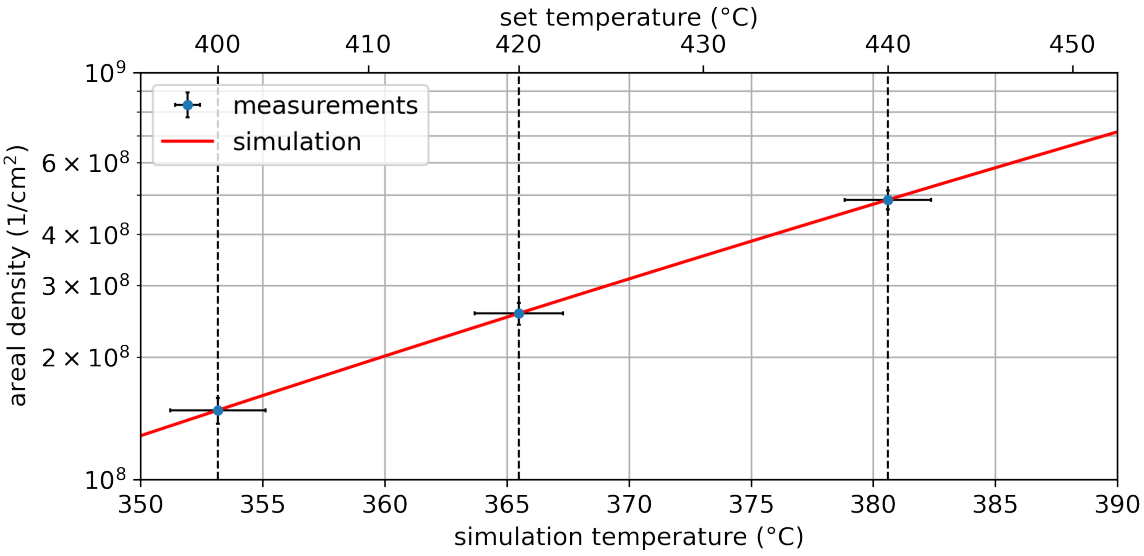

Figure 3.8: Projection of experimentally measured areal densities onto the simulated prediction curve. By mapping the measured areal densities onto the prediction from the simulation we can determine the actual atomic temperature (lower horizontal axis) corresponding to each oven set temperature (upper horizontal axis), revealing a systematic offset due to thermal losses.

3.1.6 Discussion on the Hot Atomic Beam Source

While our method of determining the atomic temperature from the absorption spectra and interaction-time simulations provides consistent results, an alternative and potentially more direct approach would be to extract the temperature via Doppler spectroscopy, as demonstrated in Ref. [2]. This technique infers the velocity distribution directly from the spectral linewidth, which might offer higher precision and fewer model assumptions.

It is important to recognize several limitations in the current simulation model. First, the surface of the lithium in the reservoir is assumed to be perfectly flat and at one equilibrium temperature, which does not fully capture the possible dynamics of molten lithium or the effects of surface tension and thermal gradients.

Second, atom-atom interactions such as Van der Waals forces are neglected, despite their potential influence on the velocity distribution and angular emission profile, especially at higher densities. Finally, we assume that lithium atoms impinging on the vacuum chamber walls are fully adsorbed and do not re-enter the atomic beam, which simplifies the simulation but may underestimate the true atomic flux in the interaction region.

In later measurements, we observe a hot atomic background signal in the spectroscopy region (Section 4.1.3). This indicates that the assumption of no scattering of lithium atoms from the chamber walls or from interatomic collisions is not entirely valid. Therefore especially the values for the atomic flux can only be a rough estimate.

Nevertheless, it is reasonable to assume that the actual temperature of the lithium oven is lower than the set temperature of the heating elements. In the following, we therefore distinguish between the oven set temperature, as defined by the heater setpoint for experimental reproducibility, and the effective oven temperature calibrated from the measured atomic flux.

Several approaches could increase the atomic flux from the oven. First, the emittance area A_{Li} could be increased, as implemented in the design described by Kerkmann *et al.* [81], which would directly enhance the atomic beam flux according to Equation 3.1. Additionally, before operating the 2D MOT Tiecke *et al.* [2] heated their lithium reservoir to 670 °C to thermally dissociate a possible lithium hydride (LiH) contamination, which can reduce the total flux of lithium.

3.2 Magnetic Field Configuration

Next, we characterize the MOT magnetic field and outline potential optimizations for the setup. As motivated in Ref. [2] the upper limit for the magnetic field gradient along the radius of the MOT in a 1D case can be described as:

$$\frac{\partial B}{\partial r} \leq \frac{(\hbar k)^{3/2}}{2\mu_B \left(m_{\mathrm{Li6}} r_{\max}\right)^{1/2}} \Gamma^{1/2}, \tag{3.6}$$

with the ^{6}Li mass m_{Li6} and the D_2 transition linewidth Γ and the maximum trap radius $r_{\max} = \sqrt{2} w_0$, which depends on the trap beam waist radius w_0. For a trap beam waist radius of approximately $w_0 = 11.5\,\mathrm{mm}$ this would result in a maximum magnetic field gradient of $\partial B/\partial r = 0.8\,\mathrm{T/m}$.

3.2.1 Magnetic Field Configuration and Measurement Setup

The used magnetic field configuration is based on the design presented in Ref. [2]. The magnetic quadrupole field is produced by four stacks of three permanent magnets[1]: Two with the field pointing parallel to the y-axis and two with the field pointing anti-parallel to the y-axis. The magnet stacks are placed in a aluminum mount, which is clamped onto the six-way cross of the 2D MOT (see Figure C.3).

For the measurement of the magnetic field, we use a custom-built magnetic field scanner based on a 3D magnetic field sensor[2] and translation stages. Figure 3.9 shows a schematic overview of the measurement setup and the magnet alignment. The distance between the magnets is measured from the center. The magnetic field vector of the magnets is indicated in the center of each magnet.

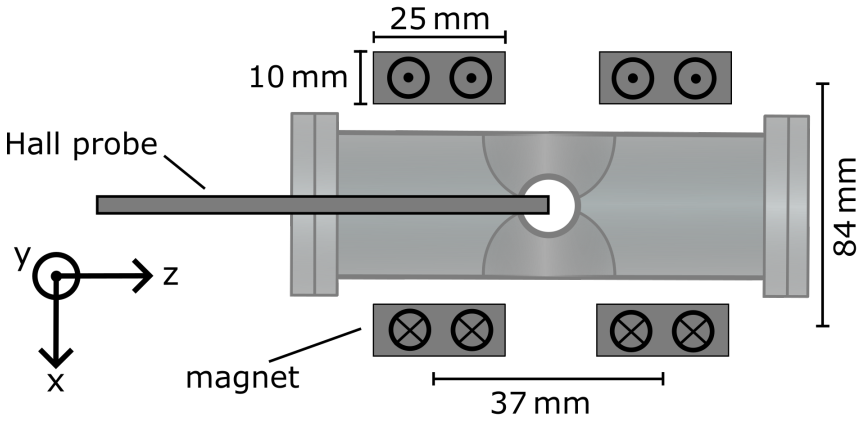

Figure 3.9: Measurement setup and the magnet alignment. The distance between the magnets is measured from the center. The magnetic field vector of the magnets is indicated in the center of each magnet.

[1] Eclipse Magnetics, N750-RB.
[2] Infineon, TLV493D-A1B6 3D Magnetic Sensor.

3.2.2 Simulation of the Quadrupole Field

We simulated the magnetic field produced in this setup with the open-source python module `magpylib` (version 5.1) [82]. More information on the simulation can be found in Ref. [83]. Figure 3.10 shows the simulation of the magnetic field in the xy-plane produced by the configuration described above.

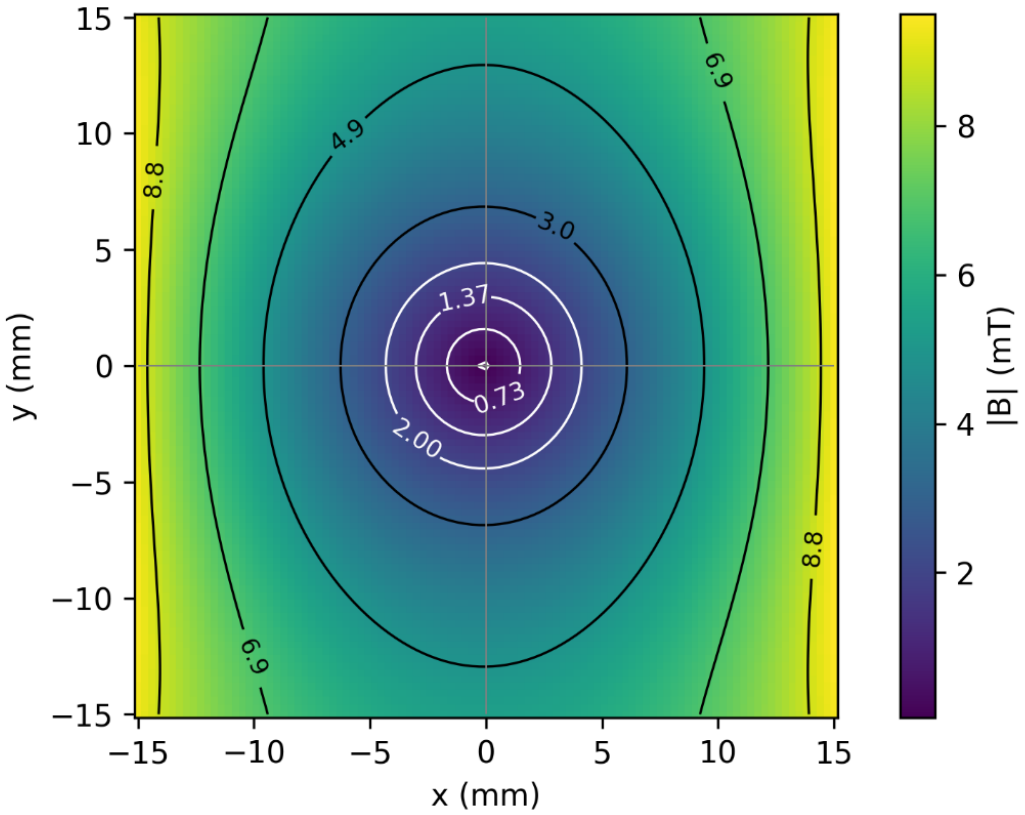

Figure 3.10: Simulation of the magnetic field in the xy-plane produced by the configuration described in Section 3.2.1. Figure taken from Ref. [83].

In the central region from -5 to $+5\,\mathrm{mm}$ the gradients along both axes are equal, yielding $\partial B/\partial x \approx \partial B/\partial y \approx 0.45\,\mathrm{T/m}$. Outside the central region, however, the magnetic field strengths along the two axes begin to deviate from one another (see Figure D.8). The field is symmetric about the z-axis, with a magnetic field minimum along $x = y = 0$ (see Figure D.9).

3.2.3 Measurement of the Quadrupole Field

We measure the magnetic field in a cubic volume of $20 \times 20 \times 40\,\mathrm{mm}^3$ without the vacuum cross. All three Magnetic field components are recorded at intervals of 1 mm in the x and y-directions, and 2 mm in the z-direction. An example of the measured quadrupole magnetic field in the xy-plane at a z-position near the center of the 2D MOT is shown in Figure 3.11. Each arrow represents the in-plane magnetic field direction at the corresponding grid point. The measured field exhibits a characteristic quadrupole structure, with opposing field directions on either side of the field minimum.

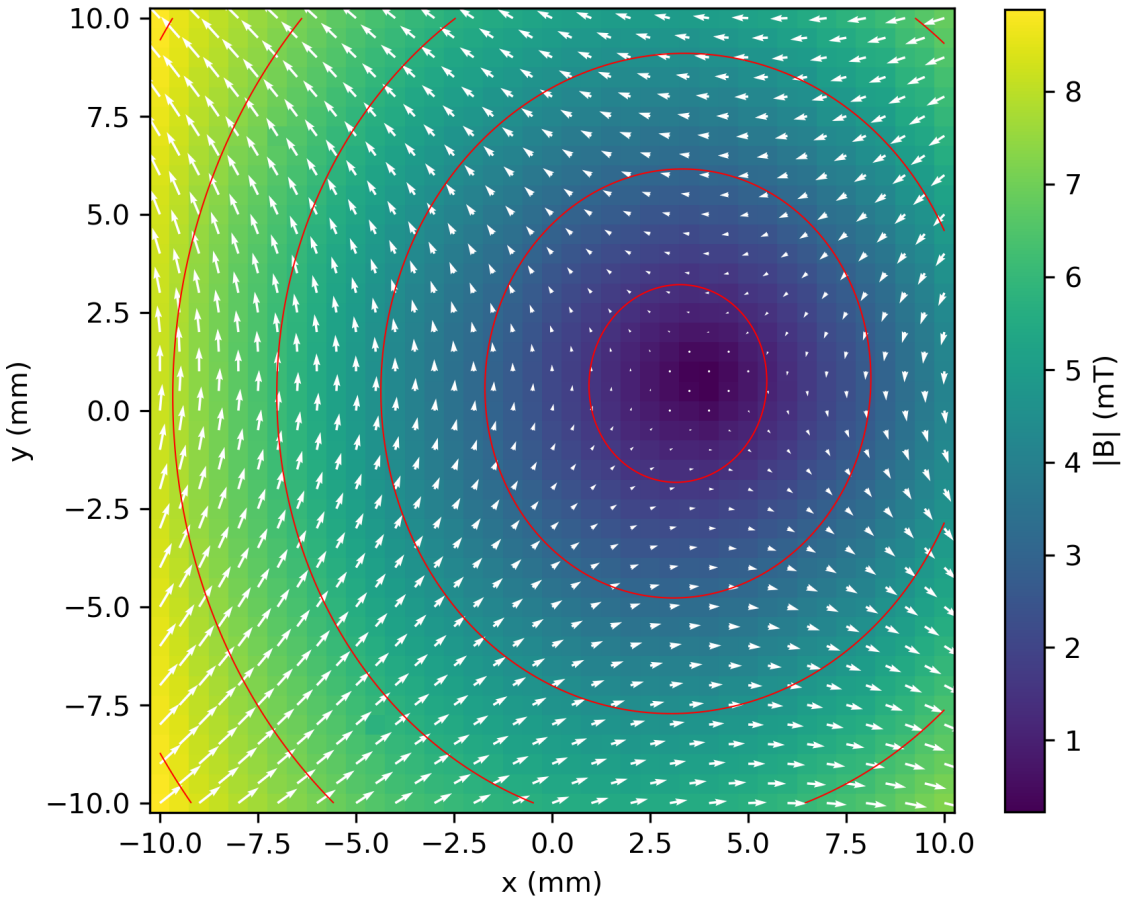

Figure 3.11: Example measurement of the quadrupole magnetic field in the vicinity of the 2D MOT center without the vacuum cross. The arrows indicate the measured magnetic field direction in the xy-plane at discrete points on a rasterized grid. Red contour lines visualize the fitted quadrupole field model according to Equation 3.7. The corresponding fit parameters are listed in Table 3.2 and the residuals are shown in Figure D.10.

The vacuum six-way cross was positioned such that its geometric center coincides with $x = (0 \pm 1)\,\mathrm{mm}$ and $y = (0 \pm 1)\,\mathrm{mm}$. However, the measured magnetic field minimum is shifted toward the upper left, by approximately 4 mm in the x-direction and 1 mm in the y-direction. Possible causes for this displacement include a slight misalignment of the apparatus and unequal magnetic field contributions from the permanent magnet stacks. This systematic offset along the x-axis is qualitatively consistent with the displacement of the cold atomic cloud we observe in the absorption measurements (e.g. Figure 3.21).

In addition to this displacement, the magnetic field $B(x, y)$ exhibits a slight elliptical shape and a rotation relative to the coordinate axes of the magnetic field scanner. To systematically characterize these deviations, a phenomenological fit function is implemented that models a conical field structure with an elliptical base with the major and minor principal axis labeled x' and y'. This choice is motivated by the approximately linear increase in magnetic field strength in the vicinity of the min-

imum, as confirmed by prior simulations of the magnetic field [69]. The magnetic field can be described as:

$$\begin{aligned} B(x,y) =& \sqrt{(m_{x'} \cdot x')^2 + (m_{y'} \cdot y')^2} + B_0, \\ \text{with } x' =& x \cdot \cos(\Theta) - y \cdot \sin(\Theta) + x_0, \\ y' =& x \cdot \sin(\Theta) + y \cdot \cos(\Theta) + y_0, \end{aligned} \tag{3.7}$$

where $m_{x'}$ and $m_{y'}$ are the magnetic field gradients along the x' and y'-axis of the ellipse and B_0 is the total offset. The rotation angle Θ describes the rotation of the ellipse's x' and y'-axis relative to the x and y-axis of the scanner, which are aligned to the six-way cross. The resulting fit function is shown in Figure 3.11 as red contour lines, while the corresponding fit residuals are plotted in Figure D.10. The fitted parameters are summarized in Table 3.2.

Table 3.2: Fit parameters corresponding to the phenomenological fit model (Equation 3.7) for the magnetic field measurement shown in Figure 3.11.

Fit parameter	**Value**
x_0	$(3.3 \pm 0.1(\text{stat}) \pm 1(\text{sys}))\,\text{mm}$
y_0	$(0.72 \pm 0.1(\text{stat}) \pm 1(\text{sys}))\,\text{mm}$
$m_{x'}$	$(0.57 \pm 0.01)\,\text{T/m}$
$m_{y'}$	$(0.51 \pm 0.01)\,\text{T/m}$
Θ	$(6 \pm 1)^\circ$
B_0	$(0.22 \pm 0.01(\text{stat}) \pm 0.1(\text{sys}))\,\text{mT}$
χ^2_{red}	1.13

The magnetic field gradient along the major axis is fitted to be $(0.57 \pm 0.01)\,\text{T/m}$, which corresponds to approximately 70 % of the maximum gradient for a trap beam waist of $w_0 = 11.5\,\text{mm}$. In contrast, the gradient along the minor axis is $(0.51 \pm 0.01)\,\text{T/m}$. This leads to a slight ellipticity of $m_{x'}/m_{y'} \approx 1.1$, which is smaller than the ellipticity we will later also observe in the atomic cloud of the 2D MOT (see Section 3.4.4). The measured magnetic field gradients are slightly larger than the calculated value of $0.5\,\text{T/m}$ reported in Ref. [2] and our own simulations, but this could be explained by a variation in the magnetization of the individual magnets. Furthermore, no measurable tilt of the magnetic field minimum with respect to the z-axis was observed within our experimental resolution.

3.2.4 Improvement of the Magnetic Field Configuration

Our simulations of the 2D MOT indicate that the capture efficiency is highly sensitive to the magnetic field gradient (see Ref. [72], Fig. 4.14). To improve both the magnitude and spatial positioning of the magnetic field gradient, we have developed a new magnetic field configuration based on four rings of permanent magnets aligned along the axis of the six-way cross vacuum chamber (see Ref. [83]). The magnet rings are placed on adjustable mounts, allowing the magnetic field gradient to be tuned by varying the axial separation between the rings. This tunability enables optimiza-

tion of the trappable atomic flux by matching the field gradient to the MOT beam geometry and detuning conditions.

Figure 3.12 shows the proposed magnetic field configuration, consisting of four concentric rings, each holding 32 permanent magnets[1]. Two of the rings are oriented with their magnetization pointing toward the center, while the other two are oriented with the magnetization pointing outward. The direction of the magnetization is indicated by arrows in the figure.

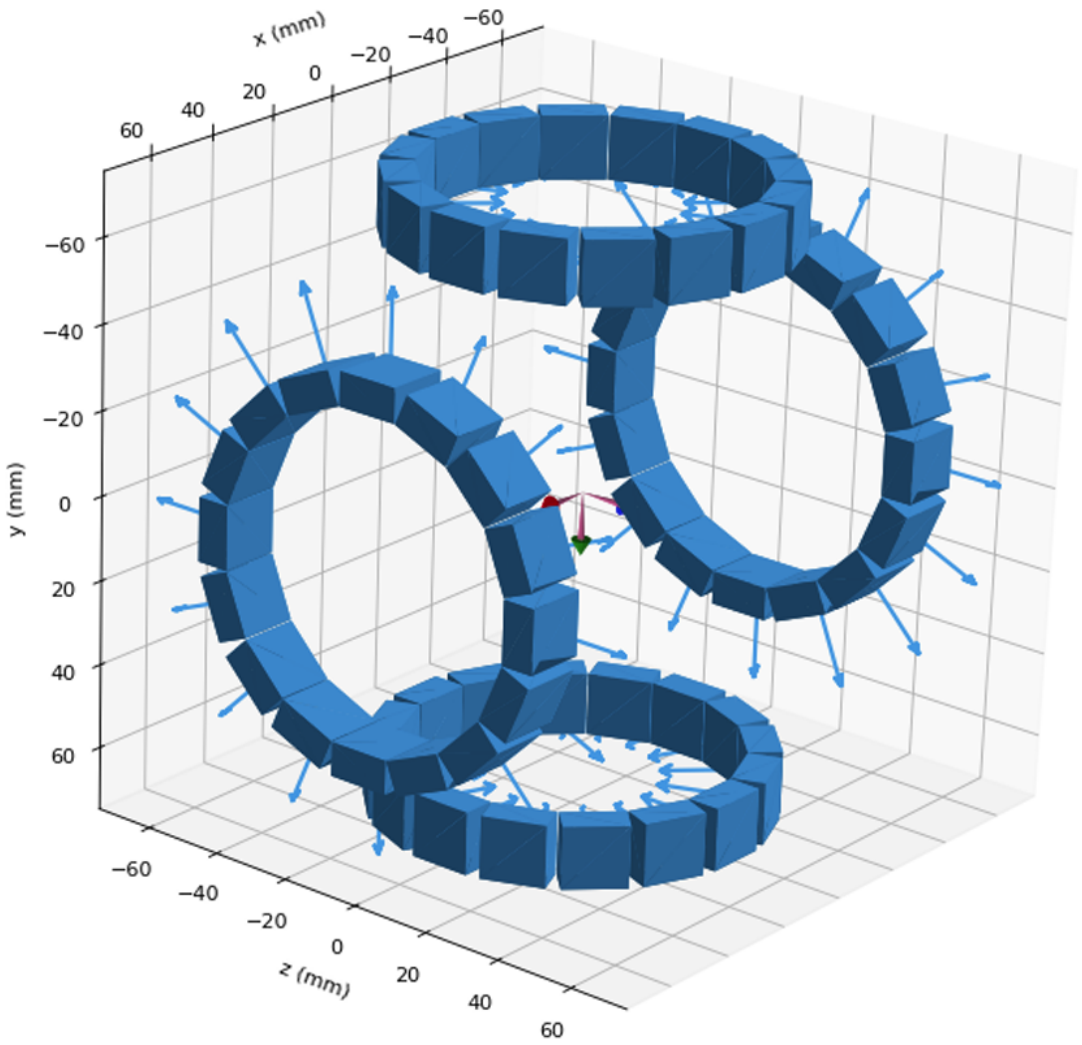

Figure 3.12: Proposed magnetic field configuration, consisting of four concentric rings, each holding 32 permanent magnets[2]. Two of the rings are oriented with their magnetization pointing toward the center, while the other two are oriented with the magnetization pointing outward. The direction of the magnetization is indicated by arrows. This allows to generate a more symmetric quadrupole field in the trapping region. Figure taken from Ref. [83].

[1]Neodymium N45, dimensions 8 mm × 15 mm × 15 mm.

The measured quadrupole field, together with the corresponding simulation, is shown in Figure 3.13. Compared to the previous configuration, the new setup produces a significantly more symmetric field that is better centered around the origin. The experimentally measured field is slightly weaker than the simulated prediction and exhibits small irregularities, which may be attributed to slightly magnetic materials in the mount.

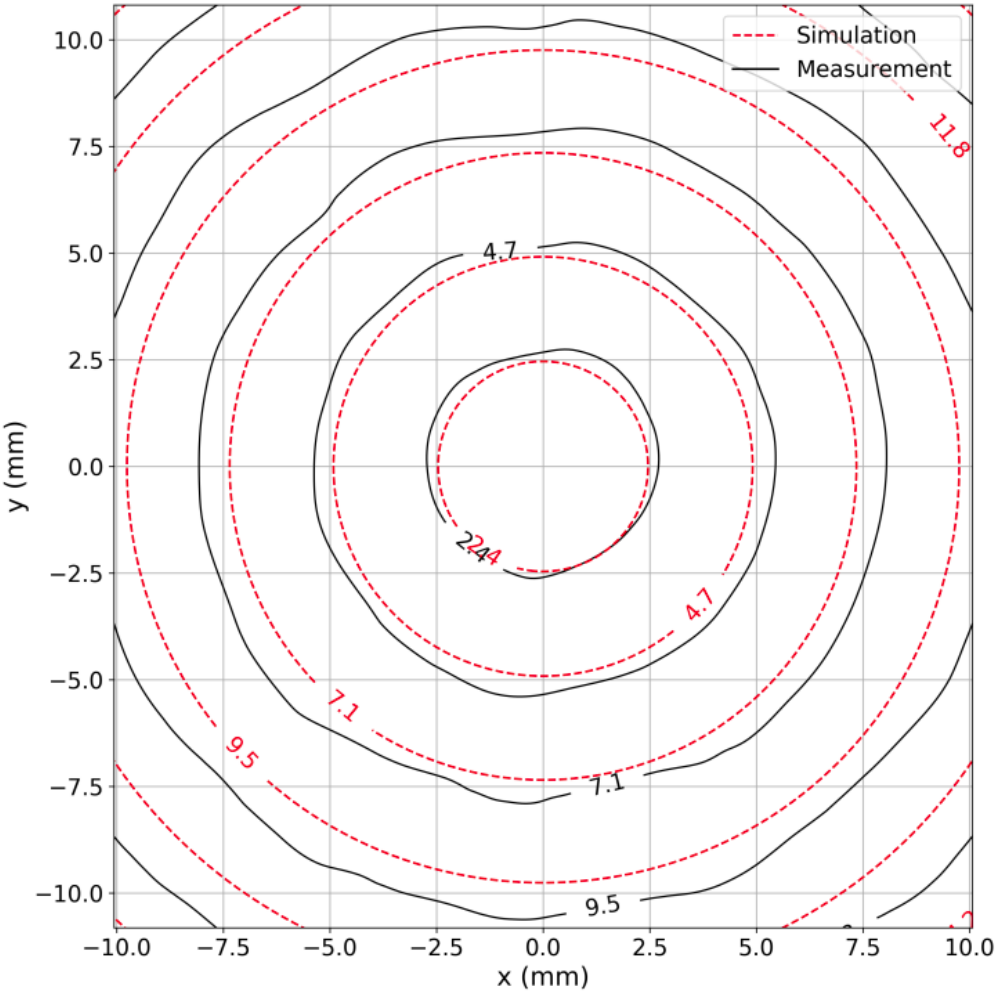

Figure 3.13: Measured (solid lines) and simulated (dashed lines) magnetic field strength in mT for the new magnetic field configuration. Compared to the previous design, the new setup generates a more symmetric field that is better centered around the origin. The measured field is slightly weaker than the simulation and shows small irregularities. Figure taken from Ref. [83].

The new magnetic field configuration has not yet been implemented in the MOT setup and remains to be experimentally tested. A detailed description of its design, simulation, and characterization is provided in Ref. [83]. Since this new configuration was developed based on insights gained from the absorption measurements of the 2D MOT, the experiments presented in the following chapters are still performed with the original setup (Section 3.2.1).

3.2.5 Outlook on the Magnetic Field Configuration

The upgraded magnetic field system will enable precise adjustment of the magnetic field gradient to optimize for trapping efficiency. Another improvement would be to implement dedicated offset coils to shift the magnetic field zero position, allowing precise alignment of the MOT center with the downstream spectroscopy setup, like presented in Ref. [84].

Additionally, auxiliary magnetic field coils could be used to displace the trap minimum along the z-axis, spatially separating the cold trapped atoms from the hot atomic beam emerging from the oven. This would reduce collisional losses and improve the achievable atomic density.

For future improvements, measuring the magnetic field inside the vacuum chamber would be advantageous. To prevent the lithium source from reacting with air, the chamber would need to be flushed with an inert gas or isolated using a gate valve positioned in front of the oven.

For high-precision spectroscopy it is important to minimize magnetic field gradients in the spectroscopy region. Tiecke *et al.* [2] report a residual magnetic field gradient of only 210 µT/m at a distance of 23 cm from the MOT center along the z-axis. For a spectroscopy beam waist on the order of mm this would correspond to a Zeeman shift on the order of 10 kHz. In Section 5.1.3 we will further discuss the influence of the magnetic field.

3.3 Loading of the 2D MOT

In the following we evaluate the loading time of the two-dimensional magneto-optical trap (2D MOT) experimentally to get an upper limit for the total number of atoms in the MOT.

When atoms are emitted from the hot atomic beam source and pass through the trapping volume of the 2D MOT, those with velocities below the capture velocity can be trapped, cooled, and accumulated in the MOT region (see Section 3.1). The number of atoms N in the 2D MOT increases until an equilibrium point is reached, where the loading rate L is equal to the loss rates α. The change in the number of atoms over time can be described by:

$$\frac{dN}{dt} = L - \alpha N. \tag{3.8}$$

Several mechanisms contribute to the loss of atoms from the trap, in the following the most important ones are discussed:

- A particularly important loss mechanism in the 2D MOT arises from the absence of confinement along the axial-/z-direction. Atoms with momentum components along this axis are not trapped and can escape from the MOT volume over time. Our simulations indicate that the axial velocity of the atoms has a standard deviation of approximately 3 m/s. For a beam waist radius of 12 mm, this results in a loss rate of roughly 300/s per atom and a residence time on the order of ms.

- Another intrinsic limitation arises from the increasing atomic density in the trap. Trapped atoms retain some residual kinetic energy and are continuously excited by the MOT beams, leading to spontaneous emission. Photons emitted within the MOT volume may be re-scattered by nearby atoms, introducing additional forces that cause heating and limit the attainable atomic density [85].

- Furthermore, fast atoms from the oven can collide with trapped atoms, leading to momentum transfer and so-called “knock-out” collisions, which eject atoms from the trap [2].

The integration of Equation 3.8 leads the temporal evolution of the atom number in the MOT:

$$N(t) = \frac{L}{\alpha}\left[1 - e^{-\alpha t}\right], \tag{3.9}$$

with the initial number of atoms $N(t = 0) = 0$.

3.3.1 Setup for Measurement of the Loading Curve

For the measurement of the loading curve, we use a balanced photodiode to detect the absorption of the push beam (see Figure 2.5). The push beam has a radius of $(400 \pm 20)\,\mu\text{m}$ at the MOT position[1]. The MOT beams have a waist radius of $(17.1 \pm 0.3)\,\text{mm}$ and a power of $(28 \pm 2)\,\text{mW}$ each for the trap and repump frequency component. The trap and repump transition are detuned by $(-9 \pm 2)\,\Gamma \pm 30\,\text{MHz}$ and $(-7 \pm 2)\,\Gamma \pm 30\,\text{MHz}$ respectively. The lithium oven is set to a temperature of 400 °C. An overview of the experimental parameters is provided in Table 3.3.

Table 3.3: Experimental parameters for the loading curve measurements.

MOT beam	trap power	$(28 \pm 2)\,\text{mW}$
	repump power	$(28 \pm 2)\,\text{mW}$
	trap detuning	$(-9 \pm 2)\,\Gamma \pm 30\,\text{MHz}$
	repump detuning	$(-7 \pm 2)\,\Gamma \pm 30\,\text{MHz}$
	waist radius	$(17.1 \pm 0.3)\,\text{mm}$
push beam	power	variable
	push frequency	variable
	radius	$(400 \pm 20)\,\mu\text{m}$
lithium oven	set temperature	400 °C

The experimental setup is shown in Figure 3.14. To rapidly switch the trapping light on and off, we fully modulate the amplitude of the AOM double pass (AOM DP), which generates the repump frequency in the MOT beams, at 52 Hz[2]. A commercial ECDL[3] is frequency-stabilized to a wavemeter[4] and coupled via a polarization-maintaining fiber into the push beam setup (see Figure 2.5). For each measurement, the push beam frequency is fine-tuned within a few megahertz to maximize the loading-curve amplitude at the corresponding atomic transition.

Absorption of the push beam is detected with a balanced photodetector[5], where the signal beam is compared against an unperturbed reference. The photodetector output voltage is converted into optical power using a linear calibration described in detail in Ref. [71]. The push beam position is optimized using a motorized periscope to maximize the absorption signal.

Finally, the modulation signal from the frequency generator[6] is used to trigger the oscilloscope[7], which records the loading curve measurements. The absorbed push beam power is measured as a function of time and averaged over 100 traces.

[1] The beam radius was measured with a beam profiler in the reference beam, at the same optical path length as the push beam in the MOT center.
[2] The AOM switching time is in the order of 100 ns.
[3] Toptica, TA pro 670-3V0.
[4] High Finesse, WS7-30.
[5] Thorlabs, PDB220A2/M – free-space balanced photodetector, UV-enhanced Si, 4.1 mm active diameter, 190–1100 nm.
[6] Rigol, DG812 – Function/Arbitrary Waveform Generator.
[7] Teledyne Lecroy, WaveRunner 8104.

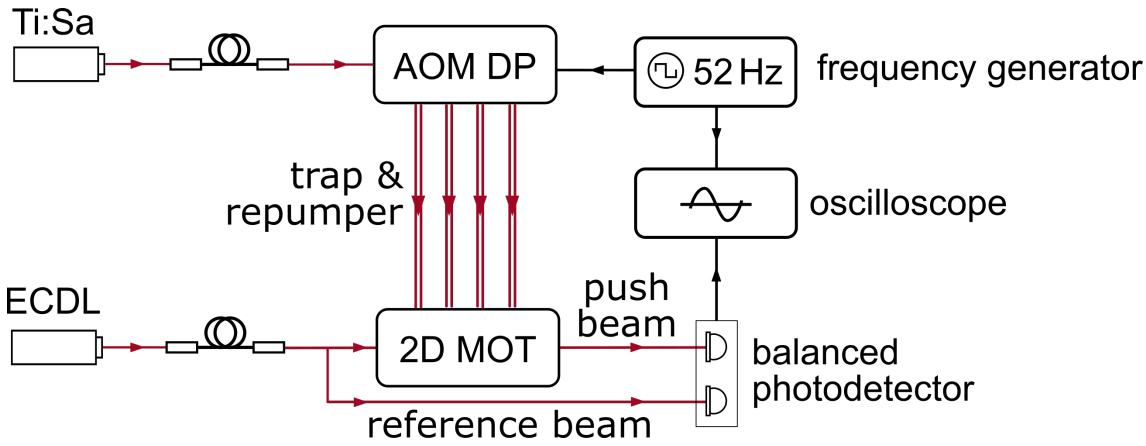

Figure 3.14: Setup for measurement of the loading curve. To rapidly switch the trapping on and off, we fully modulate the amplitude of the AOM double pass (AOM DP). This leads to rapid switching of the repump frequency in the MOT beams at 52 Hz. The external cavity diode laser (ECDL) for the push beam is locked to a wavemeter and coupled into the push beam setup (see Figure 2.5). The push beam traverses the 2D MOT region and the absorption is measured on a balanced photodetector by comparing it to a unperturbed reference beam. A frequency generator provides the modulation signal and simultaneously triggers the oscilloscope used for the acquisition of the loading curve measurements. Figure adapted from Ref. [71].

3.3.2 Measurements of the Loading Curves

Figure 3.15 shows a representative pair of loading curves for the upper and lower ground state D_2 transition recorded at a push beam power of $(5.00 \pm 0.15)\,\mu W$[1]. To correct for imperfect balancing of the photodetector, a constant baseline was fitted to the signal and subtracted from the data. Each trace is averaged over 100 repetitions. The data was then binned, and the standard deviation of the baseline was used as an estimate of the statistical uncertainty for each data point.

The red vertical dashed lines indicate the switching of the repump beam. The red curve shows a fit with the model in correspondence to Equation 3.9:

$$N(t) = A \cdot \left(1 - \exp\left(-\frac{t - t_0}{\tau}\right)\right) + B, \tag{3.10}$$

with timing offset t_0, a scaling factor A, a total offset B and the loading time $\tau = 1/\alpha$. The timing offset has been optimized to minimize the loading time τ (see Figure D.12).

We observe two distinct loading curve shapes on both the D_1 and D_2 transition, depending on the push beam frequency, which drives either the upper or the lower hyperfine ground state transition. This behavior is most likely caused by optical pumping between the two hyperfine ground states of the hot atomic background as it traverses the push beam, induced by the MOT beams.

[1]Measured with a Thorlabs, S130C slim dual-range power head with a silicon detector, with a relative uncertainty of 3 %.

A similar effect is observed when the power of the MOT beams is modulated simultaneously by using the chopper wheel in the Ti:Sa output (see Figure 2.4). Even if the formation of a MOT is suppressed by blocking one of the four MOT beams, a baseline shift is still visible (see Figure D.11). The baseline shifts for different transitions are further discussed in Ref. [71].

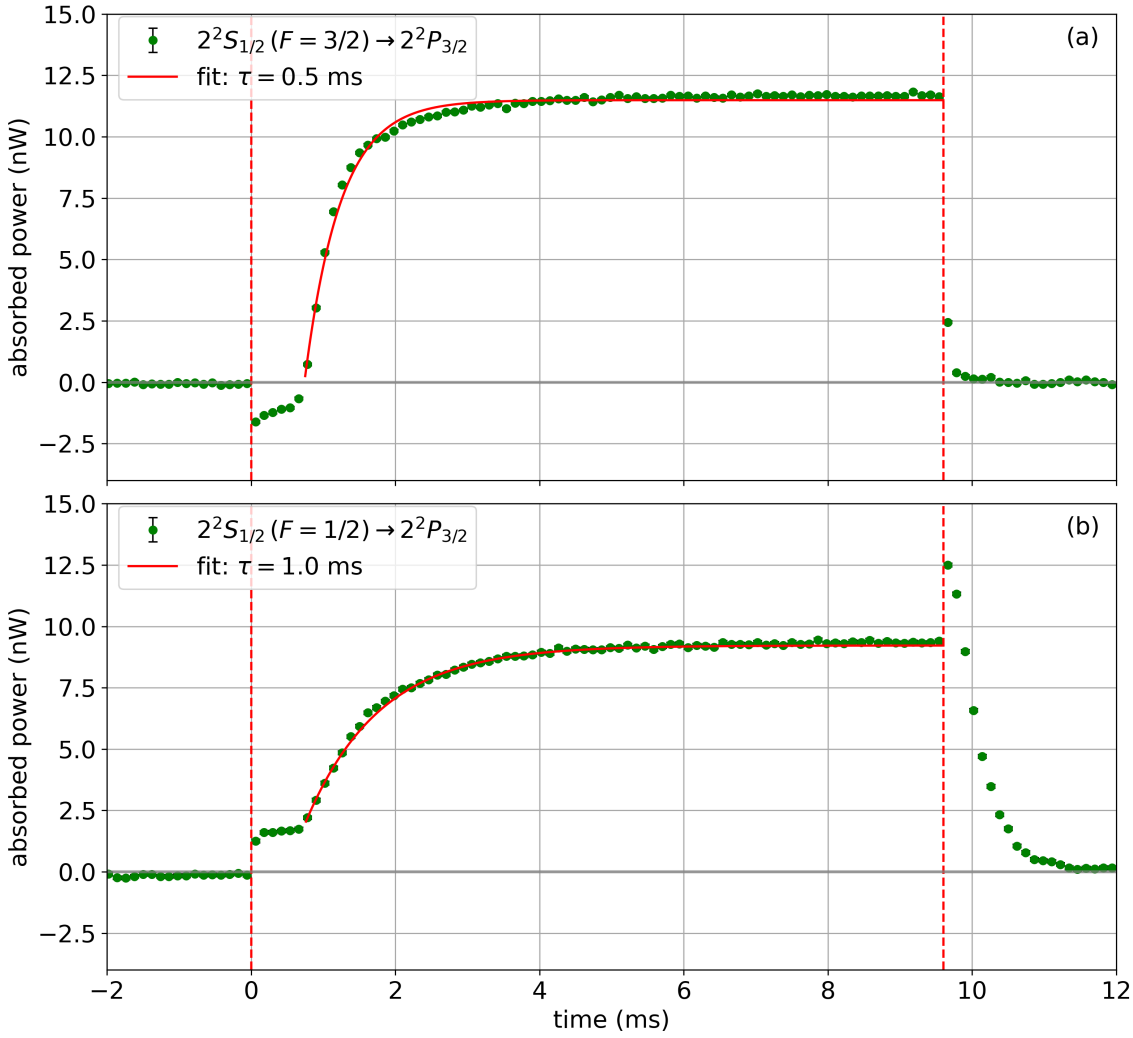

Figure 3.15: Two characteristic loading curve shapes for the D_2 transition and a push beam power of $(5.00 \pm 0.15)\,\mu W$. The push beam absorbed power is plotted as a function of time. Each trace is averaged over 100 repetitions. The red vertical dashed lines indicate the switching of the repump beam. The red curve shows a fit to the data using the model from Equation 3.10, with fit parameters provided in Table D.3. The upper ground state transition (a) and the lower ground state transition (b) have a loading time of $\sim 0.5\,ms$ and $\sim 1\,ms$, respectively. The features after the switching of the push beam are results of optical pumping between the two ground states.

3.3.3 Extrapolation to Zero Push Beam Intensity

Due to saturation effects and additional trapping along the z-axis, we expect the apparent MOT loading time to depend on the intensity of the push beam. Figure 3.16 displays the extracted loading times as a function of the push beam intensity. The peak intensity of the Gaussian push beam is calculated as $I_{\mathrm{PB}} = (2P_0)/(\pi w_{\mathrm{MOT}}^2)$, where P_0 denotes the total beam power and w_{MOT} the beam radius at the MOT position. The uncertainties in I_{PB} are obtained by propagating the errors of the power and beam radius measurements, while the error bars of the loading times reflect the uncertainties from the fitting routine described in the previous section.

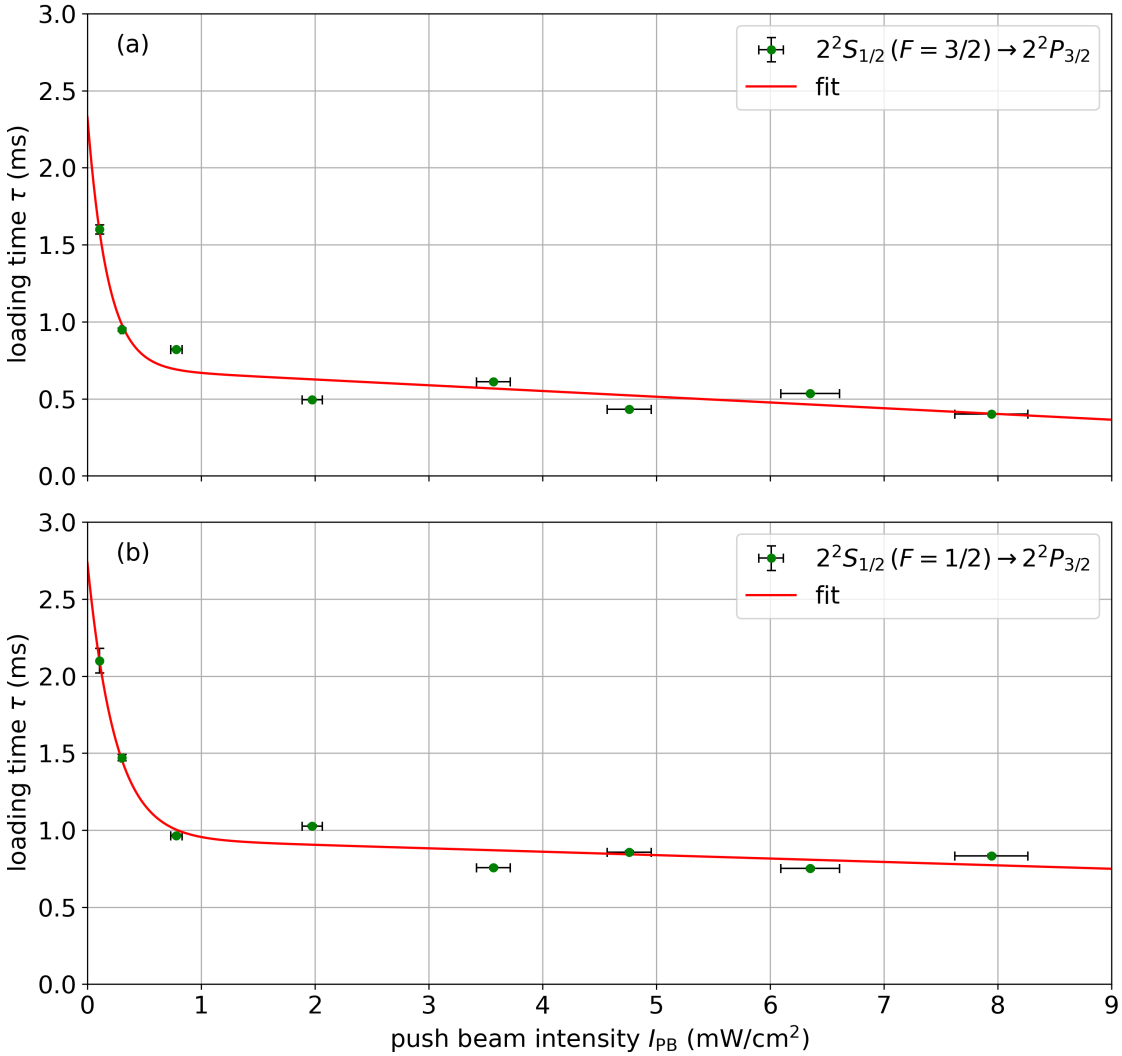

Figure 3.16: Evaluated loading times as a function of push beam intensity for the upper (a) and lower (b) ground state D_2 transition. To extrapolate to zero intensity the data was fitted with a phenomenological function (see Equation 3.11). The fit parameters can be seen in Table D.4. By extrapolating this fit to zero push beam intensity, we obtain a loading time of (2.3 ± 0.5) ms for the push beam frequency set to the upper ($F = 3/2$) ground state and a loading time of (2.7 ± 0.3) ms for the lower ($F = 1/2$) ground state.

As the push beam intensity increases, a decrease in the apparent MOT loading time is observed. This behavior can be partially explained by the push beam providing an additional confinement of the atoms in the 2D MOT along the axial (z)-direction. The observed dependence is phenomenologically fitted using a model that combines an exponential decay at low intensities with a linear dependence at higher intensities:

$$\tau(I_{\mathrm{PB}}) = a \cdot \exp(-b\, I_{\mathrm{PB}}) + c \cdot I_{\mathrm{PB}} + d. \tag{3.11}$$

Here, I_{PB} denotes the push beam intensity, and a, b, c, and d are free fit parameters. By extrapolating this fit to zero push beam intensity, we obtain a loading push beam independent time of $(2.3 \pm 0.5)\,\mathrm{ms}$ for the push beam frequency set to the upper $(F = 3/2)$ ground state and a loading time of $(2.7 \pm 0.3)\,\mathrm{ms}$ for the lower $(F = 1/2)$ ground state transition. In the following, the extracted loading times are used to determine an appropriate modulation frequency for the 2D MOT, which is required for the implementation of a lock-in detection scheme.

3.3.4 Estimate on the Atom Number from the Loading Curves

Assuming that the MOT is loaded homogeneously throughout the entire trapping volume, an upper bound for the total number of trapped atoms can be estimated. We can use the trappable atomic flux of $L \approx 8 \times 10^9/\mathrm{s}$ obtained in Section 3.1.5 as a loading rate and combine it with the average trapping efficiency $P_{\mathrm{trap}} \approx 20\,\%$ from our Monte Carlo simulations of the 2D MOT [72]. Using Equation 3.9 the steady state atom number is given by $N(t \to \infty) = L \cdot \bar{\tau} \approx 5 \times 10^6$, where $\bar{\tau} = 2.5\,\mathrm{ms}$ denotes the mean loading time.

As will be shown in the next chapter, the experimentally observed atom number is approximately one order of magnitude smaller. This discrepancy indicates the assumptions underlying this estimate are not fully realized, but this could also indicate that the trapping efficiency in the experiments might not be as large as anticipated by the Monte Carlo simulations.

3.4 2D MOT Absorption Profiles

To account for the spatial distribution of the cold atomic cloud in the two-dimensional magneto-optical trap (2D MOT), we use a motorized periscope (see Figure 2.5) to measure the absorption of the push beam at different positions along the cooling (xy)-plane. The goal of these measurements is to estimate the total number of trapped atoms and to optimize the MOT parameters to maximize it.

The following measurements were performed under the assumption of the MOT beam polarizations as shown in Figure 2.2. Shortly before the submission of this thesis, it was discovered that during an upgrade of the experimental setup the polarization of the two lower MOT beams has been interchanged. This issue went unnoticed because we did not expect formation of a cold atomic cloud under these conditions. More information on this can be found in Appendix A.

3.4.1 Absorption Spectra

Using the setup shown in Figure 2.5 we measure the absorbed power from the ensemble of cold ^{6}Li atoms while scanning the push beam frequency. Figure 3.17 shows absorption spectra with the MOT turned on and turned off. Each spectrum is averaged over 20 scans with a scan frequency of 1 Hz. Each MOT beam has a total power of (100 ± 10) mW with an equal distribution between trap and repump frequency. Apart from that the experimental settings are as described in Table 3.5. The MOT is modulated by turning the power of the repump frequency in the MOT beams on and off using the acousto-optic modulator (AOM) (see Section 2.1.2).

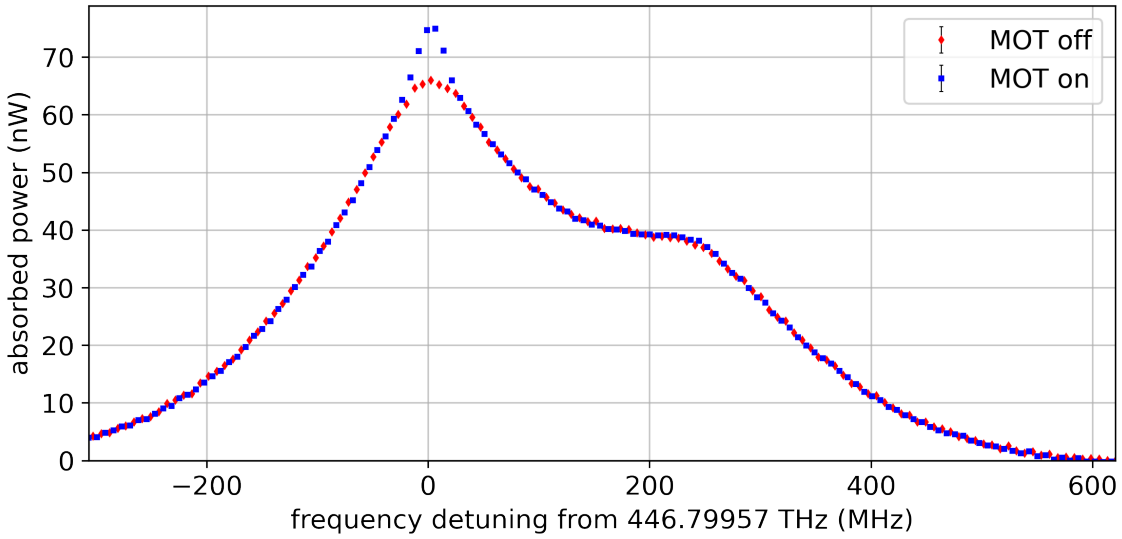

Figure 3.17: Example for absorption spectra with 2D MOT on and off. Each spectrum is averaged over 20 scans with a scan frequency of 1 Hz. Each MOT beam has a total power of (100 ± 10) mW with an equal distribution between trap and repump frequency. Apart from that the experimental settings are like described in Table 3.5. The error bars represent the standard deviation of the baseline data points and are too small to be visible in this representation.

In both spectra we observe a broad absorption spectrum from the hot atomic background originating from the lithium oven (see Section 3.1). As discussed in Section 3.1.2 the absorption from atoms in the upper ground state is about two times larger than the absorption coming from the lower ground state. Only in the spectrum with MOT repump frequency turned on one can see a narrowed peak of increased absorption around 446.799 570 THz. This narrow feature also disappears when the MOT beams are completely switched off or detuned. This indicates that the additional absorption originates from cooled atoms.

Figure 3.18 shows the difference between the two spectra. We observe one strong peak around 446.799 570 THz, which corresponds to the upper ground state ($F = 3/2$) of the D_2 transition and one weaker peak shifted by +240 MHz which corresponds to the lower ground state ($F = 1/2$) of the D_2 transition.

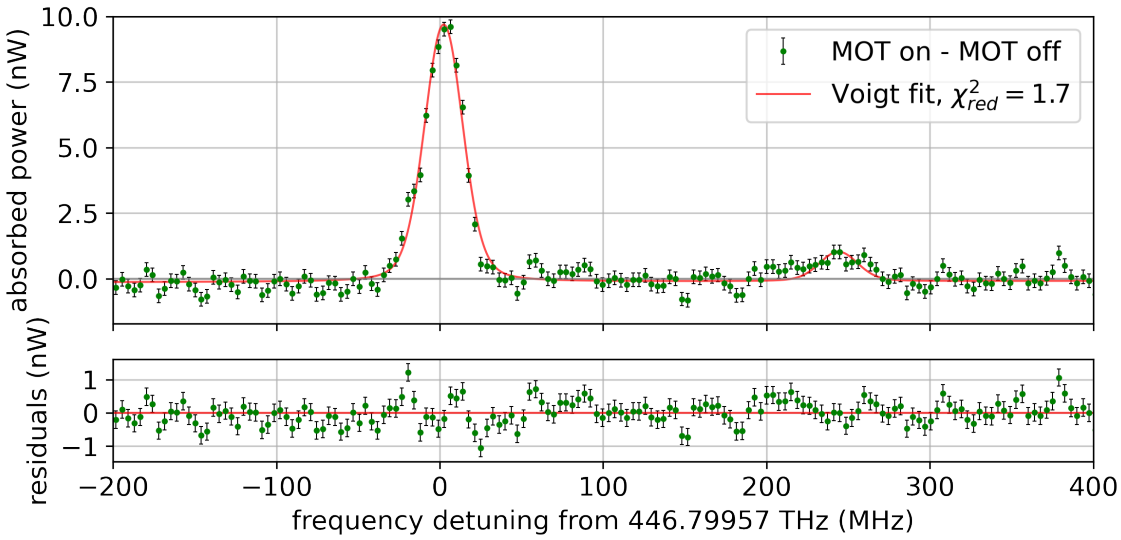

Figure 3.18: Example for the difference between absorption spectra with 2D MOT on and off with a Voigt fit on the lower ($F = 1/2$) and upper ground state ($F = 3/2$) transition. We subtract the two spectra from Figure 3.17. Each spectrum is averaged over 20 scans with a scan frequency of 1 Hz. Each MOT beam has a total power of (100 ± 10) mW with an equal power distribution between trap and repump frequency. Apart from that the experimental settings are like described in Table 3.5. The error bars represent the standard deviation of the baseline data points. The spectrum is fitted with a sum of two Voigt profiles (see Section B.3) with a fixed natural linewidth $\Gamma/2\pi = 5.9$ MHz. Table 3.4 shows the resulting fit parameters.

The spectrum is fitted with a sum of two Voigt profiles (see Section B.3) with a fixed natural linewidth $\Gamma/2\pi = 5.9$ MHz[1]. Table 3.4 shows the fit parameters and further deduced values. The resulting reduced chi squared $\chi^2_{\text{red}} = 1.7$ indicates that there could be still some systematic errors, like a frequency drift of the unlocked push beam during the scan. Further for simplicity we neglect the unresolved hyperfine splitting of the exited state in this fit.

[1]Here we neglect saturation broadening by the push beam.

The two peaks have a height ratio of about 9 to 1, which is even larger than the peak height ratio of about 2 to 1 in the hot atomic background. This could be explained by the σ-polarized MOT beams forming a closed transition between the $S_{1/2}, F = \frac{3}{2}$ and the $P_{3/2}, F = \frac{5}{2}$ level. We also observe this in our simulation of the 2D MOT (see Ref. [72]). The exact ratio of the peaks depends on the power ratio of the trap and repump frequency in the MOT beams. This motivated us to later change the power ratio from 50/50 to an increased power in the trap frequency to address the larger population in the upper ground state, which then led to an increase in the push beam absorption.

The observed splitting between the two peaks exceeds the expected ground state hyperfine splitting of 228 MHz. This discrepancy is most likely caused by a residual magnetic field if the push beam is not aligned with the magnetic field minimum. The additional shift corresponds to a magnetic field of approximately 1 mT, which in turn implies a positional offset of about 2 mm (see Section 3.2.3).

The fit converges to a standard deviation $\sigma = \Delta f_D = (10.4 \pm 0.2)$ MHz, with the error resulting from the covariance matrix of the fit. This can be attributed to the Doppler broadening Δf_D originating from a velocity distribution of the atoms along the z-axis. This translates to a Doppler velocity $v_D = c \cdot \Delta f_D / f_{D2} = (7.0 \pm 0.2)$ m/s, with the transition frequency f_{D2} and the speed of light c. This is approximately two times larger than the axial velocity distribution from our simulation of the capturable flux (see Figure 3.7).

Table 3.4: Fit parameters and deduced values from 2D MOT absorption measurement shown in Figure 3.18.

Fit parameter	**Value**
amplitude A_1	(9.82 ± 0.14) nW
amplitude A_2	(1.12 ± 0.11) nW
amplitude ratio A_1/A_2	(8.8 ± 0.9)
peak detuning δ_1	$(2.4 \pm 0.2 \pm 30.0)$ MHz
peak detuning δ_2	$(244 \pm 2 \pm 30)$ MHz
peak separation $\delta_2 - \delta_1$	(242 ± 2) MHz
broadening σ	(10.4 ± 0.2) MHz
axial velocity distribution Δv_z	(7.0 ± 0.2) m/s
reduced chi squared χ^2_{red}	1.74

To achieve a signal-to-noise ratio of approximately 30 to 1, we had to average the signal over 20 repetitions. At a scan frequency of 1 Hz, this results in a measurement time of over 20 seconds per data point. For a full 2D MOT profile consisting of roughly 200 spatial positions, this would require an impractically long total measurement of over one hour per profile measurement. Further, the spectrum in Figure 3.18 was recorded at the center of the atomic cloud, where the absorption is strongest. In the outer regions, where the atom density is lower, an even better signal-to-noise ratio is required. To address these limitations, we implement a lock-in detection technique, which is described in the following section.

3.4.2 Profile Measurement Setup

Figure 3.19 shows the setup for absorption profile measurements. The preparation of the MOT beams, as described in Section 2.1.2, is schematically represented in the green box. The MOT beams have a beam waist radius of (17.1 ± 0.3) mm and a power of (83 ± 3) mW for the trap frequency and (17 ± 2) mW for the repump frequency, if not stated otherwise. As motivated above we have adjusted this power ratio to maximize the observed absorption.

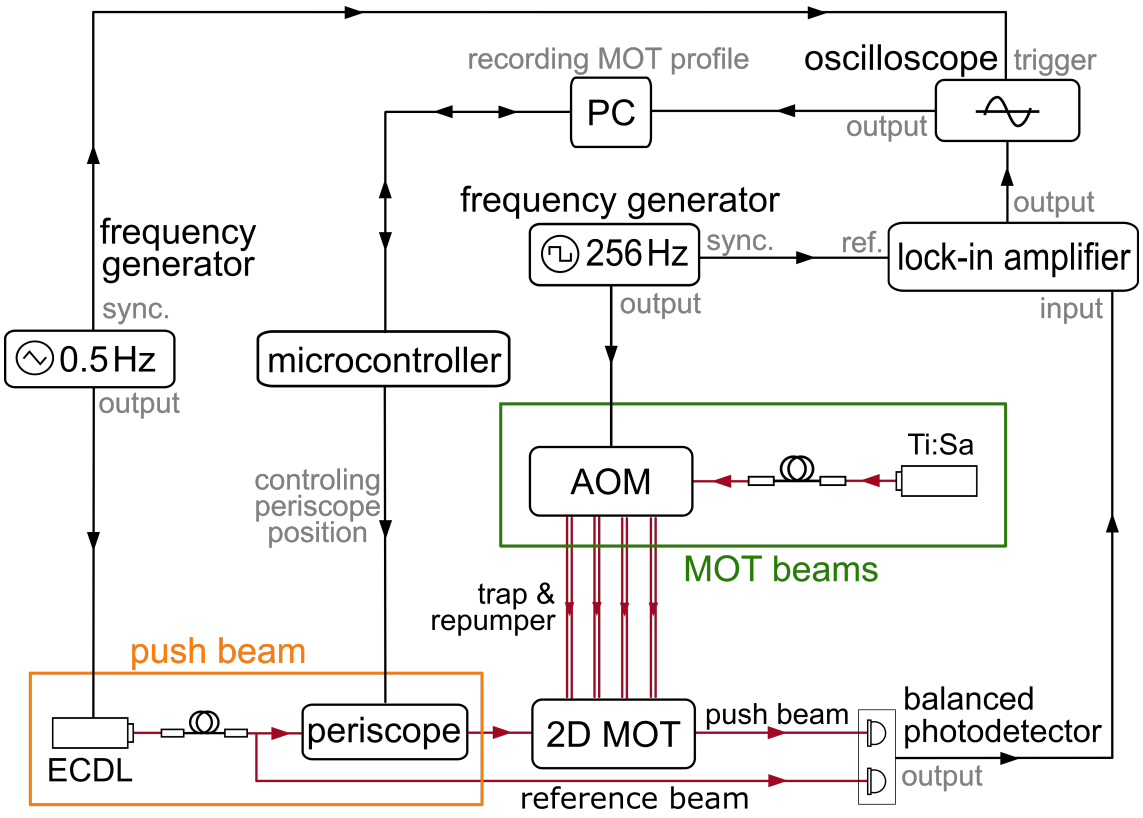

Figure 3.19: Setup used for MOT profile and areal density measurements. The preparation of the MOT beams, as described in Section 2.1.2, is schematically represented in the green box. The setup for the push beam, discussed in Section 2.2.1, is indicated in the orange box. The push beam passes through the 2D MOT region and is subsequently detected by a balanced photodetector. Absorption of the push beam by the trapped atoms is detected using a lock-in amplifier to enhance signal-to-noise ratio. To modulate the MOT absorption, the repump beam of the MOT is chopped at 256 Hz using a square-wave signal applied to the amplitude modulation input of the AOM driver. Simultaneously, the push beam is scanned over the ^{6}Li D_2 line with a 0.5 Hz triangular waveform. The resulting absorption signal is recorded on an oscilloscope and saved to a connected PC, which also controls the position of the push beam via a microcontroller that actuates the motorized periscope, as described in Figure C.10. Figure adapted from Ref. [71].

The setup for the push beam, discussed in Section 2.2.1, is indicated in the orange box. The telescope in the push beam setup (see Figure 2.5) is used to focus the push beam such that it reaches a beam waist radius of $(168 \pm 3)\,\mu m$ at the center of the MOT. The push beam has a power of $(500 \pm 15)\,nW$ corresponding to a maximum push beam intensity of $I_{PB} = (1.13 \pm 0.05)\,mW/cm^2$. According to the phenomenological fit of the loading times as a function of the push beam intensity (see Section 3.3.3) this corresponds to a loading time of less than 1 ms.

The push beam passes through the 2D MOT region and is subsequently detected by a balanced photodetector. Absorption of the push beam by the trapped atoms is measured using a lock-in amplifier[1] to enhance the signal-to-noise ratio.

To modulate the MOT absorption, the repump beam of the MOT is chopped at 256 Hz using a square-wave signal applied to the amplitude modulation input of the AOM driver, so the MOT has about 2 ms to load each cycle. With a loading time below 1 ms, this corresponds to a loading of approximately 90 % of the maximum absorption.

The sync output from the frequency generator[2] is fed into the reference input of the lock-in amplifier. Simultaneously, the push beam is scanned over the ^{6}Li D_2 line with a 0.5 Hz triangular waveform. The resulting absorption signal is recorded on an oscilloscope and saved to a connected PC. The same PC also controls the position of the push beam through a USB connection to a microcontroller[3] that actuates the motorized periscope, as described in Figure C.10. A summary of the key experimental parameters for the following measurements is provided in Table 3.5.

Table 3.5: Experimental parameters for absorption profile measurements.

MOT beams	trap power	$(83 \pm 3)\,mW$
	repump power	$(17 \pm 2)\,mW$
	trap detuning	$(-9 \pm 2)\,\Gamma \pm 30\,MHz$
	repump detuning	$(-7 \pm 2)\,\Gamma \pm 30\,MHz$
	waist radius	$(17.1 \pm 0.3)\,mm$
push beam	power	$(500 \pm 15)\,nW$
	frequency scan range	$\sim 600\,MHz$
	frequency scan frequency	$0.5\,Hz$
	waist radius	$(168 \pm 3)\,\mu m$
lithium oven	set temperature	$400\,°C$
lock-in amplifier	time constant	3 ms
	sensitivity	10 V/1 mV

[1] Stanford Research Systems, SR510 lock-in-amplifier.
[2] Rigol, DG812 – Function/Arbitrary Waveform Generator.
[3] Ardunio, Mega.

3.4.3 Absorption Spectra with a Lock-in Amplifier

Figure 3.20 shows an example for an absorption spectrum measured with the lock-in setup described above. The spectrum was taken with the settings in Table 3.5, but with each MOT beam at a total power of (100 ± 10) mW and an equal power distribution between trap and repump frequency, like in the simple absorption measurement (see Figure 3.18). The push beam was scanned with 0.5 Hz and no averaging. The lock-in amplifier is set to a time constant of 3 ms and a sensitivity of 10 V/1 mV.

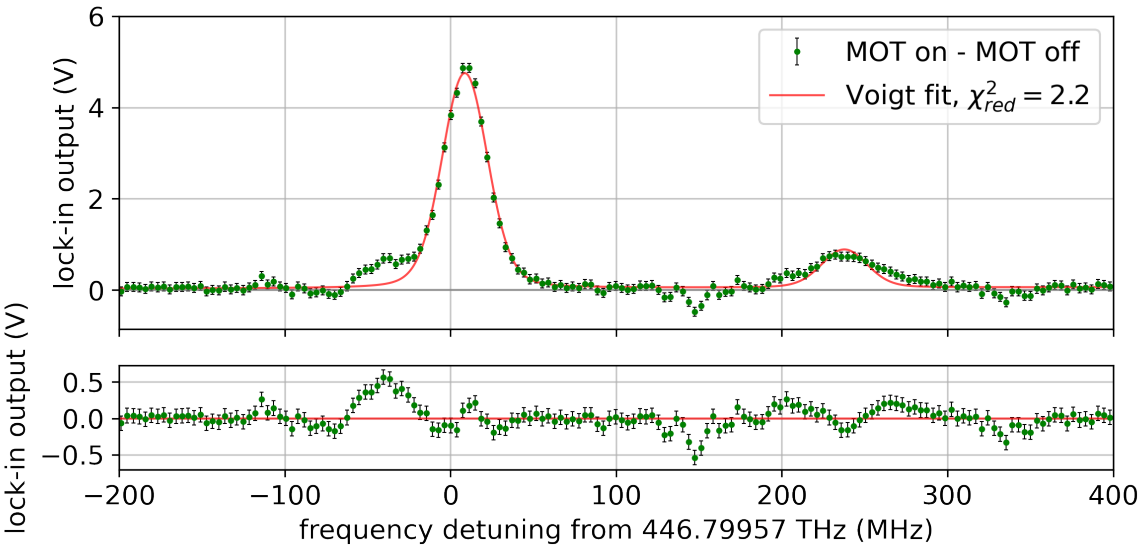

Figure 3.20: Example for a MOT absorption spectrum with lock-in amplification. Using the setup shown in Figure 3.19, we scan the push beam frequency with 0.5 Hz and measure the absorbed power on the balanced photodetector in a single shot measurement. The MOT repump beam is modulated with 256 Hz and synced with a lock-in amplifier to obtain an absorption spectrum. Each MOT beam has a total power of (100 ± 10) mW with an equal distribution between trap and repump frequency. Apart from that the experimental settings are as described in Table 3.5. The error bars represent the standard deviation of the baseline data points. The spectrum is fitted with a sum of two Voigt profiles (see Section B.3) with a fixed natural linewidth $\Gamma/2\pi = 5.9$ MHz. Table 3.6 shows the resulting fit parameters.

The spectrum resulting from the lock-in measurement also shows a much higher absorption coming from the upper ground state ($F = 3/2$) D_2 transition than from the lower ground state ($F = 1/2$) D_2 transition, although the peak from the lower ground state is more visible than in the difference signal (Figure 3.18). The spectrum is fitted with a sum of two Voigt profiles (see Section B.3) with a fixed natural linewidth $\Gamma/2\pi = 5.9$ MHz. Table 3.6 shows the resulting fit parameters.

By comparing the measurements from the calibrated photodetector with the ones from the lock-in amplifier we can deduce a linear conversion from lock-in amplitude to absorbed laser power of (2.1 ± 0.2) nW/V. The error is estimated from the fluc-

tuations of several single shot spectra. More detail on the calibration can be found in Ref. [71].

We observe that both the position and shape of the absorption features vary with the push beam location (see Figure D.13). This can be attributed to a changing magnetic field strength and accordingly the changing Zeeman shift. In the following measurements we extract the integral of the absorption signal at each position to construct the spatial profile of the MOT. From this integrated absorbed power, we can deduce an areal atomic density.

Table 3.6: Fit parameters and deduced values from lock-in absorption measurement shown in Figure 3.20.

Fit parameter	**Value**
amplitude A_1	(4.7 ± 0.1)
amplitude A_2	(0.8 ± 0.1)
amplitude ratio A_1/A_2	(5.9 ± 0.3)
peak detuning δ_1	$(8.70 \pm 0.16 \pm 30.00)\,\mathrm{MHz}$
peak detuning δ_2	$(237.7 \pm 0.9 \pm 30.0)\,\mathrm{MHz}$
peak separation $\delta_2 - \delta_1$	$(229.0 \pm 0.9)\,\mathrm{MHz}$
broadening σ	$(12.4 \pm 0.2)\,\mathrm{MHz}$
reduced chi squared χ^2_{red}	2.21

Areal Density Calculation

The absorption of monochromatic radiation in a material with constant atomic density N can be described by Beer's law [67]. The reduction of the light intensity I in dependence of the laser frequency ω and the absorption length z can be described by:

$$I(\omega, z) = I(\omega, 0) \exp\left\{-\sigma(\omega) N z\right\}, \tag{3.12}$$

with the frequency-dependent cross section $\sigma(\omega)$. Since we can only measure the whole atomic cloud with a length of $z = d$ we use the areal density $n = N \cdot d$ in the following. When scanning the laser beam, the incident intensity $I(\omega, 0) = I_0$ can be assumed to be constant.

The cross section can be described by [67]:

$$\sigma(\omega) = \frac{g_2}{g_1} \frac{\pi^2 c^2}{\omega_0^2} A_{21}\, g(\omega), \tag{3.13}$$

with the degeneracy factors g_1 of the ground state and g_2 of the exited stated and the Einstein coefficient A_{21}. For a two-level system one can assume $A_{21} = \Gamma$, with the natural linewidth $\Gamma = 2\pi \cdot 5.9\,\mathrm{MHz}$.

For the D_2 transition we have a degeneracy ratio $g_2/g_1 = 3$ for the upper and the lower ground state transition.[1]

In the ideal case the line shape $g(\omega)$ is described by a normalized Lorentzian function. In our absorption measurements the line shape can change due to several broadening mechanisms, like the Doppler broadening described in Section 3.4.1. Since the number of atoms is conserved in a steady state of the MOT, we assume that the integral over the line shape is still normalized:

$$\int_{-\infty}^{\infty} g(\omega) d\omega = 1. \tag{3.14}$$

To make our measurement insensitive to broadening mechanisms we divide the measured absorption intensity by the incident intensity[2] and then numerically integrate over all frequencies ω. This way we derive the areal density given by:

$$n = -\frac{g_1}{g_2} \frac{\omega_0^2}{\pi^2 c^2} \frac{1}{\Gamma} \int_{-\infty}^{\infty} \ln\left(\frac{I(\omega)}{I_0}\right) d\omega. \tag{3.15}$$

Applying this to the measurements displayed in Figure 3.18 we obtain an estimated areal density $n = (4.1 \pm 0.1) \times 10^6\,\mathrm{atoms/cm^2}$.

Several factors could further influence the accuracy of this estimate:

- The assumption underlying Equation 3.12 is only valid for low intensity beams. With a maximum intensity of $(1.13 \pm 0.05)\,\mathrm{mW/cm^2}$ the push beam is at about 50 % of the saturation intensity of the D_2 transition. This leads to an underestimation of the areal density, since the atoms are partially saturated and absorb less than expected. For this purpose, we will later extrapolate the areal density to zero push beam intensity (see Figure 3.27).

- Further, the push beam accelerates atoms out of the 2D MOT and therefore reduces the atomic density. This effect also depends on the push beam power.

- Although the push beam diameter cancels in Equation 3.15, the power distribution follows a 2D Gaussian distribution. Due to the non-linearity of the saturation effects this leads to an overall underestimation of the areal density in comparison to the assumed equal power distribution.

- The D_2 transition is not a two-level system. Although we are scanning over both hyperfine ground states optical pumping leads to an underestimated areal density.

The magnetic field present in the 2D MOT induces a Zeeman splitting of the atomic transitions, resulting in a broadening of the absorption spectrum. However, since we extract the areal density by integrating over the entire frequency scan, line broadening does not affect the result.

[1] For the lower ($F = 1/2$) ground the degeneracy ratio in the m_F-states is $g_2/g_1 = 6/2 = 3$ and for the upper ($F = 3/2$) ground the degeneracy ratio in the m_F-states is $g_2/g_1 = 12/4 = 3$.

[2] This way the area of the probe beam cancels out.

3.4.4 Profile Measurement and Analysis

The atomic density in the 2D MOT is not isotropic. To account for this, we measure the absorption at different push beam positions. Using the setup described above, we measure the absorption spectrum of the push beam at different positions with a spacing of 200 µm. With the analysis described above, we obtain an areal density at each position. An example of such a measurement of the MOT profile is depicted in Figure 3.21.

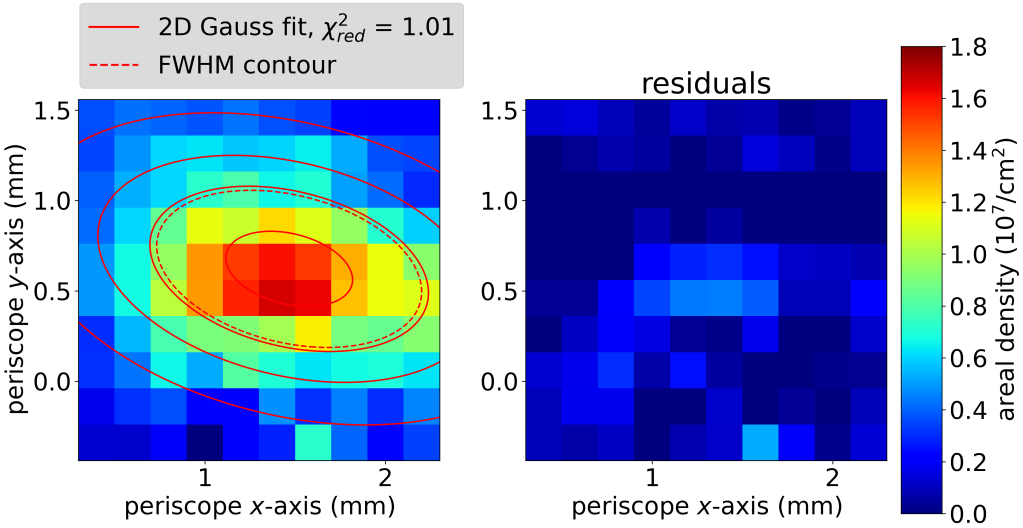

Figure 3.21: Exemplary MOT profile and fit residuals. The MOT profile shown on the left was measured with a push beam power of (500 ± 15) nW and a beam waist of (168 ± 3) µm. The trap and repump beam powers were set to (83 ± 3) mW and (17 ± 2) mW, respectively, with a MOT beam radius of (11.5 ± 0.3) mm at the trap center. The corresponding detunings were $(-10.1)\,\Gamma \pm 1$ MHz for the trap and $(-7.7)\,\Gamma \pm 1$ MHz for the repump frequency. The oven temperature was set to 400 °C. The MOT profile was fitted using Equation 3.16, and the corresponding fit residuals are shown on the right.

We apply a two-dimensional Gaussian fit to get an estimate of the width σ of the two principal axes and their rotation angle Θ with respect to the scan axis:

$$G(x,y) = n_0 \cdot \exp\left(-\left[a \cdot (x-x_0)^2 + 2b \cdot (x-x_0)(y-y_0) + c \cdot (y-y_0)^2\right]\right),$$
$$a = \frac{\cos^2(\Theta)}{2\sigma_x^2} + \frac{\sin^2(\Theta)}{2\sigma_y^2}, b = -\frac{\sin(2\Theta)}{4\sigma_x^2} + \frac{\sin(2\Theta)}{4\sigma_y^2}, c = \frac{\sin^2(\Theta)}{2\sigma_x^2} + \frac{\cos^2(\Theta)}{2\sigma_y^2}, \quad (3.16)$$

where x_0 and y_0 denote the MOT center position with respect to the geometric center of the setup and n_0 is the peak areal density.

The corresponding fit parameters are shown in Table 3.7. We rescaled the errors of the areal densities to obtain a reduced chi-squared value of one. When examining the fit residuals, we observe that the peak intensity tends to be underestimated, with residuals at the level of 10%.

Table 3.7: Fit parameters corresponding to the analyzed MOT profile in Figure 3.21.

Fit parameter	Value
n_0	$(1.3 \pm 0.1) \times 10^7\,\mathrm{atoms/cm^2}$
x_0	$(1.5 \pm 0.1(\mathrm{stat}) \pm 1(\mathrm{sys}))\,\mathrm{mm}$
y_0	$(0.6 \pm 0.1(\mathrm{stat}) \pm 1(\mathrm{sys}))\,\mathrm{mm}$
σ_x	$(0.87 \pm 0.09)\,\mathrm{mm}$
σ_y	$(0.47 \pm 0.02)\,\mathrm{mm}$
Θ	$(14 \pm 3)^\circ$
N_{atoms}	$(2.7 \pm 0.1) \times 10^5$
χ^2_{red}	1.01

From the fit we derive a FWHM of approximately 2 mm along the major principal axis and 1 mm along the minor principal axis, leading to an ellipticity $\epsilon = \sigma_x/\sigma_y \approx 2$ with a rotation of the major axis with respect to the x-axis of approximately $(14 \pm 3)^\circ$. Preliminary analysis suggests that these effects are caused by the interchanged polarization of the two lower MOT beams (see Appendix A).

We further observe a horizontal (x-axis) offset of the cold atomic cloud with respect to the geometric center of the vacuum cross[1]. This displacement is consistent, within the experimental uncertainties, with the shift measured for the magnetic field minimum (see Section 3.2.3).

By numerically integrating over the profile, we can estimate the total number of trapped atoms to be approximately $(2.7 \pm 0.1) \times 10^5$ for the shown profile. In the following we will analyze the fits of the profile measurements with respect to different MOT parameters.

3.4.5 Dependence on Oven Temperature

Using the setup described in Section 3.4.2 we measured different absorption profiles in dependence of the lithium oven temperature. The trap and repump beam are detuned by $-10.1\,\Gamma \pm 1\,\mathrm{MHz}$ and $-7.7\,\Gamma \pm 1\,\mathrm{MHz}$, respectively. We beat a part of the titanium-sapphire laser (Ti:Sa) with our frequency comb[2] to monitor the absolute frequency. The systematic error of 1 MHz corresponds to the drift of the Ti:Sa when locked to its external cavity during a profile measurement. The power of the trap and repump frequency in each MOT beam are set to $(83 \pm 3)\,\mathrm{mW}$ and $(17 \pm 2)\,\mathrm{mW}$, respectively. The MOT beams have a $1/e^2$ radius of $(11.5 \pm 0.1)\,\mathrm{mm}$ in the trap center.

Figure 3.22 shows the measured peak areal density and total number of atoms in dependence of the oven temperature. For each data point, a MOT density profile was recorded and fitted using Equation 3.16. Representative MOT profiles at oven set temperatures of 360 °C, 400 °C, and 440 °C are shown.

[1]The absolute position is estimated to have a systematic uncertainty of 1 mm, arising from the positional calibration of the motorized periscope.

[2]Menlo Systems, FC1500-Quantum frequency comb with a beat detection unit for 671 nm.

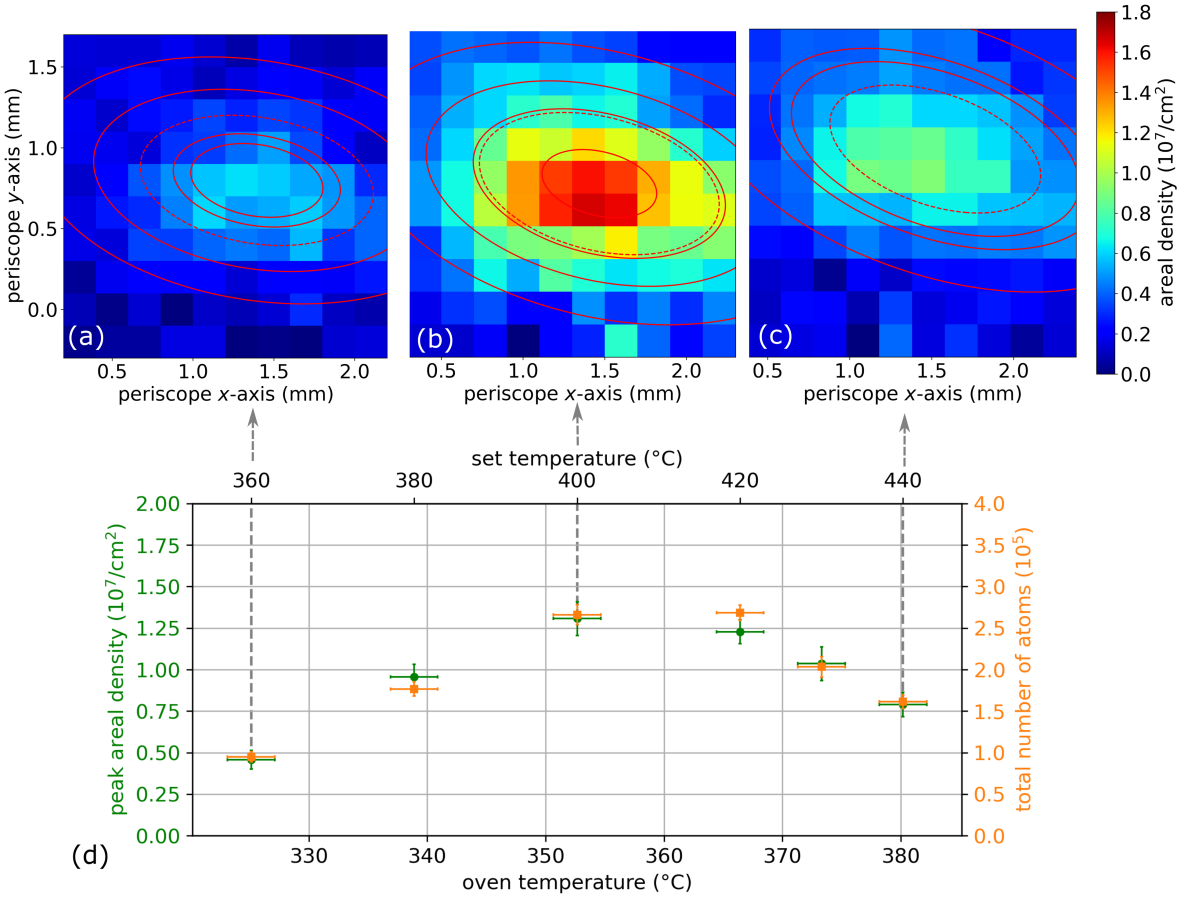

Figure 3.22: Influence of lithium oven temperature on the MOT areal density profile and total number of atoms. Exemplary MOT profiles are shown for oven set temperatures of 360 °C (a), 400 °C (b), and 440 °C (c). Contour lines represent the 2D Gaussian fit according to Equation 3.16, with the red dotted line indicating the full width at half maximum. The peak areal density (d) reaches a maximum at approximately 400 °C.

The uncertainty on the oven temperature is estimated to be around 2 °C due to the sensor accuracy and the response time of the temperature controller. The uncertainty for the peak areal density and the total number of atoms correspond to the uncertainty resulting from the fit.

The peak areal density and the total number of atoms rise with increasing temperature until a set temperature of approximately 400 °C. This can be explained by an increase of the total atomic flux increasing with the temperature (see Figure 3.3). We observe a maximum of the peak areal density at about 400 °C, which is over two times larger than the peak absorption for 360 °C. It is important to note that the actual temperature of the lithium vapor is approximately 40 °C lower (calibrated from the hot atomic in Section 3.1.5). For set temperatures above 400 °C the MOT density is decreasing. This could be explained by "knock-out" collisions from the hot atomic background [2].

Figure 3.23 shows the full width at half maximum (FWHM) of the MOT along the x- and y-axes as a function of the oven temperature. In principle, one could

expect an increase in the size of the atomic cloud proportional to the number of atoms [86]. However, in this measurement such an effect is not visible within the experimental error bars.

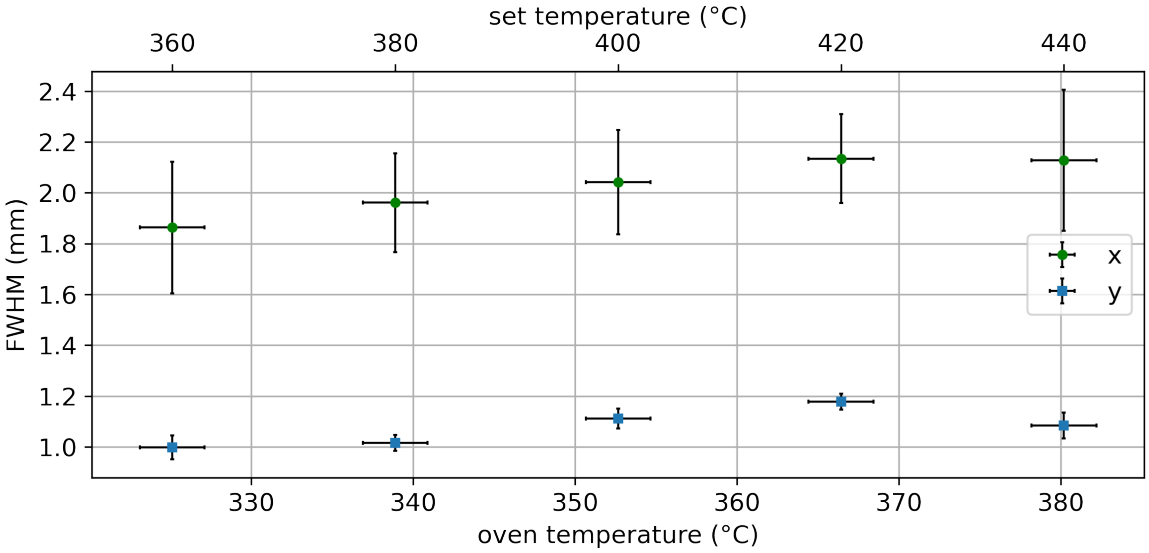

Figure 3.23: MOT shape in dependence of oven temperature. The full width at half maximum (FWHM) along the x- and y-axes stay constant within the experimental uncertainties.

Furthermore, the ellipticity and orientation of the MOT profile, as well as the position of the MOT center, remain essentially unchanged over the investigated temperature range (see Figure D.14 and Figure D.15).

Our optimal set temperature of 400 °C corresponds to an actual temperature of approximately 355 °C (see Section 3.1.5). This is comparable to the operating temperature of 350 °C reported by Tiecke *et al.* [2], but lower than measurements presented in Ref. [66], Figure 20. For the following measurements we will set the oven temperature to our optimal value of 400 °C.

3.4.6 Dependence on MOT Beam Detuning

In the following we investigate the influence of the detuning of the trap and repump frequency in the MOT beams on the MOT absorption profile. In this measurement we tune the trap and repump beam frequency simultaneously by scanning the titanium-sapphire laser (Ti:Sa) frequency. Before measuring, we optimized the trap and repump detuning independently for maximum absorption by using the double pass AOM in the MOT beam preparation setup (see Section 2.1.2). We then set the RF frequency of the AOM to 122 MHz.

Figure 3.24 shows the peak areal density and total number of atoms in dependence of the MOT beam detunings. For each data point, a MOT density profile was recorded and numerically integrated. Exemplary MOT profiles are shown a detuning of $-11.2\,\Gamma$, $-8.7\,\Gamma$ (a) and $-8.3\,\Gamma$, $-5.8\,\Gamma$ (b) for the trap and repump frequency, respectively. The other experimental parameters are as described in Table 3.8.

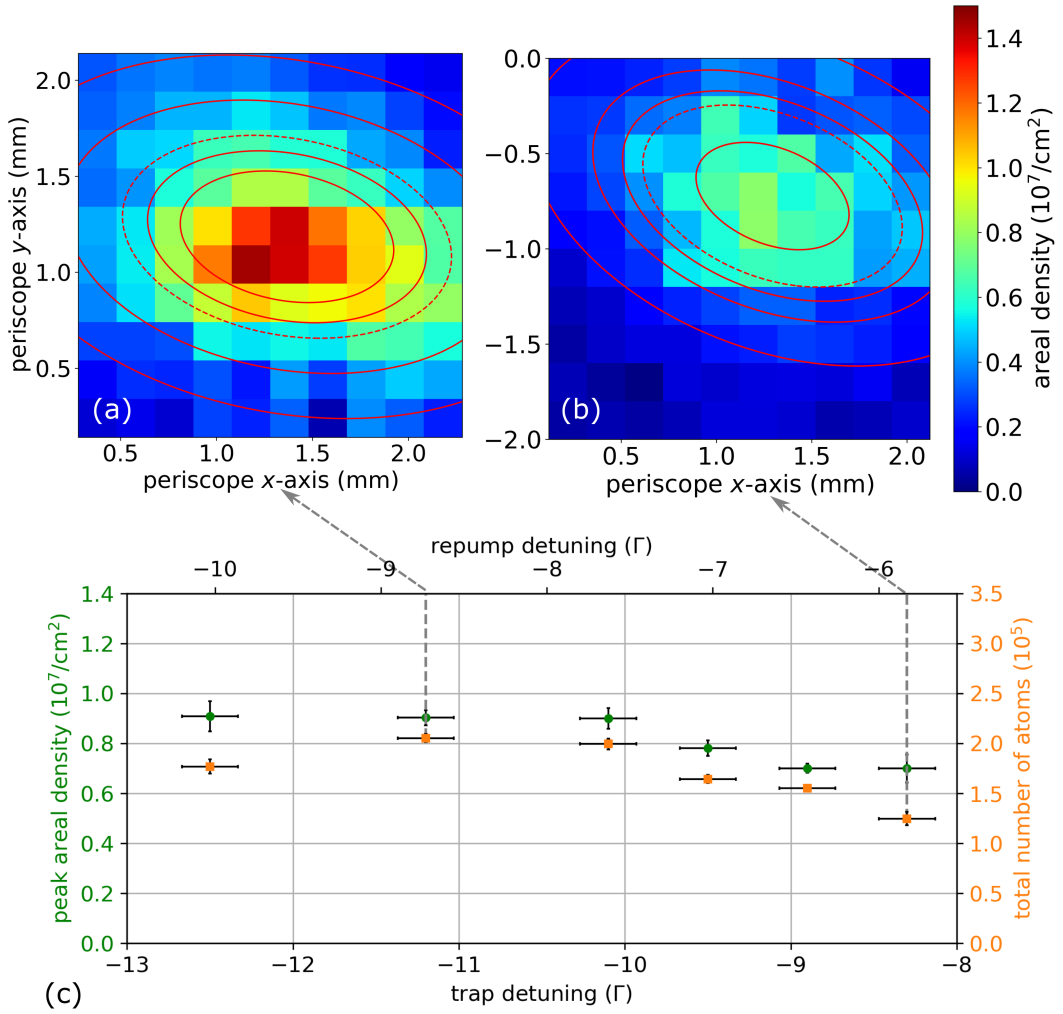

Figure 3.24: Influence of MOT beam detunings on the peak areal density and total number of atoms. Exemplary MOT profiles are shown a detuning of $-11.2\,\Gamma$, $-8.7\,\Gamma$ (a) and $-8.3\,\Gamma$, $-5.8\,\Gamma$ (b) for the trap and repump beam, respectively. Contour lines represent the 2D Gaussian fit according to Equation 3.16, with the red dotted line indicating the full width at half maximum. A maximum in the number of atoms in the MOT (c) is observed at approximately $-11.2\,\Gamma$, $-8.7\,\Gamma$ for the trap and repump beam detuning, respectively.

Measurements taken at identical MOT detuning settings were combined using a weighted average. Between successive measurements, the MOT detuning was varied randomly to be less sensitive to slow temporal drifts. As described above, we lock the Ti:Sa laser to its external cavity and measure a beat with our frequency comb to calculate the absolute frequency. The systematic detuning error of 1 MHz corresponds to the frequency drift during profile measurement. We observe a maximum in the number of atoms at approximately $-11.2\,\Gamma$ and $-8.7\,\Gamma$ for the trap and repump beam detuning, respectively. When comparing this maximum of $\sim 2 \times 10^5$ atoms with the one for detunings of $-8.3\,\Gamma$ and $-5.8\,\Gamma$ for the trap and repump beam, the total number of atoms is reduced by approximately one third.

Figure 3.25 shows the position of the MOT center in dependence of MOT beam detunings. We observe a correlation between the detuning and the position along the y-axis, while the x-position remains almost unchanged. Over a detuning range of approximately 4.2 Γ applied to both the trap and repump beams, a net displacement of about 2.7 mm is observed in the y-direction. This corresponds to a relative shift of over two times the width of the atomic cloud along the y-axis. The resulting sensitivity of the MOT position to laser detuning corresponds to an adjustment of approximately 0.1 mm/MHz in the y-direction.

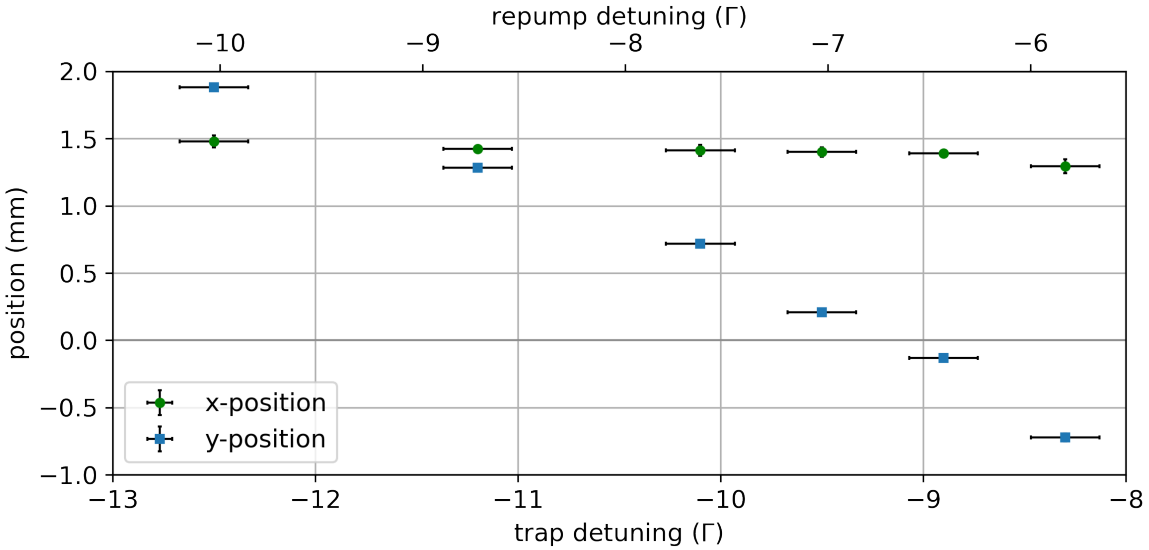

Figure 3.25: MOT position in dependence of MOT beam detunings. A strong correlation between detuning and the MOT position is observed along the y-axis, while the x-position remains largely unchanged. The absolute position is estimated to have a systematic uncertainty of 1 mm, arising from the positional calibration of the motorized periscope.

The observed constant shift along the x-axis could be attributed to the previously observed shift of the magnetic field minimum with respect to the center of the vacuum cross (see Section 3.2.3). First simulations suggests that dependence of the y-position on the MOT beam detunings can be caused by the interchanged polarization of the two lower MOT beams (see Appendix A).

In contrast, ellipticity and orientation of the MOT profile, as well as the FWHM, remain essentially unchanged over the investigated detuning range (see Figure D.16 and Figure D.17).

This position dependence could also explain the deviation of our optimal detuning values from those reported in Ref. [2]. In their setup, the presence of a differential pumping channel with a diameter of only 2 mm behind the MOT restricted the ability to adjust the push beam position. This could also explain why the optimal detunings reported in Ref. [66] deviate as well.

3.4.7 Dependence on MOT Beam Power

In the following, the dependence of the MOT areal density on the total power of the MOT beams is investigated. The power ratio between the trap and repump frequencies in each MOT beam is maintained at approximately 3.5:1 throughout all measurements. The trap and repump beam detunings are fixed at $(-9.3 \pm 0.4)\,\Gamma$ and $(-7.7 \pm 0.4)\,\Gamma$, respectively. The other experimental are as described in Table 3.8.

Figure 3.26 shows the center areal density of the MOT plotted as a function of the total power per MOT beam. The push beam is always aligned to be in the center of the MOT.

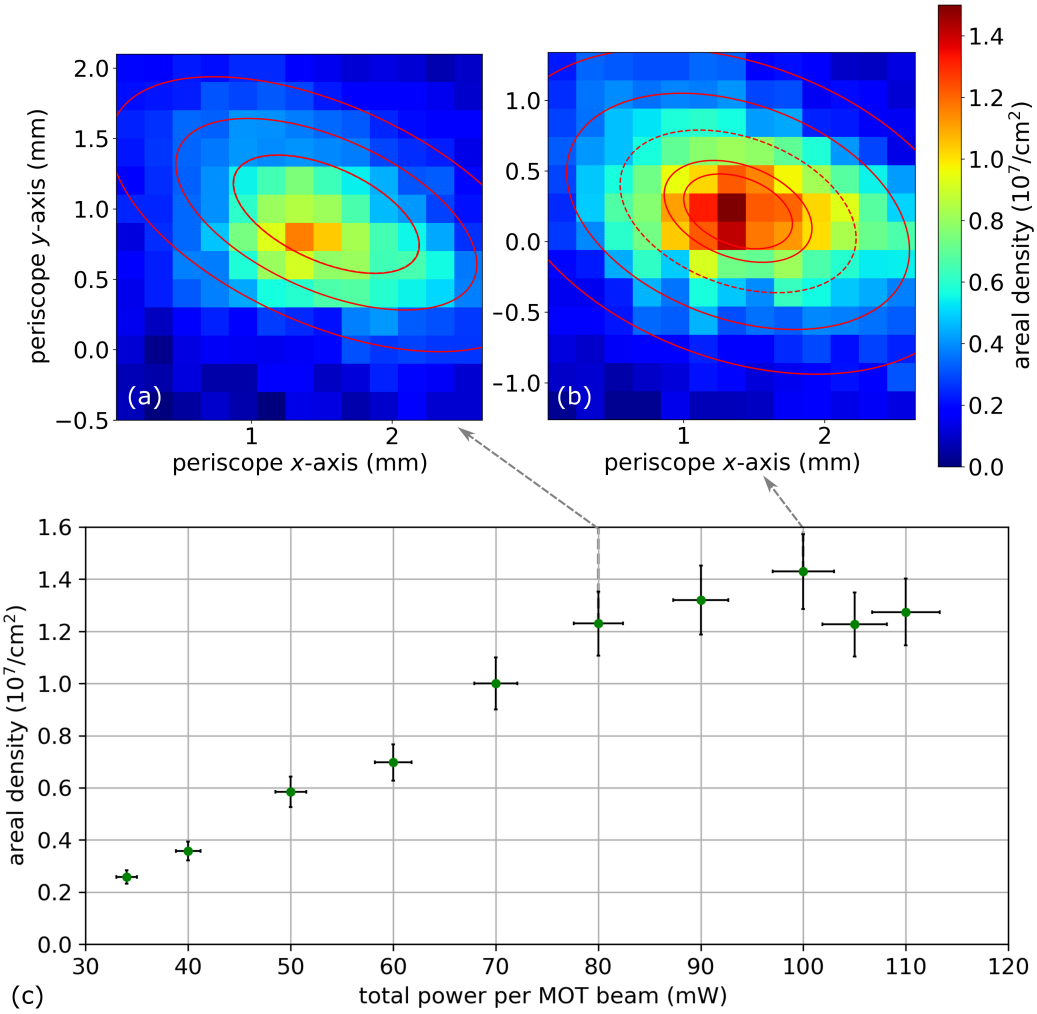

Figure 3.26: MOT areal density as a function of the total MOT beam power, with a fixed trap-to-repump power ratio of approximately 3.5:1. Multiple measurements were taken at each power setting. Error bars indicate the standard deviation of measurement fluctuations. The areal density increases with the MOT beam power up to approximately 80 mW and saturates at around $1.4 \times 10^7/\mathrm{cm}^2$. Example profile measurements are shown above for (a) 80 mW and (b) 100 mW total power.

Multiple measurements were taken at each power setting. The error bars correspond to the standard deviation of the measurement fluctuations. The uncertainty in the beam power is determined by the measurement accuracy of the power meter[1]. The MOT beam power was varied randomly between measurements to avoid correlations between slow time-dependent drifts in the experimental parameters and the measured areal density.

The peak areal density increases linearly with the MOT beam power up to approximately 80 mW. In principle, higher MOT beam powers result in enhanced photon scattering, which leads to greater deceleration of atoms from the oven as they cross the MOT region. As a result, an increasing number of atoms is captured, and the areal density rises. Above 80 mW, the density reaches a plateau, and the areal density saturates at approximately 1.4×10^7 atoms/cm^2. In this regime, density-dependent losses, such as radiation pressure [86], begin to dominate, counteracting further gains from increased scattering forces. Although the density does not increase beyond this point, the total number of atoms continues to increase along with the spatial extent of the atomic cloud [66].

Our simulations of the 2D MOT show a similar increase in the capture efficiency with the total MOT beam power (see Ref. [72], Figure 4.17). However, the saturation appears to begin at much higher intensities in the simulation. This discrepancy can be explained by the neglect of density-dependent losses in the current state of the simulation.

Furthermore, we observe that the position of the atomic cloud shifts downward along the y-axis with increasing MOT beam power. This is visible in the examples shown in Figure 3.26. For a total power of 80 mW (a), the center of the cloud is approximately 0.5 mm lower than for a total power of 100 mW (b).

The MOT setup with four independent trap beams (see Section 2.1) allows for individual adjustment of the MOT beam powers. Increasing the power of the upper MOT beams results in a downward shift of the MOT center position (see Figure D.18). This is similar to the behavior we observe for the variation of the total power. A higher power in the upper MOT beams also leads to a better slowing of the hot atoms coming from below, and therefore a higher atomic density. In the following measurements we use a 5 % to 10 % higher power for the upper MOT beams. Further we operated the MOT beam powers in the plateau region in order to minimize sensitivity to power fluctuations. Beyond that, we implemented an active power stabilization system based on a motorized half-wave plate (see Ref. [75]).

3.4.8 Dependence on MOT Beam Waist

As discussed in Section 3.1.4, the trappable flux depends on the MOT beam waist w through the solid angle defined by the overlap between the hot atomic beam and the MOT volume. In addition, the maximum capture velocity $v_{\max}$ is determined by the available slowing distance, which itself scales with the MOT beam radius. Following a simple one-dimensional model analogous to [2], the maximum capture velocity can be estimated as $v_{\max} = \sqrt{a_{\max} \cdot r_{\max}}$, where $a_{\max} = (\hbar k \Gamma)/(2 \cdot m_{\mathrm{Li6}})$ is the maximum deceleration provided by the resonant scattering force, and $r_{\max} = \sqrt{2}\, w$ denotes the maximum available slowing length in the vertical direction.

[1] Thorlabs S130C, Slim Photodiode Power Sensor, Si, 400 to 1100 nm, 500 pW to 5 mW.

It should be noted that for a fixed available laser power the beam waist also influences the beam intensity and thus the effective scattering force. This introduces a trade-off: increasing the beam waist improves the capture solid angle and slowing distance but simultaneously decreases the intensity and hence the achievable deceleration.

As observed in the previous measurements the areal density exhibits a saturation behavior at high beam intensities (see Figure 3.26). We therefore expect an optimal MOT beam waist, just below the saturation threshold, that balances capture velocity and scattering force.

Experimentally, we tested MOT beam waists of approximately 9 mm, 12 mm, and 17 mm in our setup. From these values, the best choice was found to be 12 mm.

This value is larger than the MOT beam waist of 9 mm reported by Tiecke *et al.* [2], where a total MOT beam power of approximately 100 mW was available, corresponding to an intensity of $I \sim 30\,\mathrm{mW/cm^2}$. It is, however, smaller than the beam waist of approximately 16 mm employed in Ref. [66], where a higher total beam power of about 200 mW ($I \sim 20\,\mathrm{mW/cm^2}$) was available.

In our experiment, the maximum total power per MOT beam was limited to about 130 mW, corresponding to an intensity of $I \sim 25\,\mathrm{mW/cm^2}$. This comparison indicates that the optimal MOT beam waist is primarily constrained by the available laser power, and that our experimentally determined value results in an intensity that lies between two previously reported values.

3.4.9 Discussion on the Profile Measurements

The absorption of the push beam, and therefore the extracted areal density, depends on the push beam power itself. Figure 3.27 shows the measured areal density as a function of the push beam power. The measurements were binned, and the associated uncertainties were estimated from the standard deviation within each bin.

We observe that the measured areal density increases as the push beam power decreases. This can be explained by the push beam exerting a radiation pressure force on the trapped atoms, accelerating them out of the MOT region and thereby reducing the equilibrium atom number. Consequently, measurements performed at higher push beam powers may underestimate the true areal density. To correct for this systematic effect, the data is fitted with a phenomenological model and extrapolated to zero push beam intensity.

The areal density $n_a(P)$ as a function of push beam power P is modeled as

$$n_a(P) = a\,\exp(-bP) + c\,P + d, \tag{3.17}$$

where a, b, c, and d are fit parameters accounting for the exponential saturation behavior at low power and a weak linear contribution at higher power.

A noticeable increase in scatter is observed as the push beam power approaches zero. This behavior can be explained by the exponential dependence of the absorption on the push beam intensity: close to zero power, the slope of the curve becomes steeper, such that small fluctuations in the push beam power lead to comparatively large variations in the measured absorption and, consequently, in the inferred areal density. At the time of these measurements, no active power stabilization of the push beam was available.

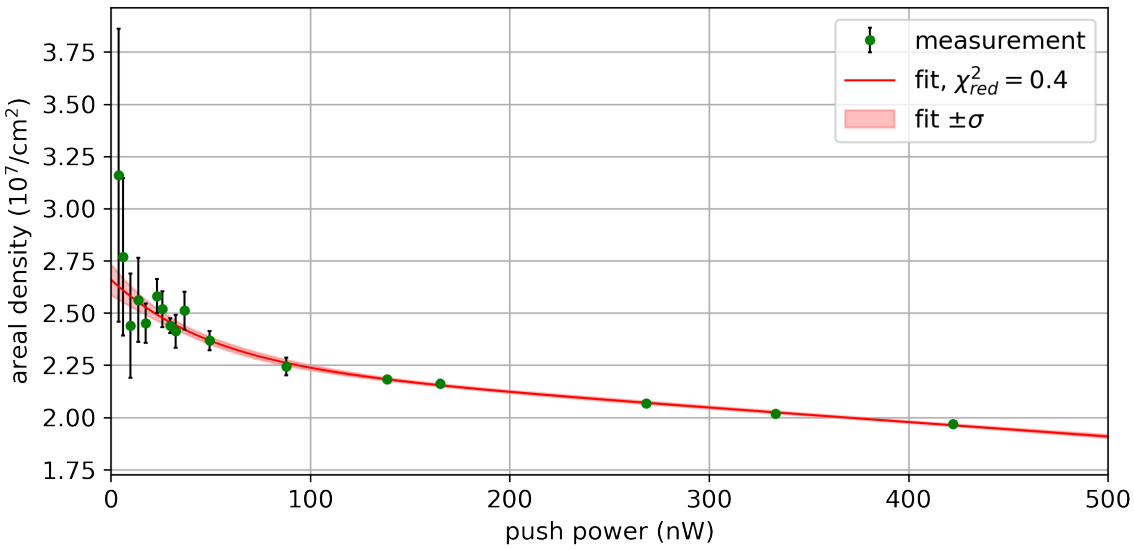

Figure 3.27: Areal density as a function of push beam power. The measured areal density increases as the push beam power is reduced, indicating that the push beam perturbs the MOT equilibrium. The data points are fitted with a phenomenological function (Equation 3.17). The resulting fit parameters are summarized in Table D.5. The red shaded band indicates the σ uncertainty of the fit.

The resulting fit parameters are summarized in Table D.5. From the extrapolation to zero push beam power, the areal density is obtained as

$$n_a(P = 0) = a + d = (2.66 \pm 0.07) \times 10^7\,\mathrm{cm}^{-2}, \tag{3.18}$$

where the quoted uncertainty corresponds to the σ uncertainty of the fit. The reduced chi squared of 0.4 indicates that uncertainties of the individual measurements might be overestimated. This value for the areal density is approximately 40% larger than the value we would evaluate at our usual measurement power of 500 nW.

This systematic effect indicates that the reported areal densities and atom numbers should be considered lower bounds on the true values. Future measurements could improve accuracy by using lower push beam powers with active power stabilization.

Furthermore, when estimating the total number of atoms in the MOT via numerical integration of the measured profiles, the total number is slightly underestimated since the profile measurement captures only the inner part of the atomic cloud. We estimate the systematic underestimation from this to be on the order of 10–20%. From the measurements presented above, we determine a total number of trapped atoms on the order of 10^5, with typical values ranging from 2×10^5 to 4×10^5 depending on the operational parameters.

3.5 Discussion on the Two-Dimensional Magneto-Optical Trap

Through systematic variation of the experimental parameters, we identified an optimal operating point for our 2D MOT setup. The optimized parameters are summarized in Table 3.8.

Table 3.8: Experimentally optimized parameters for the 2D MOT.

MOT beams	trap power	$(83 \pm 3)\,\mathrm{mW}$
	repump power	$(17 \pm 2)\,\mathrm{mW}$
	trap detuning	$(-11.2)\,\Gamma$
	repump detuning	$(-9.5)\,\Gamma$
	waist radius	$(11.5 \pm 0.1)\,\mathrm{mm}$
lithium oven	set temperature	$400\,^{\circ}\mathrm{C}$
	actual temperature	$\sim 355\,^{\circ}\mathrm{C}$

It should be noted that the optimal parameters for a 2D MOT setup depend on the specific oven geometry, magnetic field configuration, beam alignment, and polarization. Furthermore, the optimal settings may drift slowly over time due to changes in the lithium filling level in the oven [87].

With these parameters we were able to achieve an atom number typical ranging from 2×10^5 to 4×10^5 depending on the operational parameters. However, several improvements of the MOT setup can in principle increase the number of trapped atoms and subsequently the flux of cold atoms toward the spectroscopy area:

The suggestions for improved oven design and magnetic field configuration discussed in Section 3.1.6 and Section 3.2.5 could be implemented to increase the total atomic flux and improve the trapping efficiency.

Several modifications to the laser system could enhance the MOT performance: Focusing the MOT beams would provide an additional restoring force along the z-axis, potentially improving confinement and therefore increasing the total number of atoms in equilibrium.

The overall MOT beam power could be increased using either a retroreflected configuration [2] or a bow-tie geometry [66]. However, this approach sacrifices the ability to independently control the power ratios between different beam paths. Additionally, the MOT beam would repeatedly traverse atoms in the center of the MOT, reducing the intensity of the MOT beams and potentially leading to asymmetric cooling of the atoms.

Tiecke *et al.* suggested tilting the MOT beams toward the push beam direction to preferentially enhance the flux along the experiment axis [2]. The optimal tilt angle would need to be determined through simulation and experimental optimization.

Adding sidebands to the trap laser can increase the velocity capture range and improve trapping efficiency. Fischer *et al.* demonstrated a factor of four improvement in atom number using this technique [84].

Furthermore, the capturable flux could be substantially increased by implementing a Zeeman slower, as demonstrated by Lamporesi *et al.* for sodium [88]. They achieved

an order of magnitude increase in loading rate by utilizing a quadrupole magnetic field configuration. However, implementing a Zeeman slower would require careful design of the optical system to prevent degradative coating of optical elements by the hot lithium beam. This could be addressed by the use protective windows with active heating.

4 Cold Lithium Beam

A precise knowledge of the velocity distribution of the cold atomic beam extracted from the two-dimensional magneto-optical trap (2D MOT) is essential for high-precision spectroscopy. The axial and transverse velocities constitute one of the dominant systematic effects in precision measurements and understanding how they depend on the experimental parameters is important for their control and reduction.

In this chapter, we characterize these velocity components using two complementary fluorescence-based techniques. First, we employ a time-of-flight (TOF) method using a spectroscopy beam perpendicular to the lithium beam (Section 4.2.2). Second, by aligning the laser under an angle other than 90° to the atomic beam direction, we extract the axial velocity from the Doppler shift of the fluorescence spectra (Section 4.2.3).

We begin by describing the general measurement setup and the acquisition of time-resolved frequency spectra (Section 4.1). A unified analysis framework for extracting velocity information from both methods is then presented (Section 4.2). Subsequently, we investigate how the push beam parameters influence the axial velocity and the resulting velocity distribution (Section 4.3). Finally, we discuss the results and compare them to similar setups (Section 4.4).

4.1 Measurement Setup

Figure 4.1 shows the fluorescence spectroscopy setup used for the characterization of the cold lithium beam. Cold atoms emerging from the two-dimensional magneto-optical trap (2D MOT) are accelerated by the push beam and form an atomic beam. This beam passes through two collimating apertures with diameters of $(5 \pm 1)\,\mathrm{mm}$ each and intersects the spectroscopy laser beam at an angle $\alpha \approx 90°$ or $\alpha \approx 80°$ after a distance of approximately $(19 \pm 1)\,\mathrm{cm}$[1] from the MOT region.

Throughout the measurements, the MOT beams remain continuously on, while the push beam is pulsed, to reduce the background. The upper MOT beams each have a power of approximately 110 mW, and the lower MOT beams have a power of 80 mW each. In both cases, the beams include a repump frequency with a power of approximately 10 %. The push beam has a radius of 0.8 mm at the MOT position, is circularly polarized, and contains a repump frequency component, ensuring efficient acceleration of atoms from both hyperfine ground states. The position of the push beam is optimized for the best signal-to-noise ratio.

A portion of the resulting fluorescent light is collected by a lens[2] with a focal length of $f = 75\,\mathrm{mm}$, placed at a distance of approximately $2f = 150\,\mathrm{mm}$ from the interaction region. The collected light is then focused onto the active area of a

[1] This was measured with respect to the center of the MOT, but the cold lithium cloud has a certain extent along the z-axis on the order of the MOT beam diameter.

[2] Thorlabs, LA1145-B - N-BK7 Plano-Convex Lens, Ø 2", f = 75 mm, AR Coating: 650 - 1050 nm.

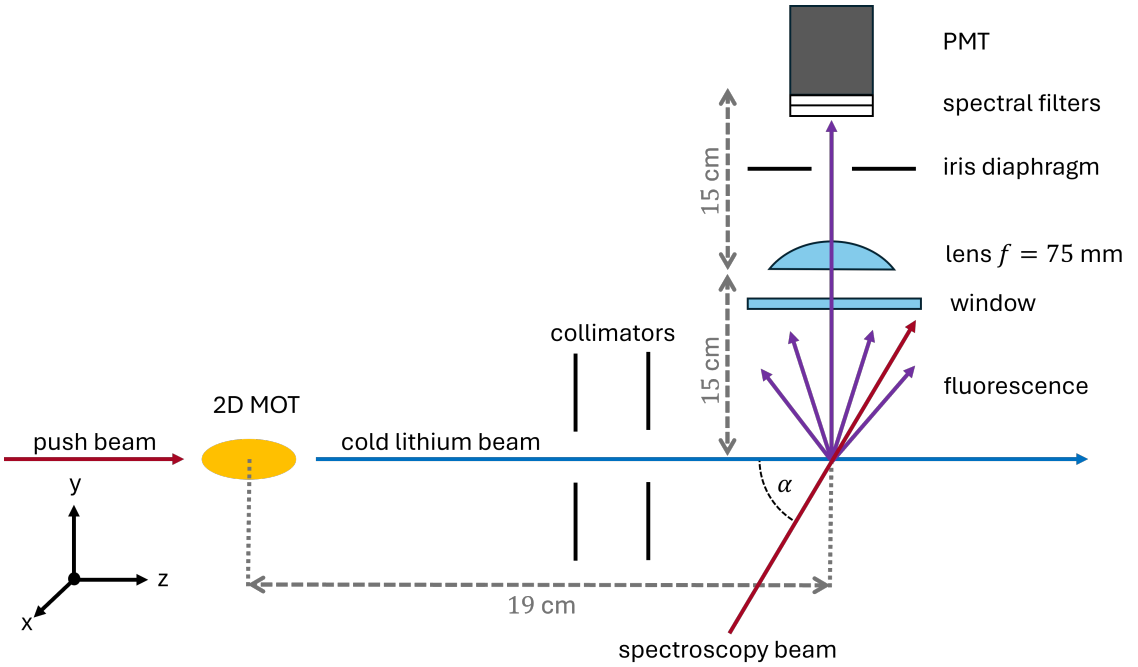

Figure 4.1: Spectroscopy setup for the characterization of the cold lithium beam. The cold atoms from the 2D MOT are accelerated by the push beam. The emerging cold atomic beam passes two collimators and is then intersected by the spectroscopy beam at an angle α. A part of the fluorescent light is collected by a lens and focused onto the active area of a photomultiplier tube (PMT). To reduce the background from ambient light and the spectroscopy beam we place spectral filters and an iris diaphragm in front of the PMT.

photomultiplier tube (PMT)[1], also placed at approximately $2f = 150\,\text{mm}$ from the lens.

To suppress background from ambient light, two spectral bandpass filters[2] are installed in front of the PMT. Additionally, the spectroscopy setup is enclosed with blackout material to reduce stray light originating from the 2D MOT region (see Figure C.13). The MOT beams themselves are further shielded to minimize scattered light. Pictures of the spectroscopy region are shown in Figure C.14.

To reduce the background signal originating from the spectroscopy beam, an iris diaphragm is positioned directly in front of the PMT[3]. Additional suppression of stray light from the spectroscopy beam is achieved through a combination of diaphragms and anti-reflection (AR) coated vacuum windows (see Figure 4.2). A black anodized aluminum inlay is placed within the spectroscopy chamber (see Figure C.15). This inlay reduces stray light in the spectroscopy section and serves as mechanical support for the two collimating apertures upstream of the interaction region, collimating the atomic beam and blocking light from the 2D MOT.

[1]Thorlabs, PMT1001/M - Multialkali Amplified PMT, 230–920 nm.
[2]Thorlabs, FBH670-10 - Hard-Coated Bandpass Filter, CWL = 670 nm, FWHM = 10 nm.
[3]The diameter can be varied from 1 to 10 mm and was optimized for good signal-to-noise ratio at a diameter of approximately 5 mm.

4.1.1 Spectroscopy Beam Setup

For the following measurements, the spectroscopy beam is tuned to resonance of the D_2 transition, incorporating two frequency components to simultaneously address the ground state hyperfine splitting. The total power of the spectroscopy beam is set to $(100 \pm 10)\,\mu W$, with beam radius of $(1.9 \pm 0.1)\,mm$ at the intersection with the cold atomic beam.

For the spectroscopy beam, we use one output of a commercial external cavity diode laser (ECDL) locked to an ultra-stable reference cavity and prepared as described in Section 2.3. This setup allows us to add a repump frequency component to the spectroscopy beam, enabling simultaneous addressing of both ground state hyperfine levels of ^{6}Li. This increases the signal-to-noise ratio dramatically, as each atom can scatter multiple photons without falling into a dark state. In the measurements presented below, the pump and repump components are adjusted to have approximately equal powers. The frequency of the spectroscopy laser can be shifted via two acousto-optic modulators (AOM).

Figure 4.2 shows a schematic of the optical setup for the spectroscopy beam. The beam power is adjusted using a combination of a half-wave plate ($\lambda/2$) and a polarizing beamsplitter (PBS). The linear polarization of the beam can be rotated with an additional half-wave plate to optimize the fluorescence signal, due to a dipole-like radiation emission pattern (see Figure 5.3).

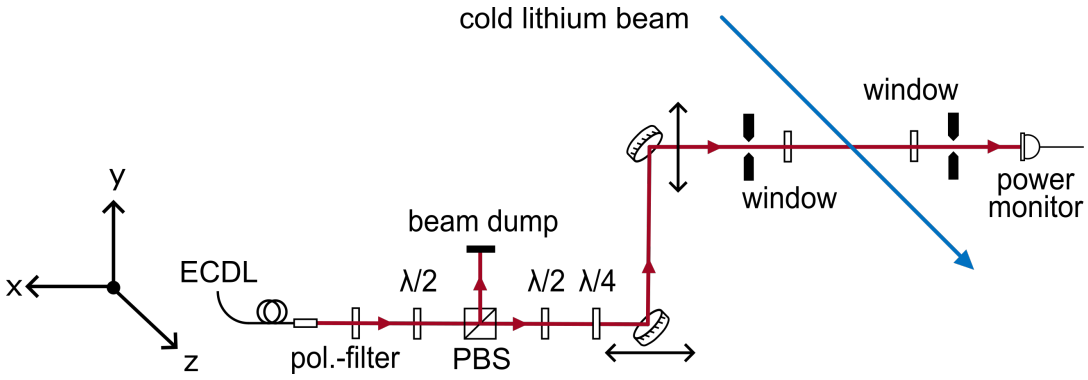

Figure 4.2: Schematic of the optical setup for the spectroscopy beam. The power can be adjusted by the combination of a half-wave plate ($\lambda/2$) and a polarizing beamsplitter (PBS). The linear polarization can be rotated by using another half-wave plate, this way we can maximize the florescence signal. We then use a periscope to align the spectroscopy beam through a CF-40 six-way cross. By moving the lower out-of-plane mirror along the x-axis we can move the spectroscopy beam along the y-axis to align it with the cold lithium beam. The spectroscopy beam then passes an iris diaphragm and an anti-reflection coated vacuum window. In the center of the six-way cross it intersects the cold lithium beam and produces fluorescent light. Afterwards the spectroscopy beam exits the vacuum chamber again through another anti-reflection coated vacuum window and another iris diaphragm. The spectroscopy beam is finally terminated on a photodiode, which is used for power stabilization.

A periscope is used to guide the spectroscopy beam through a CF-40 six-way vacuum cross. By moving the lower out-of-plane mirror along the x-axis with a micrometer stage, we can translate the beam along the y-axis to align it precisely with the cold lithium atomic beam.

The spectroscopy beam passes through an iris diaphragm and an anti-reflection (AR) coated vacuum window[1] before intersecting the cold atomic beam in the center of the six-way cross, where a part of the fluorescence is collected onto the PMT. The beam then exits the vacuum chamber through another AR-coated window and iris diaphragm to minimize stray light before being terminated on a photodiode. We use the photodiode to power stabilize the spectroscopy beam by varying the amplifier current of the ECDL.[2]

Using a flip mount we can add two mirrors in front of the vacuum cross to change the intersecting angle from $\alpha_\perp = (89.4 \pm 0.2)^\circ$ to $\alpha_\angle = (81.3 \pm 0.2)^\circ$.[3]

4.1.2 Pulsed Push Beam and Data Acquisition

Since the spectroscopy is performed on the same transition that is used both for trapping and for pushing the atoms, a substantial background fluorescence signal is present (see Section 4.1.3). To suppress this background, we employ a modulation scheme in which fluorescence is recorded only during intervals when the push beam is switched off. For this purpose, we use the first acousto-optic modulator (AOM) in the push beam preparation setup (Section 2.2.1), which provides switching times below 1 µs, as measured with an oscilloscope.

Figure 4.3 shows a schematic overview of the measurement setup for the cold atomic beam. The lithium atoms are cooled and trapped in a MOT using the beam configuration described in Section 2.1.2. The detunings of the trapping and repumping light are set to approximately $-11\,\Gamma$ and $-8\,\Gamma$, respectively, which is close to the optimal operating conditions established in the previous chapter.

The Titanium:Sapphire laser (Ti:Sa) for the MOT beams is stabilized to its tunable reference cavity (cavity 1) and, on longer time scales, to a wavemeter[4]. A fraction of the Ti:Sa output is beated with our optical frequency comb to calibrate the wavemeter, which exhibits slow drifts on the order of several megahertz during a day due to laboratory temperature fluctuations (see Section B.1.3).

Cold atoms are extracted from the MOT and accelerated toward the spectroscopy region using the push beam setup described in Section 2.2. The push beam is frequency-locked to the wavemeter, and its frequency is controlled via a computer.

In the spectroscopy region, the atomic beam is intersected by a spectroscopy laser whose frequency is stabilized to a ultra-stable reference cavity (cavity 2). The spectroscopy frequency is scanned using two acousto-optic modulators (AOMs), enabling precise and linear frequency tuning (see Section 2.3). The frequency of the signal generators[5] driving the AOMs can be controlled via the computer. The resulting

[1] Thorlabs, VPWW42-B - Ø 1.5" UVFS window, 30 min wedge, BBAR 650-1050 nm.
[2] Here we neglect the change in the power due to absorption by the cold lithium atoms, which is expected to be well below the power fluctuations of the spectroscopy beam.
[3] We measured the angle over a distance of approximately 1 m with respect to the optical table, which the push beam is aligned to.
[4] High Finesse, WS7-30
[5] Rohde & Schwarz - SMG and SMGU.

fluorescence is collected by a photomultiplier tube (PMT). The PMT output is amplified by an integrated transimpedance amplifier[1], which converts the current pulses into voltage signals.

These amplified signals are then fed into a discriminator[2] followed by a pulse shaper[3]. The purpose of these stages is to generate standardized pulses with an amplitude of 5 V and a width of approximately 1 µs, allowing reliable processing by the microcontroller.[4]

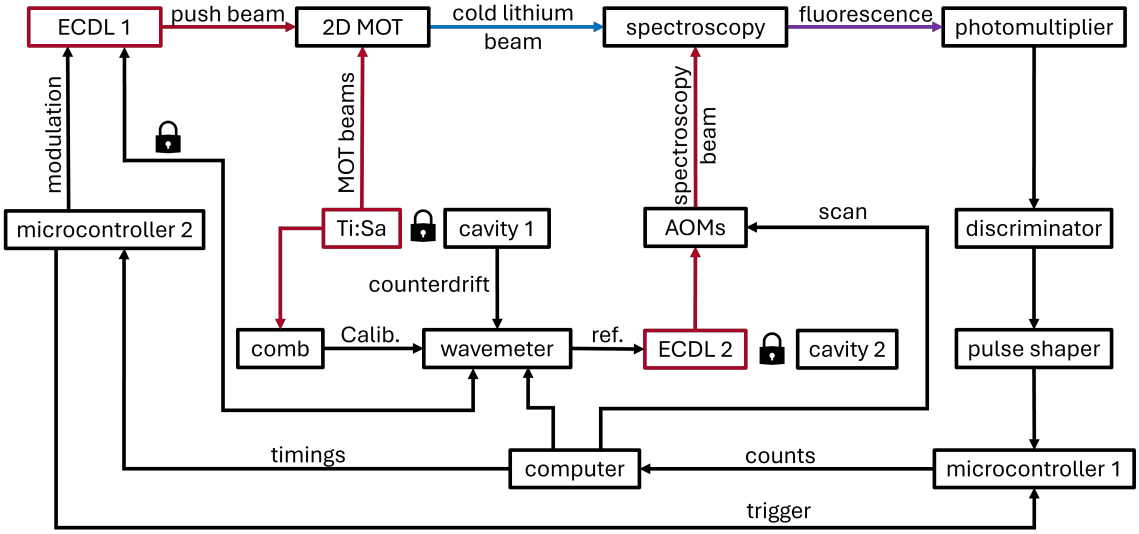

Figure 4.3: Schematic of the cold lithium beam measurement setup. The cold atoms are pushed out of the two-dimensional magneto-optical trap (2D MOT) and toward the spectroscopy section (see Figure 4.1), where the atoms are intersected by a spectroscopy laser. The emitted fluorescence is detected by a photomultiplier tube (PMT). The pulses from the PMT are then counted by a microcontroller (see Section 4.1.2). A second microcontroller triggers this counting controller to send the count to a computer synchronous with the modulation of the push beam. The computer sets the push beam frequency via a wavemeter lock and scans the spectroscopy beam via acousto-optic modulators (AOMs).

For the data acquisition, we employ a combination of two microcontrollers and a computer. Microcontroller[5] 1 is dedicated to counting the pulses from the PMT in a time resolved array. The program for the counting microcontroller is further described in Section E.1.

Microcontroller[6] 2 is responsible for controlling the timing of the measurement sequence. Initially, the MOT is loaded. Subsequently, the push beam is activated for a defined duration t_{push}. Then the counting microcontroller is triggered to begin with a counting sequence.

[1]We typically set the gain to 3 and the low pass filter to 80 MHz.
[2]LeCroy, Model 4608C - Octal Discriminator, threshold at approximately −100 mV.
[3]LeCroy, Model 222 - Dual Gate Generator, output width = 1 µs.
[4]We have verified that the microcontroller can reliably count pulse frequencies up to 1 MHz.
[5]Arduino Uno.
[6]Arduino Mega.

Following each push pulse, fluorescence counts from the PMT are recorded over a total acquisition window of 10 ms, with a temporal resolution of 100 µs per bin. Each trace can be averaged to improve the signal-to-noise ratio. The time starts with the trigger of the push beam pulse. An overview of all experimental parameters is shown in Table E.1.

4.1.3 Background Characterization

In order to accurately determine the fluorescence signal from the cold atomic beam, we characterized and quantified the various sources of background counts in our detection system. The background contributions were systematically investigated by sequentially enabling different components of the experimental setup while monitoring the count rate on the photomultiplier tube (PMT). The identified sources are summarized below.

First, the **intrinsic PMT background**, measured with all light sources turned off and the detection region fully shielded, amounts to ~ 300 counts/s. This rate is attributed to the PMT dark current and electronic noise in the signal chain, representing the fundamental noise floor of the detection system.

Activating the **magneto-optical trap (MOT) beams** while keeping the push beam and oven off resulted in an additional background of approximately 400 counts/s. This signal arises primarily from scattered MOT light entering the detection region. When the lithium oven was additionally heated to operational temperature of 400 °C, the background increased by roughly 300 counts/s. This can be attributed to additional scattering of the MOT beams with the hot lithium atoms. We were able to reach such low levels of background by placing the beam collimators in front of the spectroscopy area, which suppress scattered light from the MOT region as well as signals from hot lithium atoms (see Section E.2).

The **spectroscopy beam** has the largest influence on the background. Figure 4.4 shows the background count rate as a function of spectroscopy beam power P. A linear fit $f(P) = a \cdot P + b$ yields a proportionality constant $a = (45 \pm 1)$ counts/s/µW and a zero-power intercept $b = (1000 \pm 50)$ counts/s, which is consistent with the sum of the previously identified background sources.

Reducing the spectroscopy power decreases the background proportionally, but it also lowers the fluorescence signal, thereby degrading the overall signal-to-noise ratio. As a compromise, a probe power of 30 µW was chosen for the following measurements. The influence of the spectroscopy beam power is further discussed in Section E.3.

Changing the spectroscopy beam angle from $\alpha \approx 90°$ to $\alpha \approx 80°$ leads to an approximately 30 % increase in background due to enhanced light scattering in the spectroscopy region. At smaller angles, reflections from the viewports are no longer directed away from the interaction region but rather recirculate within the vacuum cross, increasing stray light.

Additionally, due to varying lighting conditions and slight adjustments of the shielding between measurement runs, background variations of up to 1000 counts/s were observed.

Finally, a continuously operated **push beam** produced a large background of approximately 2.2×10^5 counts/s, about two orders of magnitude higher than any other individual source. However, when the push beam was pulsed synchronously

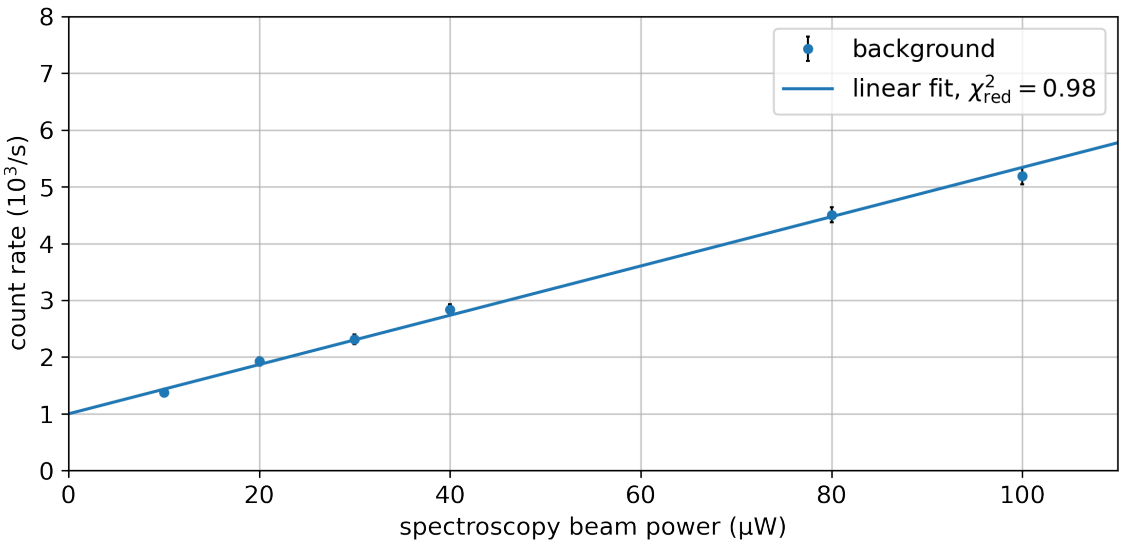

Figure 4.4: Background count rate in dependence of spectroscopy beam power P. A linear fit function $f(P) = a \cdot P + b$ yields a proportionality constant of $a = (43 \pm 1)$ counts/s/µW and a zero-power extrapolation of $b = (1000 \pm 50)$ counts/s.

with the detection sequence, the background returned to baseline levels. This clearly demonstrates that time-gated detection effectively suppresses push beam induced background.

A summary of the measured background levels is presented in Table 4.1. The relative magnitudes highlight the importance of optical shielding and synchronized push beam modulation for achieving an optimal signal-to-background ratio in fluorescence detection of the cold atomic beam.

Table 4.1: Summary of identified background sources in the cold atomic beam fluorescence measurement with roughly measured count rates.

background source	**count rate (1/s)**
PMT dark counts	~ 300
MOT beams (100 mW)	~ 400
hot atoms (oven set to 400 °C)	~ 300
spectroscopy beam (30 µW, $\alpha \approx 90°$)	~ 2000
spectroscopy beam (30 µW, $\alpha \approx 80°$)	~ 3000
total ($\alpha \approx 80°$)	~ 3000
total ($\alpha \approx 90°$)	~ 4000
push beam permanently on	$\sim 10^5$

4.2 Cold Atomic Beam Analysis

In this section the data analysis is introduced for optimized push beam settings. The push beam is circularly polarized, detuned by $+7\,\Gamma$, and operated at a total power of 1 mW. All remaining experimental parameters are listed in Table E.1. The optimization of the different push beam parameters is then later discussed using these analysis methods (see Section 4.3).

4.2.1 Time-Resolved Frequency Spectra

From the data acquisition we receive time-resolved frequency spectra. Figure 4.5 shows the detected fluorescence spectrum, binned into intervals of 100 µs and averaged over 100 push beam pulses of 1.5 ms duration. In the heat map (a) the horizontal axis corresponds to the arrival time of atoms at the detection region. The vertical axis represents the laser detuning relative to the D_2 transition. Furthermore, two slices through the maximum are shown: a *time-of-flight slice* (horizontal cut, b) corresponding to a fixed detuning, and a *spectral slice* (vertical cut, c) corresponding to a fixed arrival time. The time-of-flight slice provides information on the temporal structure and axial velocity distribution of the cold atomic beam, whereas the spectral slice highlights the Doppler-broadened resonance profile at a given moment of the pulse sequence.

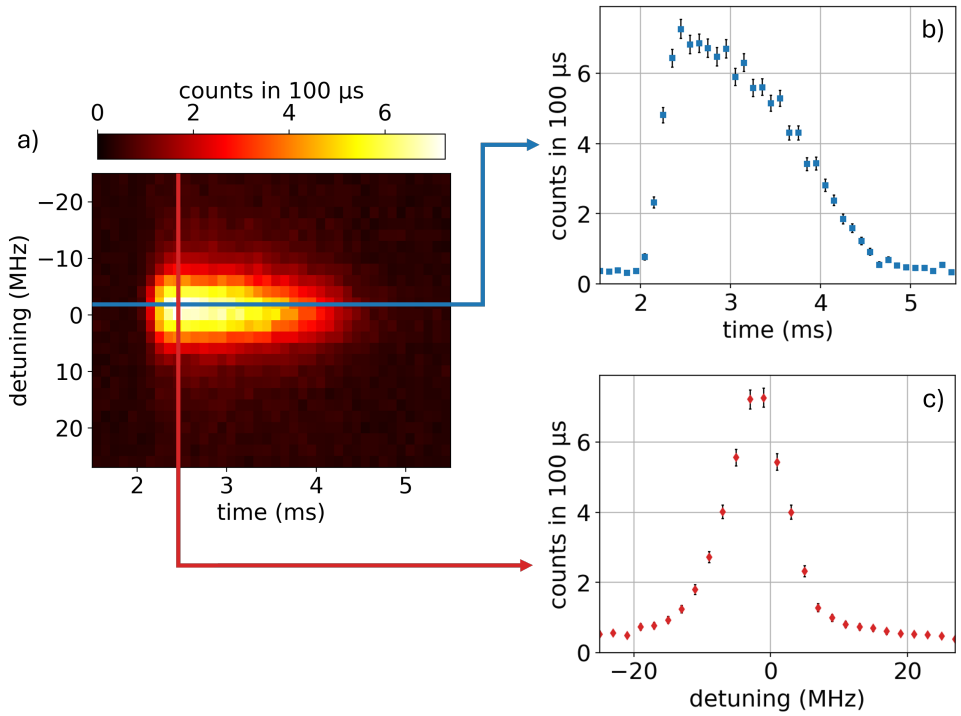

Figure 4.5: Example of a time-resolved fluorescence spectrum with two representative slices. In panel a) the vertical axis shows the detuning from the D_2 ground state transition, while the horizontal axis represents the time of flight. The color scale indicates the number of detected photon counts per time bin of 100 µs, averaged over 100 push pulses. As examples, a time-of-flight slice (b) and a spectral slice (c) through the maximum are shown on the side to illustrate the data structure.

4.2.2 Perpendicular Fluorescence Measurement

Figure 4.6 shows several time-of-flight (TOF) spectra for different spectroscopy beam detunings δ at a spectroscopy angle of $\alpha \approx 90°$. Each spectrum begins with a push pulse (shown in gray). After this pulse we start recording counts, integrated in time bins of 200 µs and averaged over 100 pulses. The overall amplitude varies with the detuning, while the line shape remains essentially unchanged.

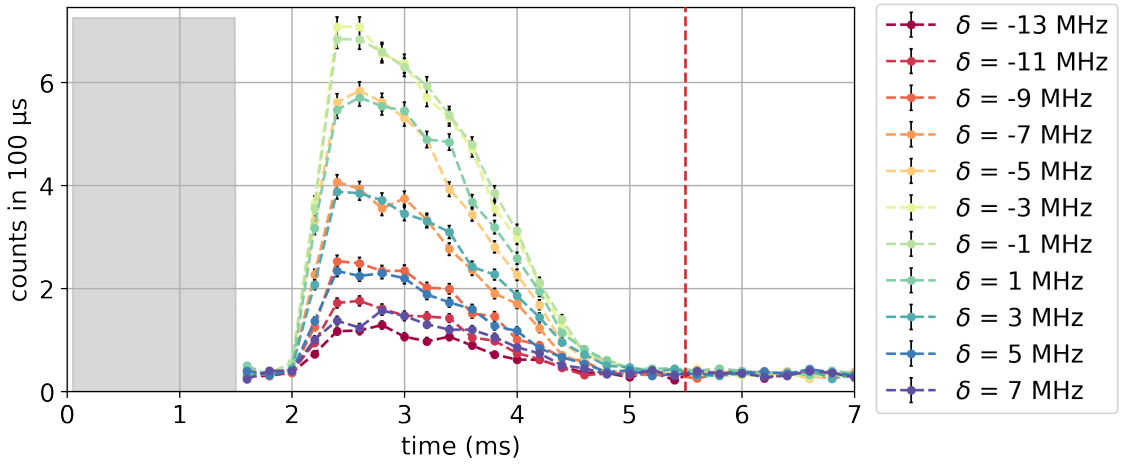

Figure 4.6: Example for time-of-flight spectra recorded for different spectroscopy beam detunings δ at a spectroscopy angle of $\alpha \approx 90°$. Each spectrum begins with a push pulse (shown in gray). After this pulse we start recording counts, integrated in time bins of 200 µs and averaged over 100 pulses. The overall amplitude varies with the detuning, while the line shape remains essentially unchanged. Data points are connected to guide the eye. The red line indicates a cut that is used to increase the signal-to-noise ratio in the frequency spectra.

It is difficult to directly deduce a quantitative velocity distribution from the time-of-flight spectrum, since the exact temporal influence of the push pulse, which is convolved with the underlying velocity distribution, is not precisely known. In particular, effects such as the depletion and subsequent reloading of the magneto-optical trap during a single push pulse influence the observed TOF signal. A more detailed interpretation therefore requires a numerical simulation that models these dynamics. Nevertheless, the TOF spectrum allows us to estimate upper and lower bounds for the axial velocity of the cold atomic beam.

For the upper velocity limit, we consider the shortest observed flight times. No detectable signal is observed below $t_{\mathrm{min}} = 2\,\mathrm{ms}$. The corresponding maximum velocity can be estimated from the flight distance $z_{\mathrm{TOF}} = (19 \pm 1)\,\mathrm{cm}$ via

$$v_{\mathrm{max}} = \frac{z_{\mathrm{TOF}}}{t_{\mathrm{min}}}\,, \tag{4.1}$$

which yields $v_{\mathrm{max}} = (95 \pm 5)\,\mathrm{m/s}$, where the uncertainty is dominated by the imprecision in the distance measurement.

For the lower velocity limit, we examine the longest arrival times. In this dataset, no signal is detected beyond $t_{\mathrm{max}} = 5\,\mathrm{ms}$. To obtain the true flight time of the

slowest atoms, the duration of the push pulse $t_{\mathrm{pulse}} = 1.5\,\mathrm{ms}$ must be subtracted, since the latest arriving atoms are also the ones released at the end of the pulse. The corresponding velocity is then given by

$$v_{\mathrm{min}} = \frac{z_{\mathrm{TOF}}}{t_{\mathrm{max}} - t_{\mathrm{pulse}}}\,, \tag{4.2}$$

resulting in $v_{\mathrm{min}} = (54 \pm 3)\,\mathrm{m/s}$.

To quantitatively analyze the time-of-flight spectra, we first subtract a constant baseline from each trace to remove background contributions and then integrate the remaining signal to obtain an estimate of the total number of atoms in each bunch. In addition, we determine the arrival time $\hat{t}$ corresponding to the maximum count. From this, we estimate the most probable velocity $\hat{v}$ of the atomic bunch according to $\hat{v} = z_{\mathrm{TOF}}/\hat{t}$.

Figure 4.7 shows the integral under the TOF spectrum and most probable velocity of the time-of-flight spectra shown in Figure 4.6. The data points are connected using linear interpolation. The integral shows a maximum near the resonance. The most probable velocity remains approximately constant at around 80 m/s.

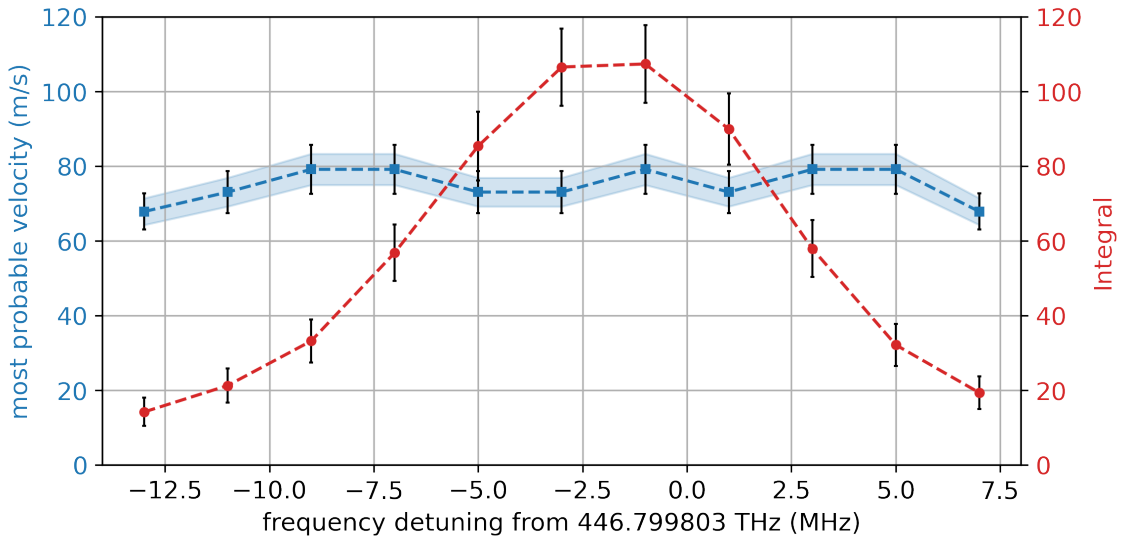

Figure 4.7: Integral and most probable velocity of the time-of-flight spectra shown in Figure 4.6. The data points are connected using linear interpolation. The integral shows a maximum near the resonance. The most probable velocity remains approximately constant at around 80 m/s. The blue band indicates a correlated systematic uncertainty originating from the uncertainty of the flight distance.

The information contained in the time-of-flight spectra can be used to extract an averaged frequency spectrum with improved signal-to-noise ratio, by discarding the portion of the data after 5.5 ms (see Figure 4.6), which mainly contains residual background. If we then integrate over all bins with lower flight times and divide by the effective measurement time of 4 ms, we obtain a averaged fluorescence spectrum.

Figure 4.8 shows an example of such spectrum corresponding to the data presented in Figure 4.5. The resulting spectrum was fitted with a Voigt profile (see

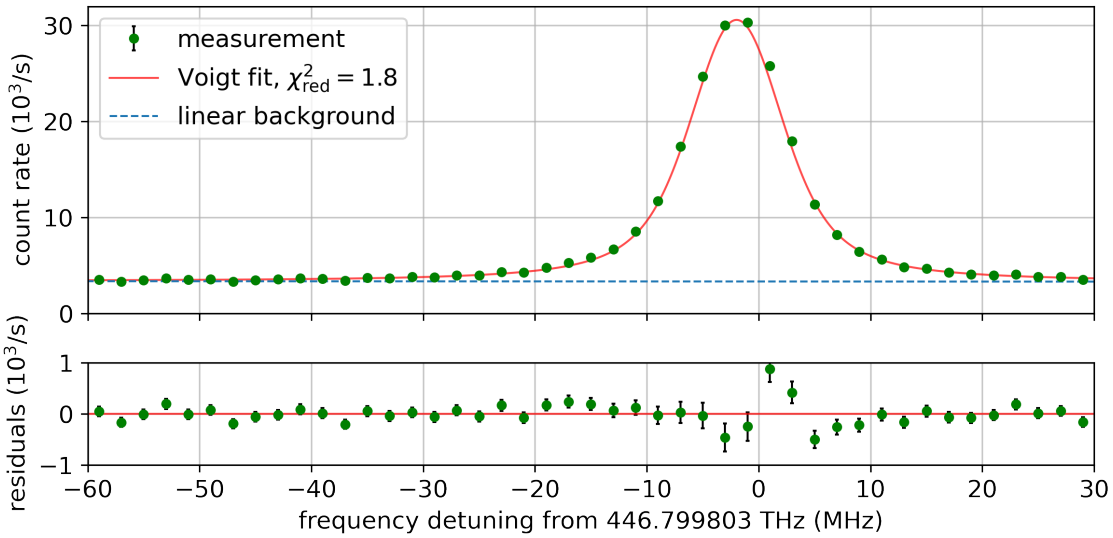

Figure 4.8: Example for a mean fluorescence spectrum obtained from the time-resolved data shown in Figure 4.5. The time-of-flight data was integrated over the time interval from 1.5 ms to 5.5 ms. The counts were converted to a count rate by dividing by the effective measurement duration of 4 ms. The spectrum is fitted with a Voigt profile (see Section B.3) with the Lorentzian width fixed to the natural linewidth. The residuals of the fit are shown below the main plot, and the corresponding fit values are shown in Table 4.2.

Section B.3) to extract information about the resonance detuning and broadening. The corresponding fit parameters are summarized in Table 4.2. During the fitting procedure, the Lorentzian contribution was fixed to the natural linewidth of the lithium D_2 transition. The increased value for the reduced chi squared and the systematic structure observed in the residuals indicate that the model does not fully reproduce the measured line shape, suggesting the presence of additional broadening mechanisms or slight asymmetries not captured by the simple Voigt model (further discussed in Section E.3).

Furthermore, the fitted line center shows a systematic shift toward lower frequencies compared to the expected transition frequency of approximately 2 MHz. This shift can be attributed to a small misalignment between the atomic and spectroscopy beams: a measured angle of $\alpha = (89.4 \pm 0.2)^\circ$ results in a first-order Doppler shift of (-1.3 ± 0.4) MHz for atoms traveling at a velocity of 80 m/s. The remaining deviation is consistent with an overall systematic frequency uncertainty of $\Delta f_{\text{sys}} = 1$ MHz.

The extracted Gaussian broadening amounts to (2.7 ± 0.1) MHz, which corresponds to a FWHM of approximately 6.4 MHz and is larger than expected from purely geometrical considerations. Based on the beam geometry, the maximum transverse velocity estimated as $v_t \approx 1.2$ m/s for an axial velocity of $v_z = 90$ m/s, corresponding to a Doppler shift of ≈ 1.8 MHz (further discussed in Section 4.4). The additional broadening can be partially explained by the Zeeman splitting due to earth magnetic field, which is around 1 MHz. The broadening could also be a result of the axial velocity distribution in combination with a non-perpendicular spectroscopy beam, which we will discuss in the following.

Table 4.2: Fit parameters corresponding to Figure 4.8 for a Voigt fit with the Lorentzian width fixed to the natural linewidth of the lithium D_2 transition.

fit parameter	**value**
broadening σ	$(2.7 \pm 0.1)\,\mathrm{MHz}$
amplitude a	$(27.2 \pm 0.2)\,10^3/\mathrm{s}$
frequency offset δ_0	$(-2.0 \pm 0.1)\,\mathrm{MHz}$
linear background m	$(-0.3 \pm 0.5)/(\mathrm{s\,MHz})$
background b	$(3.35 \pm 0.02)\,10^3/\mathrm{s}$

4.2.3 Angled Fluorescence Measurement

To gain more information about the axial velocity of the cold atomic beam and its distribution, we varied the spectroscopy beam angle to $\alpha_\angle = (81.3 \pm 0.2)^\circ$ while keeping all other experimental parameters unchanged.

Figure 4.9 shows the time-resolved spectra for both configurations: the perpendicular measurement (a) and the angled measurement (b). Due to the Doppler shift the angled measurement exhibits a clear shift toward lower frequencies and a noticeable tilt toward higher frequencies at longer time-of-flight values, due to a decreased velocity component along the direction of the spectroscopy beam.

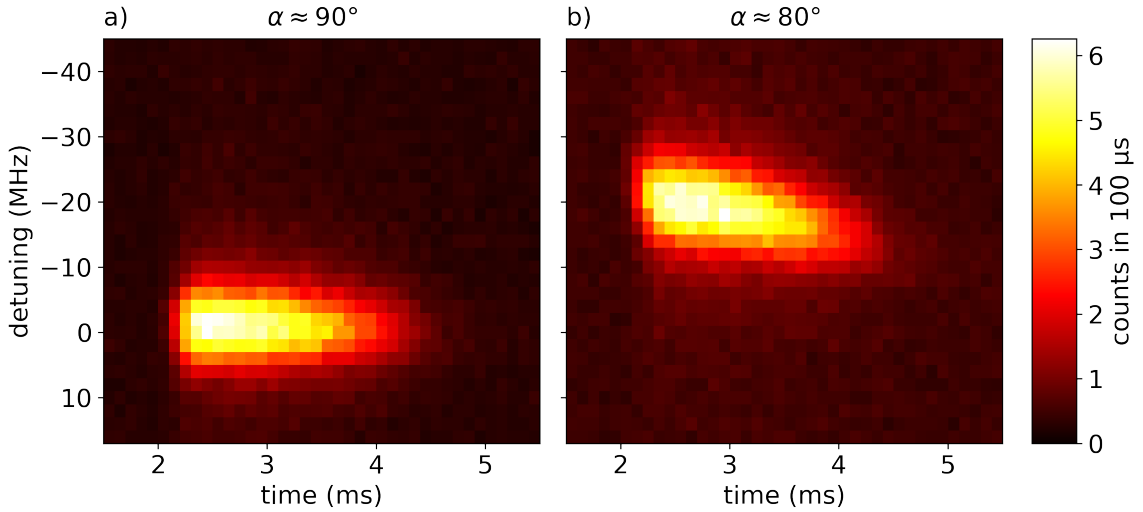

Figure 4.9: Example of time-resolved spectra for two different spectroscopy beam angles. The vertical axis shows the detuning from the D_2 ground state transition, while the horizontal axis represents the time of flight. Panel a) corresponds to a spectroscopy angle of $\alpha \approx 90^\circ$, and panel b) to $\alpha \approx 80^\circ$. The color scale indicates the number of detected counts per time bin of 100 µs, averaged over 100 push pulses with a duration of 1.5 ms.

To further investigate the observed frequency shift, we extracted the mean frequency spectra as described previously. Figure 4.10 shows the averaged fluorescence spectra recorded with the spectroscopy beam oriented perpendicular to the atomic

beam ($\alpha \approx 90°$) and at an angle ($\alpha \approx 80°$). Both datasets were fitted with Voigt profiles using the same fixed natural linewidth. The spectrum recorded under an angle is clearly shifted toward lower frequencies and appears slightly broader compared to the nearly perpendicular configuration.

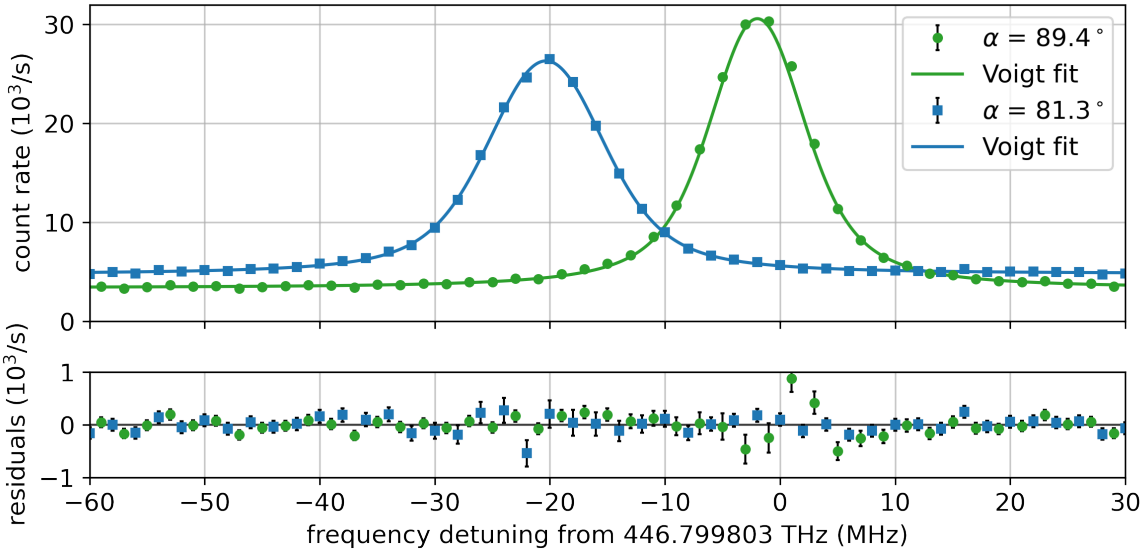

Figure 4.10: Comparison of frequency spectra for perpendicular ($\alpha \approx 90°$) and angled ($\alpha \approx 80°$) spectroscopy beam configurations. Both spectra are fitted with Voigt profiles using a fixed natural linewidth. The angled spectrum shows a clear shift toward lower frequencies and appears slightly broader than the perpendicular case.

The frequency difference between the two spectra can be attributed to the first-order Doppler shift. By comparing the fitted line centers for the perpendicular ($f_\perp$) and angled ($f_\angle$) configurations, the Doppler shift $\Delta f_{\text{Doppler}} = f_\angle - f_\perp$ is independent of the absolute frequency calibration.

The corresponding axial atomic velocity can then be obtained from

$$v_z = \frac{c \cdot \Delta f_{\text{Doppler}}}{f_{\text{Li6,D2}} \left(\cos(\alpha_\angle) - \cos(\alpha_\perp)\right)}, \tag{4.3}$$

where $f_{\text{Li6,D2}}$ denotes the transition frequency of the ^{6}Li D_2 line and c is the speed of light. For the shown example, we obtain an axial velocity of $v_z = (82.4 \pm 0.2)\,\text{m/s}$, where the quoted uncertainty reflects only the propagated statistical error from the two fit results.

In addition, there is a correlated systematic uncertainty arising from the determination of the beam angles $\alpha_\perp = (89.4 \pm 0.2)°$ and $\alpha_\angle = (81.3 \pm 0.2)°$, corresponding to a relative uncertainty in v_z of approximately $\pm 5\,\%$. A further contribution originates from the possible frequency drift of the wavemeter between the two measurements. Since this drift was monitored only within a detuning range of ± 1 MHz, the resulting systematic uncertainty in velocity is estimated to be about $\pm 3\,\text{m/s}$. Including these errors, the determined value is in agreement with the one evaluated from the TOF spectra at the perpendicular configuration above.

Figure 4.11 shows frequency spectra recorded at different flight times. With increasing flight time, the center frequency shifts toward smaller detunings. In contrast, no such shift is observed in the perpendicular measurement (see Figure E.5).

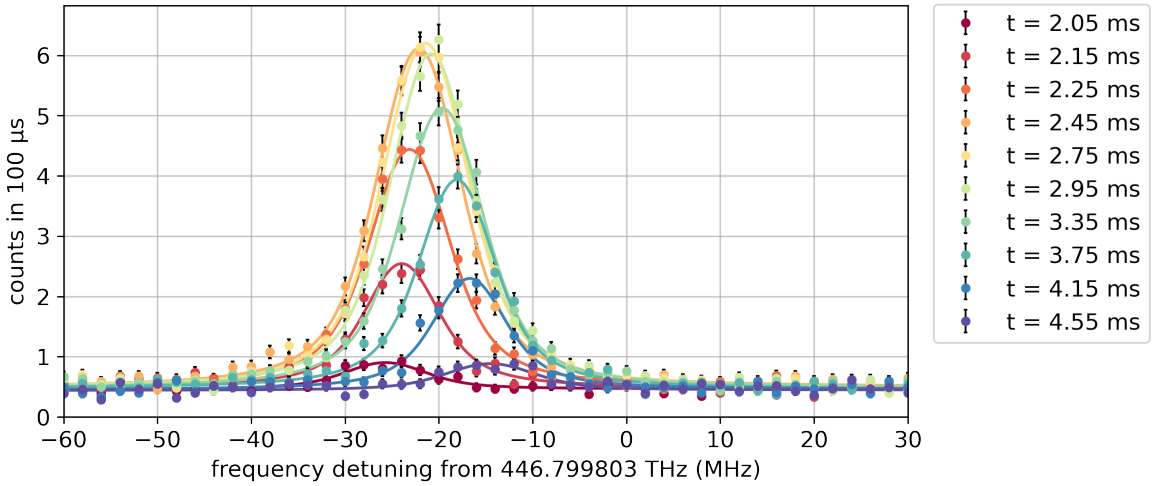

Figure 4.11: Example of frequency spectra at different atomic flight times for an angled spectroscopy beam. Each frequency spectrum was fitted with a Voigt profile with a fixed linewidth. The center frequency shifts toward smaller detunings for longer flight times.

This behavior is consistent with expectations: atoms with lower axial velocities reach the detection region at later times and therefore experience a reduced Doppler shift. The same effect is also apparent in the time-of-flight spectra recorded for different spectroscopy beam detunings (see Figure E.8). To quantify this effect, each frequency spectrum was fitted with a Voigt profile with a fixed linewidth, and the resulting fit parameters were plotted as a function of flight time.

Figure 4.12 shows the fitted amplitudes and center detunings. The detuning approaches zero for longer flight times, reflecting the reduced axial velocity, while the amplitude follows the temporal structure of the atomic pulse, resembling the time-of-flight spectrum. Within the statistical uncertainties, no systematic change in the broadened linewidth can be observed (see Figure E.11), although one would expect a small change due to different flight times leading to different possible radial velocities due to a geometrical cut off by the apertures for the cold beam.

Using Equation 4.3, the measured center detunings can be converted into corresponding atomic velocities, yielding the axial velocity distribution of the cold atomic beam. Figure 4.13 shows the resulting velocity distribution derived from the data presented in Figure 4.12.

The vertical error bars represent the statistical uncertainties propagated from the individual Voigt fits. The blue shaded band indicates the correlated relative systematic uncertainty originating from the angle determination, while the correlated absolute systematic uncertainty due to frequency calibration is depicted in the upper-left corner of the plot.

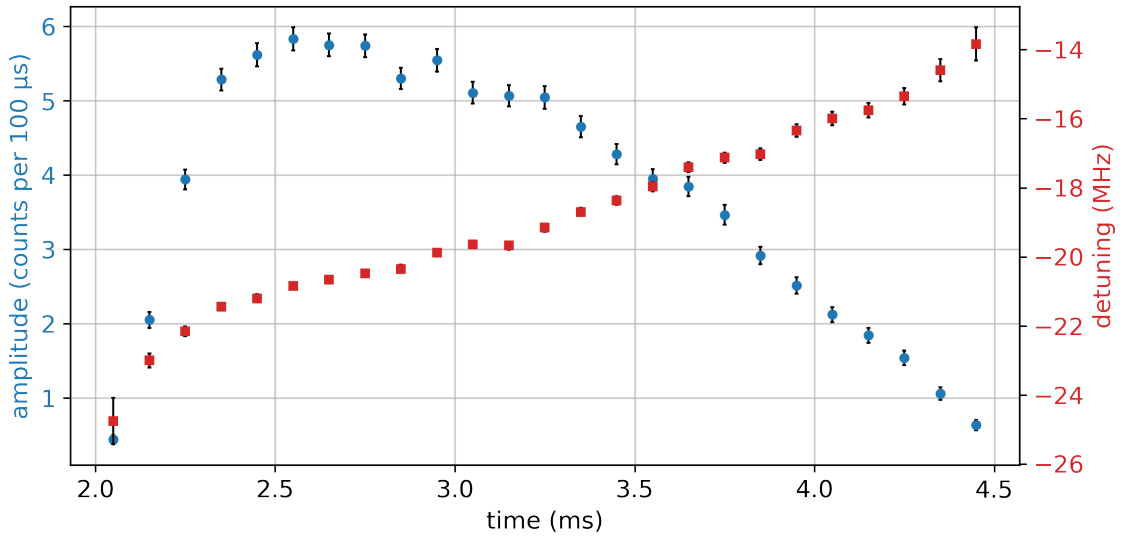

Figure 4.12: Amplitude and detuning of Voigt profiles for different flight times from Figure 4.11. The amplitude follows the time-of-flight profile, while the detuning approaches zero for longer flight times, consistent with slower atomic velocities.

The resulting velocity distribution yields a weighted mean axial velocity of

$$\bar{v}_z = (82.7 \pm 0.2\,(\text{stat}) \pm 5.0\,(\text{sys}))\,\text{m/s},$$

which is in good agreement with the velocity obtained from the shift of the mean frequency spectra. The distribution exhibits a full width at half maximum (FWHM) of approximately 24 m/s and shows a slight asymmetry, with a higher population of atoms at lower velocities.

The slowest detected atoms have velocities of

$$v_{\text{min}} = (63 \pm 3\,(\text{stat}) \pm 4\,(\text{sys}))\,\text{m/s},$$

which lies well above the lower velocity limit estimated from the time-of-flight (TOF) spectrum.

The fastest atoms, on the other hand, reach velocities of

$$v_{\text{max}} = (107 \pm 3\,(\text{sys}) \pm 6\,(\text{sys}))\,\text{m/s},$$

slightly exceeding the upper limit derived from the TOF analysis but still remaining within the combined uncertainties. This indicates that the Doppler-based analysis tends to overestimate the velocity of the cold atomic beam.

The observed FWHM of approximately 25 m/s is broader than the initial velocity distribution of the atoms before extraction, which was measured to be about 16 m/s (see Section 3.4.1), and also broader than the 11 m/s reported by Tiecke *et al.* [2]. This indicates that the velocity distribution is modified during the acceleration process driven by the push beam pulse and depends on the push beam parameters.

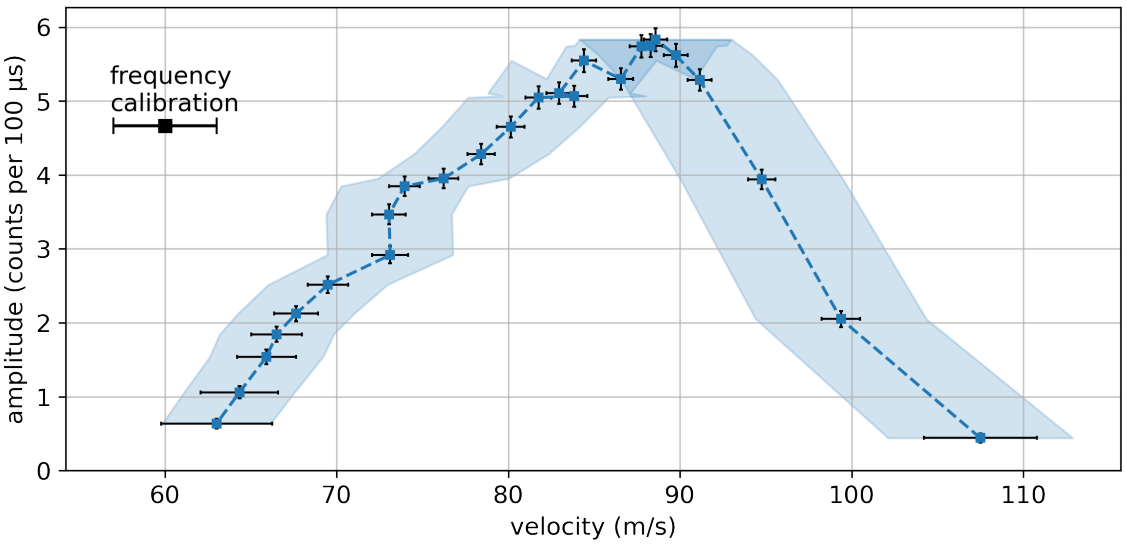

Figure 4.13: Velocity distribution derived from Doppler shifts in Figure 4.12. Error bars denote statistical fit uncertainties, while the blue shaded region represents the correlated relative systematic error from the angle measurement. The absolute systematic uncertainty due to the frequency calibration is indicated in the upper-left corner.

4.2.4 Discussion on the Cold Atomic Beam Analysis

A quantitative verification of the final velocity distribution is currently limited by the lack of a theoretical model. Although the initial velocity distribution along the push beam axis is characterized by our Monte Carlo simulations of the hot atomic beam (see Section 3.1.4), extending the simulation of the 2D MOT [72] to include the push beam dynamics would provide valuable insight into the resulting velocity distribution in the future. Nevertheless, the extracted minimum and maximum velocities are consistent with the independent estimates obtained from the TOF measurements.

Several considerations support the plausibility of the measured velocity ranges: The minimum velocity depends on the gravitational acceleration during the flight leading to the slowest atoms to fall below the aperture in front of the spectroscopy region. For our geometry, this lower bound is at approximately 10 m/s, and no atoms are observed below this threshold. The photon-scattering rate on resonance is of order 10^6 /s, with a recoil velocity of approximately 0.1 m/s. This is sufficient to accelerate the atoms to the observed velocities within the 1.5 ms push pulse duration. The measured mean velocity exceeds the resonant velocity corresponding to the applied detuning (approximately 30 m/s). This is consistent with the presence of saturation broadening of several natural linewidths at the push beam intensity of $I_{\mathrm{push}} \approx 160\,\mathrm{W/m^2}$, which keeps the atoms in resonance over a larger velocity range and therefore allows additional acceleration in combination with the generally high scattering rate.

Compared to the results of Tiecke *et al.* [2], our mean velocity of 82 m/s is substantially higher than their most probable velocity of 36 m/s. This difference is consistent

with the fact that their push beam was red detuned, while our optimized configuration employs a strongly blue detuned push beam (see Section 4.3.3). Furthermore, the experimental optimization goals differ: Tiecke *et al.* optimized the recapture efficiency of a downstream 3D MOT, which favors lower axial velocities, whereas our optimization prioritizes maximizing the detected photon count in spectroscopy measurements, which benefits from stronger acceleration.

In the following section, we investigate in detail how different push beam parameters influence the axial velocity distribution of the cold atomic beam.

4.3 Push Beam Dependence

In the following, we investigate the dependence of the axial velocity and the total number of atoms on the push beam parameters: the pulse length, the detuning and the power. For this purpose, we use the previously established analysis of the time-of-flight spectra and the Doppler shift. The push beam frequency is referenced to the upper hyperfine ground state transition, which is the most populated one due to optical pumping in the 2D MOT (see Section 3.4.1). The following measurements were conducted with a circular polarized push beam on resonance with the upper ground state transition including a repump frequency power of approximately 30 % since this setting exhibits the highest count rates on the PMT and thus the best signal-to-noise ratio.

4.3.1 Dependence on Push Pulse Duration

To investigate the influence of the push pulse duration on the time-of-flight spectrum, we recorded spectra for several pulse lengths, as shown in Figure 4.14. The circularly polarized push beam was operated at a power of 1 mW, including approximately 40 % repump frequency component. The detuning of the push beam was set to approximately 7 Γ. Each trace represents an average over 100 measurements, and the data points are connected by lines for visual guidance.

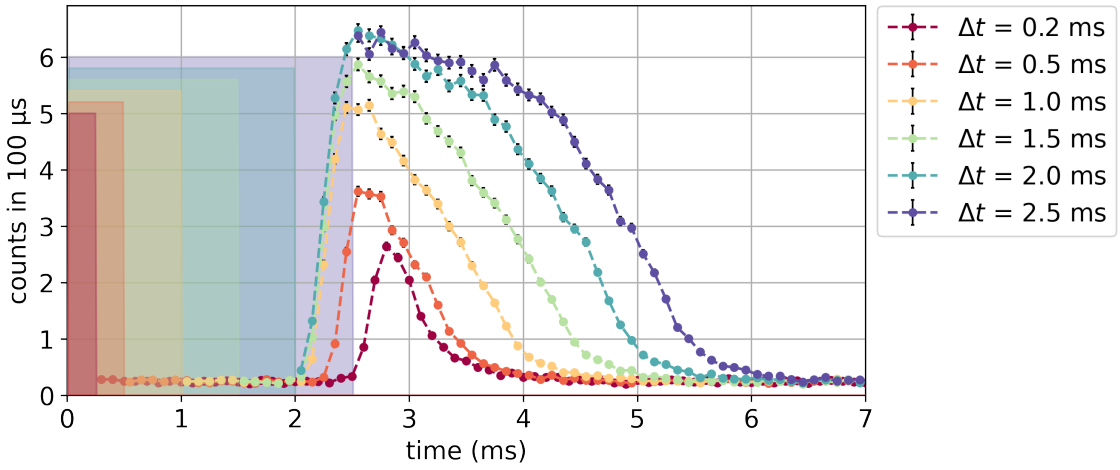

Figure 4.14: Time-of-flight spectra of the cold atomic beam for different push pulse durations Δt. The push beam power is set to 1 mW and includes a repump frequency component. The push beam detuning is $\sim 7\,\Gamma$. Each trace represents an average of 100 measurements. The data points are connected by linear interpolation. The shaded areas at the beginning of each spectrum indicate the push pulse starting at $t = 0$. The pulse height is only varied for visualization.

When looking at the shape of the TOF spectra we can see that especially the ones for long push pulse durations do not have a flat top like the push pulse but rather an almost linearly decreasing top. This could indicate an emptying of the MOT due to the constant pushing.

Figure 4.15 shows the integral and the FWHM of the time-of-flight spectra for push pulse durations below approximately 2 ms. For push pulse durations above approximately 2 ms, the recorded spectra become truncated, since data acquisition only starts after the push beam has been switched off.

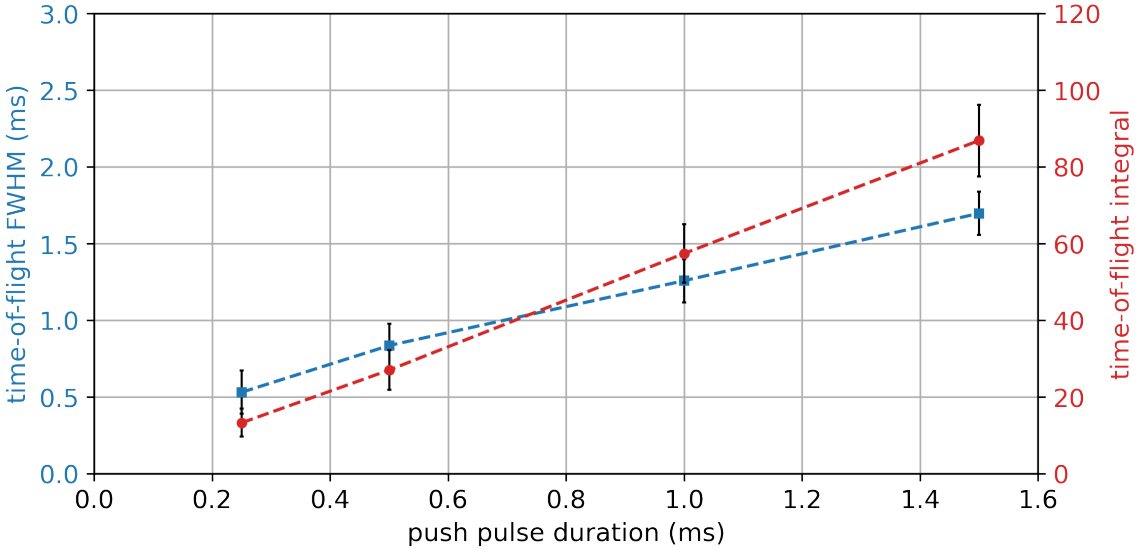

Figure 4.15: Integral and full width at half maximum (FWHM) of the TOF spectra in Figure 4.14 in dependence of the push pulse duration. The total number of detected atoms and the FWHM increase with push pulse duration. The data points are connected to guide the eye.

With increasing push pulse duration, the TOF spectra broaden noticeably. The full width at half maximum (FWHM) of the distribution increases continuously with the pulse length. Furthermore, the signal amplitude rises with longer pulses but begins to saturate for durations beyond $\Delta t = 2\,\text{ms}$, while the integral further increases.

The minimum flight time, corresponding to the upper velocity limit, remains nearly constant for pulse durations above $\Delta t = 1\,\text{ms}$, suggesting that atoms cease to experience further acceleration beyond this point as they fall out of resonance.

If we subtract the pulse length from the maximum flight time above a certain threshold the flight time stays almost constant at round 3.5 ms. This indicates that the minimum velocity is not largely affected by the pulse length. Minimal and maximal flight time for the TOF spectra for different push pulse durations are shown in Figure 4.16.

As described in Section 4.2.3, the axial velocity of the cold atomic beam can be determined from the Doppler shift between angled and perpendicular spectroscopy measurements. By comparing the fitted line centers of the mean frequency spectra at $\alpha \approx 80°$ and $\alpha \approx 90°$ we obtain the mean velocity for each push pulse duration.

Figure 4.17 shows the resulting axial velocities for different push pulse durations, together with the corresponding amplitudes extracted from the Voigt profile fits.

The observed increase in both amplitude and axial velocity with push pulse duration reflects the longer acceleration due to a longer push beam pulses. However, the apparent saturation beyond approximately 2 ms may arise from two factors:

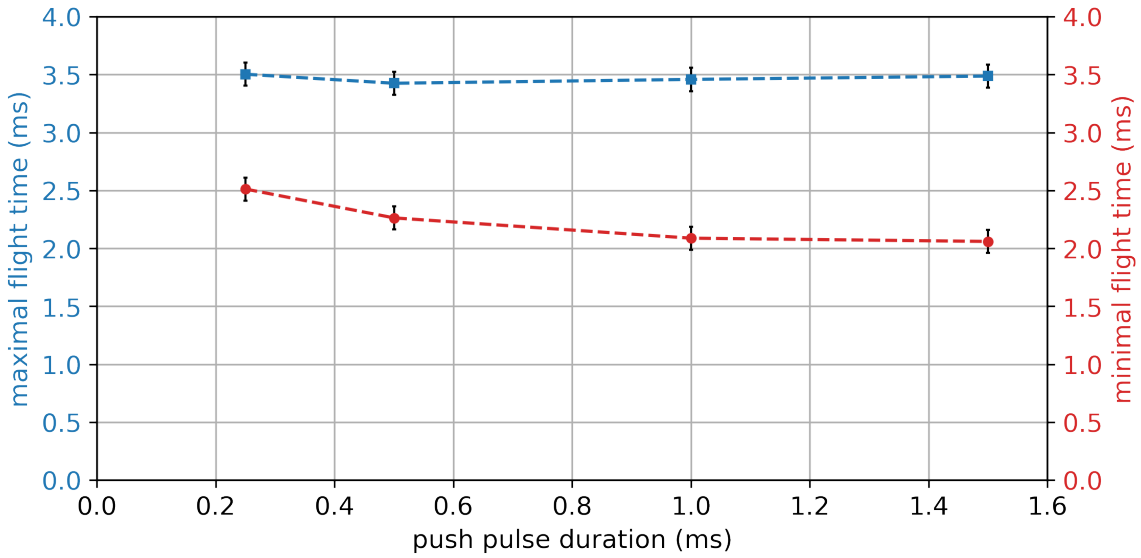

Figure 4.16: Minimal and maximal flight time for the TOF spectra in Figure 4.14 in dependence of the push pulse duration. The minimum time of flight decreases with increasing pulse duration, indicating that the maximum atomic velocity rises a longer acceleration time. In contrast, the maximum flight time remains approximately constant.

First, the depletion of atoms in the MOT reservoir during extended push pulses, and second, the truncation of the time-of-flight spectra discussed above.

To gain further insight we extracted axial velocity distributions for different push pulse durations using the frequency spectra at different flight times, as explained in Section 4.2.3. Figure 4.18 shows that the entire velocity distribution extends toward higher velocities with increasing pulse length, consistent with a longer acceleration. Nevertheless, the upper velocity limit appears to saturate around 110 m/s, while the lower bound remains largely unaffected by the pulse duration.

Based on these results, a push pulse duration of 1.5 ms was selected for subsequent measurements. This duration provides an optimal compromise between maximizing the signal-to-noise ratio and avoiding truncation of the TOF spectrum.

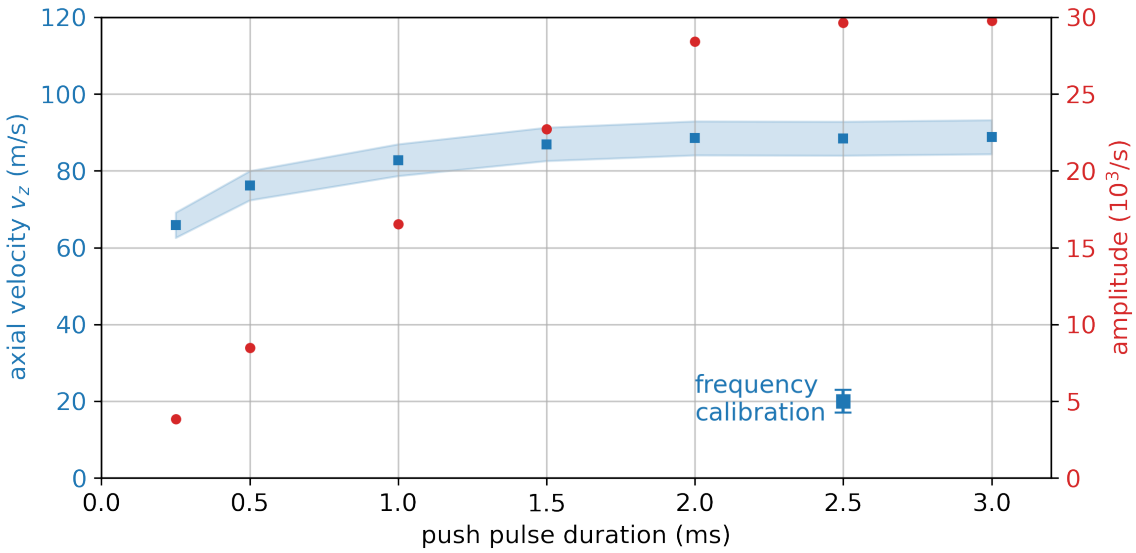

Figure 4.17: Mean axial velocities and amplitudes for different push pulse durations obtained from Doppler shift measurements. The blue band indicates the relative systematic uncertainty due to the angular uncertainty of the spectroscopy beam, while the absolute frequency calibration uncertainty is illustrated in the lower-right corner. Both the amplitude and the mean axial velocity increase with longer push pulse durations, until approaching saturation.

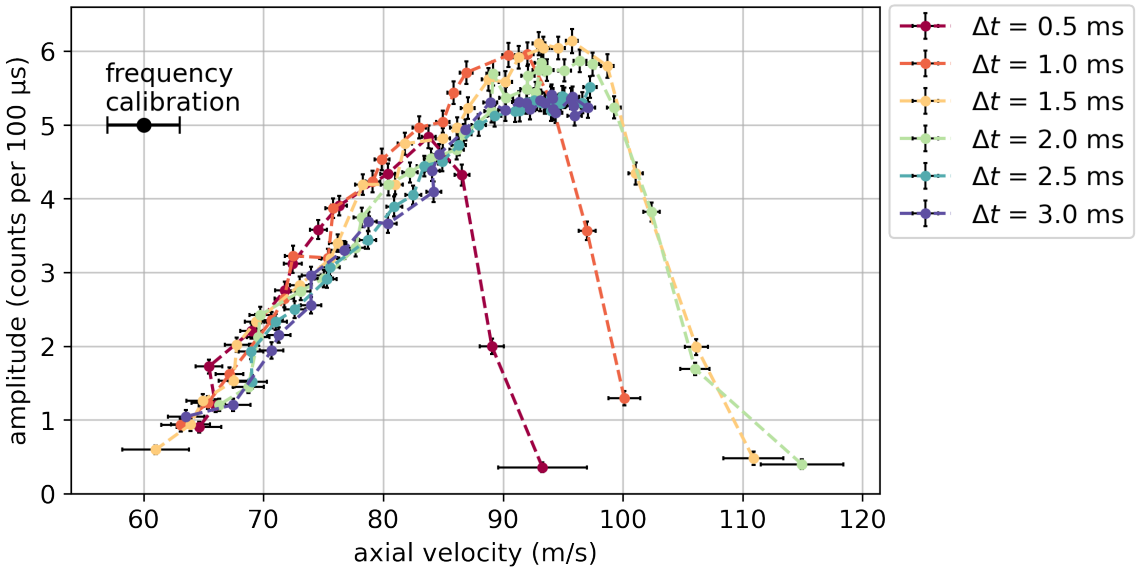

Figure 4.18: Axial velocity distributions for different push pulse durations Δt. The correlated systematic frequency error is indicated in the upper-right corner. The relative systematic error of 5 % due to the angle measurement (see Figure 4.13) is left out for a better visibility. Longer push pulses extend the distribution toward higher velocities but show saturation at approximate 110 m/s. The lower velocity bound remains nearly constant across all pulse durations.

4.3.2 Dependence on Push Pulse Power

In the following, we investigate the influence of the push beam power on the time-of-flight (TOF) spectra of the cold atomic beam. Figure 4.19 shows the TOF spectra for various push beam powers P, each including approximately 40 % repump frequency component. The push beam has a radius of 0.8 mm at the position of the MOT. For a Power of 1 mW this would correspond to a maximum intensity of approximately 100 mW/cm^2.

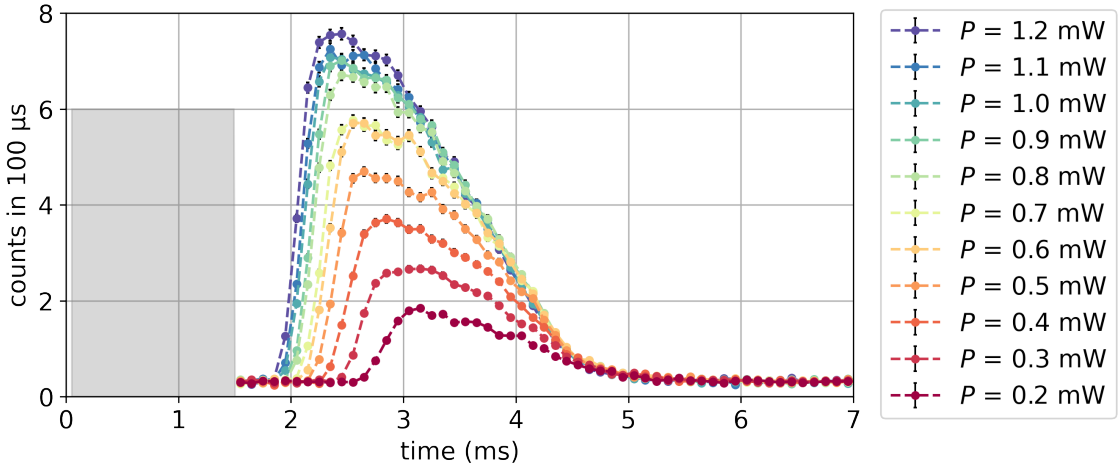

Figure 4.19: Time-of-flight spectra of the cold atomic beam for different push beam powers P. The gray shaded area at the beginning of each trace indicates the 1.5 ms-long push pulse. The push beam detuning is $\sim 7\,\Gamma$. Each trace represents an average over 100 measurements, and data points are connected by linear interpolation. With increasing push beam power, the signal amplitude rises, and the distribution shifts toward shorter flight times.

As expected, the total number of detected atoms increases with push beam power, while the overall line shape remains nearly constant. The full width at half maximum (FWHM) stays around 1.7 ms for all powers, as shown in Figure 4.20.

The minimum time of flight decreases with increasing push power, indicating that the maximum atomic velocity rises due to enhanced photon scattering and power broadening, allowing atoms to remain in resonance for longer. In contrast, the maximum flight time remains approximately constant, suggesting that the slowest atoms are largely unaffected by changes in push beam intensity (see Figure E.12). This is compatible with the interpretation that the slowest atoms are those which are accelerated shortly before the push beam is switched off.

Following the same approach as described earlier, we determine the mean axial velocity of the atomic beam from angled Doppler shift measurements. Figure 4.21 shows the resulting mean velocities and signal amplitudes in dependence of the push beam power.

The signal amplitude rises with increasing push beam power and begins to saturate around 0.8 mW, corresponding to an intensity of approximately 80 mW/cm^2 (maximum intensity). For powers above 1 mW, the measured amplitudes show increased scatter beyond the expected statistical uncertainty of the Voigt fits. This

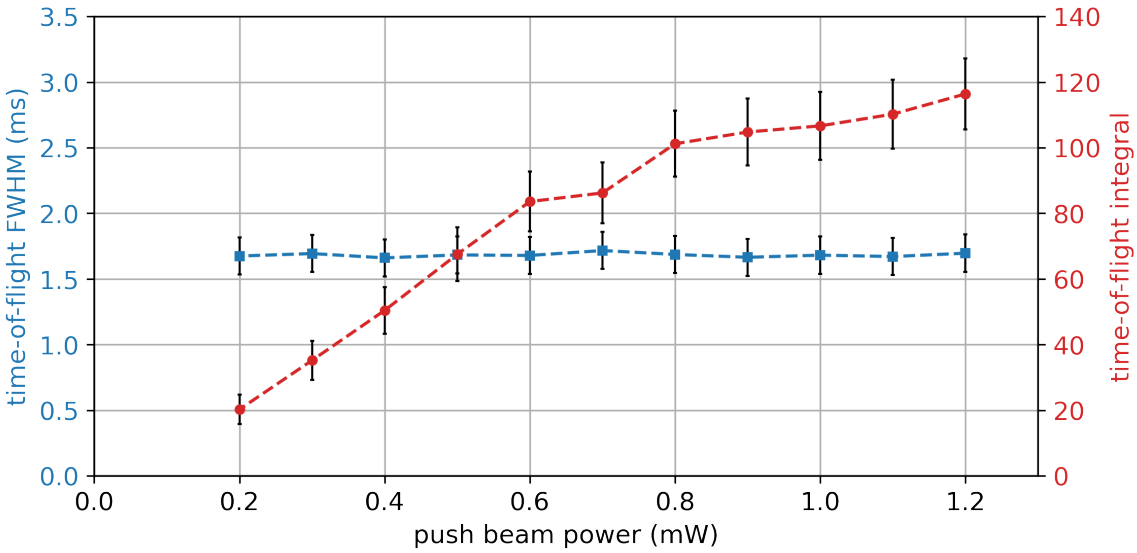

Figure 4.20: Integral and full width at half maximum (FWHM) of the TOF spectra in Figure 4.19 in dependence of the push beam power. The total number of detected atoms increases with push beam power, while the FWHM stays around 1.7 ms for all powers. The data points are connected to guide the eye.

may be attributed to instabilities of the custom-built laser system, which was operated close to its maximum output power.

The mean axial velocity exhibits a similar trend, increasing with power and beginning to flatten around 0.4 mW, corresponding to an intensity of maximum 40 mW/cm^2. A similar saturation behavior has been observed by Tiecke *et al.* [2] (see Figure 1.7) although the absolute velocities reported there are approximately 40 m/s lower than in this work. This can be mostly explained by a different push beam detuning, which we will discuss in the following section.

As described above, we can extract the temporal evolution of the Voigt fits and convert the corresponding frequency shifts into axial velocities to obtain a velocity distribution. Figure 4.22 shows the resulting axial velocity distributions for different push beam powers.

We observe that increasing the push beam power leads to a noticeable extension of the velocity distribution toward higher velocities, while the lower velocity limit remains essentially unchanged within the statistical uncertainty. This indicates that saturation broadening contributes to a widening of the overall velocity spread. For instance, at a push beam power of $P = 1.2\,\mathrm{mW}$ ($I_{\mathrm{max}} \approx 120\,\mathrm{mW/cm^2}$), the power broadening can reach approximately 30 MHz, corresponding to a velocity broadening of about 20 m/s. This is also consistent with the measurements from Tiecke *et al.* [2] who reported a FWHM of 11 m/s for an intensity of 37 mW/cm^2.

The custom-built diode laser system exhibits power fluctuations at higher output powers, as also visible in Figure 4.21. For the following measurements, the system was stable up to powers of 1 mW. Consequently, we fixed the push beam power at 1 mW, which still provided a strong and stable signal.

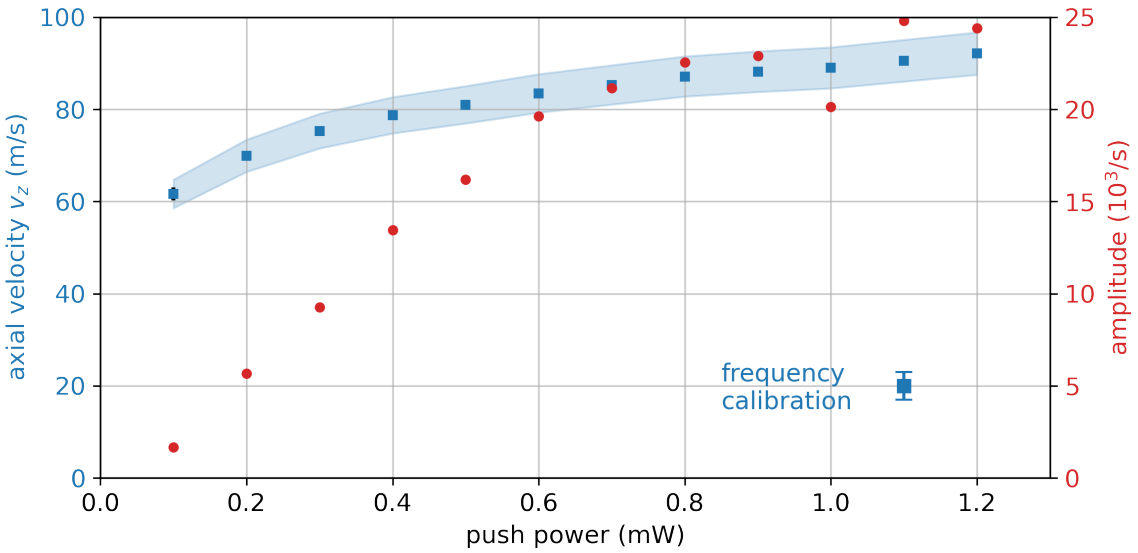

Figure 4.21: Mean axial velocities and amplitudes for different push beam powers obtained from Doppler shift measurements. The blue band indicates the relative systematic uncertainty arising from the angular alignment of the spectroscopy beam, while the absolute frequency calibration uncertainty is shown in the lower-right corner. Both the amplitude and the mean axial velocity increase with push beam power, eventually approaching saturation.

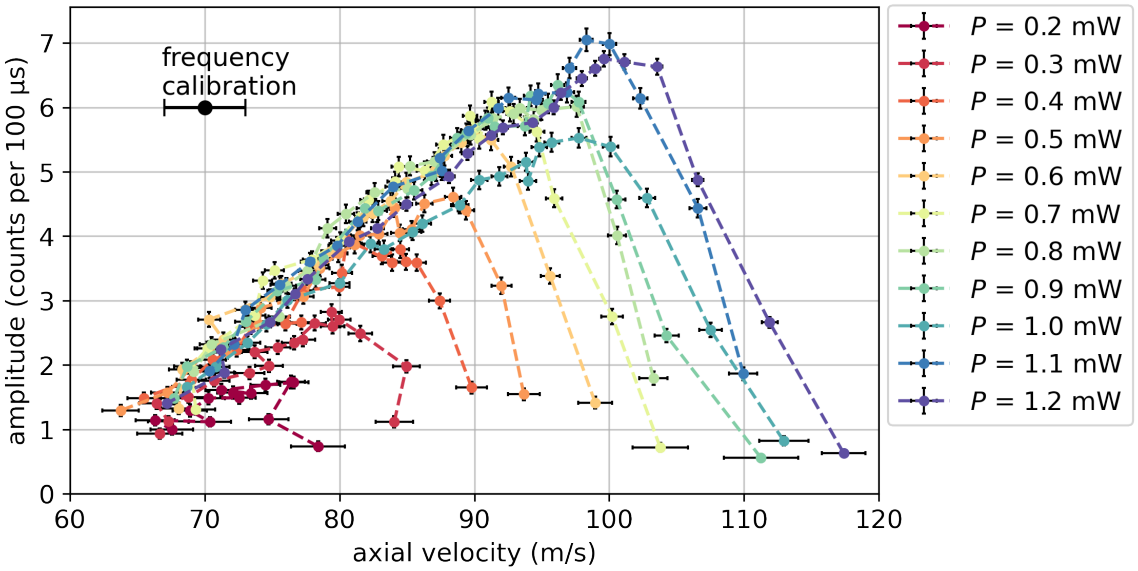

Figure 4.22: Axial velocity distributions for different push beam powers P. The correlated systematic frequency uncertainty is indicated in the upper-left corner. For clarity, the relative systematic uncertainty of 5 % arising from the angle measurement (see Figure 4.13) is omitted here. With increasing push beam power, the distributions extend toward higher velocities, while the lower velocity bound remains nearly constant within the statistical uncertainties across all powers.

4.3.3 Dependence on Push Pulse Detuning

In the following we investigate the influence of the push beam detuning on the time-of-flight (TOF) spectra. Figure 4.23 shows the TOF spectra of the cold atomic beam for different push beam detunings δ.

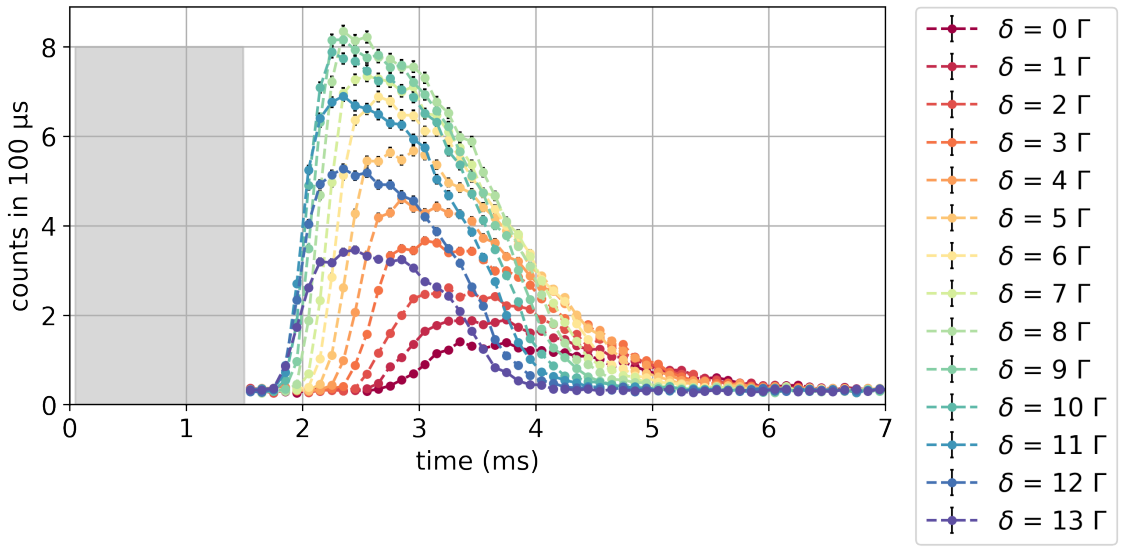

Figure 4.23: Time-of-flight spectra of the cold atomic beam for different push beam detunings δ. The gray shaded area at the beginning of each trace indicates the 1.5 ms-long push pulse. The push beam power is approximately 1 mW including a 40 % repump frequency component. Each trace represents an average over 100 measurements, and data points are connected by linear interpolation. The amplitude of the TOF spectra shows a maximum around a detuning of approximately 8 Γ. With increasing detuning, the TOF spectrum shifts toward shorter flight times.

The amplitude of the TOF spectra exhibits a clear maximum around a detuning of approximately 8 Γ, while the full width at half maximum (FWHM) decreases for larger (more blue detuned) push beam frequencies until approaching a value of approximately 1.5 ms, as shown in Figure 4.24.

With increasing detuning, the TOF spectra shift toward shorter flight times, indicating that the atoms are accelerated to higher velocities. This behavior is also visible in the dependence of the minimal and maximal flight times on the push beam detuning presented in Figure 4.25.

Following the same procedure described earlier, we determined the mean axial velocity of the cold atomic beam from angled Doppler shift measurements. Figure 4.26 shows the resulting mean velocities and corresponding signal amplitudes as a function of push beam detuning.

The amplitude shows a maximum around 9 Γ push beam detuning. The mean velocity increases nearly linearly with the push beam detuning, which is consistent with the expectation that atoms remain in resonance for higher velocities and thus experience a longer acceleration. From the observed slope, we find an increase of

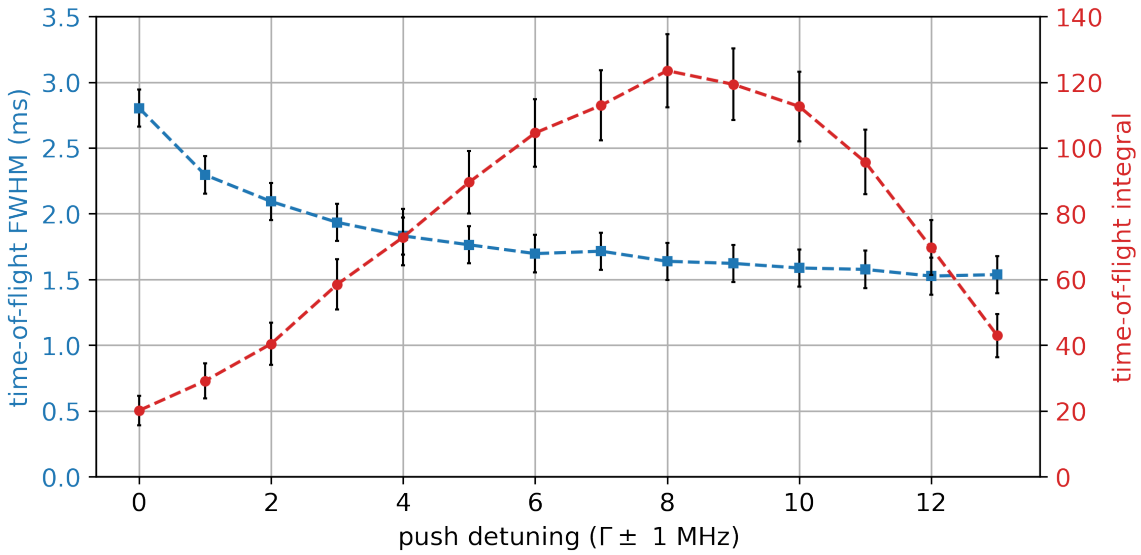

Figure 4.24: Integral and full width at half maximum (FWHM) of the TOF spectra in Figure 4.23 in dependence of the push beam detuning. The integral of the TOF spectra shows a maximum around 8 Γ detuning while the FWHM seems to decrease with a more blue detuned push beam. The data points are connected to guide the eye.

approximately 40 m/s between 0 Γ and 10 Γ detuning, which agrees well with the relation expected from the first-order Doppler shift,

$$\frac{v_z}{\delta} = \frac{c}{f_{\mathrm{Li6,D2}}} \approx \frac{4\,\mathrm{m/s}}{\Gamma}, \tag{4.4}$$

where $f_{\mathrm{Li6,D2}}$ is the transition frequency of the ^{6}Li D_2 line.

The increase in count rate for detunings up to approximately 9 Γ suggests a reduction of the geometrical cut-off effect for faster atoms. At higher velocities, atoms have less time to spread radially and hit the aperture of the collimation system.

The axial velocity of approximately 60 m/s for zero push beam detuning indicates that atoms can be accelerated out of resonance by several natural linewidths. A velocity of 60 m/s corresponds to a detuning of roughly 15 Γ. This explains why the detected count rate only begins to decrease and the velocity approaches saturation at detunings larger than about 10 Γ, as the atoms start to fall out of resonance.

Assuming a saturation-broadened linewidth of roughly 27 MHz, even atoms detuned by up to 10 Γ (corresponding to velocities of about 90 m/s) still experience scattering rates on the order of 10^5 /s, sufficient to maintain acceleration.

In contrast, Tiecke *et al.* [2] used a red detuned push beam (−3.5 Γ). Their optimization strategy focused on maximizing the recapture efficiency into a 3D MOT, which has a capture velocity of approximately 45 m/s. If we extrapolate our measured velocity–detuning dependence to this detuning, we obtain a value that is close to their reported capture velocity.

As described previously, the axial velocity distribution of the atomic beam can be extracted from the Doppler broadening of the spectral profiles. Figure 4.27 shows the resulting velocity distributions for different push beam detunings. A clear shift of

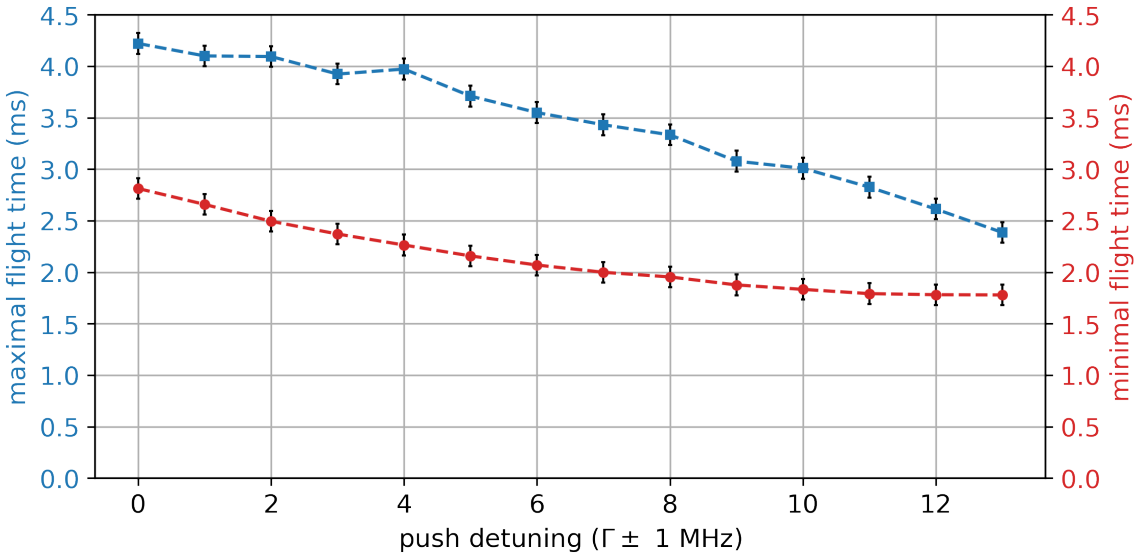

Figure 4.25: Minimal and maximal flight time for the TOF spectra in Figure 4.23 in dependence of the push beam detuning. The minimal and maximal flight times decrease with an increases detuning.

the distributions toward higher velocities is observed with increasing detuning, while the full width at half maximum (FWHM) remains nearly constant at approximately 25 m/s. This behavior is qualitatively consistent with the observations from the time-of-flight spectra. For a constant velocity spread, one expects the temporal spread of the TOF signal to decrease as the mean velocity increases. These findings indicate that the overall velocity spread of the cold atomic beam is largely independent of the push beam detuning, even though the mean velocity increases.

In the subsequent measurements, a push beam detuning of approximately $7\,\Gamma$ was used. This value represents an optimal compromise: it lies close to the detuning that yields the maximum count rate, yet corresponds to comparatively lower atomic velocities, which are of particular interest for high-precision spectroscopy.

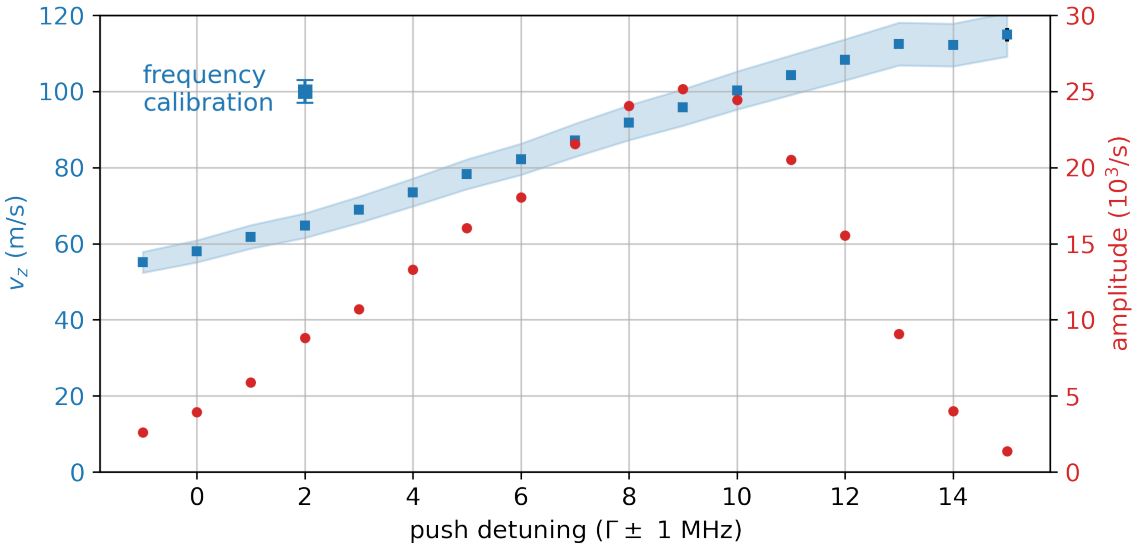

Figure 4.26: Mean axial velocities and amplitudes for different push beam detunings obtained from Doppler shift measurements. The blue band indicates the relative systematic uncertainty due to the angular calibration of the spectroscopy beam, while the absolute frequency calibration uncertainty is illustrated in the upper-left corner. The amplitude exhibits a maximum near 9 Γ, and the mean velocity increases approximately linearly with detuning.

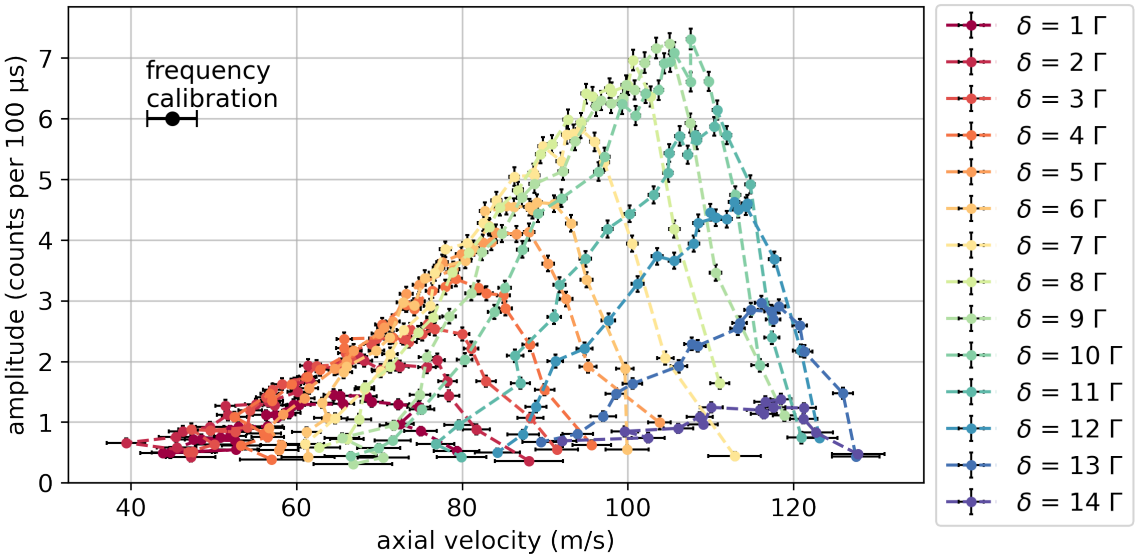

Figure 4.27: Axial velocity distributions for different push beam detunings δ. The correlated systematic frequency uncertainty is indicated in the upper-right corner. For clarity, the relative systematic error of 5 % arising from the angle measurement (see Figure 4.13) is omitted here. With increasing detuning, the distributions shift toward higher velocities, while their widths remain approximately constant.

4.3.4 Discussion of the Push Beam Dependence

We have demonstrated that the mean axial velocity of the cold atomic beam can be tuned over the range 60 m/s to 120 m/s by adjusting the push beam power and detuning. Furthermore, the velocity spread can be controlled between approximately 10 m/s to 35 m/s (FWHM) by varying the push beam power and the pulse duration.

The maximum fluorescence signal was obtained for a push beam detuning of 9 Γ at a power of typically 1 mW, corresponding to a mean axial velocity of about 90 m/s.

Throughout the measurements, it was found that a circularly polarized push beam containing a repump frequency component of approximately 30 % yields the highest fluorescence count rates and, consequently, the best signal-to-noise ratio. For comparison, the same analysis was repeated using a circularly polarized push beam without a repump frequency component, and a linearly polarized push beam with an additional repump beam.

In the absence of a repump frequency, the detected count rate decreased by approximately a factor of five compared to the configuration including a repump component. Within the range of 10 % to 50 % repump power fraction, the count rate showed no significant dependence on the exact ratio.

Measurements with a linearly polarized push beam yielded approximately half the count rate obtained with circular polarization. This could be explained by a difference in the transition strengths (see Ref. [23]). For the linear polarization schemes, the push beam detuning with the maximum count rate was found to be around 7 Γ, which is about 2 Γ lower than for a circular push beam.

We also investigated the influence of the push beam diameter on both the axial and transverse velocity distributions. Decreasing the beam diameter enhanced the integrated signal, which can be attributed primarily to the higher push beam intensity at the MOT center. Within the experimental uncertainty, no significant change in the transverse velocity distribution was observed. This insensitivity may be explained by the geometrical cutoff imposed by the final apertures, which limits the detectable transverse velocity range, as discussed in the following.

To get a deeper understanding of the acceleration by the push beam and the pumping processes it would be helpful to extend the simulation of the 2D MOT [72] with a push sequence. For future measurements the data acquisition could be improved by employing a microcontroller with a higher clock frequency, which would allow for finer time binning and thereby improve the accuracy of the time-resolved fluorescence spectra.

4.4 Discussion on the Cold Lithium Beam

We have shown that both the mean axial velocity and the velocity distribution of the cold atomic beam can be controlled through the push beam parameters. For high-precision spectroscopy, a slow atomic beam with a narrow velocity spread is, in principle, advantageous, as it minimizes residual Doppler shifts, one of the dominant sources of systematic uncertainty. However, reducing the velocity and narrowing the distribution inevitably leads to a lower atomic flux in the spectroscopy region. Thus, an optimization must balance two competing aspects: the signal-to-noise ratio, which determines the statistical uncertainty, and the residual Doppler shift, which contributes to the systematic uncertainties. A quantitative evaluation of this trade-off will have to be performed for the final spectroscopy setup.

For the optimized settings used here, the system produces approximately 300 counts on the PMT per push pulse. With a pulse duration of 1.5 ms and a MOT reloading time of roughly 2.5 ms, a repetition rate of about 250 Hz is achievable.

By combining these results with the estimated trap population, on the order of 2×10^5 to 4×10^5 atoms (see Section 3.5), we can obtain a total cold atomic flux of approximately 1×10^8/s. While this value is an order of magnitude lower than the maximum output flux of $\sim 3 \times 10^9$/s reported by Tiecke *et al.* [2] at a temperature of 700 K (430 °C), it compares more favorably to their typical recapture rate of $(1.8 \pm 0.6) \times 10^8$/s achieved at 623 K (350 °C). Given that Tiecke *et al.* demonstrated a recapture fraction of $\sim 30\,\%$, the current discrepancy suggests potential for further optimization of the present setup. A primary candidate for improvement is the correction of the interchanged polarization configuration of the two lower MOT beams, as discussed in Appendix A.

In comparison to the setup reported by Tiecke *et al.* [2], our experiment includes a repump component in the push beam. While they employed a red detuned push beam with a detuning of $-3.5\,\Gamma$, we find optimal operation for blue detunings in the range of $+7$ to $+9\,\Gamma$.

The inclusion of a repump frequency in the push beam allows atoms to remain in the cycling transition over a longer interaction length, resulting in significantly higher detected count rates. At the same time, this configuration leads to larger axial velocities, since atoms can be continuously accelerated beyond the MOT region. In contrast, in the setup of Tiecke *et al.*, acceleration was effectively limited to the MOT volume, where repumping light was present only.

For the experiments like reported by Tiecke *et al.*, the primary goal was the efficient loading of a three-dimensional MOT, which had a capture velocity of approximately 45 m/s. In this context, lower axial velocities were advantageous, motivating the use of a red detuned push beam.

By contrast, for applications prioritizing high atomic flux rather than low longitudinal velocity, larger blue detunings can be beneficial. Indeed, blue detuned push beams with detunings of up to $+5\,\Gamma$ have also been reported in the literature, for example in Ref. [84].

Due to the geometry of our setup, only atoms that pass through the final collimation aperture can reach the detection region. Atoms with a transverse velocity v_t will deviate from the beam axis during their flight time $t = z/v_z$, leading to a transverse

displacement $r = v_t \cdot t$. The maximum admissible transverse velocity $\hat{v}_t$ that still allows transmission through the aperture of radius r_{aperture} is thus given by

$$\hat{v}_t = \frac{r_{\text{aperture}}}{z} v_z. \tag{4.5}$$

This means that the geometrical cutoff in transverse velocity depends linearly on the axial velocity v_z. Consequently, faster atoms have a larger acceptance cone and are more likely to pass through the final aperture. Therefore, the optimal velocity and detuning largely depends on the geometry of the setup.

The observed increase in detected count rate with higher axial velocity therefore implies that the initial transverse velocity distribution extends beyond this geometrical limit for lower velocities.

For instance, given an axial velocity of $v_z = 90\,\text{m/s}$ (corresponding to the highest observed count rates) and a flight distance of $z = 19\,\text{cm}$, an aperture radius of $r_{\text{aperture}} = 2.5\,\text{mm}$ imposes a cutoff transverse velocity of approximately $\hat{v}_t = 1.2\,\text{m/s}$. This is comparable to the transverse velocity distribution observed in the hot atomic beam experiments of Sansonetti *et al.* [55]. This would correspond, to a transverse beam temperature of:

$$T_t \approx \frac{m_{\text{Li6}} \hat{v}_t^2}{2k_B} \approx 0.5\,\text{mK}. \tag{4.6}$$

In comparison, Tiecke *et al.* estimated a transverse temperature of $T_t = 1.4\,\text{mK}$ for the 2D MOT. This suggests that the transmitted flux in the current setup is limited by the geometric constraints of the aperture. Consequently, the usable flux could be increased by enlarging the aperture diameter, but at the expense of increased Doppler broadening.

5 Conclusion, Discussion and Outlook

We have demonstrated that the cold ^{6}Li atomic beam produced by our two-dimensional magneto-optical trap (2D MOT) is a viable source for high-precision spectroscopy. By optimizing the cooling and extraction parameters, we achieved a cold beam flux on the order of 1×10^8/s. This results in fluorescence count rates in the order of 1×10^3/s, comparable to those obtained in hot beam experiments [55], while operating at significantly lower mean axial velocities between 60 m/s and 120 m/s and with a substantially reduced velocity spread ranging from 10 m/s to 35 m/s (FWHM). Achieving this performance required a systematic optimization of the 2D MOT and a detailed characterization of both the trapped atom cloud and the extracted cold atomic beam.

The optimization of the 2D MOT was presented in Chapter 3. Key parameters influencing the areal atomic density, including MOT beam detunings, power ratios, beam waists, and oven temperature, were optimized by measuring absorption profiles of the cold atomic cloud (see Section 3.4). We found that not only the atomic density, but also the spatial position of the MOT cloud depends on the laser detuning (see Section 3.4.6). This observation demonstrates that, for a given experimental geometry, no universal optimum detuning exists. Consistent with this finding, numerical simulations of the 2D MOT indicate that the optimal parameters also depend on the magnetic field configuration (see Ref. [72]).

A detailed characterization of the magnetic field revealed an offset relative to the geometric center of the setup (see Section 3.2). This horizontal offset is also apparent in the measured MOT density profiles (see Section 3.4.4).

Measurements and simulations of the hot atomic beam source were used to calibrate the lithium oven temperature and to estimate the trappable atomic flux (see Section 3.1). Combining this flux estimate with the measured loading time yielded an expected steady-state atom number of approximately 5×10^6 in the MOT (see Section 3.3).

By numerically integrating the measured absorption profiles, we obtained an experimental estimate of the total atom number in the range of 2×10^5 to 4×10^5, which is approximately one order of magnitude lower than the value inferred from the trappable flux and loading time analysis. This discrepancy may indicate either an overestimation of the atomic flux or oven temperature, or a lower effective trapping efficiency of the MOT under experimental conditions.

The push beam extraction process was characterized in detail in Chapter 4. We established a pulsed push beam detection scheme that allows to measure time-resolved spectra with low background count rates. Via Doppler shift measurements we found that both the mean axial velocity and the velocity distribution of the cold atomic beam depend strongly on the push beam detuning, power, and pulse duration.

The mean axial velocity can be tuned over the range 60 m/s to 120 m/s, while the velocity spread (FWHM) can be controlled between 10 m/s to 35 m/s. Due to trans-

verse cooling in the 2D MOT and subsequent geometric collimation, the transverse velocity can be limited to below 1.2 m/s.

Additionally, the push beam can be used to optically pump atoms into specific hyperfine ground states (see Section 5.1.3), enabling state preparation for subsequent spectroscopy. In principle, the pulsed push beam detection scheme can be used for velocity-selective detection. However, a shorter pulse duration would be advantageous to increase the velocity resolution. While a continuous push beam could increase the total atomic flux, it would require significantly improved shielding against stray light leading to increased background count rates (see Section 4.1.3).

Further improvements are currently under investigation. In particular, reducing the MOT beam detuning may lead to lower atomic temperatures and thereby reduce geometric losses due to decreased transverse velocities. However, this approach comes at the expense of a reduced capture velocity and, consequently, a potentially smaller number of trapped atoms. Identifying the optimal compromise between these competing effects requires further systematic study. The associated uncertainties and the reproducibility of the relevant experimental parameters are analyzed in detail in Appendix B.

Under current conditions, we obtain fluorescence count rates on the ^{6}Li D_2 line on the order of 4×10^3/s on the peak with a spectroscopy beam power of 5 µW, comparable to results from hot atom beam experiments [55]. in the following, we present preliminary fluorescence measurements and demonstrate that our current fit model yields a line center uncertainty on the order of 10 kHz.

5.1 Toward High-Precision Spectroscopy

Although the AFR system (see Section 1.2.3) is not yet operational, we performed a series of preliminary measurements to identify the dominant systematic effects and to assess the requirements for future high-precision spectroscopy.

Here we use a $+9\,\Gamma$ blue detuned circularly polarized push beam with a power of 1 mW including a repump component to maximize the count rate as we previously optimized (see Section 4.3). A low power spectroscopy beam (5 µW), without an additional repump component, was used to probe the resonances associated with the two hyperfine ground states of the D_2 line. The spectra were recorded with a polarization angle of $(50 \pm 10)°$, close to the magic angle of approximately 55°, which minimizes quantum interference effects (see Section 5.1.1). Apart from that the experimental settings are as stated in Table E.1.

The time-resolved spectra were cut after 5.5 ms, and each data point represents an average over 100 push pulses. One scan takes approximately 3 minutes. Each spectrum was fitted with a sum of Voigt profiles, where the hyperfine splitting was fixed to the literature values [1] (assuming no Zeeman shift), the Doppler broadening parameter σ was fixed to 1.8 MHz (corresponding to the calculated upper limit from geometrical cut off), and the amplitude ratios were optimized to minimize the reduced chi squared.

The population distribution between the two ground states can be controlled via the push beam parameters: tuning the push beam close to the upper ground state transition depleted that state, thereby enhancing the signal on the lower ground

state transition, whereas adding a repump component increased the upper state population again.

Figure 5.1 shows an example spectrum recorded on the lower hyperfine ground state D_2 transition. The spectrum is fitted with a sum of two Voigt profiles, the resulting fit parameters are summarized in Table 5.1.

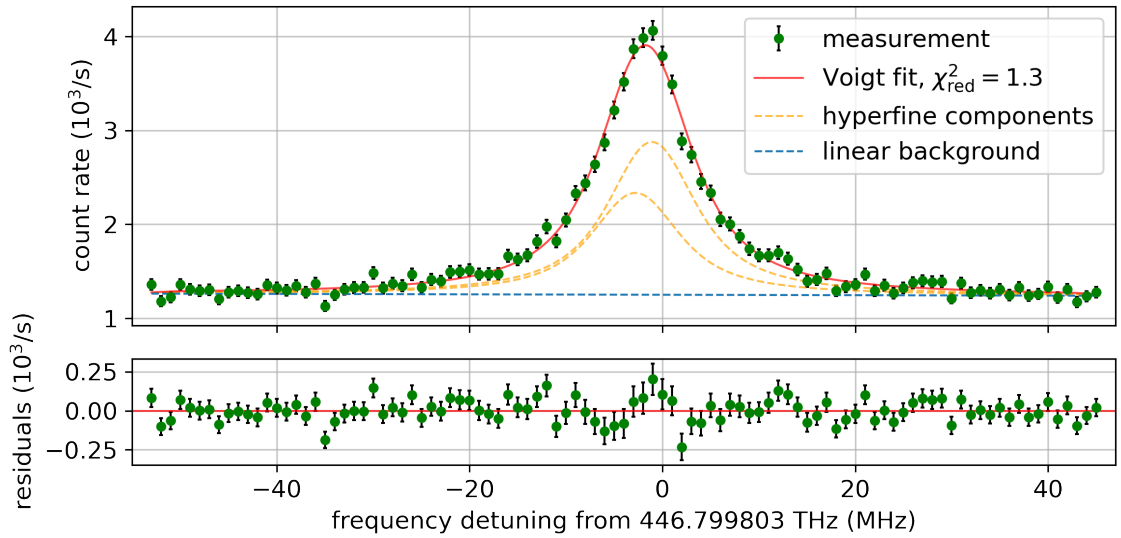

Figure 5.1: Spectrum recorded on the lower hyperfine ground state D_2 transition using a spectroscopy beam power of 5 µW and a polarization angle of $(50 \pm 10)°$. Each data point represents an average over 100 push pulses. The data is fitted with a sum of two Voigt profiles (dashed orange line) with a fixed hyperfine splitting and Doppler broadening. The fit parameters are shown in Table 5.1.

Table 5.1: Fit parameters for the lower hyperfine ground state transition (Figure 5.1). The fit uses a sum of two Voigt profiles with fixed hyperfine splitting, Doppler broadening, and optimized amplitude ratios.

fit parameter	**value**
lorentzian linewidth γ	(9.3 ± 0.3) MHz
amplitude a	$(2.71 \pm 0.04)\, 10^3$/s
frequency offset δ_0	(-1.14 ± 0.08) MHz
background b	(1249 ± 9)/s

The residuals indicate systematic deviations from the fitted line shape, particularly near the peak. This suggests that the simple Voigt model does not fully capture the experimental line shape. A plausible explanation is a residual magnetic field in the spectroscopy region, which would induce Zeeman splitting of the transitions (see Section 5.1.3) and residual line distortion due to quantum interference (see Section 5.1.1).

The high frequency component corresponding to the ($F = \frac{1}{2} \rightarrow F' = \frac{1}{2}$) transition is found at

$$\nu_{1/2\rightarrow 1/2} = (446\,799\,801.9 \pm 0.1\,(\text{stat}) \pm 1\,(\text{sys}))\,\text{MHz}.$$

After correcting for the residual Doppler shift arising from a slight misalignment of the spectroscopy beam ($\sim 0.5°$) with respect to the atomic beam axis[1], this value agrees with the measurement reported by Brown *et al.* [1] within our present uncertainty.

Figure 5.2 shows a spectrum recorded on the upper hyperfine ground state transition under comparable experimental conditions. Here, the spectrum is fitted with a sum of three Voigt profiles, again with fixed hyperfine splitting and Doppler broadening. The corresponding fit parameters are listed in Table 5.2.

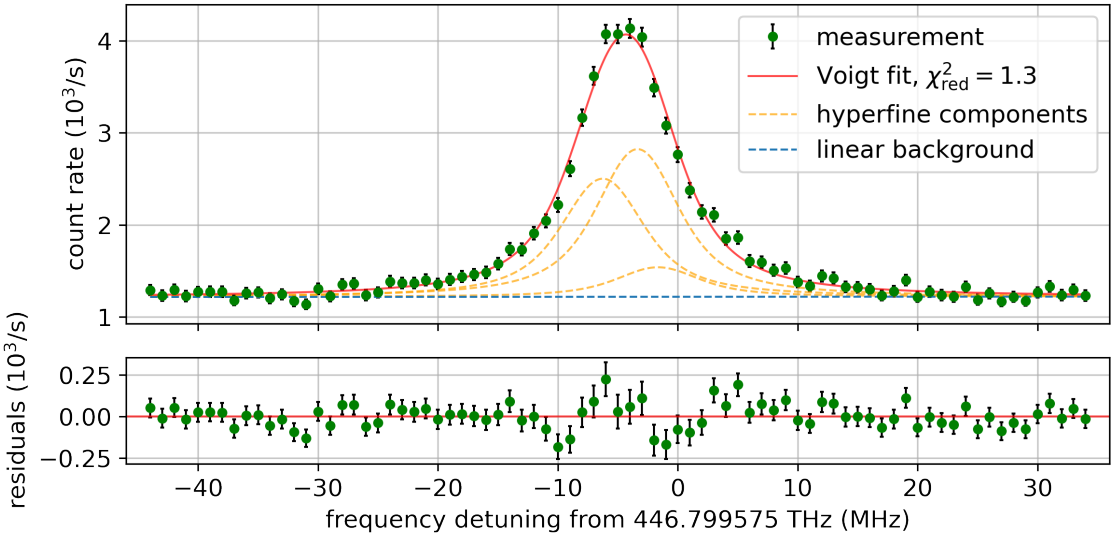

Figure 5.2: Spectrum recorded on the upper hyperfine ground state D_2 transition using a spectroscopy beam power of 5 µW and a polarization angle of $(50 \pm 10)°$. The data is fitted with a sum of three Voigt profiles (dashed orange line) with fixed hyperfine splitting and Doppler broadening. The fit parameters are shown in Table 5.2.

Table 5.2: Fit parameters for the upper hyperfine ground state transition (Figure 5.2). The fit uses a sum of three Voigt profiles with fixed hyperfine splitting, Doppler broadening, and optimized amplitude ratios.

fit parameter	**value**
lorentzian linewidth γ	(6.0 ± 0.2) MHz
amplitude a	$(3.20 \pm 0.06)\,10^3$/s
frequency offset δ_0	(-3.39 ± 0.07) MHz
background b	(1220 ± 9)/s

[1]With the present push beam settings we have a residual Doppler shift of (-1.5 ± 0.1) MHz.

The central component, corresponding to the ($F = \frac{3}{2} \rightarrow F' = \frac{3}{2}$) transition, is found at

$$\nu_{3/2\rightarrow 3/2} = (446\,799\,571.6 \pm 0.1\,(\text{stat}) \pm 1\,(\text{sys}))\,\text{MHz}.$$

After correcting for the residual Doppler shift, this value also agrees with the results of Brown *et al.* [1] within our uncertainty.

Comparing the Lorentzian linewidths of the two spectra, we observe that the lower ground state transition (9.2 MHz) is significantly broader than the upper ground state transition (6.0 MHz). This difference can be attributed to differences in transition strengths and branching ratios between the hyperfine states, as explained in Ref. [89].

At the current level of statistics, we achieve a statistical uncertainty of below 100 kHz on the extracted line center frequencies. To reach sub-10 kHz precision, required for meaningful comparison with state-of-the-art measurements, an improved line shape model accounting for quantum interference and Zeeman effects, longer averaging times, and higher fluorescence count rates will be necessary.

5.1.1 Quantum Interference

Although our current spectroscopy setup is comparatively simple, it is already evident that a model based on a sum of Voigt profiles does not fully describe the measured line shapes. In particular, we resolve systematic effects that can be attributed to quantum interference. Figure 5.3 shows the fitted detuning and amplitude of the Voigt profile for the upper hyperfine ground state transition as a function of the spectroscopy beam polarization angle.

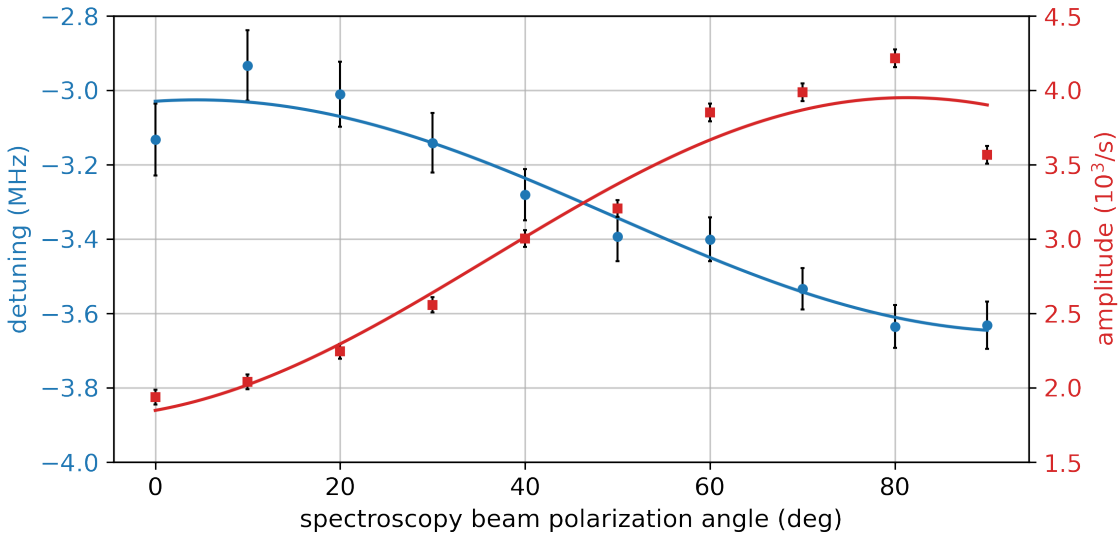

Figure 5.3: Detuning and amplitude of the Voigt fit to the upper ground state transition as a function of the spectroscopy beam polarization angle: Both data sets are fitted with a sinusoidal function. The corresponding fit parameters are shown in Table F.1. The sinusoidal dependence of the detuning is consistent with quantum interference effects [1].

As reported in Ref. [1], the systematic frequency shift due to quantum interference exhibits a sinusoidal dependence on the polarization angle with a period of 180° (see Figure 1.5). In our measurements, the observed shift is also on the order of 1 MHz. A quantitative comparison, however, requires a more complete model that accounts for the finite opening angle of the fluorescence collection optics and a proper description of the residual Zeeman effect.

The fitted amplitude shows a similar sinusoidal dependence on the polarization angle. This behavior is consistent with the angular emission pattern of an electric-dipole transition, which modifies the detected fluorescence intensity depending on the relative orientation between the dipole and the detection axis. The corresponding fit parameters for the sinusoidal dependence are shown in Table F.1.

In addition, we observe a polarization-dependent variation of the fitted background level, as shown in Figure 5.4. This effect may arise from polarization-dependent reflection and transmission at the vacuum windows, further highlighting the advantages of implementing a fully fiber-based spectroscopy system.

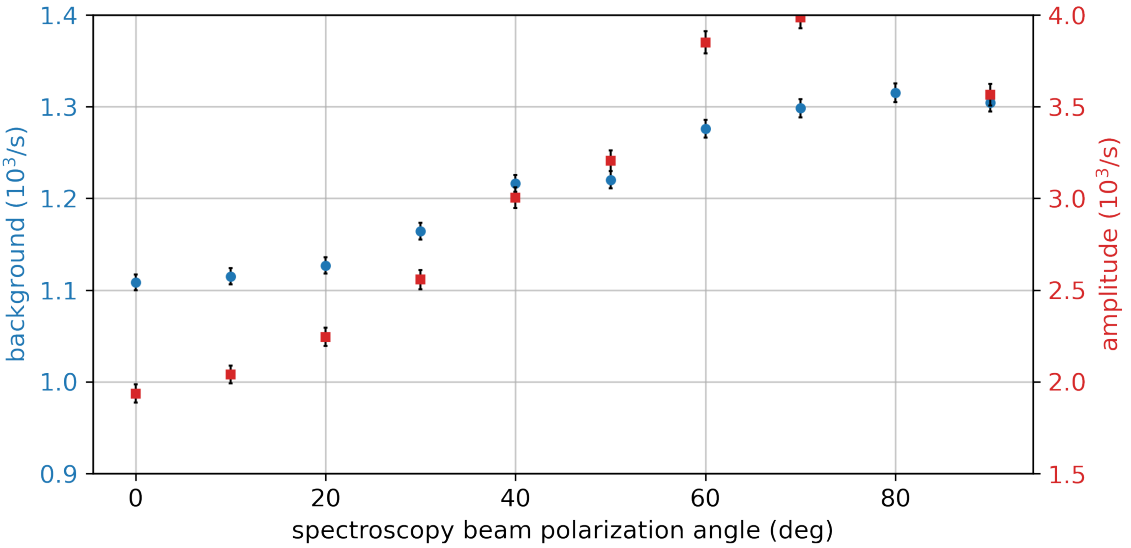

Figure 5.4: Amplitude and background level of the Voigt fit to the upper hyperfine ground state transition as a function of the spectroscopy beam polarization angle.

A complete description of the line shape including quantum interference effects will only be meaningful once all other experimental parameters, such as magnetic fields, beam alignment, and window-induced distortions, are sufficiently controlled.

In future work, it may be advantageous to implement a polarization-switching unit to modulate the spectroscopy beam polarization rapidly. This would enable to a quick differential measurement averaging long term drifts, as described in Ref. [90].

5.1.2 Power Broadening

In addition, we observe a clear power dependence of both the spectral linewidth and the line center frequency. Figure 5.5 shows a spectrum of the lower hyperfine ground state transition recorded with a spectroscopy beam power of 30 µW. This corresponds to a maximum intensity of approximately 0.5 mW/cm^2.

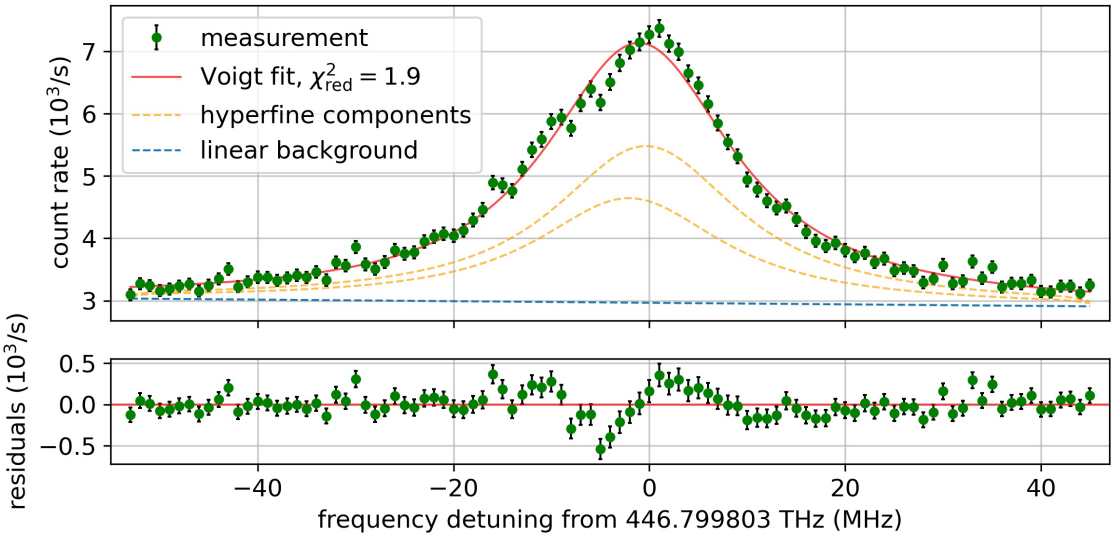

Figure 5.5: Spectrum of the lower hyperfine ground state transition recorded with a spectroscopy beam power of 30 µW. The fitted Lorentzian linewidth of 22 MHz is significantly larger than both the natural linewidth (5.9 MHz) and the linewidth observed at 5 µW (Figure 5.1).

The fitted Lorentzian linewidth of 22 MHz is nearly four times larger than the natural linewidth of the D_2 transition (5.9 MHz) and more than twice as broad as the linewidth observed at 5 µW (9.2 MHz, see Table 5.1). This broadening is also significantly more pronounced than in spectra recorded with an additional repump component (see Figure 4.8).

The observed broadening exceeds the value expected from pure saturation broadening, indicating that additional mechanisms may contribute. One possible explanation is the acceleration of the cold atoms by the spectroscopy beam itself. As atoms scatter multiple photons, they acquire momentum in the direction of beam propagation, which can result in an additional Doppler shift. The stochastic nature of photon scattering can therefore result in an effective broadening of the spectral line.

In addition to the increased linewidth, we observe a systematic shift of the fitted line center toward higher frequencies with increasing spectroscopy beam power. This behavior is consistent with an acceleration of the atoms along the propagation direction of the spectroscopy beam, effectively shifting the resonance condition.

Figure 5.6 shows the power dependence of both the fitted linewidth and the line center detuning after correcting for the residual Doppler contribution due to a non-perpendicular angle between the spectroscopy beam and the cold atomic beam.

These findings underscore the importance of operating at low spectroscopy beam intensities, on the order of a few µW. For future measurements with the AFR system,

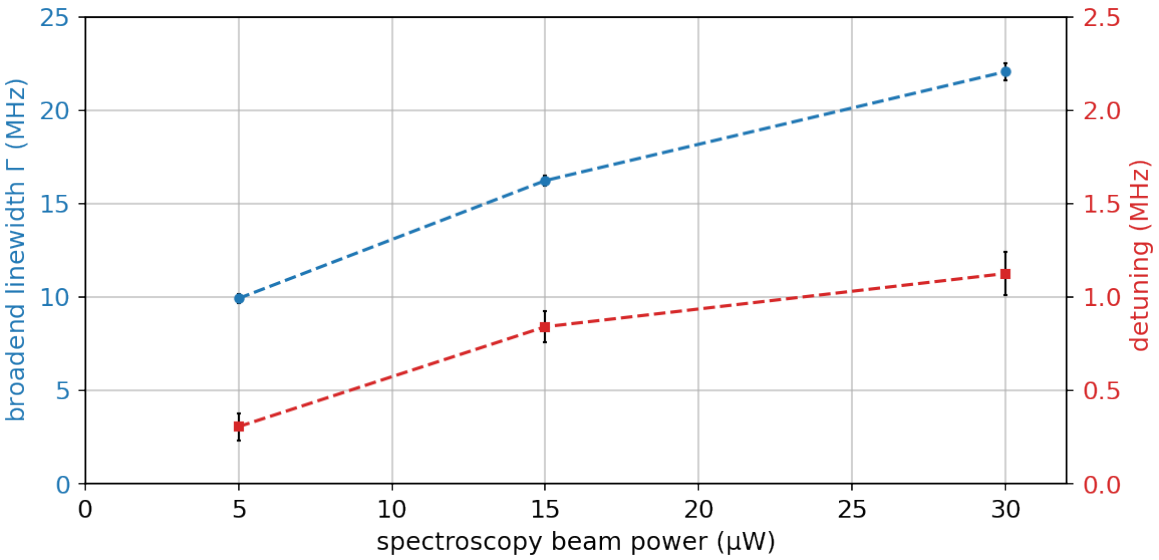

Figure 5.6: Dependence of the fitted Lorentzian linewidth and line center frequency on the spectroscopy beam power. The linewidth increases with power, while the line center exhibits a systematic shift of several hundred kHz over the investigated power range.

a spectroscopy beam with a waist radius of approximately 2.2 mm will be employed, thereby reducing the peak intensity at a given beam power. In addition, the use of a retro-reflected beam can, in principle, mitigate effective line shifts arising from photon recoil.

A detailed investigation of these effects is beyond the scope of the present preliminary study, particularly since their magnitude may change when transitioning to the AFR configuration.

5.1.3 Zeeman Splitting

The residuals observed in the fits presented above (see Figure 5.1 and Figure 5.2) suggest that unresolved Zeeman splitting contributes to the measured line shapes. To qualitatively investigate this effect and see its impact on the extracted transition frequencies, we deliberately introduced an external magnetic field in the spectroscopy region.

A pair of permanent magnets was positioned at a distance of (17 ± 1) cm close to the six-way cross of the spectroscopy region (see Figure F.3), generating a roughly homogeneous magnetic field of (1.1 ± 0.3) mT in the center of the spectroscopy region.

Figure 5.7 shows a spectrum recorded on the upper hyperfine ground state transition in the presence of this magnetic field. The Zeeman splitting is clearly resolved: Each of the three hyperfine components ($F = \frac{3}{2} \rightarrow F' = \frac{1}{2}, \frac{3}{2}, \frac{5}{2}$) splits into multiple Zeeman components corresponding to transitions between different m_F sublevels. Here we only fit the three most prominent transitions. For the 1.1 mT field used here, the Zeeman shifts are on the order of 20 MHz, larger than the residual Doppler broadening and therefore nicely observable in our spectra.

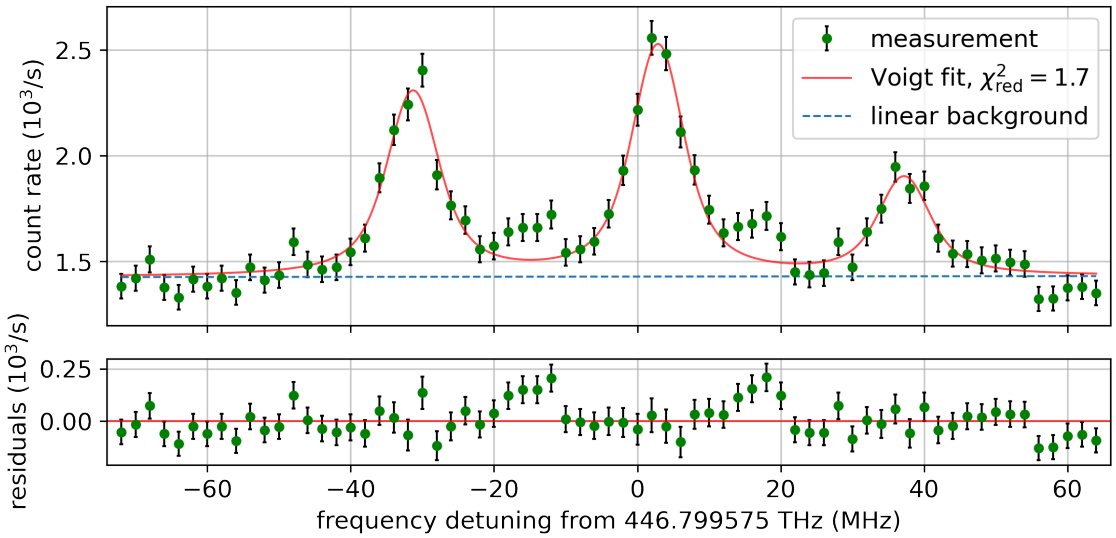

Figure 5.7: Spectrum of the upper hyperfine ground state D_2 transition in the presence of a (1.1 ± 0.3) mT magnetic field oriented at approximately 45° to the linearly polarized spectroscopy beam for a for a left-handed circular polarized push beam. Each hyperfine component is split into multiple Zeeman components. The three most prominent transitions are fitted with a sum of Voigt profiles. The relative amplitudes of the components depend on the spectroscopy beam polarization and the magnetic sublevel population prepared by the push beam.

The relative amplitudes of the Zeeman components vary with the polarization of the push beam (see Figure F.4 for a right-hand circular polarized push beam). This demonstrates that the push beam optically pumps atoms into specific m_F states, thereby preparing a non-thermal magnetic sublevel distribution. By adjusting the push beam polarization, we can selectively enhance or suppress individual Zeeman components, a capability that could be exploited in future experiments.

A quantitative interpretation of these spectra was not attempted, but the observations highlight the need of a good magnetic field suppression for future spectroscopy. First measurements have shown that the magnetic field is expected to be below 0.1 mT, but to have a splitting below 1 kHz we would need to stabilize the magnetic field on the order of 10 nT. To address this systematic effect, we are currently implementing a three-axis magnetic field compensation system consisting of three orthogonal pairs of Helmholtz coils. This system will allow us to compensate for any magnetic field in the spectroscopy region. Moreover, by applying controlled fields of known magnitude and direction, we will be able to systematically study Zeeman shifts and extrapolate to zero magnetic field.

5.2 Outlook

The measurements presented in this thesis demonstrate that our cold ^{6}Li atomic beam provides a promising platform for high-precision spectroscopy. Several technical improvements and systematic studies remain necessary to reach a precision below the current level. In this section, we outline the planned next steps, from near-term technical implementations to long-term applications of the apparatus.

The immediate priority is the installation and commissioning of the active fiber-based retroreflector (AFR) system [73]. Once the improved magnetic field configuration for the 2D MOT [83] has been implemented and characterized, we will integrate the AFR into the spectroscopy setup.

The AFR provides two key advantages over the current free-space spectroscopy beam. First, it ensures retracing wavefronts, suppressing first-order Doppler shifts. This will allow precise characterization of the axial velocity of the cold atomic beam and eliminate one of the dominant systematic uncertainties in the present setup. Second, by coupling both the incoming and retroreflected beams through optical fibers, the AFR system avoids systematic effects arising from reflections and birefringence of any vacuum windows.

The modified geometry will also improve the signal-to-noise ratio in several ways. The PMT will be positioned closer to the spectroscopy region, increasing the solid angle for fluorescence collection by approximately a factor of three. More importantly, background from scattered spectroscopy light should be drastically reduced, as the fiber-coupled AFR is designed to minimize stray light and no additional vacuum windows are required in the beam path. However, the larger distance between the 2D MOT and the spectroscopy region (33 cm instead of approximately 19 cm) will reduce the atomic flux due to geometric divergence. If the signal-to-noise ratio in the florescence count rate remains a limiting factor, we will consider implementing a cooled PMT, which can reduce the dark count rate by more than one order of magnitude.

With an operational AFR system, the focus will shift to systematic characterization and mitigation of the effects identified in this thesis:

- **Magnetic field compensation:** The three-axis Helmholtz coil system currently under development will enable nulling of residual magnetic fields and systematic studies of Zeeman shifts by applying controlled fields and extrapolating to the zero-field limit.

- **Quantum interference:** Measurements as a function of the spectroscopy beam polarization angle will be performed with improved statistics to refine our understanding of quantum interference effects.

- **Power broadening and optical pumping:** The larger beam waist in the AFR setup will reduce intensity-dependent systematics. Furthermore, a higher signal-to-noise ratio will allow for reduction of the spectroscopy beam power. Complementary measurements with varying spectroscopy power will allow extrapolation to the zero-intensity limit.

- **Frequency calibration:** The combination of the lock onto an ultra-stable reference cavity and the frequency measurements with our frequency comb will enable precise measurements with a precision way below the 1 kHz level.
- **Line shape modeling:** A comprehensive line shape model incorporating all identified systematic effects will enable robust extraction of transition frequencies.

Once these systematic effects are under control and a reliable spectroscopy routine with uncertainties at or below 10 kHz has been established, we will extend the measurements to the D_1 line by reconfiguring the AOM setup of the spectroscopy laser. The shift between the D_1 and D_2 line provides access to fine-structure splitting (see Table 1.2).

The ultimate goal of this project is the determination of the ^{6}Li–^{7}Li isotope shift with high precision (see Section 1.1.2). This requires adapting the apparatus for ^{7}Li, which has a significantly larger ground state hyperfine splitting (803.5 MHz compared to 228.2 MHz for ^{6}Li [91]). The repump frequency for both the 2D MOT and the push beam will need to be generated by a separate laser system or an additional AOM, allowing independent control and optimization.

Beyond high-precision spectroscopy of lithium, the expertise and infrastructure developed in this project lay the groundwork for buffer gas cooling of hydrogen using ultracold lithium (see Ref. [92]). This goal requires trapping ^{7}Li in a magnetic trap. Our simulations of the 2D MOT indicate that atoms are predominantly optically pumped into the $m_F = -\frac{5}{2}$ state, which is high-field-seeking and therefore not trappable in a purely magnetic trap. However, the present work demonstrates that the push beam can be used for state preparation via optical pumping. By tuning the push beam polarization and frequency, it should be possible to transfer a significant fraction of atoms into low-field-seeking states suitable for magnetic trapping. This could be further investigated by expanding the simulation of the 2D MOT for a push beam.

Overall, the result of this thesis can help to further establish the 2D MOT setup as a source for cold atomic beams and a platform for cold atomic experiments and high-precision spectroscopy. Ultimately, this will enable improved determinations of the ^{6,7}Li isotope shift and stringent tests of atomic theory through comparison with new precise nuclear charge-radius measurements from muonic lithium [28].

Appendix A

Addendum

Shortly before the submission of this thesis, it was discovered that during an upgrade of the experimental setup the polarization of the two lower MOT beams had mistakenly been interchanged.

For the measurements of the loading curve (Section 3.3) and the dependence on the upper to lower MOT beam power ratio (Figure D.18), the beam polarization corresponded to the configuration shown in Figure 2.2, which resembles the "textbook" configuration. In contrast, for the MOT profile measurements (Section 3.4) and all measurements of the extracted cold atomic beam (Chapter 4), the "switched" polarization configuration was used as shown in Figure A.1, where the handedness of the lower MOT beams is interchanged.

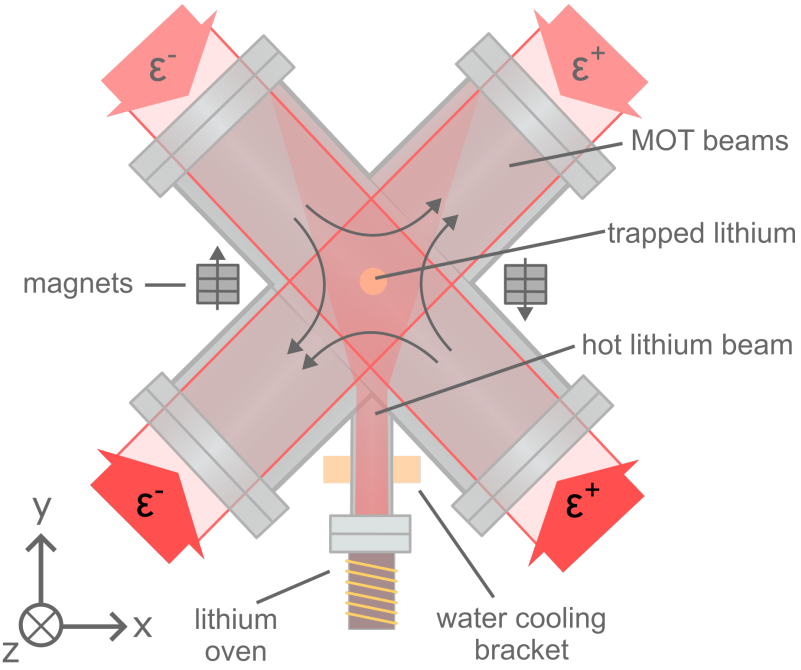

Figure A.1: Schematic of the 2D MOT configuration with the polarization of the lower MOT beams "switched" in contrast to the "textbook" configuration shown in Figure 2.2.

This issue remained unnoticed, as magneto-optical trapping was not expected to operate under these polarization conditions. Furthermore, any changes in MOT behavior were either subtle or attributed to other modifications introduced during the same upgrade. Other polarization configurations were tested; however, apart from the two configurations discussed here, none produced a fluorescent atomic cloud.

These observations indicate that the polarization of the upper MOT beams must follow the textbook configuration (see Figure 1.6), driving the σ^- transition to ensure stable trapping. Remarkably, the polarization of the lower MOT beams can be inverted without preventing the formation of a cold atomic cloud, although with modified characteristics.

Figure A.2 compares the measured MOT areal density profiles obtained with the textbook polarization configuration (a), as shown in Figure 2.2, and with the switched polarization configuration (b), as shown in Figure A.1. A qualitative comparison already reveals clear differences between the two cases.

In the switched polarization configuration, the atomic cloud is noticeably larger and displaced upward relative to the geometrical trap center. In contrast, the cloud obtained with the textbook polarization is located much closer to the geometric center.[1]

In both configurations the MOT exhibits an elliptical shape. However, the major principal axis of the ellipse is oriented toward the y-axis for the textbook polarization, whereas it is rotated more toward the x-axis in the switched configuration.

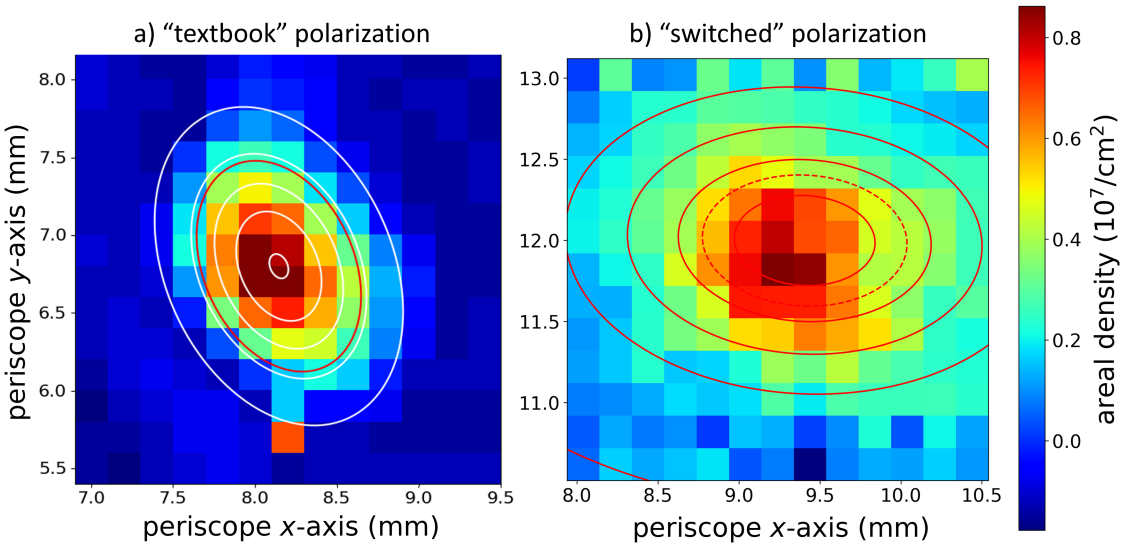

Figure A.2: Comparison of the MOT areal density profiles measured with the textbook polarization configuration (a), shown in Figure 2.2, and with the switched lower beam polarization configuration (b), shown in Figure A.1. The textbook configuration yields a cloud that is more centrally located, while the switched configuration results in a larger and upwards shifted atomic cloud.

A direct comparison of the absolute profile amplitudes is challenging, as they depend on the total MOT beam power available during the respective measurements. An analysis based on the available data suggests that the textbook configuration produces a higher peak areal density, whereas the switched polarization leads to a larger spatial extent of the cloud.

[1]The absolute cloud position with respect to the geometrical trap center is subject to a systematic uncertainty of approximately 1 mm, which may also have changed during the experimental upgrade.

Usually the working principle of a MOT relies on combining a velocity-dependent damping force arising from Doppler cooling by counter-propagating, red detuned laser beams (optical molasses), and a position-dependent restoring force generated by a spatially varying Zeeman shift in a magnetic field gradient.

At present, we do not have a complete intuitive understanding of the mechanism that allows magneto-optical trapping to operate under the switched polarization configuration. Nevertheless, some insight can be gained by considering a simplified one-dimensional MOT model. Figure A.3 illustrates the basic trapping principle for a two level atom with a $J = 0$ ground state and a $J = 1$ excited state.

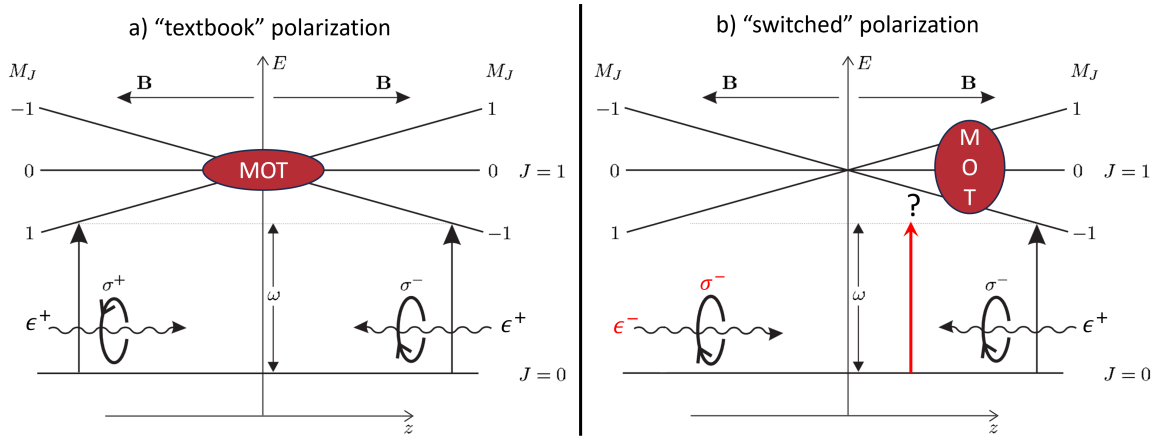

Figure A.3: Qualitative illustration of possible trapping mechanisms in a one-dimensional MOT. (a) Textbook configuration with identical circular polarization handedness of the counter-propagating beams, resulting in a position-dependent restoring force via the Zeeman shift. (b) Switched polarization configuration, where both beams predominantly drive the same σ^- transition; trapping may occur at a position offset from the magnetic field minimum due to modified resonance conditions.

In the textbook configuration shown in panel (a), the counter-propagating laser beams have the same handedness. For the quantization axis z as shown here, the beams drive either $\Delta M_J = +1$ (σ^+) or $\Delta M_J = -1$ (σ^-) transitions. The magnetic field gradient pointing outward from the trap center leads to a position-dependent Zeeman shift and hence to a restoring force toward $z = 0$.

In the switched configuration shown in panel (b), the two counter-propagating beams have opposite handedness and therefore drive the same $\Delta M_J = -1$ transition as σ^- light. For red detuned light, both beams may thus become resonant at similar position $z > 0$ displaced from the magnetic field minimum.

In this scenario, cooling and trapping would no longer occur at the magnetic field minimum, but instead at a finite offset position where the Zeeman shift mostly compensates for the laser detuning. At first sight, it is therefore not evident how such a polarization configuration can generate a cloud of cold atoms.

One possible interpretation is that the mechanism resembles a combination of a Zeeman slower and an optical molasses. The upper MOT beams may predominantly provide a Zeeman-slower-like force along the magnetic field gradient, while all four MOT beams together contribute to a local optical molasses at the position where the Zeeman shift compensates for most of the laser detuning. In this picture, atoms are

decelerated and cooled at a displaced equilibrium position, which could lead to the formation of a cold atomic cloud despite the switched polarization configuration. An additional contribution may also arise from the presence of the two resolved hyperfine ground states (see Figure 2.3) and the corresponding repump frequency component in the MOT beams.

To gain further understanding, we performed numerical simulations of the 2D MOT for the two polarization configurations discussed above. Consistent with the experimental observations, stable trapping is obtained only for these two configurations. This supports the experimental observations, that in the present geometry, the polarization of the upper MOT beams must follow the textbook configuration in order to achieve efficient cooling and trapping.

Figure A.4 compares the simulated number of cold atoms in the MOT for the textbook polarization configuration (a), shown in Figure 2.2, and for the switched lower beam polarization configuration (b), shown in Figure A.1. Qualitatively consistent with the experimental observations, the simulated atomic cloud in the textbook configuration is smaller and located close to the geometric center of the trap. In contrast, the switched polarization configuration yields a more extended cloud that is displaced upward with respect to the geometrical trap center.

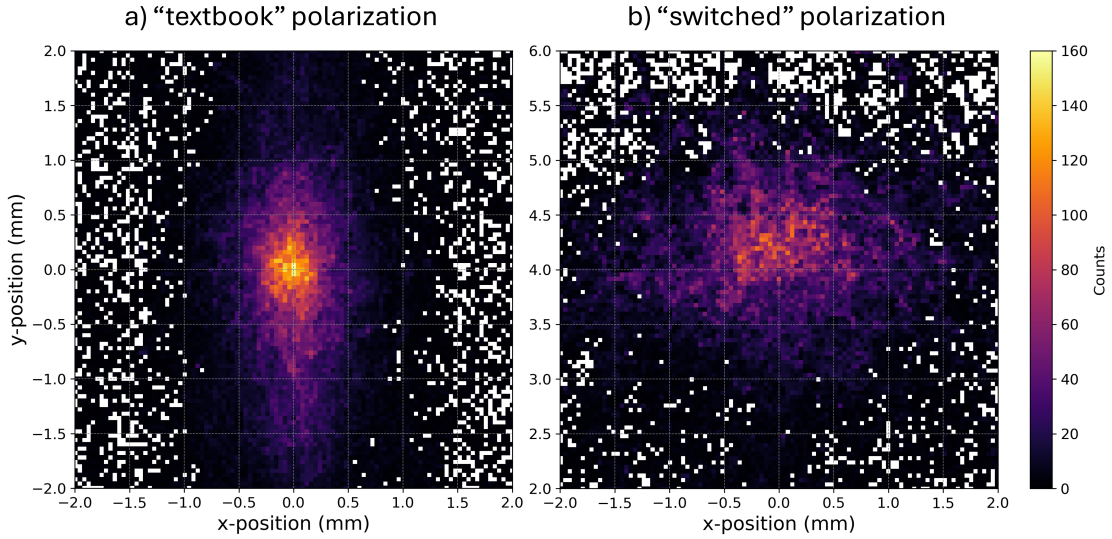

Figure A.4: Simulated number of cold atoms in the MOT for the textbook polarization configuration (a), shown in Figure 2.2, and the switched lower beam polarization configuration (b), shown in Figure A.1. The textbook configuration produces a smaller, denser cloud centered at the geometric trap center, while the switched configuration results in a larger cloud that is vertically displaced. This is qualitatively consistent with the experimental observations in Figure A.2.

The simulation further reproduces the qualitative differences in cloud shape observed experimentally. In the textbook configuration, the atomic cloud exhibits an elliptical shape with its major principal axis oriented even more clearly along the y-axis, whereas in the switched polarization configuration the ellipse is rotated and aligned to the x-axis.

Despite the differences in size and density, the simulations suggest that the total number of trapped atoms is comparable for both polarization configurations. The textbook configuration yields a higher peak density within a smaller volume, while the switched configuration results in a larger but more dilute cloud.

Using the simulation, we can also investigate how the position of the atomic cloud center along the y-axis depends on the detuning of the MOT beams for the switched polarization configuration. Figure A.5 shows the simulated dependence of the MOT center position on the MOT beam detuning. The y-position of the atomic cloud exhibits an approximately linear decrease with a decreasing detuning, while the position along the x-axis remains essentially unchanged. The absence of a corresponding shift along the x-axis is consistent with the mirror symmetry of the setup.

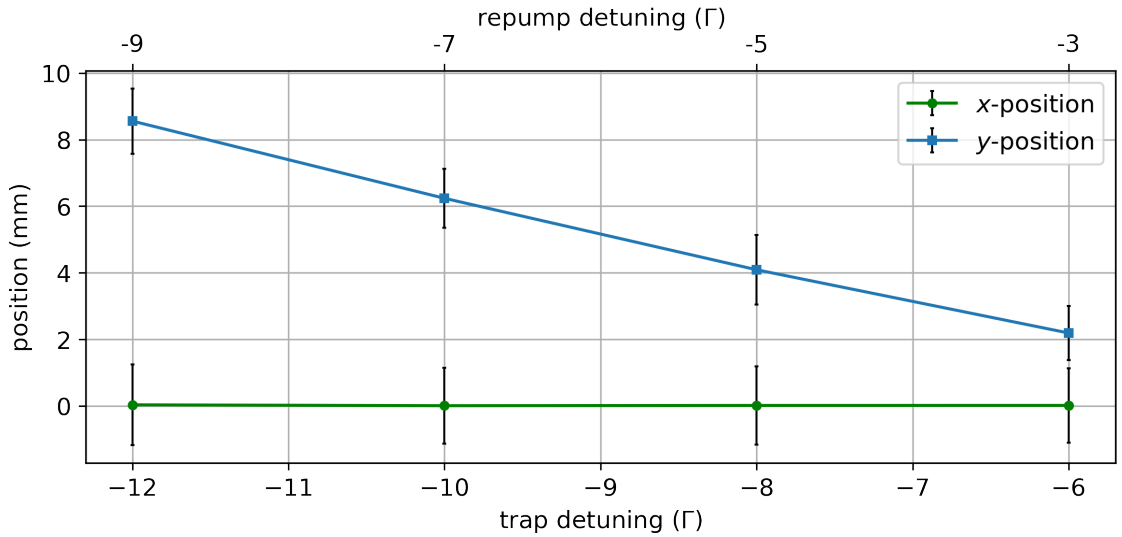

Figure A.5: Simulated dependence of the atomic cloud center position on the MOT beam detuning for the switched polarization configuration. The center position along the y-axis shifts approximately linearly with detuning, while the x-position remains unchanged.

The magnitude of the simulated effect is approximately a factor of two larger than that observed experimentally (see Figure 3.25), although the overall trend is well reproduced. This discrepancy may arise from the neglect of loss mechanisms in the simulation.

At present, the physical origin of this behavior is not fully understood. One possible explanation is that changing the laser detuning shifts the resonance condition along the spatially varying Zeeman-split energy levels (see Figure A.3). For smaller detunings, a reduced Zeeman shift is required to reach resonance, causing the equilibrium position of the MOT to move closer to the magnetic field minimum at the trap center.

In contrast, no comparable detuning dependent displacement is observed in the simulations of the textbook polarization configuration. This behavior was also confirmed in preliminary measurements performed with the upgraded magnetic field system (see Section 3.2.4) using the textbook polarization.

Furthermore, the optimal oven temperature appears to be largely independent of the polarization configuration of the MOT beams. However, the optimal laser detuning is slightly lower for the textbook polarization configuration, and the areal atomic density reaches saturation at smaller MOT beam powers as the power is increased. Preliminary evaluations also suggest that the switched polarization configuration results in shorter loading times [93].

Recent measurements of the cold atomic beam indicate that operating with the textbook polarization configuration in combination with the improved magnetic field geometry increases the fluorescence signal amplitude by at least a factor of two compared to the configuration used for measurements in this thesis.

A quantitative comparison with the results presented here would require reverting to the original magnetic field setup (see Section 3.2.1) and repeating the measurements using the textbook polarization. At the time of submission of this thesis, such measurements have not yet been performed.

Appendix B

Acquisition, Uncertainty and Reproducibility of Experimental Parameters

B.1 Uncertainty Estimation and Analysis

B.1.1 Laser Power

The laser powers were measured using a Thorlabs S130C slim dual-range power sensor with a silicon photodiode detector (often referred as power meter). According to the manufacturer's specifications, the relative measurement uncertainty of this device is 3 %.

In addition to the intrinsic measurement uncertainty, we observed significant power fluctuations over time, which were primarily caused by polarization changes in the optical fibers. These fluctuations introduced an additional source of uncertainty, particularly in long-term measurements. To quantify this contribution, we evaluated the standard deviation of the recorded power values, assuming normally distributed fluctuations, and used it as an effective measure of power instability.

For all the measurements in Chapter 4, an active power stabilization scheme was implemented for the MOT beams and the spectroscopy beam. This significantly reduced long-term drifts and power fluctuations, thereby improving the reproducibility of the measurements. Similar stabilization schemes will be required for the push beam in future experiments.

Power Calibration of the Balanced Photodetector

For the push beam absorption measurements in Chapter 3, a free-space balanced photodetector[1] was employed. To convert the measured output voltage into absorbed optical power, the photodetector response was calibrated against our power meter.

The resulting calibration yields a linear relation between optical power P and detector voltage V:

$$P = \frac{V - b}{a}, \tag{B.1}$$

where the proportionality constant is $a = (139 \pm 3)\,\mathrm{mV/\mu W}$ and the offset is $b = (18 \pm 2)\,\mathrm{mV}$. The offset depends on the degree of balancing between the two photodiodes and may vary slightly between measurement runs. However, since the

[1] Thorlabs PDB220A2/M, UV-enhanced Si balanced photodetector, active diameter 4.1 mm, spectral range 190–1100 nm.

absorption measurements are based on relative power changes, this offset largely cancels out (see Figure 3.18).

B.1.2 Laser Beam Radius

The radii of the MOT beams were determined using the knife-edge method. In this approach, the transmitted optical power is recorded as a function of the knife edge position and fitted with an error function, assuming a near Gaussian beam profile. The uncertainties were then deduced from the fit routine.

For the push and spectroscopy beams, the beam radii were measured using a commercial beam profiler[1]. The uncertainty of the extracted beam waist is determined by the quality of the Gaussian profile fit and by the positional uncertainty along the beam axis. To minimize the latter contribution, the beam profiler was positioned as close as possible to the location of interest. When this was not feasible, beam profiles were recorded at multiple axial positions and the waist at the desired location was obtained by extrapolation assuming a Gaussian beam propagation.

B.1.3 Laser Frequency

The laser frequencies used in the experiment were initially determined using a wavemeter[2]. The absolute resolution of this device was 1 MHz, while the absolute accuracy was limited to approximately 30 MHz. In addition, we observed a noticeable temperature dependence of the wavemeter, corresponding to a frequency drift of about 8 MHz/°C, which had to be taken into account for long-term measurements.

At a later stage of this work, access to a frequency comb became available. This enabled frequency measurements with an absolute uncertainty of about 1 MHz. The remaining error was primarily due to the simplicity of the beating scheme employed, which, however, was sufficient for the purposes of the measurements presented in this thesis.

B.1.4 Counting

The statistical uncertainty of the detected counts N is governed by Poissonian statistics. For each measurement we therefore assign an error

$$\Delta N = \sqrt{N}. \tag{B.2}$$

In order to improve the signal-to-noise ratio, each data point shown in the spectra represents the average of multiple repeated measurements. For M repetitions, the averaged count is given by

$$\bar{N} = \frac{1}{M} \sum_{i=1}^{M} N_i, \tag{B.3}$$

with a statistical uncertainty

$$\Delta \bar{N} = \frac{\sigma_N}{\sqrt{M}}, \tag{B.4}$$

where σ_N is the standard deviation of the individual measurements N_i.

[1] DataRay WinCamD LCM-4, 2048 × 2048 pixels, pixel size 5.5 µm × 5.5 µm.
[2] High Finesse, WS7-30.

In the case where the measurement is purely limited by counting statistics, this reduces to

$$\Delta\bar{N} = \frac{\sqrt{\bar{N}}}{\sqrt{M}}. \tag{B.5}$$

Thus, averaging reduces the relative statistical error by a factor of $1/\sqrt{M}$ with respect to a single-shot measurement.

B.2 Reproducibility

During the analysis of different measurement series, several factors limiting the reproducibility of the data became apparent.

Within individual data sets (only a single experimental parameter was varied) we occasionally observed fluctuations in the push beam power. These fluctuations originated from instabilities of the tapered amplifier in our custom-built laser system. To mitigate this, the push beam power was monitored between successive data sets. If deviations larger than 10 % were detected, the corresponding measurement series was repeated. For future experiments, an active power-stabilization system would be highly beneficial.

Between measurement sequences taken on the same day, frequency drifts occurred due to the temperature sensitivity of the wavelength meter. To compensate for this effect, the beat note with the optical frequency comb was checked between data sets at the 1 MHz level. The Ti:Sa laser and the push beam lock point were then adjusted accordingly, and the resulting residual drift was corrected during data analysis. A more robust solution would involve referencing the ultra-stable cavity lock directly to the frequency comb and operating both the Ti:Sa laser and the push beam under an offset-lock scheme relative to this stabilized reference.

Whenever the spectroscopy beam angle was changed, the associated shieldings before and after the spectroscopy region had to be manually realigned. This procedure was not fully reproducible and resulted in fluctuations of the background baseline. With the implementation of the AFR system, such manual realignment will no longer be necessary, eliminating this source of systematic variation.

Between different experimental days, the total powers and power ratios of the MOT beams varied at the 10 % level. These variations arose from day-to-day performance changes of the Ti:Sa laser as well as small drifts in fiber-coupling efficiencies of the trap and repump frequencies. Potential improvements include implementing active power stabilization for each MOT beam and implementing a beam-pointing stabilization system.

B.3 Spectral Line Fitting

To analyze the absorption and fluorescence spectra of the hot and cold lithium atoms, the spectral lines were fitted using Gaussian, Lorentzian, and Voigt profiles. The fits were implemented in `Python` using the `NumPy` (version 1.19.2) and `SciPy` (version 1.5.2) packages.

The Gaussian profile is defined as

$$G(x;\sigma,\mu) = \frac{1}{\sigma\sqrt{2\pi}} \exp\left(-\frac{(x-\mu)^2}{2\sigma^2}\right), \tag{B.6}$$

with mean μ and standard deviation σ.

The Lorentzian profile is given by

$$L(x;\Gamma,x_0) = \frac{\frac{\Gamma}{2\pi}}{(x-x_0)^2 + \left(\frac{\Gamma}{2}\right)^2}, \tag{B.7}$$

with full width at half maximum (FWHM) Γ and line center x_0.

The Voigt profile is constructed as the convolution of a Gaussian and Lorentzian:

$$V(x;\sigma,\Gamma,x_0) = \int_{-\infty}^{\infty} G(x';\sigma,0)\, L(x-x';\Gamma,x_0)\, \mathrm{d}x', \tag{B.8}$$

where σ describes the Gaussian width, Γ the Lorentzian width, and x_0 the line center. In practice, the `scipy.special.voigt_profile` function was used. For fitting, linear background contributions were included and the height was normalized.

The fitting was performed with using `scipy.curve_fit`. For the errors of the fit parameters, we use the square-root of the corresponding diagonal elements in the covariance matrix.

Appendix C

Pictures of the Experimental Setup

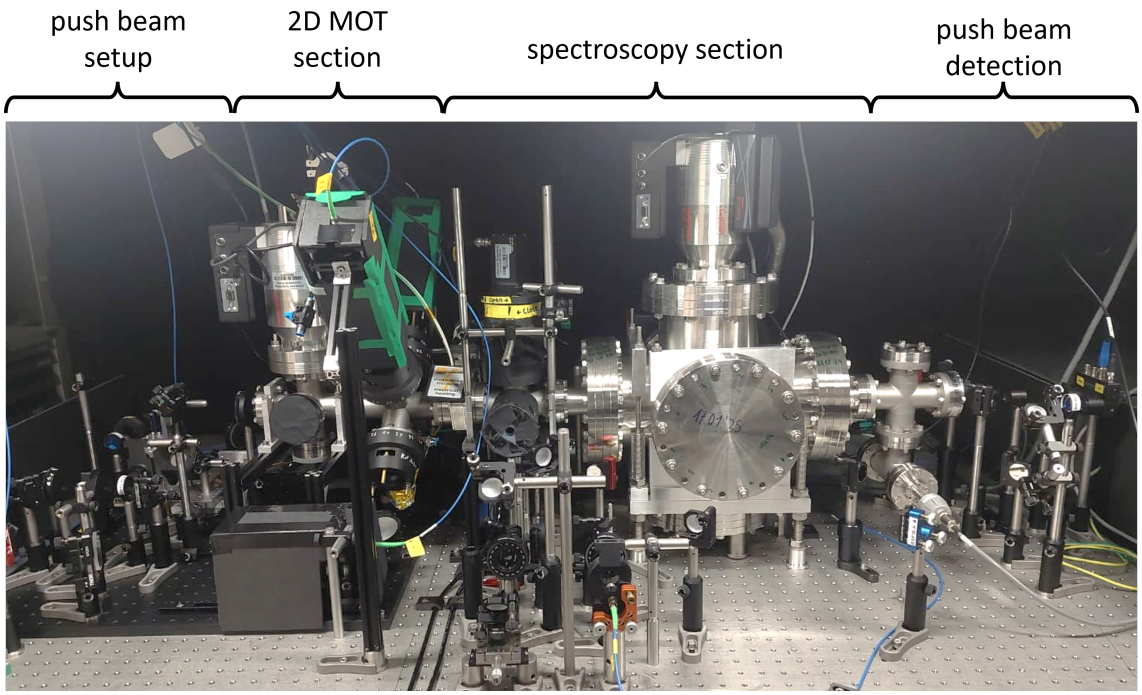

Figure C.1: Overview of the experimental setup. The push beam optics (see Figure C.9) are located on the left. After passing the motorized periscope (see Figure C.10), the push beam enters the 2D MOT region (see Figure C.2). The accelerated cold atoms are subsequently probed in the downstream spectroscopy section (see Figure C.14). After exiting the vacuum chamber, the push beam is directed onto a photodetector, which is used for the absorption measurements of the 2D MOT.

C.1 2D MOT Setup

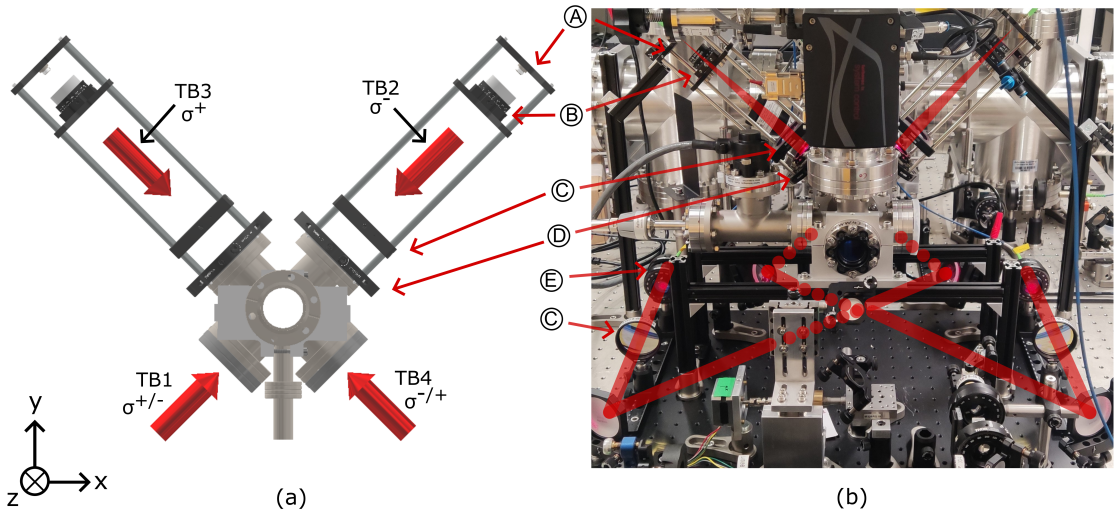

Figure C.2: Overview of the 2D MOT realization. (a) Detailed model of the 2D MOT components. (b) Photograph of the 2D MOT setup in the laboratory. The MOT trapping beams (TB) are indicated in red and labeled TB1 to TB4, with the corresponding circular polarizations (σ^+ or σ^-). The fiber coupler (A), the quarter-wave plate (B), and the collimating lenses (C) for the upper MOT beams (TB2 and TB3) are mounted to a cage-system (D), which is clamped to the vacuum flange of the upper vacuum windows. A combination of a half-wave and a quarter-wave plate (E) is used to generate circular polarization for the lower MOT beams (TB1 and TB4). The laser beam alignment is mirrored between TB2/TB4 and TB1/TB3. Figure adapted from Ref. [71].

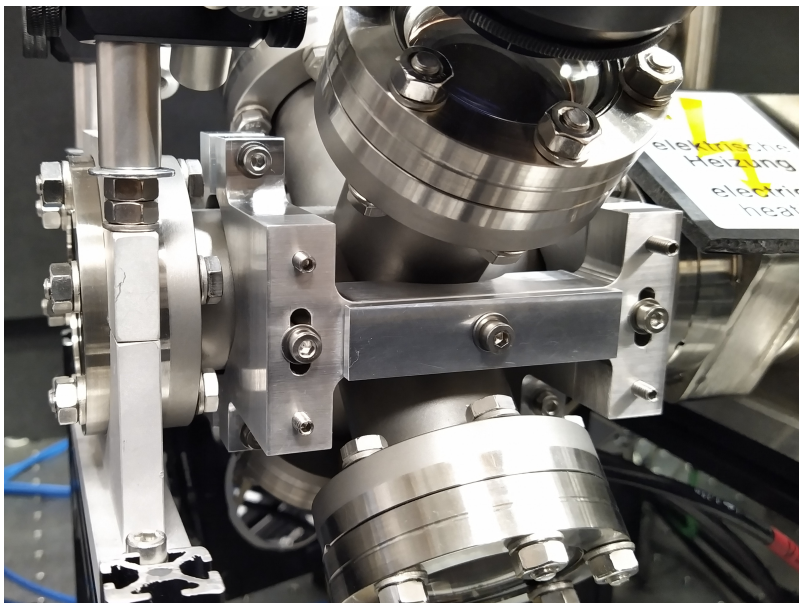

Figure C.3: Mount for the bar magnets generating the quadrupole field of the 2D MOT, clamped at the center of the six-way vacuum cross. Fine adjustment of magnet position and separation is achieved via threaded rods and sliding elements.

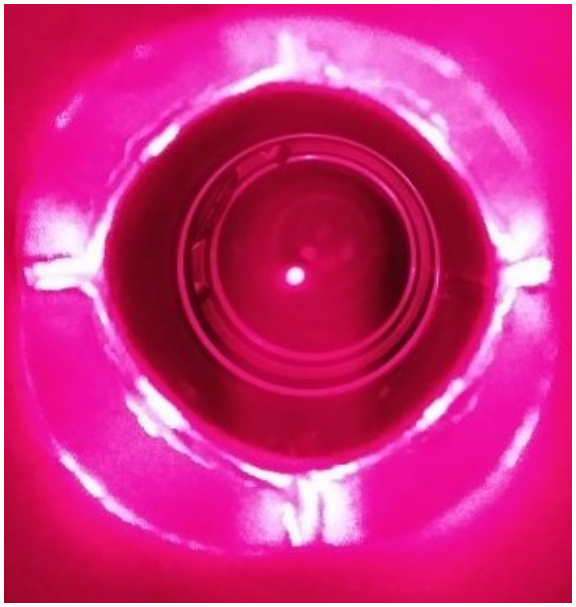

Figure C.4: Fluorescent light of the cold atomic cloud in the 2D MOT. The cold atom cloud appears as the bright central region, while hot atoms emerging from the oven below are visible as a faint vertical background glow. The remaining features originate from stray reflections of the MOT beams on the vacuum chamber cross.

C.2 MOT Beam Setup

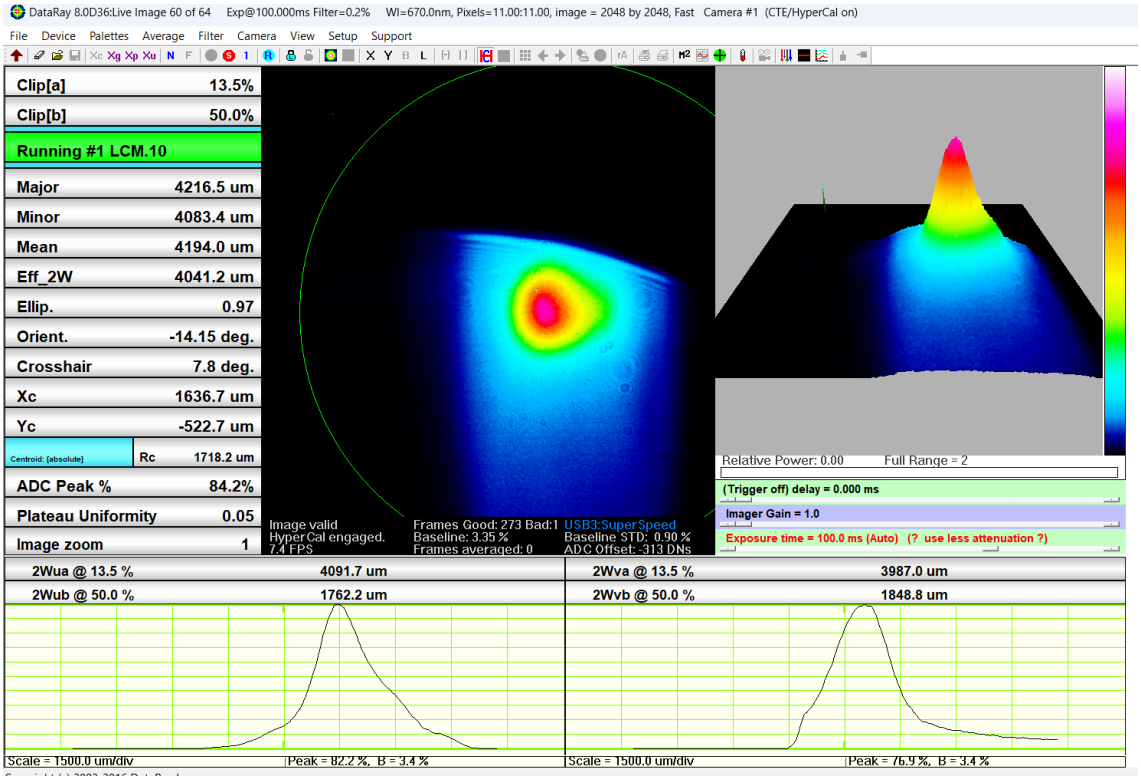

Figure C.5: Beam profile of the Ti:Sa output measured after the external cavity, directly behind the first mirror of the periscope (see Figure C.7). The spatial mode deviates from an ideal Gaussian profile, and its shape is sensitive to the alignment of the Ti:Sa cavity. The intensity cut visible at the top of the profile results from clipping at the mirror mount.

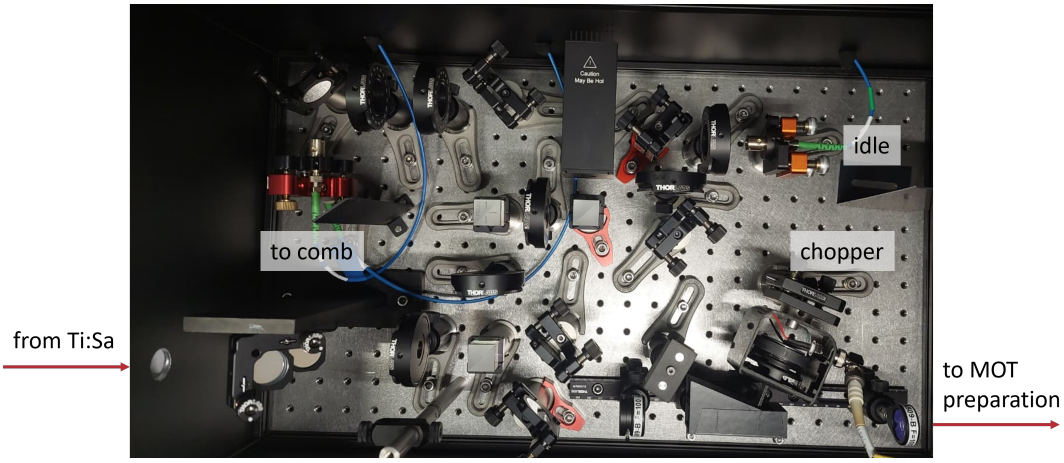

Figure C.6: Photograph of the so-called Ti:Sa hub. The outcoupled beam from the Ti:Sa enters the setup via a periscope equipped with a backside-polished mirror, which allows monitoring of the Ti:Sa beam profile (see Figure C.5). The beam is subsequently split using polarizing beamsplitters: one part is directed to the frequency reference, while another passes through a mechanical chopper and is sent to the MOT beam preparation setup (see Figure C.7).

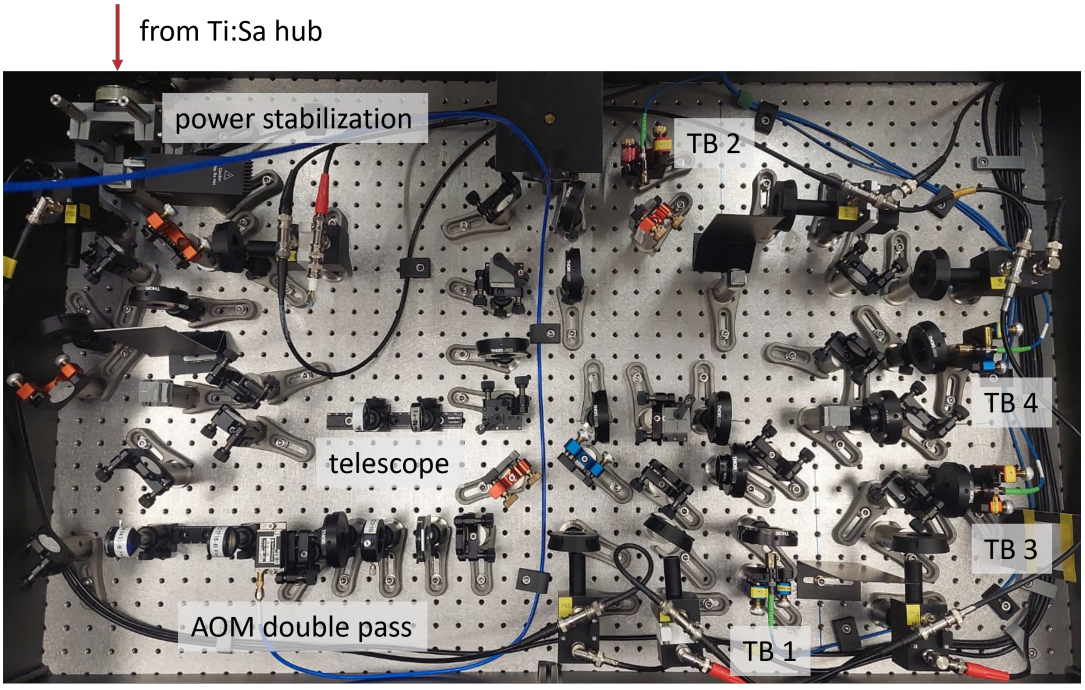

Figure C.7: Photograph of the MOT beam preparation setup (see Figure 2.4). The beam from the Ti:Sa hub (see Figure C.6) passes through a motorized half-wave plate, which is used for active power stabilization. A fraction of the beam is then sent through a double pass AOM to generate the repump frequency. The cooling and repump beams are first overlapped using a 50/50 beamsplitter and subsequently split and coupled into optical fibers, which deliver the four trap beams (TB) to the 2D MOT setup (see Figure C.2).

C.3 Push Beam Setup

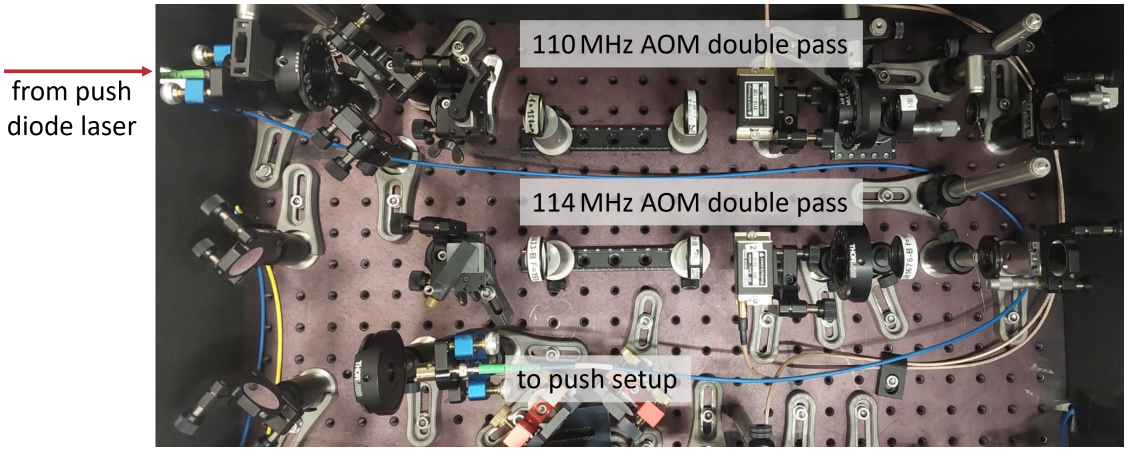

Figure C.8: Photograph of the push beam preparation setup (see Figure 2.6). The output of the custom-built ECDL is fed to the setup via an optical fiber. The beam passes two AOM double passes each at approximately 110 MHz: the first is used for push beam modulation, and the second for the generation of the repump frequency. The combined beam is then coupled into a fiber to the push beam setup (see Figure C.9).

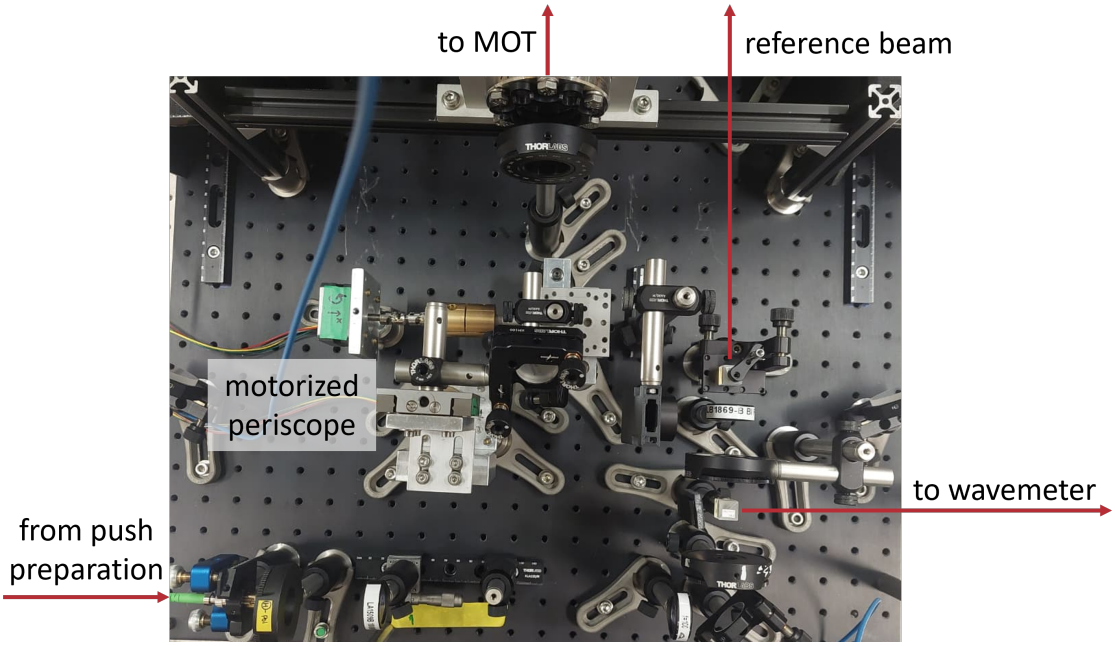

Figure C.9: Photograph of the push beam setup (see Figure 2.5). The push beam is split into two equal parts: one beam passes through the 2D MOT region, while the other serves as a reference and bypasses the experiment. Both beams are subsequently detected with a balanced photodetector. The beam position can be adjusted using a motorized periscope (see Figure C.10).

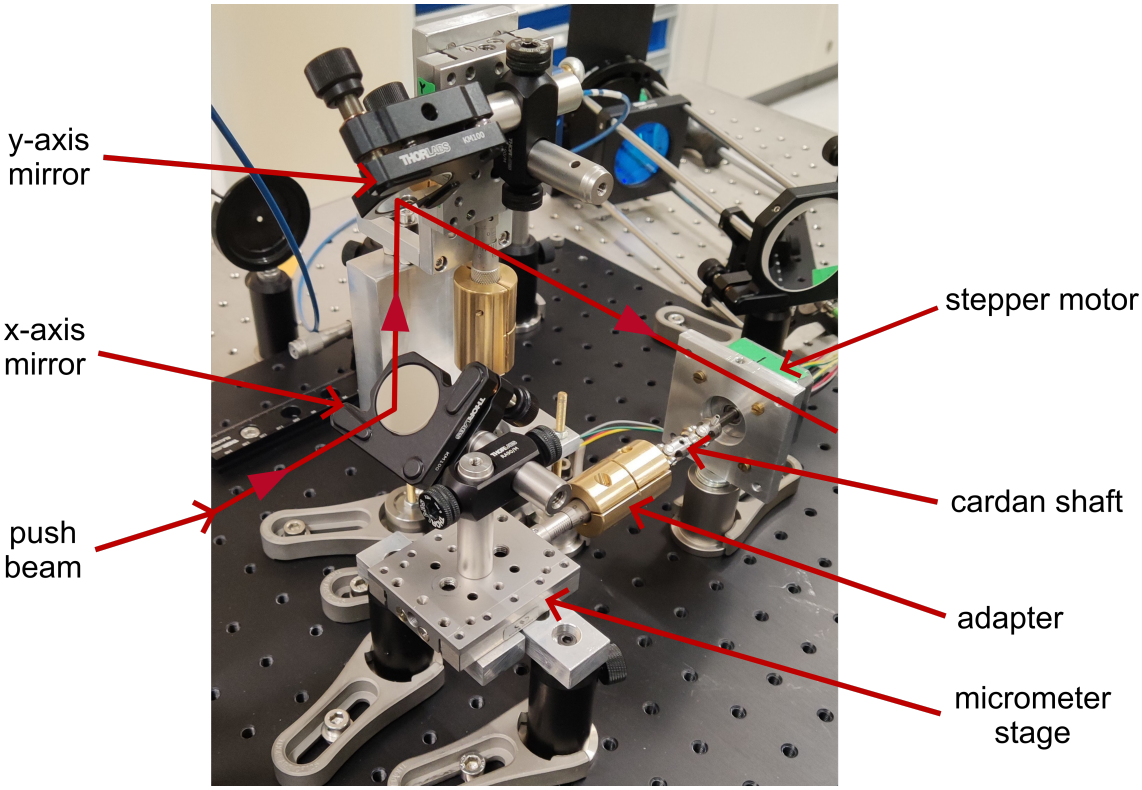

Figure C.10: Photograph of the motorized periscope assembly used for the absorption profile measurements. Each axis is independently adjusted by a mirror mounted on a micrometer stage. Motorized control of the two axes is achieved by attaching stepper motors to the micrometer screws. Cardan shafts are used to decouple the motors from the micrometer screws and to reduce transverse mechanical load. The periscope is further described in [71].

C.4 Spectroscopy Setup

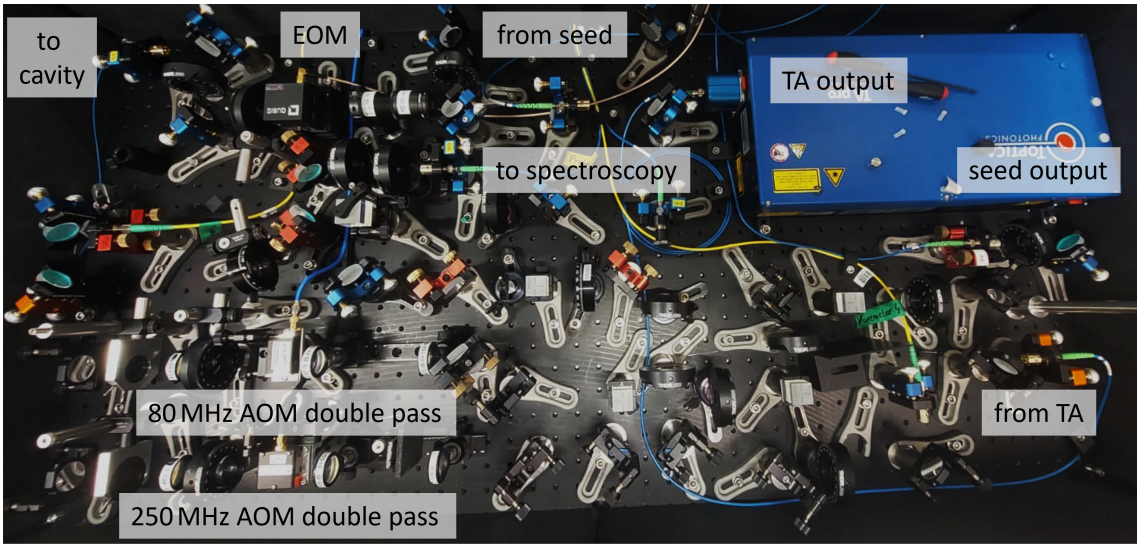

Figure C.11: Photograph of the spectroscopy scan and lock setup (see Figure 2.7). The tapered amplifier (TA) output passes through two AOM double passes before being directed to the spectroscopy beam preparation setup (see Figure C.12). The seed output is sent through an electro-optic modulator (EOM) and subsequently directed to the reference cavity for frequency stabilization.

Figure C.12: Photograph of the spectroscopy preparation setup (see Figure 2.8). The output of the spectroscopy laser is sent through an AOM double pass operating at 114 MHz to generate the repump frequency component. After combining of the frequency components, one part of the beam is directed to the wavemeter for monitoring, while the other is guided to the spectroscopy setup (see Figure C.14).

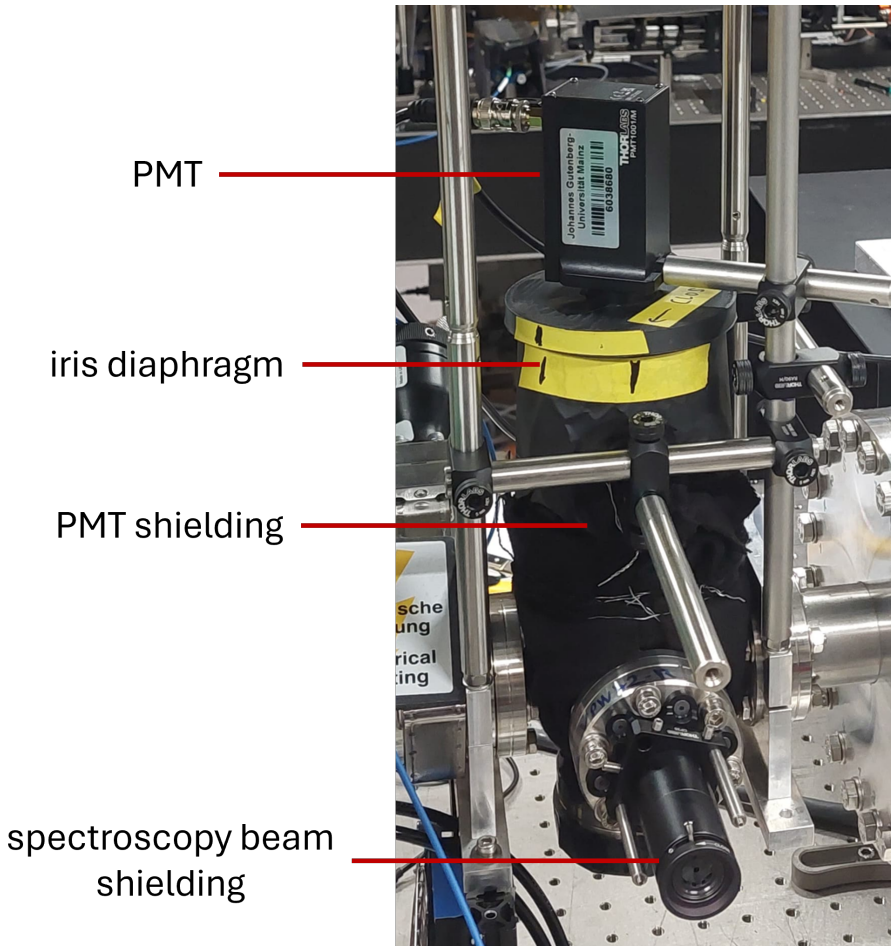

Figure C.13: Photograph of the cold atomic beam fluorescence detection setup. The photomultiplier tube (PMT) is mounted at the top of the assembly. An adjustable iris diaphragm in front of the PMT is used to control the amount of collected fluorescence light. The vacuum cross, including the observation window and the collimating lens, is enclosed by a 3D-printed light shield additionally wrapped in blackout material to suppress stray light. The incoming and outgoing spectroscopy beam is further shielded using a lens tube and an iris diaphragm on both sides of the six-way cross.

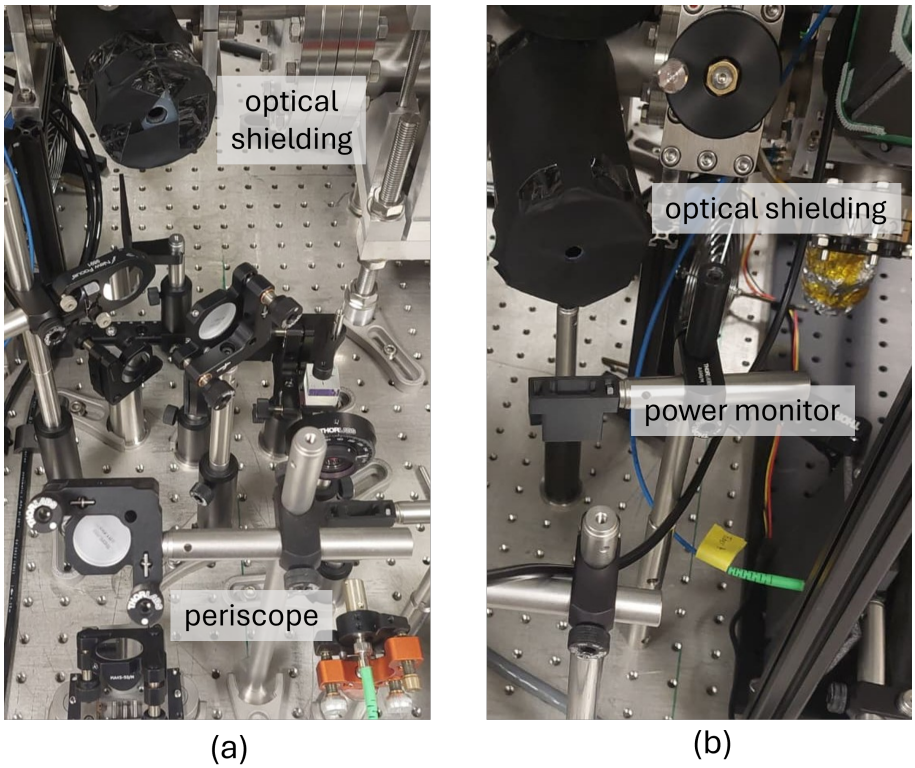

Figure C.14: Pictures of the spectroscopy setup and its shielding (see Figure 4.2). (a) shows the optical setup for the spectroscopy beam in front of the interaction region. (b) shows the optical shielding and power monitor behind the interaction region.

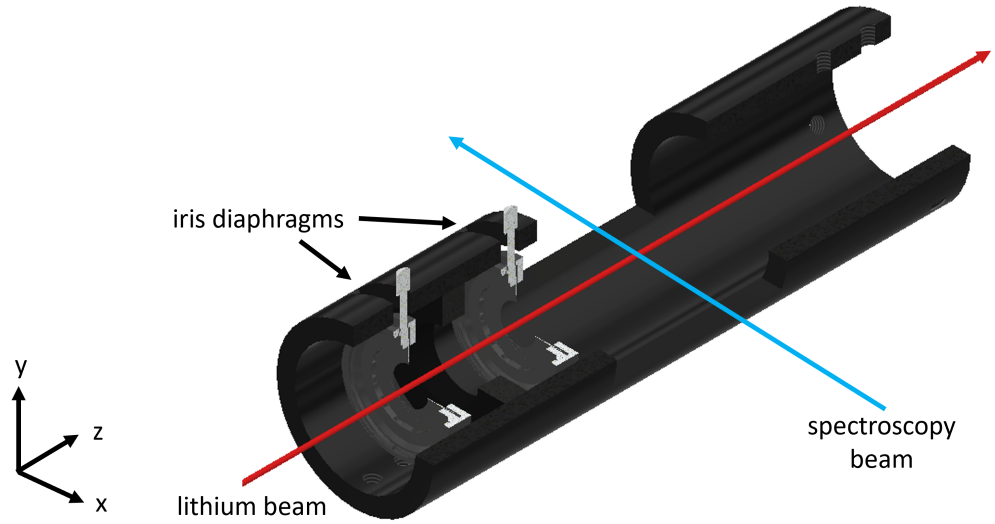

Figure C.15: Sketch of the spectroscopy inlay. A black-anodized inlay is mounted in the spectroscopy six-way cross to suppress stray light originating from the 2D MOT region. Two iris diaphragms with a diameter of approximately 5 mm collimate the cold lithium beam and provide additional reduction of background contributions from the hot atomic beam (see Section E.2).

Appendix D

Characterization of the Two-Dimensional Magneto-Optical Trap

D.1 Supplementary Figures and Tables

D.1.1 Supplementary Figures and Tables on Section 3.1

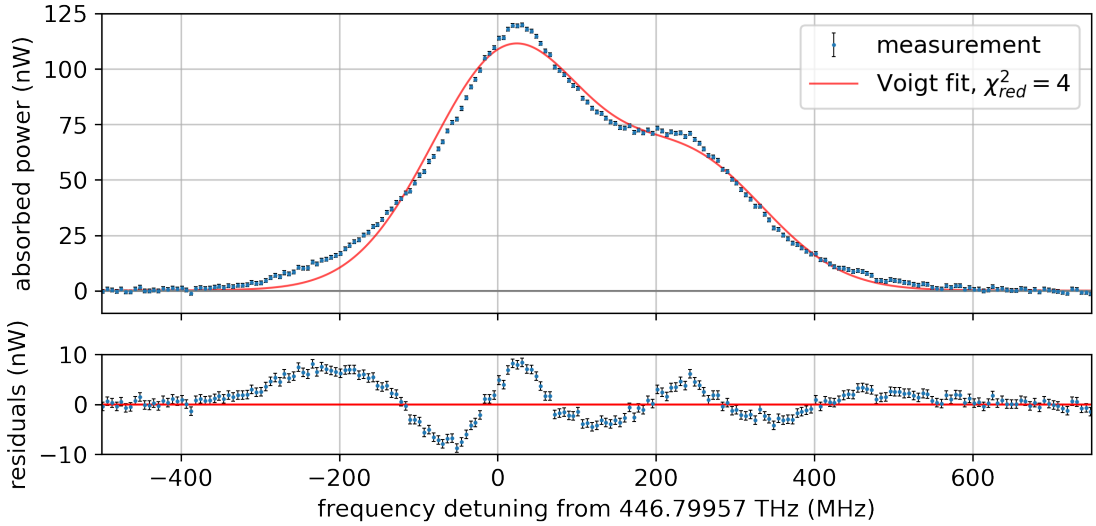

Figure D.1: Absorption measurement of hot atomic beam emitted from the lithium oven set to (420±2) °C. The push beam has a diameter of (750 ± 50) µm, a power of (1.35±0.05) µW and intersects the atomic beam (116±5) mm above the lithium reservoir. A fit consisting of two Voigt profiles, each with a Lorentzian width fixed to the natural linewidth, is shown as a red line. The fit parameters are summarized in Table D.1. The residuals shown below reveal systematic deviations, indicating that the fit does not fully capture the measured line shapes. The observed narrower features can be attributed to geometric velocity selection, as demonstrated by Monte Carlo simulations (see Figure 3.4).

Table D.1: Fit parameters and areal density at $T_{\mathrm{set}} = (420 \pm 2)\,^{\circ}\mathrm{C}$.

Fit parameter	**Value**
amplitude A_1	$(107.0 \pm 0.1)\,\mathrm{nW}$
amplitude A_2	$(57.2 \pm 0.1)\,\mathrm{nW}$
amplitude ratio A_1/A_2	(1.87 ± 0.01)
peak detuning δ_1	$(14.4 \pm 0.1 \pm 30.0)\,\mathrm{MHz}$
peak detuning δ_2	$(242.6 \pm 0.3 \pm 30.0)\,\mathrm{MHz}$
peak separation $\delta_2 - \delta_1$	$(228.2 \pm 0.3)\,\mathrm{MHz}$
broadening σ	$(97.08 \pm 0.11)\,\mathrm{MHz}$
axial velocity distribution Δv_z	$\sim 65\,\mathrm{m/s}$
reduced chi squared χ^2_{red}	4
areal density	$(3.8 \pm 0.2)\,10^8/\mathrm{cm}^2$

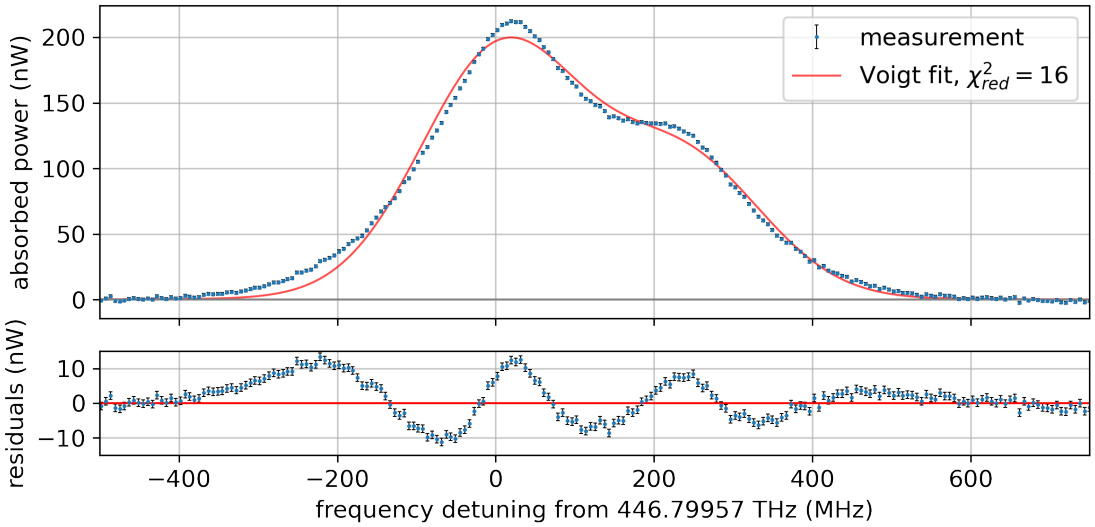

Figure D.2: Absorption spectrum of the hot atomic beam emitted from the lithium oven set to (440±2) °C. The push beam has a diameter of $(750 \pm 50)\,\mu\mathrm{m}$, a power of (1.35±0.05) µW and intersects the atomic beam (116±5) mm above the lithium reservoir. A fit consisting of two Voigt profiles, each with a Lorentzian width fixed to the natural linewidth, is shown as a red line. The fit parameters are summarized in Table D.2. The residuals shown below reveal systematic deviations, indicating that the fit does not fully capture the measured line shapes. The observed narrower features can be attributed to geometric velocity selection, as demonstrated by Monte Carlo simulations (see Figure 3.4).

Table D.2: Fit parameters and areal density at $T_{\text{set}} = (440 \pm 2)\,°\text{C}$.

Fit parameter	**Value**
amplitude A_1	$(189.9 \pm 0.1)\,\text{nW}$
amplitude A_2	$(105.8 \pm 0.2)\,\text{nW}$
amplitude ratio A_1/A_2	(1.80 ± 0.01)
peak detuning δ_1	$(7.0 \pm 0.1 \pm 30.0)\,\text{MHz}$
peak detuning δ_2	$(236.0 \pm 0.2 \pm 30.0)\,\text{MHz}$
peak separation $\delta_2 - \delta_1$	$(229.0 \pm 0.2)\,\text{MHz}$
broadening σ	$(100.5 \pm 0.1)\,\text{MHz}$
axial velocity distribution Δv_z	$\sim 68\,\text{m/s}$
reduced chi squared χ^2_{red}	16
areal density	$(7.3 \pm 0.4)\,10^8/\text{cm}^2$

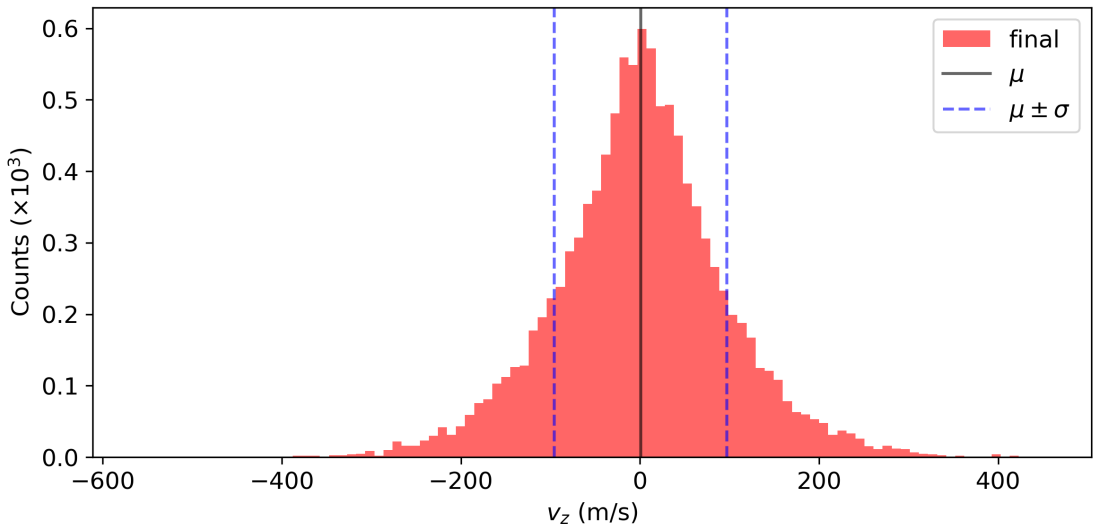

Figure D.3: Simulated velocity distribution in the push beam along z-axis for a lithium oven at 400 °C. The standard deviation of the distribution is approximately 100 m/s.

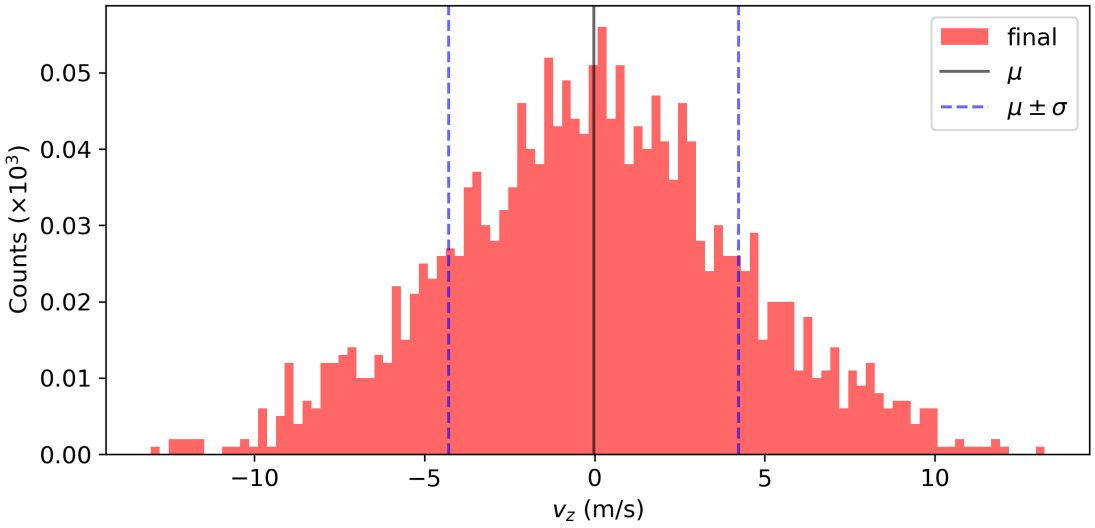

Figure D.4: Simulated velocity distribution of the capturable atoms in the trap region along z-axis for a lithium oven at 400 °C for initially 1×10^6 atoms with a total velocity below 100 m/s. The mean μ of the distribution is around zero and the standard deviation is approximately $\sigma = 4.3$ m/s. For higher initial velocities the standard deviation increases compared to Figure 3.7.

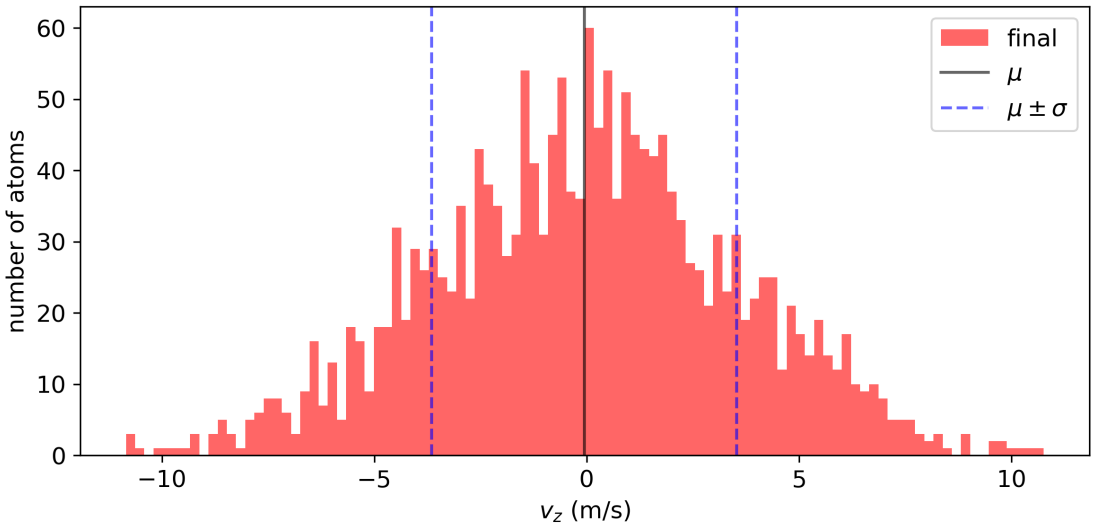

Figure D.5: Simulated velocity distribution of the capturable atoms in the trap region along z-axis for a lithium oven at 400 °C for initially 1×10^6 atoms with a total velocity below 85 m/s and a MOT beam radius of 17.1 mm. The mean μ of the distribution is around zero and the standard deviation is approximately $\sigma = 3.6$ m/s. We observe no significant change in the velocity distribution for larger MOT beams compared to Figure 3.7.

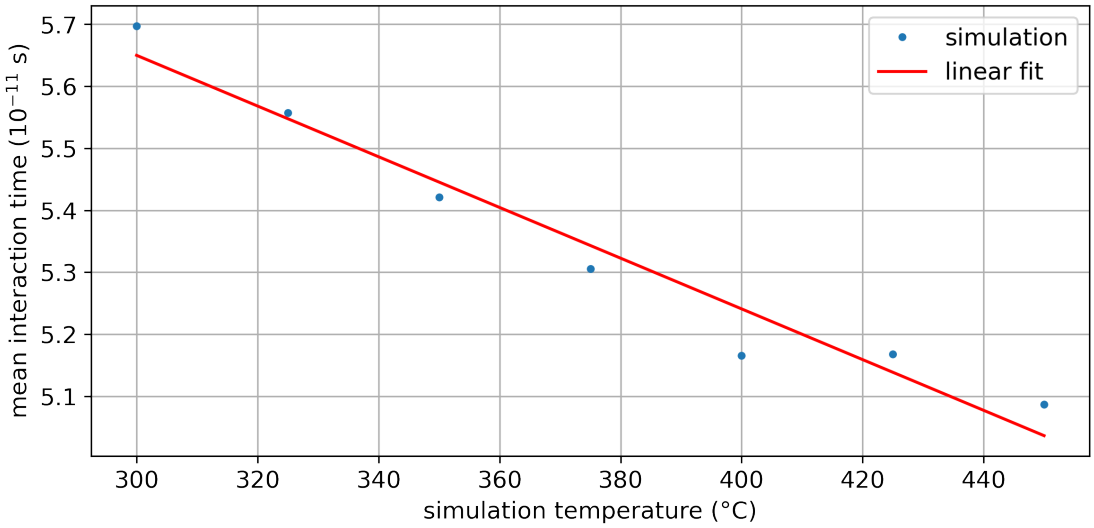

Figure D.6: Mean interaction time of the hot atoms with the push beam in dependence of the simulated oven temperature. As expected, the mean interaction time decreases with an increasing temperature. The simulation can be fitted with a linear function for further analysis.

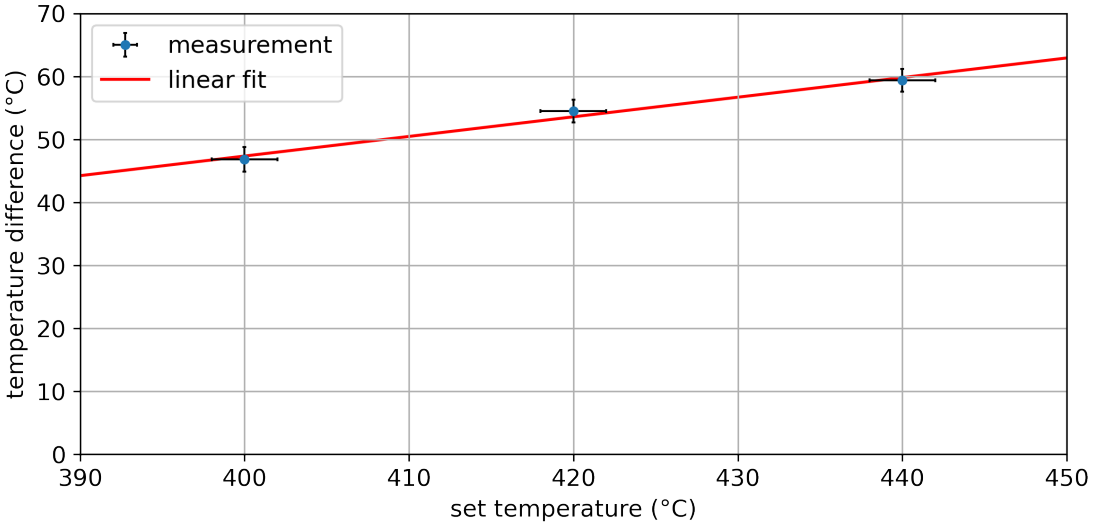

Figure D.7: Difference between the set and actual atomic temperatures in dependence of the set temperature. The deviation increases with higher set temperatures. A linear fit can be used to convert the set temperature into an estimate for the actual atomic temperature.

D.1.2 Supplementary Figures and Tables on Section 3.2

Figure D.8 shows the simulated magnetic field strength along the x- and y-axes, as well as the corresponding gradients in the central region from -5 to $+5$ mm. The dashed lines indicate linear fits to the red-marked data points in the center. Within this region, the gradients along both axes are equal, yielding $\partial B/\partial x \approx \partial B/\partial y \approx 0.45\,\mathrm{T/m}$. Outside the central region, however, the magnetic field strengths along the two axes begin to deviate from one another.

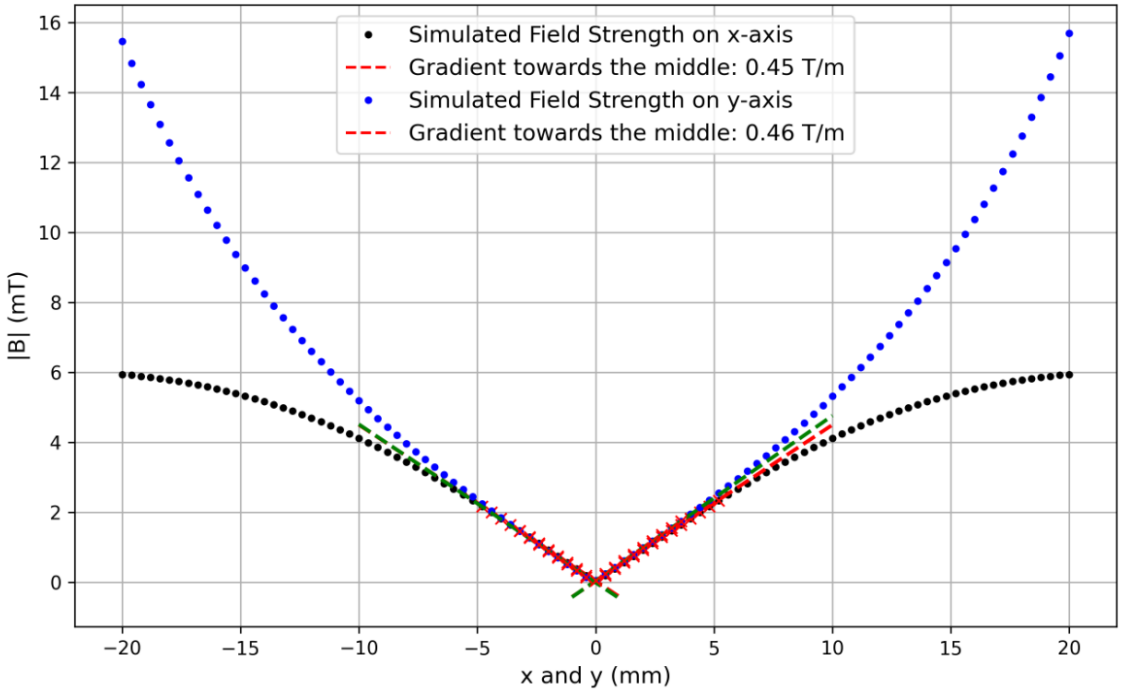

Figure D.8: Simulated magnetic field strength along the x- and the y-axis for the configuration described in Section 3.2.1. The dashed lines display a linear fit for the red marked data points in the center. The gradient in the center is the same for both axes. In the outer region the magnetic field strengths deviate from each other. Figure taken from Ref. [83].

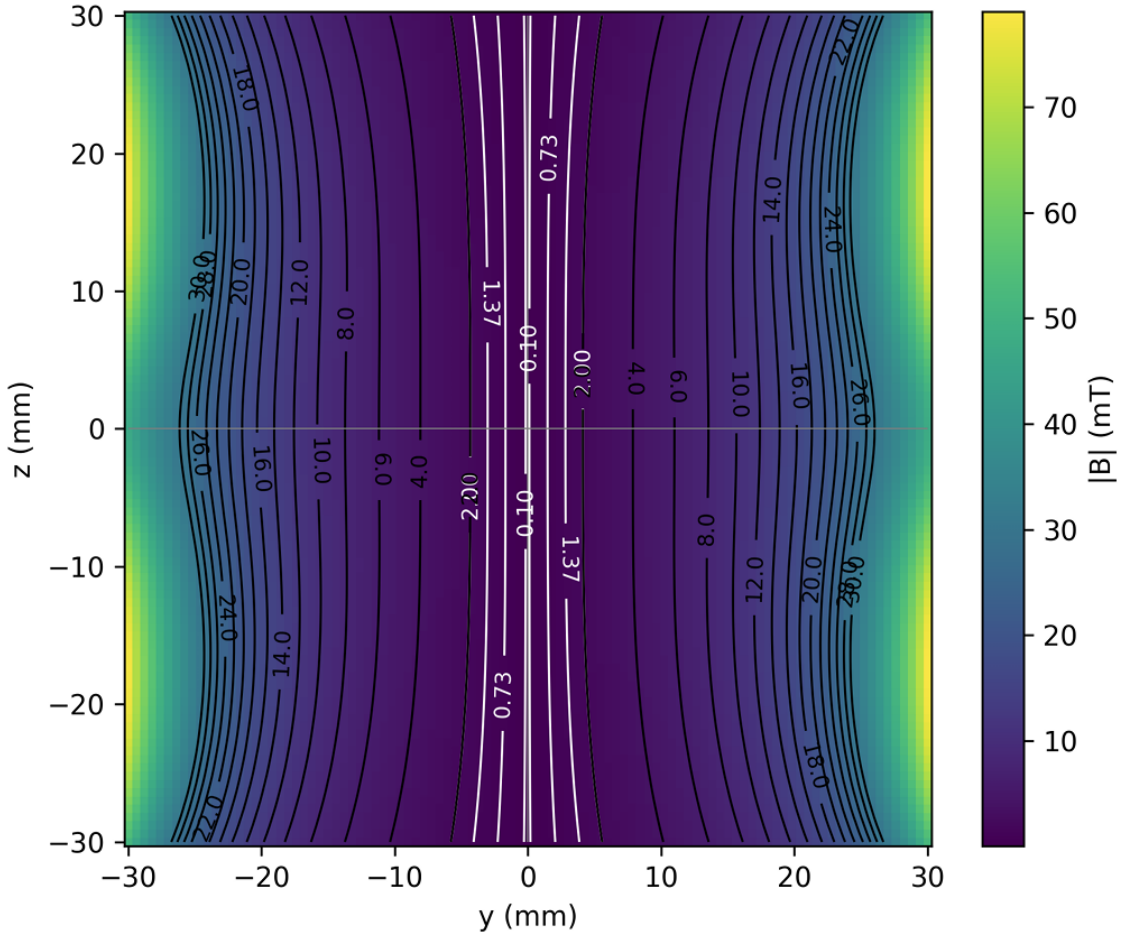

Figure D.9: Simulated magnetic field in the yz-plane for the magnetic field configuration described in Section 3.2.1. The field is symmetric about the z-axis, with a magnetic field minimum along $x = y = 0$. Figure taken from Ref. [83].

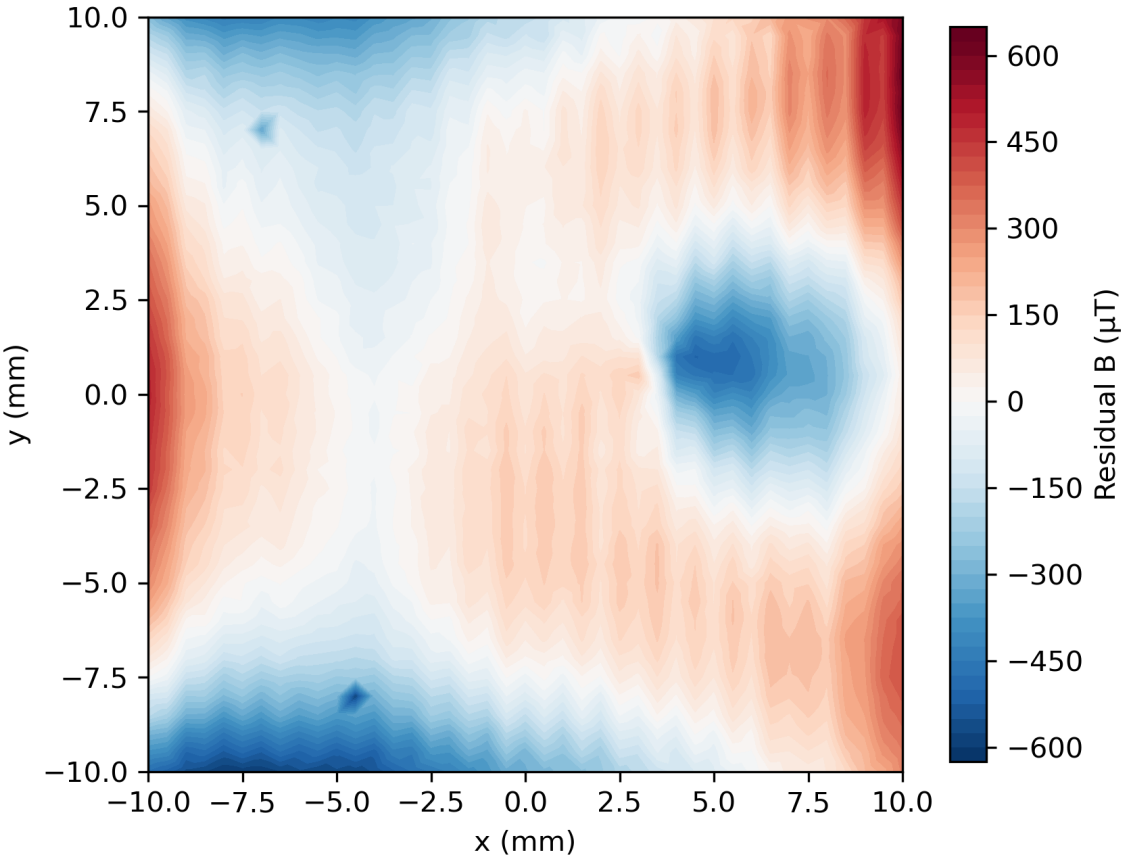

Figure D.10: Residuals to the data and the fit shown in Figure 3.11.

D.1.3 Supplementary Figures and Tables on Section 3.3

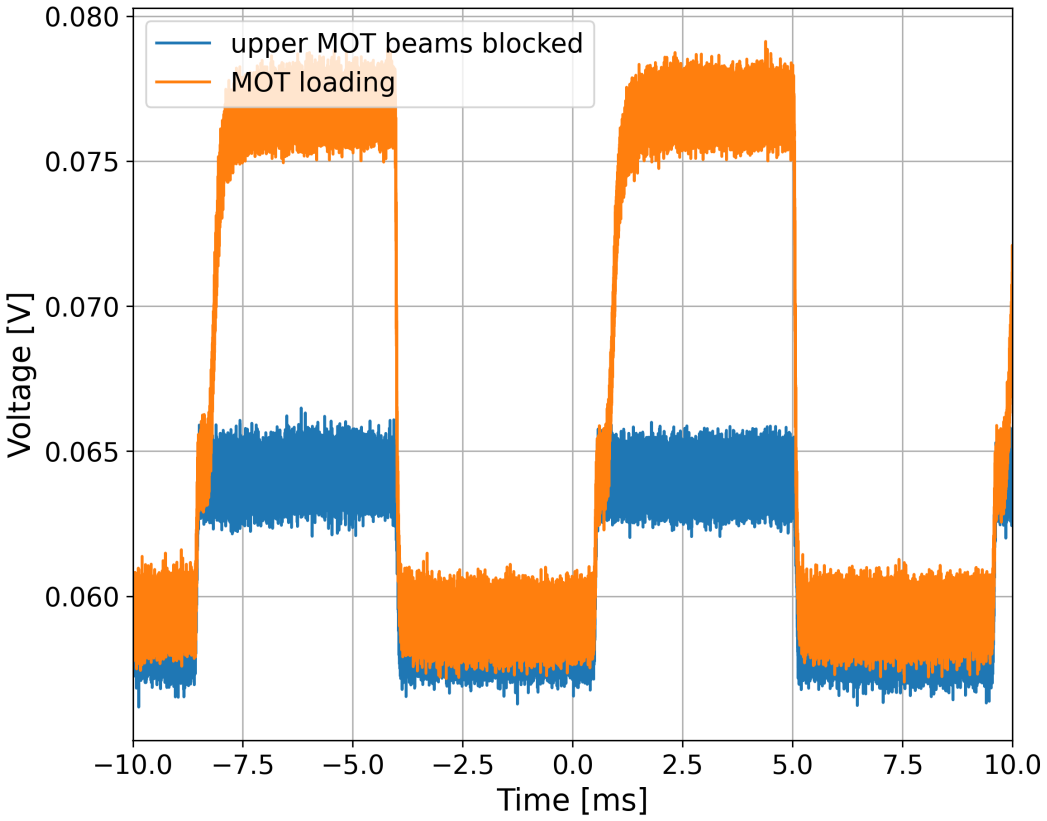

Figure D.11: Loading curve for simultaneously modulated MOT beams (orange signal). The MOT beams are modulated simultaneously by using the chopper wheel in the Ti:Sa output (see Figure 2.4). Even if the formation of a MOT is suppressed by blocking one of the four MOT beams, a baseline shift is still visible (blue signal). Figure taken from Ref. [71].

Table D.3: Fit parameter corresponding to the loading curves shown in Figure 3.15.

plot	A (nW)	t_0 (ms)	B (nW)	t_{start} (ms)	τ (ms)	χ^2_{red}
(a)	12.691 ± 0.006	0.686 ± 0.003	-1.2 ± 0.2	0.76 ± 0.06	0.495 ± 0.003	2.50
(b)	7.621 ± 0.009	0.698 ± 0.006	1.6 ± 0.1	0.76 ± 0.06	1.027 ± 0.009	1.09

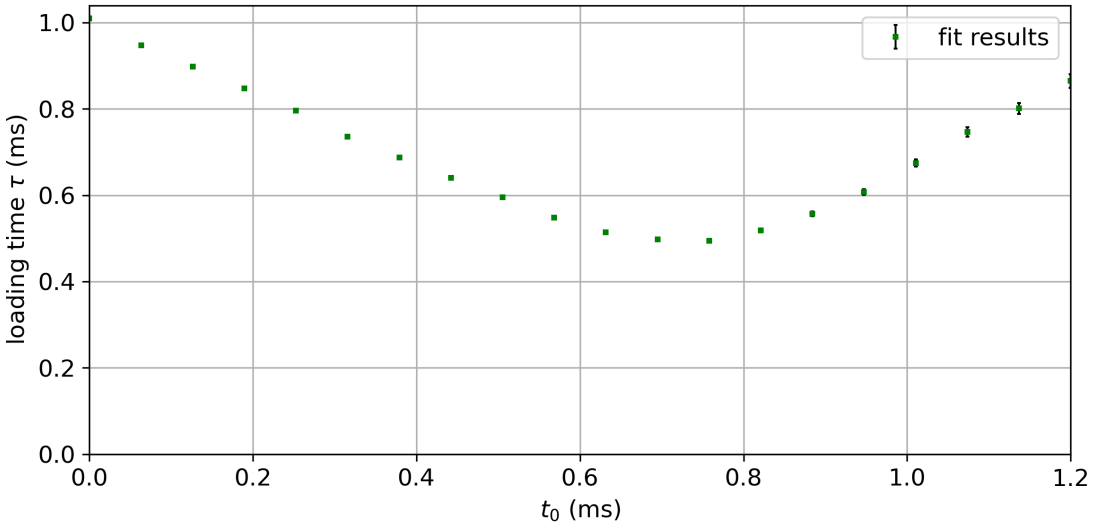

Figure D.12: Loading time in dependence of the timing offset t_0.

Table D.4: Fit parameter corresponding to Figure 3.16.

Push beam frequency	a (ms)	b (cm^2/mW)	c (ms $\times$ cm^{2}mW^{-1})	d (ms)
446.79957 THz	1.6 ± 0.5	6 ± 2	0.0 ± 0.02	0.7 ± 0.1
446.79980 THz	1.8 ± 0.3	4 ± 1	0.0 ± 0.02	0.9 ± 0.1

D.1.4 Supplementary Figures and Tables on Section 3.4

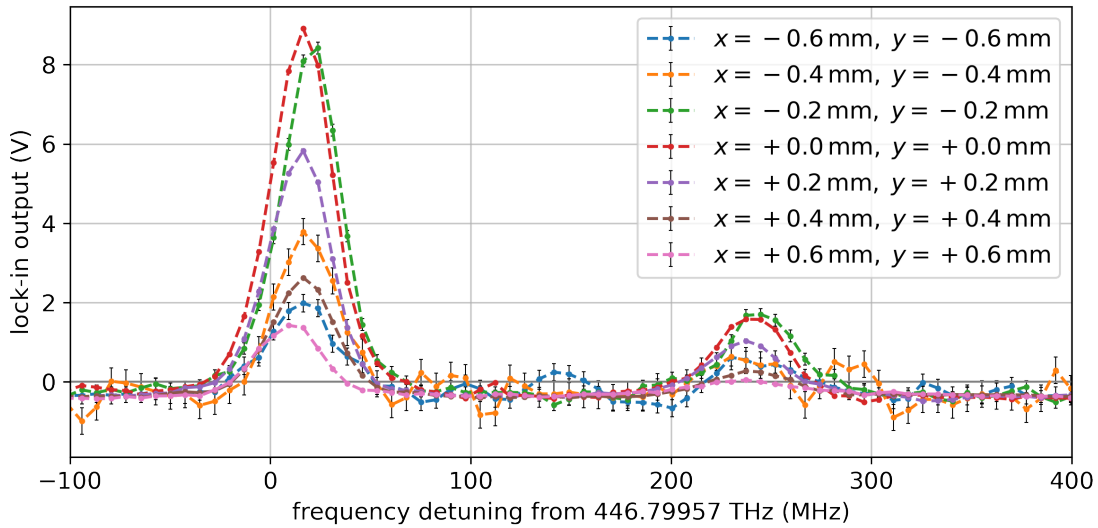

Figure D.13: MOT absorption spectra recorded at different positions of the push beam. The strong variation in the spectral amplitude reflects the spatial density distribution of the atomic cloud and illustrates the principle of the profile scan. In addition, small position-dependent shifts and changes in the splitting are observed, indicating the Zeeman shift due to the inhomogeneous magnetic quadrupole field in the 2D MOT. This demonstrates the necessity of integrating over the full spectrum in order to obtain a position-independent measure of the atomic density that is also insensitive to spectral broadening effects.

Dependence on Oven Temperature

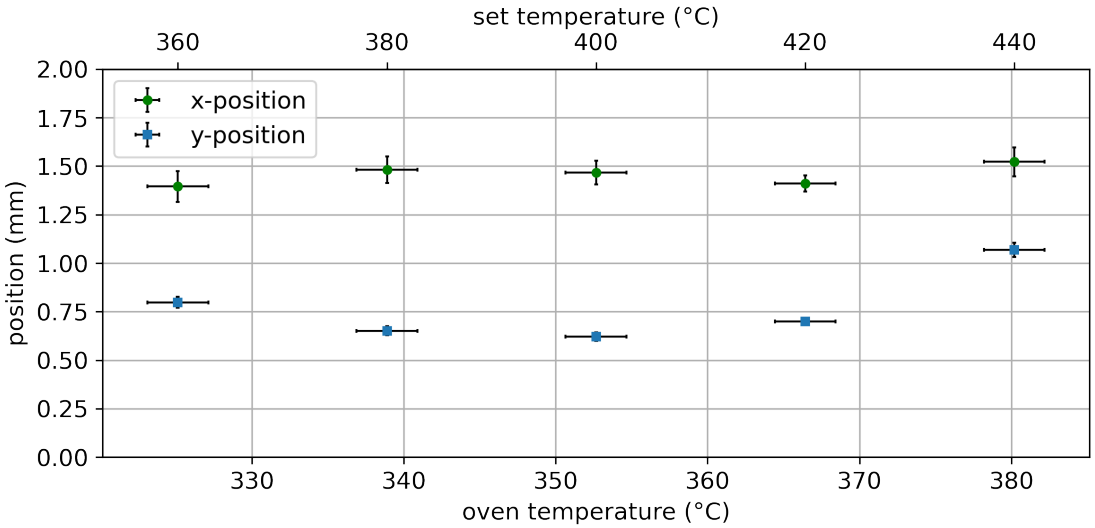

Figure D.14: MOT position in dependence of oven temperature. The MOT position seems to be mostly unaffected by changes in oven temperature.

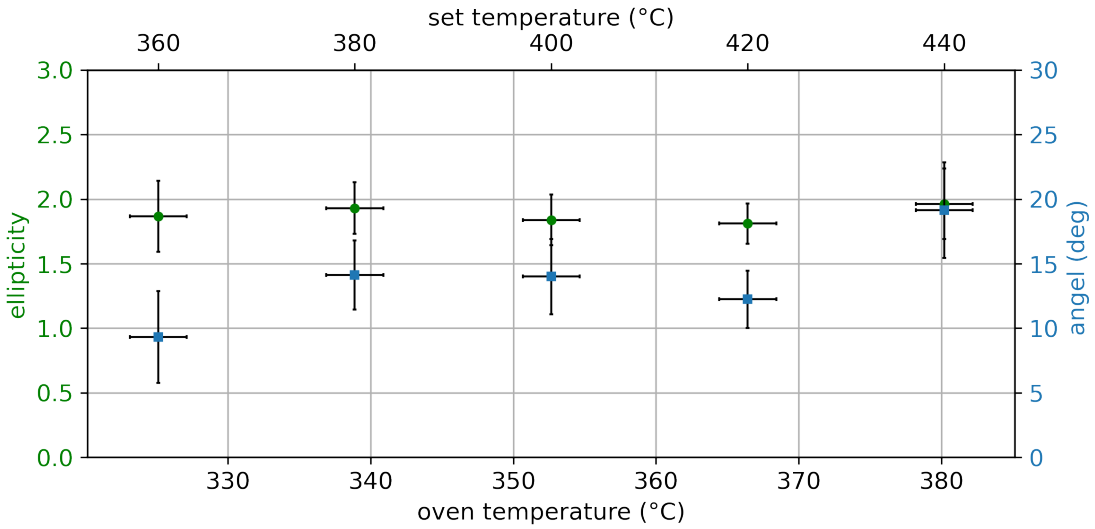

Figure D.15: MOT shape in dependence of oven temperature. The ellipticity and the rotation angle seem to be unaffected by the oven temperature.

Dependence on MOT Beam Detuning

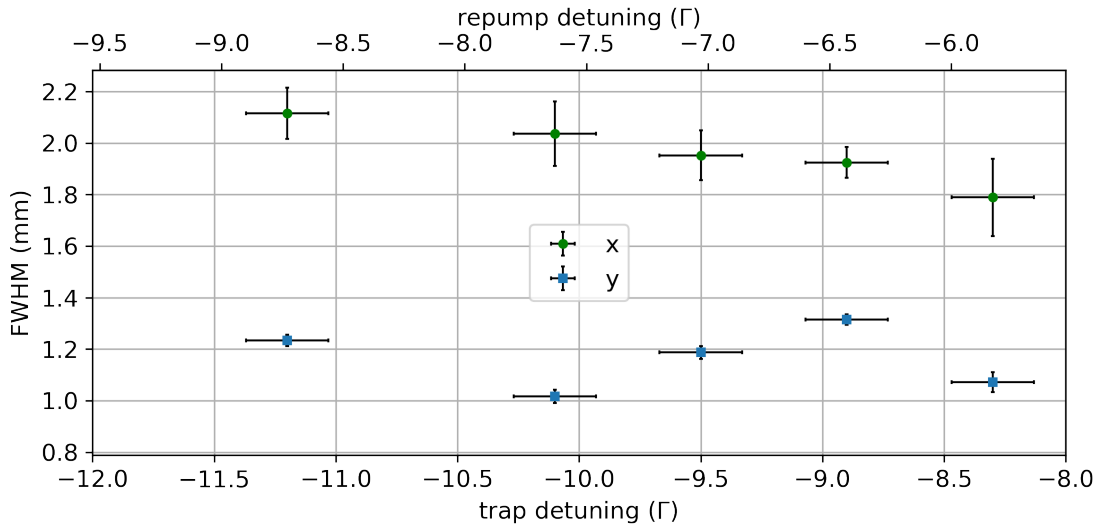

Figure D.16: MOT shape in dependence of the MOT beam detunings. The MOT shape seems to be unaffected by the MOT beam detunings.

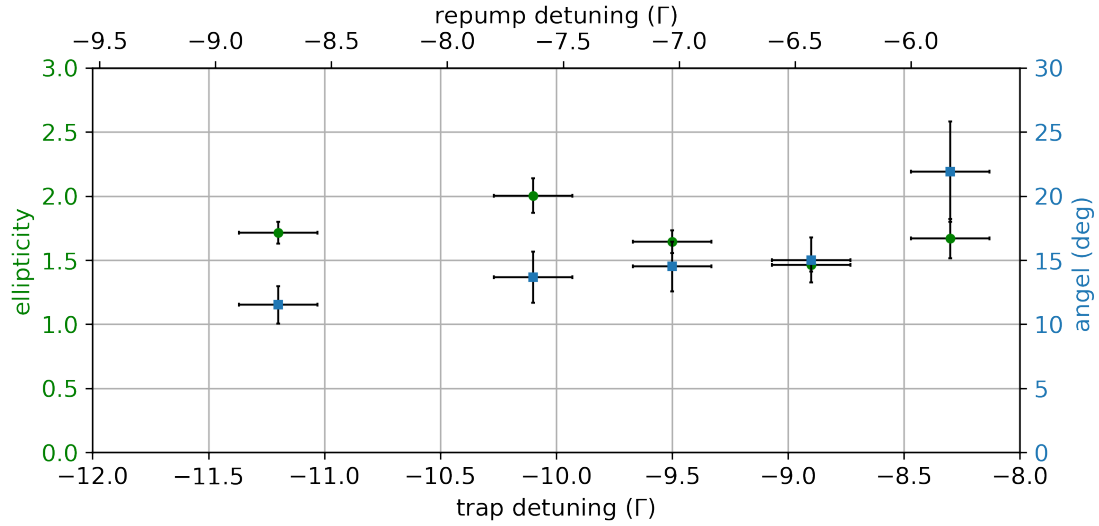

Figure D.17: MOT shape in dependence of the MOT beam detunings. The MOT shape seems to be unaffected by the MOT beam detunings.

Dependence on MOT Beam Power Ratios

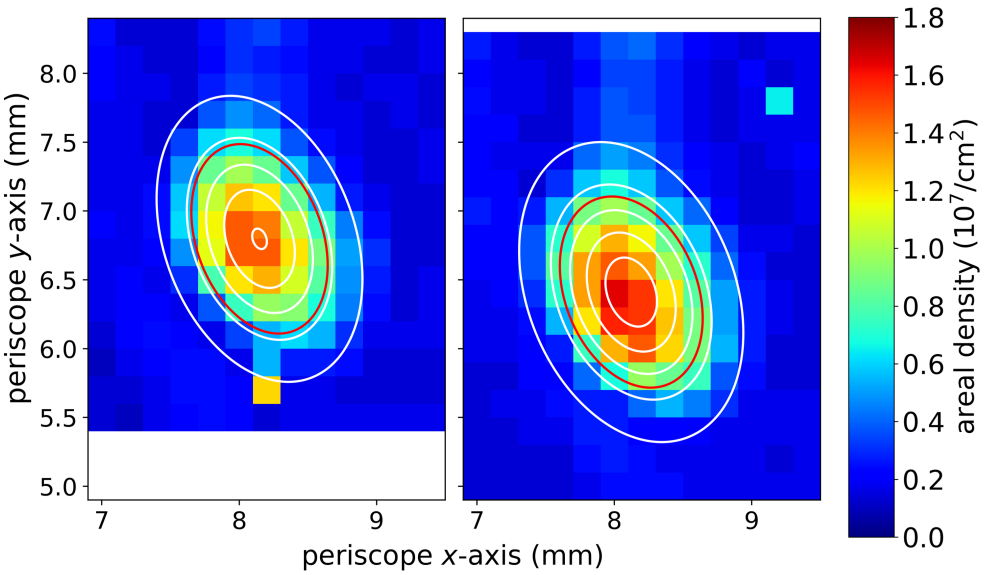

Figure D.18: MOT absorption profile for different beam power ratios. The trap and repump beam powers are equal in this example. On the left side each MOT beam has a power of 60 mW. On the right side the upper two MOT beams each have a power of 70 mW and the lower MOT beams each have a power of 50 mW. For a larger power in the upper MOT beams a higher areal density can be achieved, but the atomic cloud seems to be shifted downwards. Figure adapted from Ref. [71].

Dependence on Push Beam Power

Table D.5: Fit parameters obtained from the push beam power dependence shown in Figure 3.27.

Fit parameter	**Value**
a	$(0.41 \pm 0.07) \times 10^7\,\mathrm{cm}^{-2}$
b	$(0.020 \pm 0.006)\,\mathrm{nW}^{-1}$
c	$(-6.9 \pm 0.6)\,\mu\mathrm{W}^{-1}\mathrm{cm}^{-2}$
d	$(2.25 \pm 0.02) \times 10^7\,\mathrm{cm}^{-2}$
χ^2_{red}	0.4
$n_a(P=0)$	$(2.66 \pm 0.07) \times 10^7\,\mathrm{cm}^{-2}$

Appendix E

Cold Lithium Beam

Table E.1: Experimental parameters for the cold atomic beam measurements with varying push beam settings.

MOT beams	upper beam powers	85 mW
	lower beam powers	80 mW
	repump power	10 mW
	trap detuning	$-11\,\Gamma$
	repump detuning	$-8\,\Gamma$
push beam	beam radius	0.8 mm
	repump power	$\sim 30\,\%$
spectroscopy beam	total power	30 µW
	beam radius	1.9 mm
	repump power	$\sim 50\,\%$
data acquisition	acquisition window	10 ms
	temporal resolution	100 µs

E.1 Arduino Code for PMT Pulse Counting

The following Arduino program was used to acquire time-resolved pulse data from a photomultiplier tube (PMT) in our experiments. The program implements a hardware-based pulse counting scheme using the Arduino's timers:

- **Timer1** is configured as an external counter that increments on each rising edge of the PMT signal. This allows accurate counting of fast pulses.
- **Timer2** generates a fixed sampling interval (here 100 µs), creating discrete time bins for the pulse count.
- An external `gatePin` is used to trigger the start of each measurement. Once triggered, the program collects a predefined number of bins (`numSamples`) before stopping the acquisition.
- After the measurement is complete, the collected pulse counts are transmitted via the serial interface to a computer for further processing.

This approach allows the acquisition of high-resolution, time-binned pulse data without software delays interfering with the counting process. The program is robust to high pulse rates of up to 1 MHz and provides precise temporal binning suitable for statistical analysis of atom arrival times.
The following code presents the full Arduino implementation used in the experiments:

```
const byte gatePin  = 3;  // External trigger to start a measurement
const byte countPin = 5;  // PMT pulses (Timer1 external clock input)

// Measurement parameters
const int binLength   = 100;   // us per bin (set via Timer2)
const int numSamples  = 100;   // Number of bins per measurement

// Shared variables (used in interrupts, must be volatile)
volatile bool measuring   = false;
volatile bool readyToPrint = false;
volatile int counts[numSamples];  // Array to store counts per bin
volatile int index = 0;           // Current bin index

volatile uint32_t counterMulti = 0;  //overflow handling

// Timer1 Compare Match ISR (count overflows)
ISR(TIMER1_COMPA_vect) {
  counterMulti++;
}

// Timer2 Compare Match ISR (fires every 100 us)
// - Reads out Timer1 (PMT pulse counter) into bins
ISR(TIMER2_COMPA_vect) {
  if (measuring) {
    counts[index] = TCNT1;  // Read current pulse count
    index++;                // Advance bin index

```

```
28        if (index >= numSamples) {
29          measuring = false;    // Stop measurement after last bin
30          readyToPrint = true; // Data ready for printing
31        }
32      }
33    }
34
35    // Gate event ISR: triggered by rising edge on gatePin
36    // - Starts a new measurement
37    void GateEvent() {
38      // Reset everything before starting
39      TCNT1 = 0;           // Reset Timer1 counter
40      TCNT2 = 0;           // Reset Timer2 counter
41      index = 0;
42      counterMulti = 0;
43
44      measuring = true;
45      readyToPrint = false;
46    }
47
48    // Setup
49    void setup() {
50      Serial.begin(2000000);
51
52      pinMode(gatePin, INPUT);
53      pinMode(countPin, INPUT);
54
55      noInterrupts();  // Disable interrupts during setup
56
57      //Timer1: external pulse counter
58      TCCR1A = 0;    // Reset control register A
59      TCCR1B = 0;    // Reset control register B
60      TCNT1  = 0;    // Reset counter
61      TIFR1  = 1;    // Reset overflow flag
62      TIMSK1 |= (1 << OCIE1A);  // Enable compare A interrupt (optional)
63
64      // External clock source on pin D5 (T1), rising edge
65      // CS12:CS11:CS10 = 111 --> External clock on T1 pin (rising edge)
66      TCCR1B = (1 << CS12) | (1 << CS11) | (1 << CS10);
67
68      //Timer2: sample clock (100 us = 10 kHz)
69      TCCR2A = 0;    // Reset control register A
70      TCCR2B = 0;    // Reset control register B
71      TCNT2  = 0;    // Reset counter
72
73      OCR2A = 199;                // Compare match at 200 ticks
74      TCCR2A |= (1 << WGM21);     // CTC mode (Clear Timer on Compare)
75
76      //Prescaler = 8 --> 16 MHz / 8 = 2 MHz tick rate
77      // --> 200 counts = 100 us
78      TCCR2B |= (1 << CS21);
79      TIMSK2 |= (1 << OCIE2A);    // Enable compare match interrupt
80
81      interrupts();  // Enable global interrupts
82      // External interrupt on gatePin (start measurement trigger)
83      attachInterrupt(digitalPinToInterrupt(gatePin), GateEvent, RISING);
84    }
```

```
85
86  // Main loop
87  void loop() {
88    // If measurement finished, print results
89    if (!measuring && readyToPrint) {
90      for (int i = 0; i < numSamples; i++) {
91        Serial.print(counts[i]);
92        Serial.print(i < numSamples - 1 ? "," : "\n");
93      }
94      readyToPrint = false;  // Prevent re-printing
95      delay(10);             // Delay to avoid flooding
96    }
97  }
```

E.2 Hot Atomic Background

In our first measurements on the cold atomic beam, we observed a frequency dependent background signal that only appears when the lithium reservoir was heated. We attribute this contribution to fluorescence from hot lithium atoms.

Figure E.1 shows the corresponding fluorescence spectrum together with a Voigt profile fit (see Section B.3). For this measurement, the push beam was turned off. We therefore expect no florescence signal originating from cold atoms. Each data point represents an average of 20 measurements. All other experimental parameters are given in Table E.1. The residuals of the fit are shown below the main plot, and the extracted fit parameters are summarized in Table E.2.

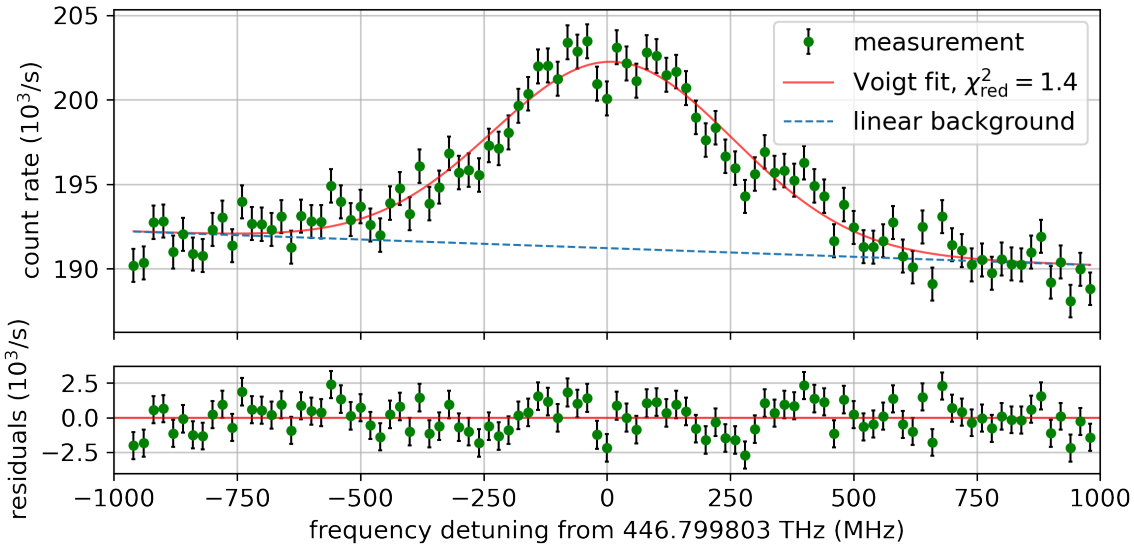

Figure E.1: Fluorescence spectrum of hot atomic background together with a Voigt profile fit. The push beam is turned off. Each data point represents an average of 20 measurements. The spectroscopy beam contains a repump frequency and has a power of 100 µW. All other experimental parameters are as stated in Table E.1.

For the Voigt fit, the Lorentzian width is fixed to saturation broadened linewidth of $\Gamma_S = 6.8\,\mathrm{MHz}$. The extracted Gaussian broadening is $(242 \pm 9)\,\mathrm{MHz}$, which corresponds to a transverse velocity of $v_t \approx 162\,\mathrm{m/s}$. However, to interpret this value and understand the underlying velocity distribution, further simulations of the hot lithium atoms in the vacuum chamber would be required. To suppress this effect, we then implemented collimator for the cold atomic beam (see Figure C.15). For the spectra of the cold atomic beam, we perform a first-order approximation by assuming a linear background.

Table E.2: Fit parameter corresponding to Figure E.1 for a Voigt fit (Section B.3).

Fit parameter	**Value**
broadening σ	$(242 \pm 9)\,\mathrm{MHz}$
amplitude a	$(11.0 \pm 0.3)\,10^3/\mathrm{s}$
frequency offset δ_0	$(13 \pm 7)\,\mathrm{MHz}$
linear background m	$(-1.0 \pm 0.2)/(\mathrm{s\,MHz})$
background b	$(191.0 \pm 0.2)\,10^3/\mathrm{s}$

E.3 Influence of the Spectroscopy Beam Power

When analyzing the recorded frequency spectra for the cold beam measurements, we observe clear deviations from a Voigt profile. These deviations become increasingly pronounced with higher spectroscopy beam power, as illustrated in Figure E.2. This trend is quantitatively reflected in Figure E.3, which shows a systematic increase in the reduced chi-squared with increasing power. Furthermore, Figure E.4 demonstrates that the apparent line center shifts toward higher frequencies as the spectroscopy beam power is raised. Importantly, these effects persist for both forward and reverse frequency scans, as well as for randomized scan sequences, indicating that they are not caused by scan-direction–dependent hysteresis or slow frequency drifts.

Several mechanisms may contribute to the observed power dependence:

- **Residual Zeeman splitting:** The residual earth magnetic field in the spectroscopy region may introduce unresolved Zeeman splitting of approximately 1 MHz. While such splitting generally broadens the spectral line, it alone cannot explain the power dependence unless the spectroscopy beam induces different optical pumping among magnetic sublevels at higher intensities.

- **Repump frequency uncertainty:** The repump frequency is set relative to the hyperfine splitting with an uncertainty of approximately 1 MHz. A mismatch between the actual and intended repump detuning can lead to a splitting of the line shape. This can lead to power dependent asymmetric line shape, if there is optical pumping into a certain hyperfine ground state. Notably, the power dependent line shift also appears in measurements without a repump frequency, suggesting that unresolved hyperfine structure of the excited state contributes as well (see Section 5.1.2).

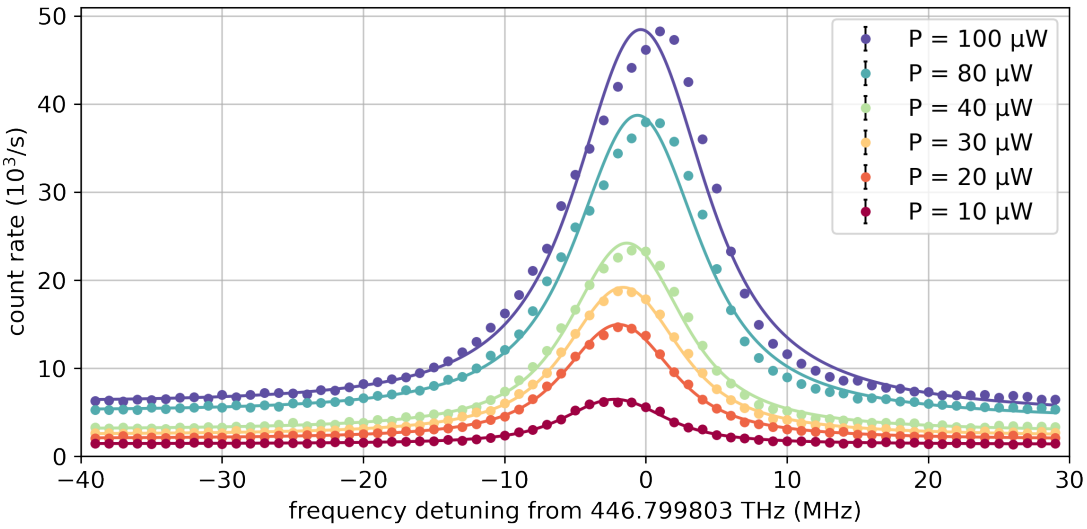

Figure E.2: Florescence spectrum of cold atomic beam for different spectroscopy beam powers. We observe that for an increasing power the line shape deviates more and more from a Voigt profile, with a fixed Doppler broadening $\sigma = 1.8\,\mathrm{MHz}$.

- **Residual Doppler effect:** As shown earlier, the atomic beam possesses a finite axial velocity distribution. Even a slight deviation of the spectroscopy beam from perfect orthogonality introduces a Doppler shift proportional to the mean axial velocity. A small residual angle can therefore shift the line center dependent on the velocity (see Figure E.6). The power dependence may originate from the fact that slower atoms scatter more photons at higher spectroscopy intensities, making them disproportionately represented in the detected signal. Since slower atoms experience a smaller Doppler shift for an angle slightly below 90°, the measured line center appears to shift toward higher frequencies with increasing spectroscopy power. In addition, radiation pressure from the spectroscopy beam can accelerate the cold atoms as they scatter multiple photons, introducing a further Doppler contribution that may lead to additional broadening and a systematic shift of the line center.

Taken together, these observations suggest that the deviations from an ideal Voigt profile, as well as the power dependent line center shift, likely arise from a combination of residual Doppler effects, power dependent optical pumping, and unresolved Zeeman splitting or hyperfine structure. A comprehensive quantitative model that includes the full multilevel structure, atomic beam velocity distribution, and exact optical geometry would be required to fully account for the observed line shapes, but such an analysis lies beyond the scope of this thesis.

To balance the competing requirements of a high signal-to-noise ratio and a reasonably well described spectral line shape, we chose a spectroscopy beam power of 30 µW for the cold beam measurements. Furthermore, if we assume that the power dependent shifts of the line center also occur in the angled measurements, this systematic effect cancels when determining the velocity of the cold atomic beam by subtracting the perpendicular and angled line centers (see Equation 4.3).

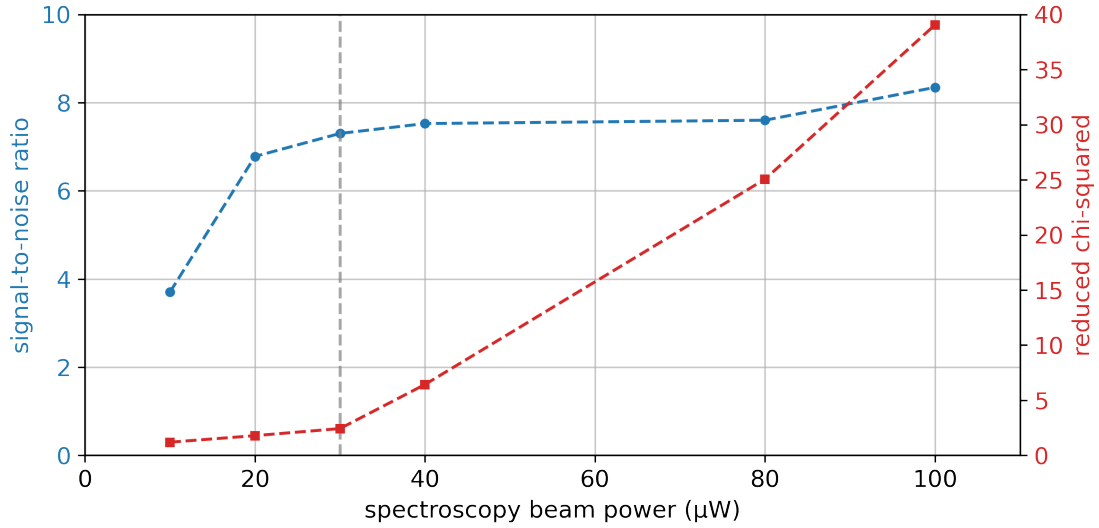

Figure E.3: Signal-to-noise ratio and reduced chi-squared in dependence of the spectroscopy beam power. We try to find a tradeoff between a good signal-to-noise ratio and fitting of the line shape and therefore decided to use a spectroscopy beam power of 30 µW in the measurements of the cold atomic beam velocity.

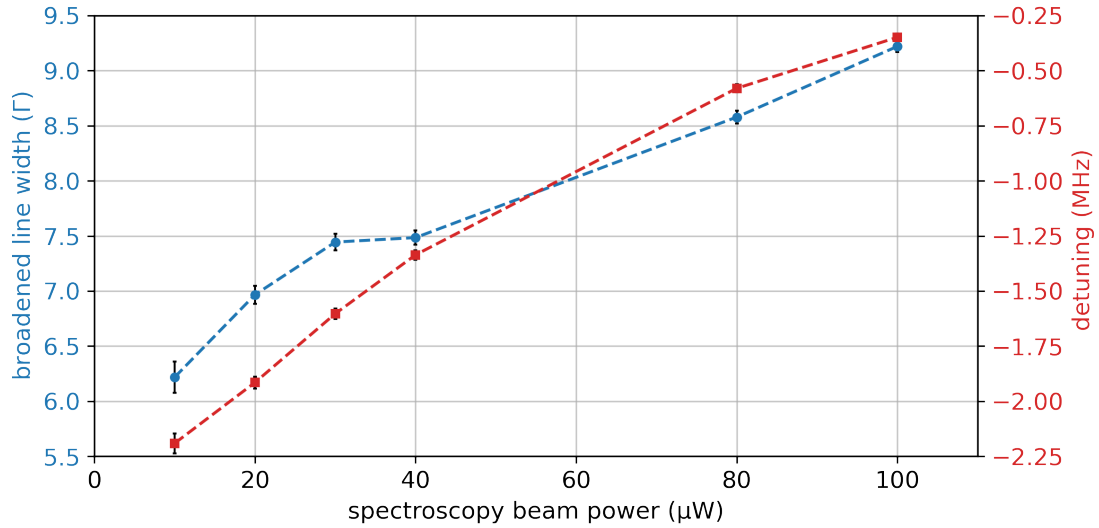

Figure E.4: Power-broadened linewidth and line center as a function of the spectroscopy beam power. As expected, the linewidth increases with increasing spectroscopy beam power due to power broadening. In addition, a shift of the line center with power is observed. For the determination of the axial velocity of the cold atomic beam, this shift is expected to cancel when taking the difference between the perpendicular and angled measurements.

E.4 Supplementary Figures and Tables

E.4.1 Perpendicular Measurements

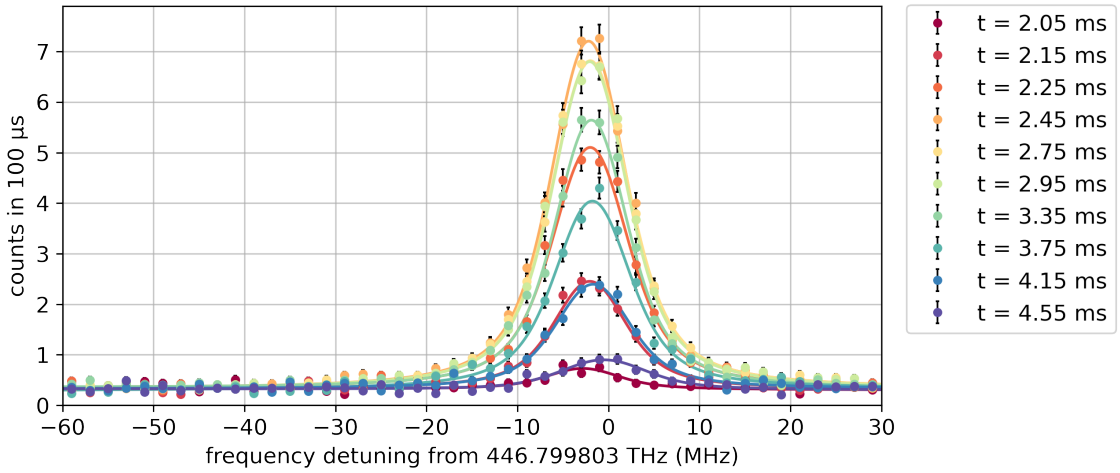

Figure E.5: Example of frequency spectra at different atomic flight times for a perpendicular spectroscopy beam. Each frequency spectrum was fitted with a Voigt profile with a fixed linewidth. The center frequency slightly shifts toward smaller detunings for longer flight times, due to a non-perfect perpendicular alignment. But effect is much smaller than for the angled measurement (see Figure 4.11).

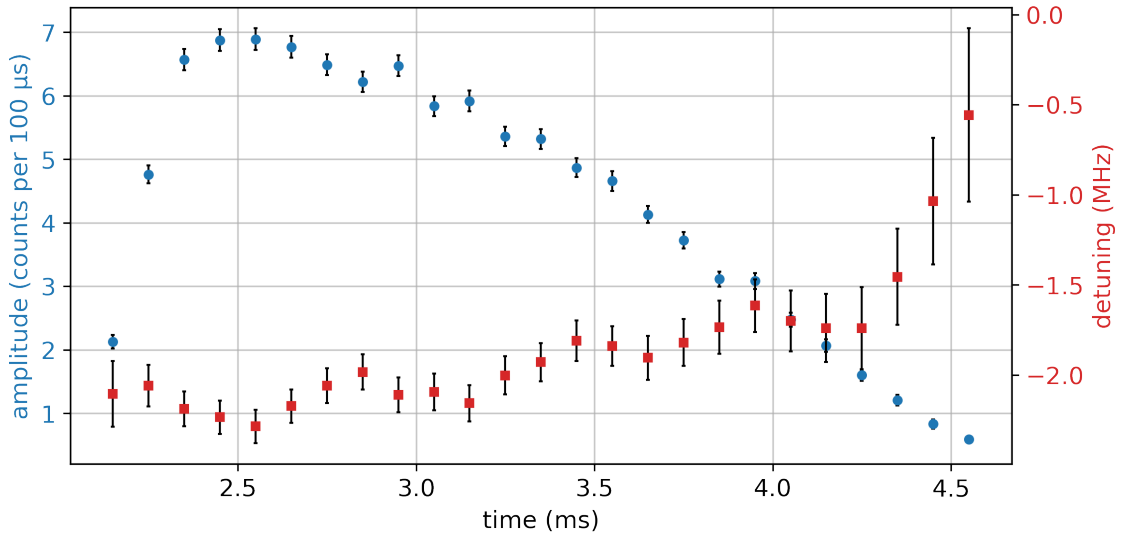

Figure E.6: Amplitude and broadening of Voigt profiles for different flight times from Figure E.5. The amplitude follows the time-of-flight profile, while the detuning approaches zero for longer flight times, consistent with slower atomic velocities. But effect is much smaller than for the angled measurement (see Figure 4.12).

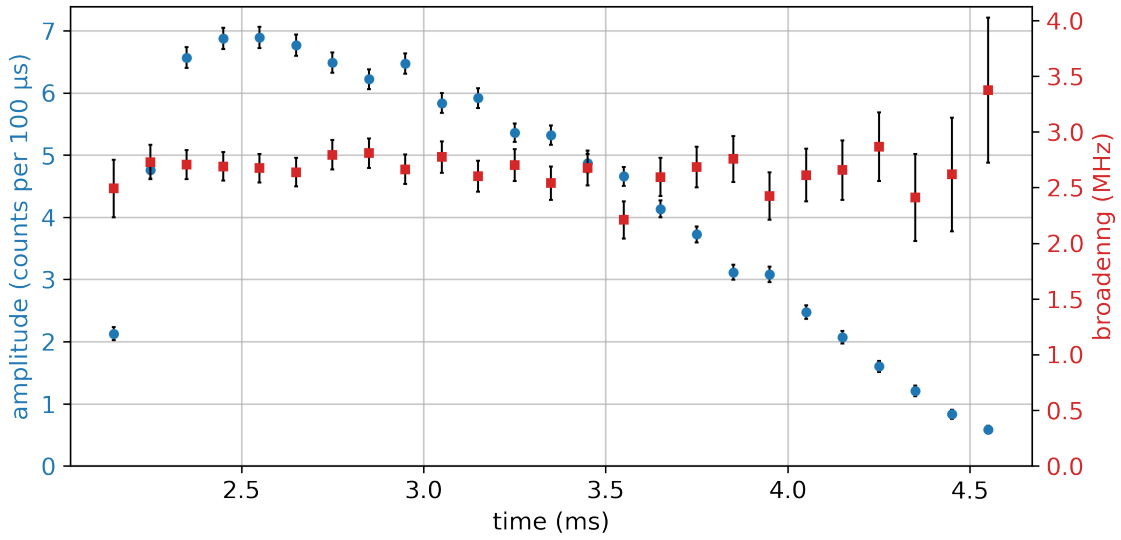

Figure E.7: Amplitude and broadening of Voigt profiles for different flight times from Figure E.5. The amplitude follows the time-of-flight profile, while the broadening stays constant.

E.4.2 Angled Measurements

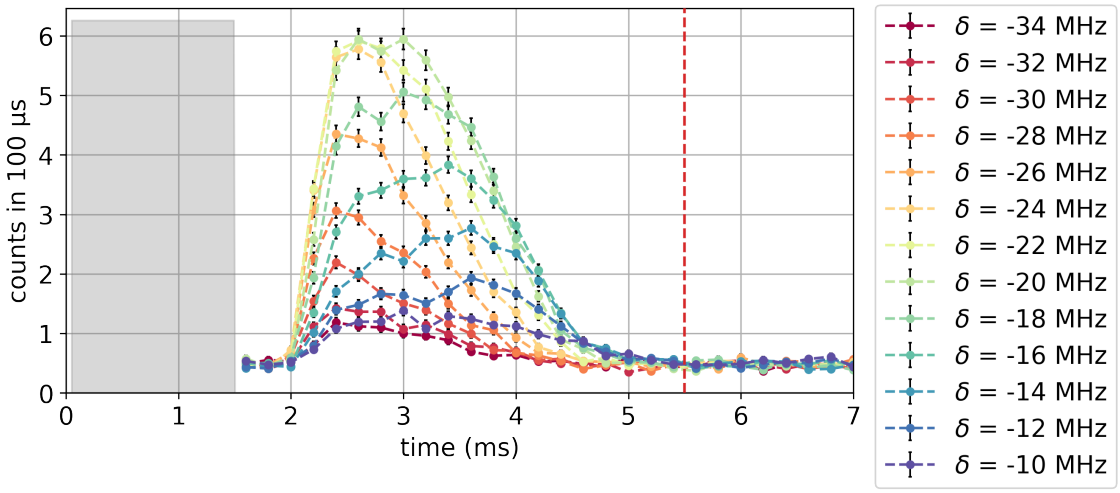

Figure E.8: Example for time-of-flight (TOF) spectra recorded for different spectroscopy beam detunings δ at a spectroscopy angle of $\alpha \approx 80°$. Each spectrum begins with a push pulse (shown in gray). After this pulse we start recording counts, integrated in time bins of 200 µs and averaged over 100 pulses. Data points are connected to guide the eye. The red line indicates a cut that is used to increase the signal-to-noise ratio. The overall amplitude and position of the maximum vary with the detuning.

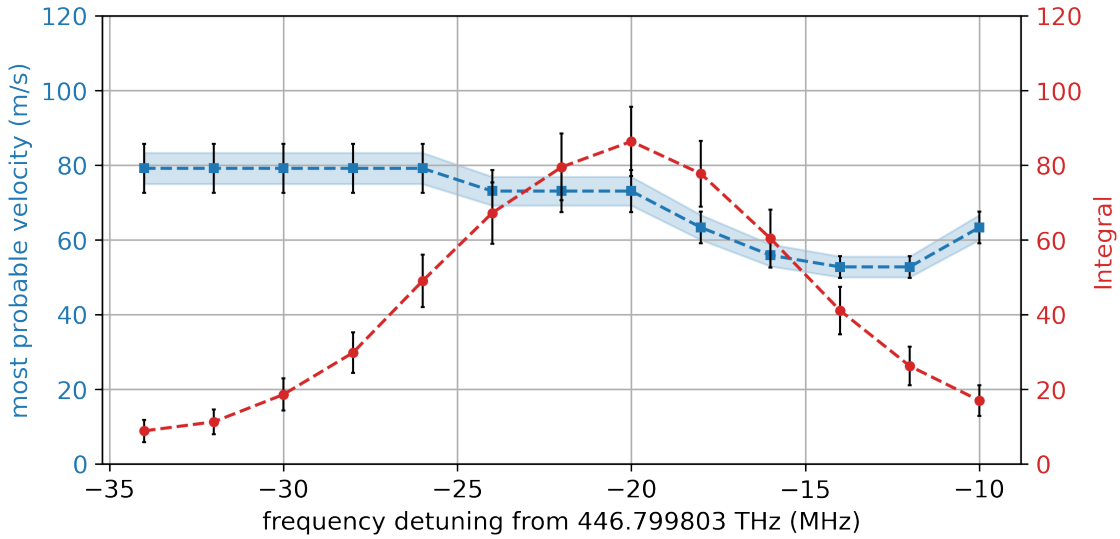

Figure E.9: Integral and most probable velocity of the time-of-flight spectra shown in Figure E.8. The data points are connected using linear interpolation. The integral shows a maximum near the resonance. The most probable velocity decreases with the detuning. The blue band indicates a correlated systematic uncertainty originating from the uncertainty of the flight distance.

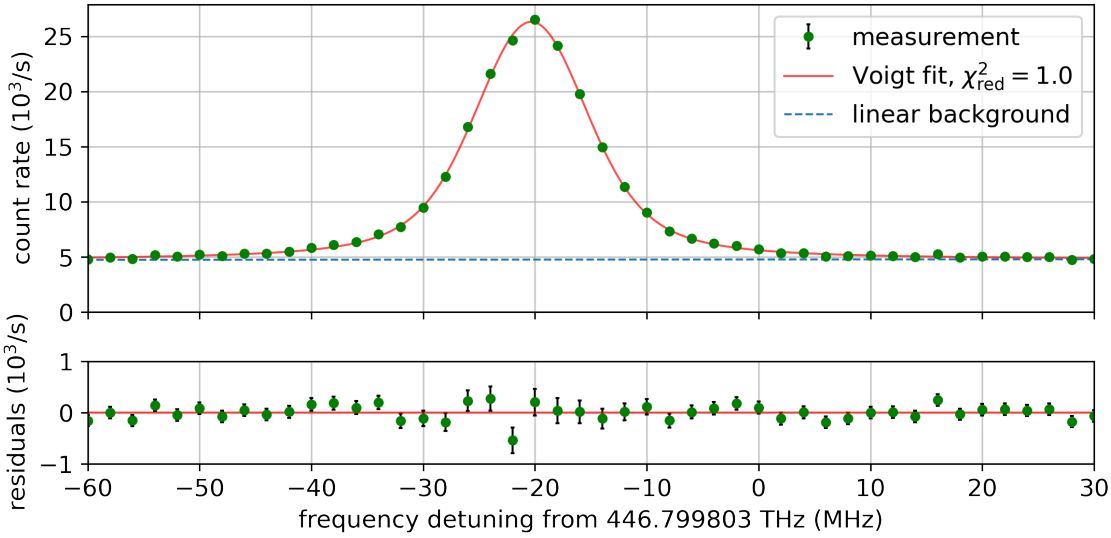

Figure E.10: Example for mean fluorescence spectrum for an angled measurement obtained from time-resolved data from Figure 4.9. The data is fitted with a Voigt profile. The residuals of the fit are shown below the main plot, and the fit values are shown in Table E.3.

Table E.3: Fit parameter corresponding to Figure E.10 for a Voigt fit.

fit parameter	**value**
broadening σ	(3.67 ± 0.04) MHz
amplitude a	$(21.6 \pm 0.2)\, 10^3$/s
frequency offset δ_0	(-4.34 ± 0.03) MHz
linear background m	$(0.47 \pm 0.58)/(\text{s MHz})$
background b	$(4.77 \pm 0.02)\, 10^3$/s

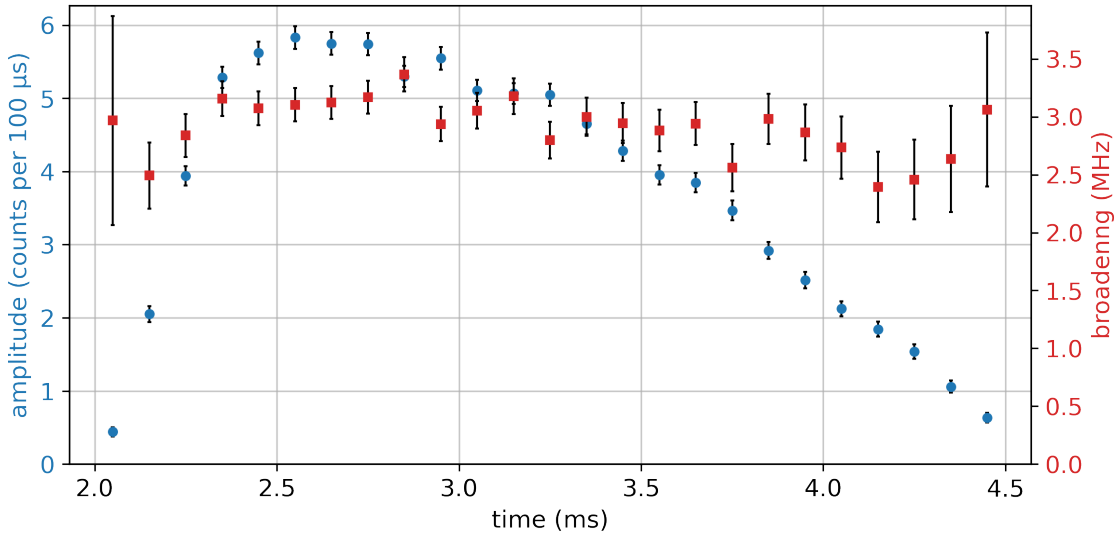

Figure E.11: Amplitude and broadening of Voigt profiles for different flight times from Figure 4.11. The amplitude follows the time-of-flight profile, while the broadening stays constant.

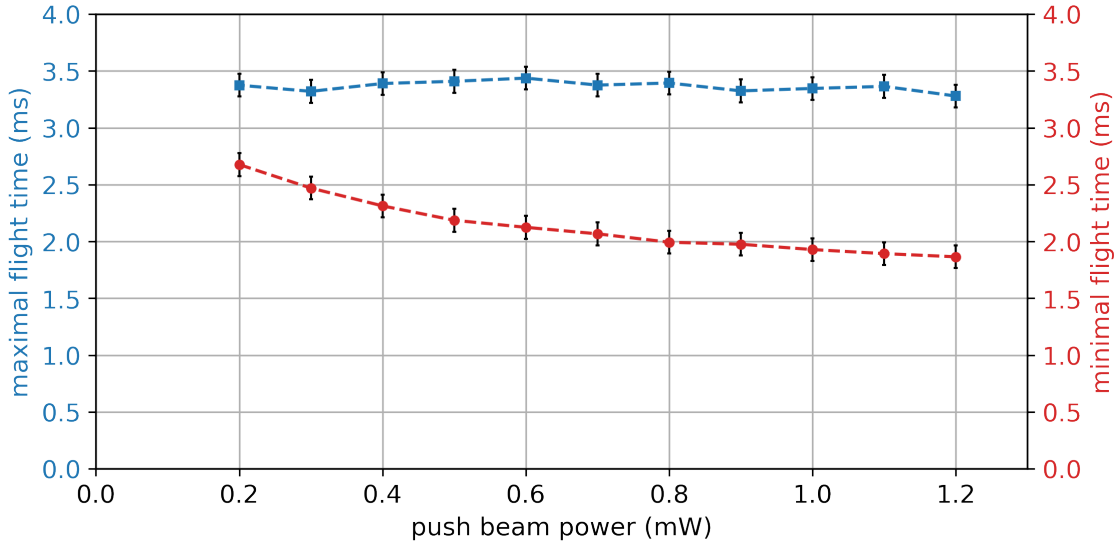

Figure E.12: Minimal and maximal flight time for the TOF spectra in Figure 4.19 in dependence of the push beam power. The minimum time of flight decreases with increasing push power, indicating that the maximum atomic velocity rises due to enhanced photon scattering and power-broadening, allowing atoms to remain in resonance for longer. In contrast, the maximum flight time remains approximately constant.

Appendix F

Toward High-Precision Spectroscopy on a Cold Lithium Beam

F.1 Supplementary Tables on Section 5.1

Table F.1: Fit parameters for the sinusoidal dependence of the fitted detuning and amplitude on the spectroscopy beam polarization angle (see Figure 5.3). The fit function is of the form $f(\theta) = A \cdot \sin(2(\theta - x_0)) + y_0$.

parameter	**detuning**	**amplitude**
A	(0.30 ± 0.03) MHz	$(-1.08 \pm 0.03)\, 10^3$/s
x_0	$(4.5 \pm 6.0)^\circ$	$(-9 \pm 1)^\circ$
y_0	(-3.34 ± 0.05) MHz	$(2.88 \pm 0.03)\, 10^3$/s
χ^2_{red}	0.7	11

F.2 Frequency Stabilization

For frequency stabilization of the spectroscopy laser, a Pound-Drever-Hall (PDH) lock is implemented using an ultra-stable reference cavity. The finesse of the cavity is determined via a cavity ring-down measurement. For this purpose, a fast photodetector is placed behind the cavity to monitor the transmitted optical power. By rapidly switching off the incident laser light with an acousto-optic modulator (AOM), the exponential decay of the intra-cavity field can be observed in the transmitted signal.

The cavity finesse $\mathcal{F}$ is related to the ring-down time constant τ by

$$\mathcal{F} = 2\pi\nu_{\mathrm{FSR}}\tau = (1.510 \pm 0.002) \times 10^5, \tag{F.1}$$

where ν_{FSR} denotes the free spectral range of the cavity. Using $\nu_{\mathrm{FSR}} = 1.5\,\mathrm{GHz}$ and the fitted decay time of $\tau = (16.02 \pm 0.02)\,\mu\mathrm{s}$.

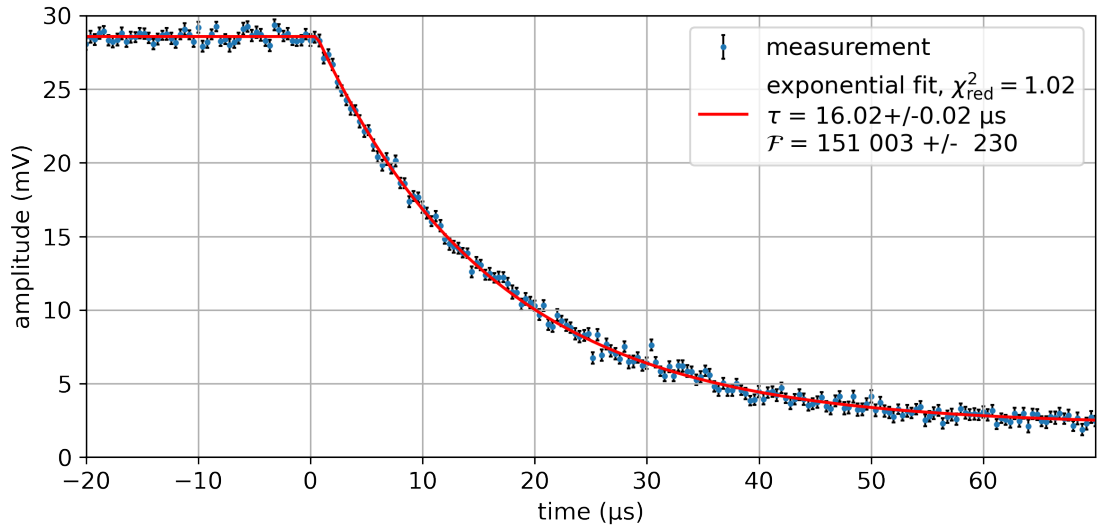

Figure F.1: Cavity ring-down measurement of the ultra-stable reference cavity used for spectroscopy. The transmitted optical power is recorded after switching off the incident laser light using an AOM. The exponential decay of the signal is fitted to extract the cavity ring-down time and determine the cavity finesse.

From the measured finesse we can determine a cavity linewidth of approximately $\delta\nu_{\mathrm{cav}} \approx \nu_{\mathrm{FSR}}/\mathcal{F} \approx 10\,\mathrm{kHz}$. When combined with PDH locking, this provides the basis for achieving a stabilized laser linewidth on the order of 10 Hz.

F.3 Active Fiber-Based Retroreflector

Our active fiber-based retroreflector (AFR) design is largely based on the concept introduced by Beyer *et al.* [3]. In the course of a master's thesis [73] an initial implementation of this design was realized, as shown in Figure F.2. The central idea of the AFR is to generate a retroreflected beam with retracing wavefronts by placing a high-reflectivity mirror at the position of the beam waist while using an optical fiber as a collimator. When the reflected beam matches the incident beam, it couples back efficiently into the fiber. The retroreflection quality can therefore be optimized by maximizing the optical power coupled back into the fiber.

To achieve this, the mirror is mounted on a piezo-actuated mount and incorporated into a feedback loop that continuously maximizes the returned power. In this configuration, the reflected beam closely retraces the incident wavefronts, thereby minimizing residual angular misalignment. As a result, systematic frequency shifts arising from the first-order Doppler effect are significantly suppressed (see Figure 1.8).

The entire assembly is mounted on a motorized rotation stage, which allows precise adjustment of the angle between the lithium atomic beam and the spectroscopy beam. This enables systematic investigations of residual Doppler shifts by varying the angle between the cold lithium and the spectroscopy beam. For future measurements, the mechanical rigidity of the construction should be improved to reduce vibrational noise. In addition, a mechanism for controlled rotation of the linear polarization will be implemented in order to correct for quantum interference effects.

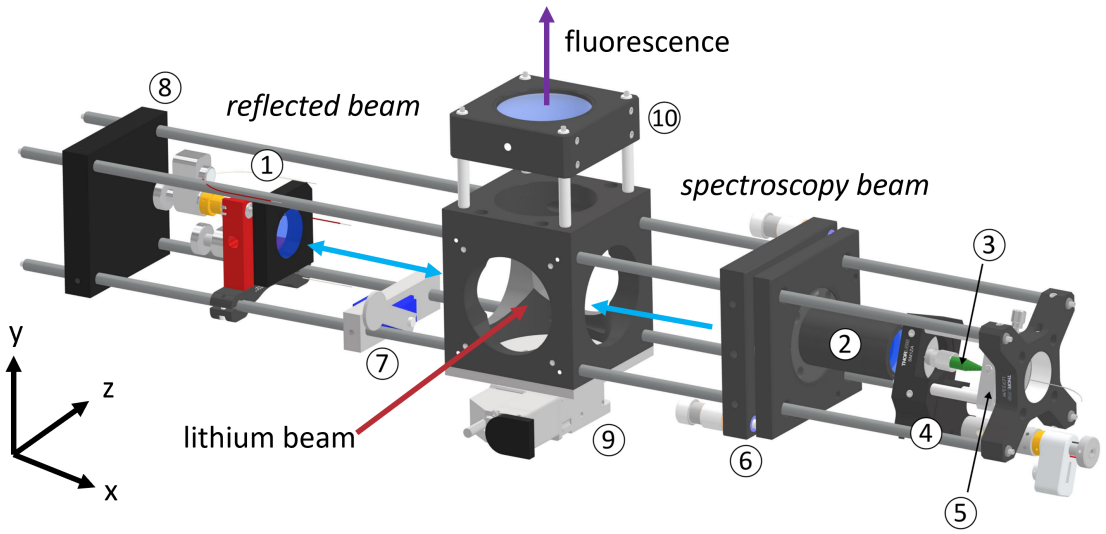

Figure F.2: Prototype of the active fiber-based retroreflector (AFR) setup. The spectroscopy beam is reflected by a mirror in a piezo mount (1). The collimator (2) is placed after a polarization-maintaining fiber (3). The collimator position can be adjusted using a x-translation stage (4) and a yz-translation stage (5). Angular alignment is achieved with a mirror mount (6). A shutter (7) allows blocking of the retroreflected beam. The entire assembly is installed on a motorized rotation stage (9), mechanically balanced by a counterweight (8). A lens (10) collimates the fluorescent light onto a detector. Figure adapted from Ref. [73].

F.4 Zeeman Splitting

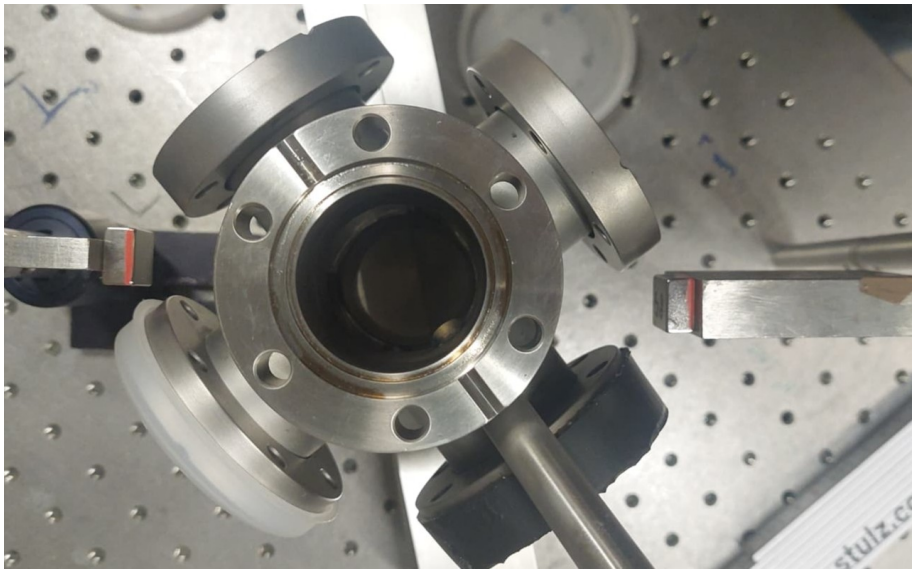

Figure F.3: Picture of the setup for the test of the Zeeman splitting. A pair of permanent magnets was positioned at a distance of (17 ± 1) cm close to the six-way cross, generating a roughly homogeneous magnetic field of (1.1 ± 0.3) mT in the center of the spectroscopy region.

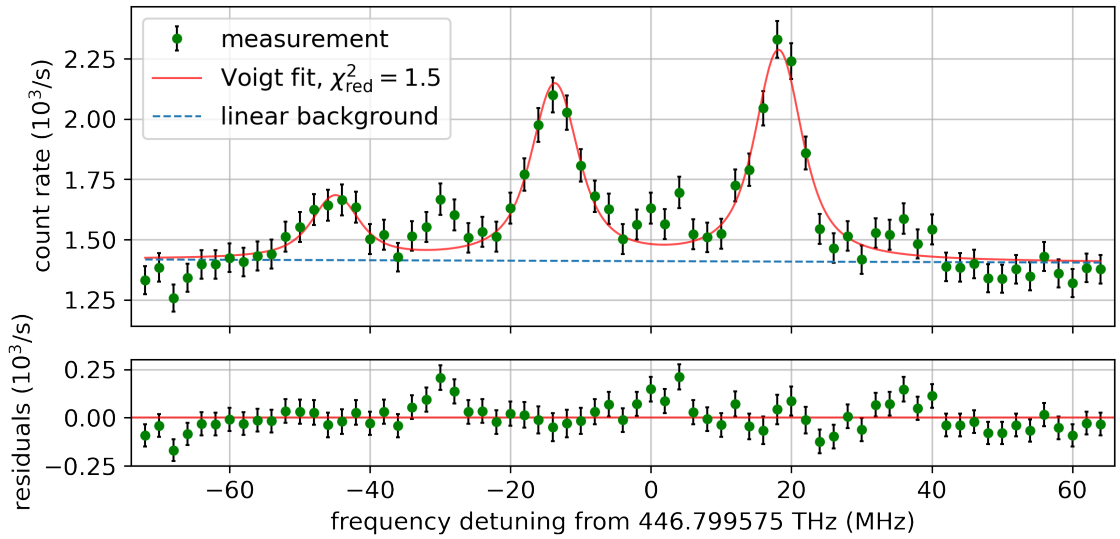

Figure F.4: Spectrum of the upper hyperfine ground state D_2 transition in the presence of a (1.1 ± 0.3) mT magnetic field oriented at approximately 45° to the linearly polarized spectroscopy beam for a for a right-handed circular polarized push beam. Each hyperfine component is split into multiple Zeeman components. The relative amplitudes are differently compared to the measurement with a left-handed circular polarized push beam (see Figure 5.7).

References

[1] R. C. Brown et al., "Quantum interference and light polarization effects in unresolvable atomic lines: Application to a precise measurement of the ^{6,7}Li D_2 lines", Physical Review A **87**, 032504 (2013).

[2] T. G. Tiecke et al., "A high-flux 2D MOT source for cold lithium atoms", Physical Review A **80**, 013409 (2009).

[3] A. Beyer et al., "Active fiber-based retroreflector providing phase-retracing anti-parallel laser beams for precision spectroscopy", Optics Express **24**, 17470 (2016).

[4] G. W. Drake and Z. .-. Yan, "High-precision spectroscopy as a test of quantum electrodynamics in light atomic systems", Canadian Journal of Physics **86**, 45–54 (2008).

[5] M. I. Eides, H. Grotch, and V. A. Shelyuto, "Theory of light hydrogenlike atoms", Physics Reports **342**, 63–261 (2001).

[6] Z.-T. Lu et al., "*Colloquium* : Laser probing of neutron-rich nuclei in light atoms", Reviews of Modern Physics **85**, 1383–1400 (2013).

[7] E. Tiesinga et al., "CODATA Recommended Values of the Fundamental Physical Constants: 2018", Journal of Physical and Chemical Reference Data **50**, 033105 (2021).

[8] T. W. Hänsch, "Precision Spectroscopy of Atomic Hydrogen", AIP Conference Proceedings **323** (1994).

[9] C. G. Parthey et al., "Improved Measurement of the Hydrogen 1S - 2S transition frequency", Physical Review Letters **107**, 203001 (2011).

[10] A. Grinin et al., "Two-photon frequency comb spectroscopy of atomic hydrogen", Science **370**, 1061–1066 (2020).

[11] R. Pohl et al., "The size of the proton", Nature **466**, 213–216 (2010).

[12] C. G. Parthey et al., "Precision Measurement of the Hydrogen-Deuterium 1S - 2S isotope shift", Physical Review Letters **104**, 233001 (2010).

[13] R. Pohl et al., "Laser spectroscopy of muonic deuterium", Science **353**, 669–673 (2016).

[14] K. Pachucki and V. A. Yerokhin, "Fine structure of helium-like ions and determination of the fine structure constant", Physical Review Letters **104**, 070403 (2010).

[15] V. Patkóš, V. A. Yerokhin, and K. Pachucki, "Complete $\alpha^7 m$ Lamb shift of helium triplet states", Physical Review A **103**, 042809 (2021).

[16] V. Patkóš, V. A. Yerokhin, and K. Pachucki, "Radiative $\alpha^7 m$ QED contribution to the helium Lamb shift", Physical Review A **103**, 012803 (2021).

[17] Y. R. Sun and S.-M. Hu, "Precision spectroscopy of atomic helium", National Science Review **7**, 1818–1827 (2020).

[18] E. Riis et al., "Lamb shifts and hyperfine structure in $^6Li^+$ and $^7Li^+$: Theory and experiment", Physical Review A **49**, 207–220 (1994).

[19] P. Imgram et al., "Collinear Laser Spectroscopy of $2^1S_3 \rightarrow 2^3P_J$ Transitions in Helium-like $^{12}C^{4+}$", Physical Review Letters **131**, 243001 (2023).

[20] K. Schuhmann et al., "The helion charge radius from laser spectroscopy of muonic helium-3 ions", (2025).

[21] J. J. Krauth et al., "Measuring the α-particle charge radius with muonic helium-4 ions", Nature **589**, 527–531 (2021).

[22] W. I. McAlexander, E. R. I. Abraham, and R. G. Hulet, "Radiative lifetime of the 2p state of lithium", Physical Review A **54**, R5–R8 (1996).

[23] M. E. Gehm, "Preparation of an optically-trapped degenerate Fermi gas of ^6Li: Finding the route to degeneracy", PhD thesis (2003).

[24] C. E. Simien et al., "Progress at NIST in measuring the D lines of Li isotopes using an optical frequency synthesizer", Canadian Journal of Physics **89**, 59–62 (2011).

[25] A. Nogga et al., "Spectra and binding energy predictions of chiral interactions for ^7Li", Physical Review C **73**, 064002 (2006).

[26] E. Epelbaum et al., "Lattice calculations for $A = 3, 4, 6, 12$ nuclei using chiral effective field theory", The European Physical Journal A **45**, 335–352 (2010).

[27] Y. Yang et al., "Zemach radii and nuclear structure effects in hyperfine splitting of Lithium", `10.48550/arXiv.2509.01303` (2025).

[28] B. Ohayon et al., "Towards Precision Muonic X-Ray Measurements of Charge Radii of Light Nuclei", Physics **6**, 206–215 (2024).

[29] S. S. Li Muli, A. Poggialini, and S. Bacca, "Muonic Lithium atoms: nuclear structure corrections to the Lamb shift", SciPost Physics Proceedings, 028 (2020).

[30] C. E. Carlson, "The Proton Radius Puzzle", Progress in Particle and Nuclear Physics **82**, 59–77 (2015).

[31] D. Tucker-Smith and I. Yavin, "Muonic hydrogen and MeV forces", Physical Review D **83**, 101702 (2011).

[32] C. E. Carlson and B. C. Rislow, "New physics and the proton radius problem", Physical Review D **86**, 035013 (2012).

[33] M. Puchalski, D. Kedziera, and K. Pachucki, "D_1 and D_2 lines in $^{6,7}Li$ including QED effects", Physical Review A **87**, 032503 (2013).

[34] M. Puchalski and K. Pachucki, "Ground state hyperfine splitting in $^{6,7}Li$ atoms and the nuclear structure", Physical Review Letters **111**, 243001 (2013).

[35] M. Puchalski and K. Pachucki, "Quantum Electrodynamics Corrections to the 2P fine splitting in Li", Physical Review Letters **113**, 073004 (2014).

[36] M. Puchalski, D. Kędziera, and K. Pachucki, "Ground state of Li and Be^+ using explicitly correlated functions", Physical Review A **80**, 032521 (2009).

[37] Z.-C. Yan and G. W. F. Drake, "Bethe Logarithm and QED Shift for Lithium", Physical Review Letters **91**, 113004 (2003).

[38] M. Puchalski and K. Pachucki, "Relativistic, QED, and finite nuclear mass corrections for low-lying states of Li and Be^+", Physical Review A **78**, 052511 (2008).

[39] M. Puchalski and K. Pachucki, "Fine and hyperfine splitting of the 2P state in Li and Be^+", Physical Review A **79**, 032510 (2009).

[40] G. Li et al., "High-energy electron scattering from ^{6}Li", Nuclear Physics A **162**, 583–592 (1971).

[41] W. Nörtershäuser et al., "Isotope-shift measurements of stable and short-lived lithium isotopes for nuclear-charge-radii determination", Physical Review A **83**, 012516 (2011).

[42] W. Nörtershäuser et al., "Charge radii and ground state structure of lithium isotopes: Experiment and theory reexamined", Physical Review C **84**, 024307 (2011).

[43] L. R. Suelzle, M. R. Yearian, and H. Crannell, "Elastic Electron Scattering from ^{6}Li and ^{7}Li", Physical Review **162**, 992–1005 (1967).

[44] F. A. Bumiller et al., "Elastic Electron Scattering from ^{6}Li and ^{7}Li at Low Momentum Transfer", Physical Review C **5**, 391–395 (1972).

[45] C. De Jager, H. De Vries, and C. De Vries, "Nuclear charge-and magnetization-density-distribution parameters from elastic electron scattering", Atomic data and nuclear data tables **14**, 479–508 (1974).

[46] B. A. Bushaw et al., "Hyperfine splitting, isotope shift, and level energy of the 3S states of ^{6,7}Li", Physical review letters **91**, 043004 (2003).

[47] G. Ewald et al., "Nuclear charge radii of ^{8,9}Li determined by laser spectroscopy", Physical review letters **93**, 113002 (2004).

[48] W. Nörtershäuser et al., "Isotope Shift Measurements of Stable and Short-Lived Lithium Isotopes for Nuclear Charge Radii Determination", Physical Review A **83**, 012516 (2011).

[49] Y.-H. Lien et al., "Absolute frequencies of the ^{6,7}Li $2s\ ^2S_{1/2} \rightarrow 3s\ ^2S_{1/2}$ transitions", Physical Review A **84**, 042511 (2011).

[50] C. J. Sansonetti et al., "Measurements of the resonance lines of ^{6}Li and ^{7}Li by doppler-free frequency-modulation spectroscopy", Physical Review A **52**, 2682 (1995).

[51] W. Scherf et al., "Re-measurement of the transition frequencies, fine structure splitting and isotope shift of the resonance lines of lithium, sodium and potassium", Zeitschrift für Physik D Atoms, Molecules and Clusters **36**, 31–33 (1996).

[52] J. Walls et al., "Measurement of isotope shifts, fine and hyperfine structure splittings of the lithium D lines", The European Physical Journal D **22**, 159–162 (2003).

[53] G. Noble et al., "Isotope shifts and fine structures of ^{6,7}Li D lines and determination of the relative nuclear charge radius", Physical Review A—Atomic, Molecular, and Optical Physics **74**, 012502 (2006).

[54] D. Das and V. Natarajan, "Absolute frequency measurement of the lithium D lines: Precise determination of isotope shifts and fine-structure intervals", Physical Review A **75**, 052508 (2007).

[55] C. J. Sansonetti et al., "Absolute Transition Frequencies and Quantum Interference in a Frequency Comb Based Measurement of the ^{6,7}Li D Lines", Physical Review Letters **107**, 023001 (2011).

[56] M. Horbatsch and E. A. Hessels, "Shifts from a distant neighboring resonance", Physical Review A **82**, 052519 (2010).

[57] T. Udem et al., "Quantum Interference Line Shifts of Broad Dipole-Allowed Transitions", Annalen der Physik **531**, 1900044 (2019).

[58] R. Li et al., "Absolute Frequency Measurement of ^{6}Li D Lines with kHz-Level Uncertainty", Physical Review Letters **124**, 063002 (2020).

[59] M. Willig, "Cooling and Slowing Towards a Lithium MOT for High Precision Laser Spectroscopy", PhD thesis (JGU Mainz, Sept. 2024).

[60] K. Dieckmann et al., "Two-dimensional magneto-optical trap as a source of slow atoms", Physical Review A **58**, 3891–3895 (1998).

[61] N. Castagna et al., "A novel simplified two-dimensional magneto-optical trap as an intense source of slow cesium atoms", The European Physical Journal Applied Physics **34**, 21–30 (2006).

[62] S. Zhang et al., "A dark-line two-dimensional magneto-optical trap of ^{85}Rb atoms with high optical depth", Review of Scientific Instruments **83**, 073102 (2012).

[63] S. Dörscher et al., "Creation of Quantum-Degenerate Gases of Ytterbium in a Compact 2D-/3D-MOT Setup", Review of Scientific Instruments **84**, 043109 (2013).

[64] S. Jin et al., "A two-dimensional magneto-optical trap of dysprosium atoms as a compact source for efficient loading of a narrow-line three-dimensional magneto-optical trap", Physical Review A **108**, 023719 (2023).

[65] K. Li et al., "Enhanced trapping of cold ^{6}Li using multiple-sideband cooling in a two-dimensional magneto-optical trap", Physical Review A **92**, 013419 (2015).

[66] T. Hammel et al., "Modular quantum gas platform", Physical Review A **111**, `10.1103/physreva.111.033314` (2025).

[67] C. J. Foot, *Atomic physics*, Oxford Master Series in Physics 7. Atomic, Optical, and laser physics (Oxford University Press, Oxford ; New York, 2005).

[68] A. Westerhoff, "Aufbau einer 2D MOT für Lithium", BA thesis (JGU Mainz, May 2021).

[69] H.-L. Schumacher, "Two-dimensional magneto-optical Trap for Lithium Atoms", MA thesis (JGU Mainz, Nov. 2022).

[70] B. M. Tscharn, “A Cold Lithium Beam from a Two-Dimensional Magneto-Optical Trap”, MA thesis (JGU Mainz, Aug. 2023).

[71] T. Redelbach, “Optimisation of a two-dimensional magneto-optical trap for high-precision laser spectroscopy of lithium”, MA thesis (JGU Mainz, Jan. 2025).

[72] C. F. Staudt, “Precision Simulation of a 2D MOT for Lithium-6”, MA thesis (JGU Mainz, Nov. 2025).

[73] H. K. Jost, “Active Fibre-Based Retroreflector for High-Precision Laser Spectroscopy on Lithium”, MA thesis (JGU Mainz, May 2024).

[74] A. Westerhoff, “Building a fiber noise cancellation system for a 100 m fiber link”, MA thesis (JGU Mainz, Feb. 2024).

[75] C. Hammer, “Laserintensitätsstabilisierung zur Lithiumspektroskopie”, BA thesis (JGU Mainz, Aug. 2024).

[76] D. Lutz, “Aufbau und Charakterisierung eines analogen PID-Reglers zur Laserintensitätsstabilisierung”, BA thesis (JGU Mainz, Feb. 2025).

[77] T. Redelbach, “Dopplerfreie Sättigungsspektroskopie an Lithium mittels auf einem Interferenzfilter basierenden External Cavity Diode Laser”, BA thesis (JGU Mainz, Nov. 2022).

[78] E. Arimondo, M. Inguscio, and P. Violino, “Experimental determinations of the hyperfine structure in the alkali atoms”, Reviews of Modern Physics **49**, 31–75 (1977).

[79] S. J. Blundell and K. M. Blundell, *Concepts in thermal physics* (Oup Oxford, 2010).

[80] C. B. Alcock, V. Itkin, and M. Horrigan, “Vapour pressure equations for the metallic elements: 298–2500k”, Canadian metallurgical quarterly **23**, 309–313 (1984).

[81] A. Kerkmann, “A novel Apparatus for Quantum Gas Microscopy of Lithium Atoms”, PhD thesis (Universität Hamburg, 2019).

[82] M. Ortner and L. G. C. Bandeira, “Magpylib: a free python package for magnetic field computation”, SoftwareX **11**, 100466 (2020).

[83] F. Hees, “Optimized Magnetic System for a 2D MOT”, BA Thesis (JGU Mainz, Aug. 2025).

[84] M. S. Fischer, “A matter-wave microscope for lithium atoms in a tunable optical lattice”, PhD thesis (Universität Hamburg, Aug. 2023).

[85] A. M. Steane, M. Chowdhury, and C. J. Foot, “Radiation force in the magneto-optical trap”, Journal of the Optical Society of America B **9**, 2142 (1992).

[86] T. Walker, D. Sesko, and C. Wieman, “Collective behavior of optically trapped neutral atoms”, Physical Review Letters **64**, 408–411 (1990).

[87] M. H. Hagemann, “A Setup for High-Resolution Imaging of Ultracold Lithium Atoms”, PhD thesis (Universität Hamburg, 2020).

[88] G. Lamporesi et al., “Compact high-flux source of cold sodium atoms”, Review of Scientific Instruments **84**, 10.1063/1.4808375 (2013).

[89] I. Sydoryk et al., “Broadening and intensity redistribution in the Na(3p) hyperfine excitation spectra due to optical pumping in the weak excitation limit”, Physical Review A **77**, 042511 (2008).

[90] L. Maisenbacher, “Precision Spectroscopy of the 2S-nP Transitions in Atomic Hydrogen”, PhD thesis (Dec. 2020).

[91] A. Beckmann, K. D. Böklen, and D. Elke, “Precision measurements of the nuclear magnetic dipole moments of ^{6}Li,^{7}Li,^{23}Na,^{39}K and ^{41}K”, Zeitschrift für Physik **270**, 173–186 (1974).

[92] S. Schmidt et al., “The next generation of laser spectroscopy experiments using light muonic atoms”, Journal of Physics: Conference Series **1138**, 012010 (2018).

[93] L. Ahlvers, “Optimierung einer 2D-MOT für Lithium-6 durch Einbau eines neuen Magnetsystems”, BA thesis (JGU Mainz, Feb. 2026).